Synthesis of π-Conjugated Oligomers for Controlling the Nanostructure in Organic Thin Film Solar Cells

（π共役系オリゴマーの合成と有機薄膜太陽電池のナノ構造制御）

Takeshi NISHIZAWA
Hashiomoto Laboratory

Department of Applied Chemistry
Graduate School of Engineering, The University of Tokyo

Table of Contents

Chapter 1. General Introduction

Chapter 2. Supramolecular Formation of Fibrous Nanostructure in Donor-Acceptor Dyad Film

Chapter 3. Effect of crystallinity in donor groups on performance of photovoltaic devices based on oligothiophene-fullerene dyad

Chapter 4. Efficient Dyad-Based Organic Solar Cells with a Highly Crystalline Donor Group

Chapter 1.

General Introduction

1.1. Background and objective of this study

1.1.1. Background

Nanostructure control in organic thin solid films is of great importance for investigating the correlation between the nanostructure of molecular assembly and (opto-)electronic processes such as intermolecular photo-induced energy and electron transfer as well as hole and electron transport (i.e. usually carrier hopping), and thus for understanding the mechanism of such phenomena in the solid state. There have been tremendous number of studies on intra- and intermolecular photo-induced energy and electron transfer processes with electron donor and acceptor linked molecules (e.g. donor-acceptor dyads) or the physical mixture of the donor and the acceptor in solution to reveal that the spatial distance of the donor and acceptor as well as the orientation of them are of great importance in such phenomena [1-12]. However, there have been few such studies in the solid state and thus it is of great interest to elucidate the important factors in intermolecular opto-electronic and carrier transport processes in the solid state. In the solid state, in which no solvent exists, the order and orientation of the molecules through their intermolecular interactions such as van der Waals interactions are expected to be important factors in intermolecular opto-electronic and carrier transport processes. In fact, highly ordered and oriented π-conjugated oligomers and polymers achieve high, anisotropic carrier mobility in the films [13-22]. Therefore it is of great desire to control the nanostructure in molecular level to comprehensively understand to what extent the order and orientation of the molecules in aggregated state affect the intermolecular opto-electronic and carrier transport processes.

The main theme of this dissertation is thus to control the nanostructures in the thin solid film in molecular level by means of molecular designs. This study especially focuses on controlling the nanostructure of electron-donating and accepting molecules in organic thin film solar cells.

Organic thin film solar cells, especially ones made from soluble organic materials such as π-conjugated oligomers, polymers, and fullerene derivatives have recently drawn much attention as a sustainable energy source with low fabrication cost [23, 24]. The basic structure of the cells is depicted in Figure 1.1.1. The organic thin film is sandwiched in between a transparent electrode such as indium tin oxide (ITO) and a metal electrode such as aluminum. In the organic film are used π-conjugated oligomers and polymers such as poly(3-hexylthiophene-2,5-diyl) as donor materials, and a fullerene derivative, phenyl-C_{61}-butyric acid methyl ester (PCBM) as an acceptor material (Figure 1.1.2).

The working principle of the cells is composed of following 4 steps: 1. Light absorption, 2. exciton diffusion, 3. charge separation at the interface of the donor and organic acceptor, and 4. charge transport to the electrodes. In the first step, light absorption in the film generates excitons which are bounded hole and electron pairs with Coulombic force. In the next step these generated excitons diffuse to the interface of the donor and the acceptor where charge separation takes place (the third step). Then the separated charges transfer to the electrode by intermolecular hole and electron hopping.

One promising structure to efficiently achieve these steps above and thus to achieve a high efficiency is bulk heterojunction structure (i.e. randomly dispersed structures of the donor and the acceptor in the film) depicted in Figure 1.1.3. Bulk heterojunction structure achieves a large interface of the donor and acceptor, resulting in the efficient charge separation. When the donor and acceptor domains form interpenetrating network (i.e. mutually percolated domains of the donor and the acceptor throughout the film), efficient charge transport can also be achieved. In such a case, high efficiencies of 4-5% have been achieved [25-40]. However, the formation of such appropriate nanostructure of the donor and the acceptor in bulk heterojunction system is not always guaranteed and is often difficult to reproduce since it is simply achieved by spontaneous (without any control) phase separation and crystallization of donor and acceptor materials during spin-coating and post thermal annealing processes. As a result, formation of inappropriate nanostructures such as large phase separation or dead ends (i.e. disconnected carrier pathways to the electrodes) often happens. Large phase separation can easily occur in 100 nm or a larger scale when the miscibility of the materials is low or the annealing condition

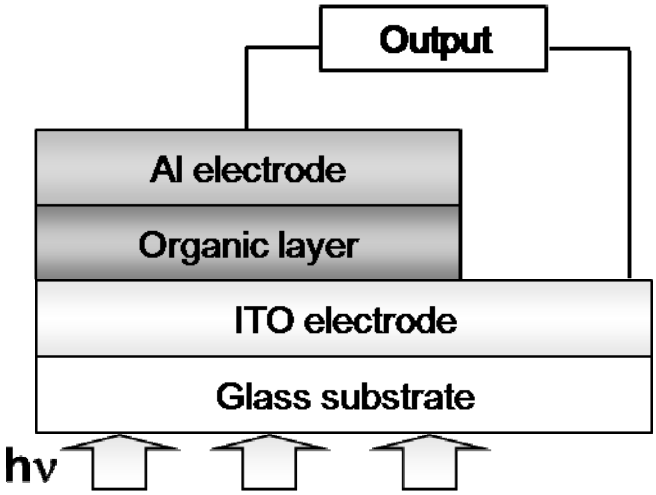

Figure 1.1.1. The basic structure of organic thin film solar cells.

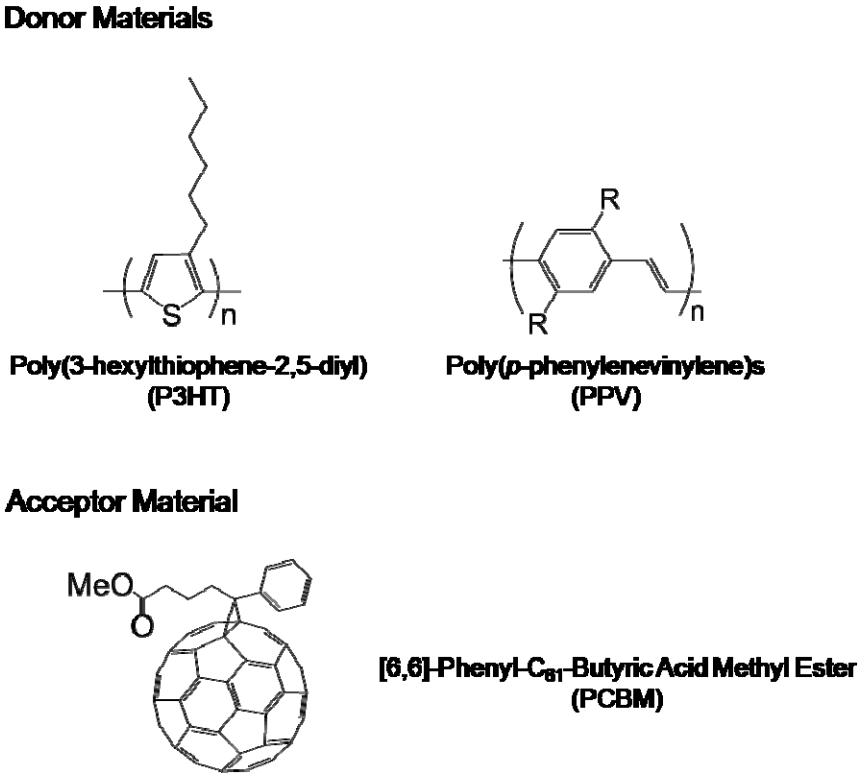

Figure 1.1.2. Electron donor and acceptor materials used in organic thin film solar cells.

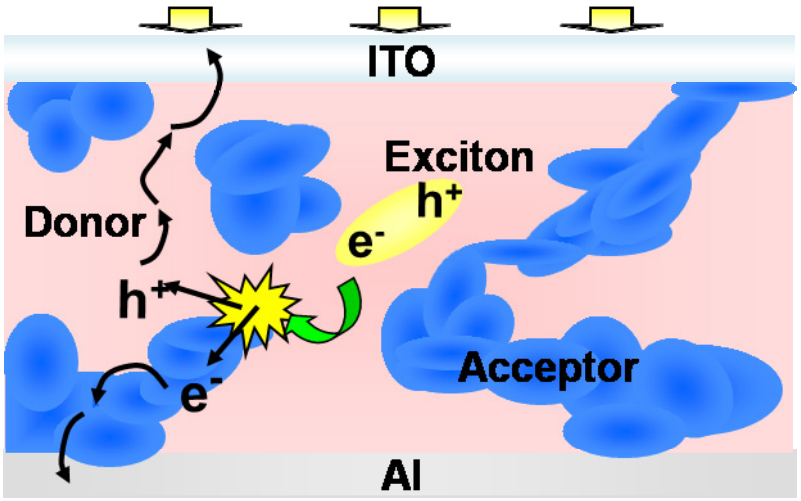

Figure 1.1.3. Schematic image of bulk heterojunction structure.

is not appropriate. Since the exciton diffusion length of general organic materials is within 10 nm [41-54], such large phase separation prevents the excitons from reaching the interface and thus results in deterioration in charge separation. Dead end formation is also likely to occur since bulk heterojunction structure is a randomly mixed structure of the donor and the acceptor. As a result it prevents the charges separated at the interface of the donor and acceptor from transporting to the electrodes and thus results in deterioration in charge transport. Therefore nanostructure control of the donor and the acceptor in the film is of high importance to achieve efficient organic thin film solar cells. However, the almost all the recent studies are based on bulk heterojunction structure aiming at a higher efficiency by simply optimizing device fabrication techniques and conditions such as mixing ratio of the donor and acceptor or annealing temperature and so on, and little consideration is taken at *deliberate* nanostructure control, especially by means of molecular designs.

1.1.2. Objective of this study

The objective of this study is to control the nanostructure of the donor and acceptor in 10 nm scale by means of molecular designs. In this study, molecular designs are based on π-conjugated oligomers since they are easily purified, monodispersed, and their bulk properties are also easily controlled by molecular design. The following three nanostructures are considered to be important in this study (Figure 1.1.4). Firstly, the formation of large interface of the donor and acceptor is considered to be of importance to achieve efficient charge separation. To achieve such large interface, the domain sizes of the donor and acceptor must be controlled to be smaller than 10-20 nm which corresponds to the exciton diffusion length of the organic materials. Secondly, the control in molecular ordering is considered to be of importance to achieve efficient charge transport. Introduction of molecular ordering, with the domain sizes small, can form the carrier paths to the electrodes and thus results in efficient charge transport. Thirdly, the control in molecular orientation is also considered to be of importance to achieve efficient charge transport. Introduction of anisotropic orientation of the molecules can control the carrier flow and thus further improve the charge transport. Through formation and investigation of the nanostructures described above as well as evaluation of the solar cell with the nanostructures, this study also aims at investigating the correlation between the nanostructure and efficiencies of photo-induced charge separation and subsequent charge transport in the solar cells (in thin solid film). Furthermore, this study also aims at acquiring knowledge on molecular design for synthesizing "model" molecules to form the nanostructure described above.

In chapter 2, a covalently linked donor and acceptor dyad is introduced to form the large interface of the donor and acceptor. In such a dyad molecule, no phase separation occurs and moreover, intramolecular photo-induced charge separation is possible. Therefore, a dyad can be a model molecule for controlling the interface and thus for achieving the efficient charge separation.

In chapter 3-5, the strong molecular interactions are utilized to control the molecular ordering. In chapter 3 and 4, ordering of dyad molecules are investigated. By ordering dyads, it is possible to achieve the ordered nanostructure of both donor and acceptor at the same time. Therefore, a

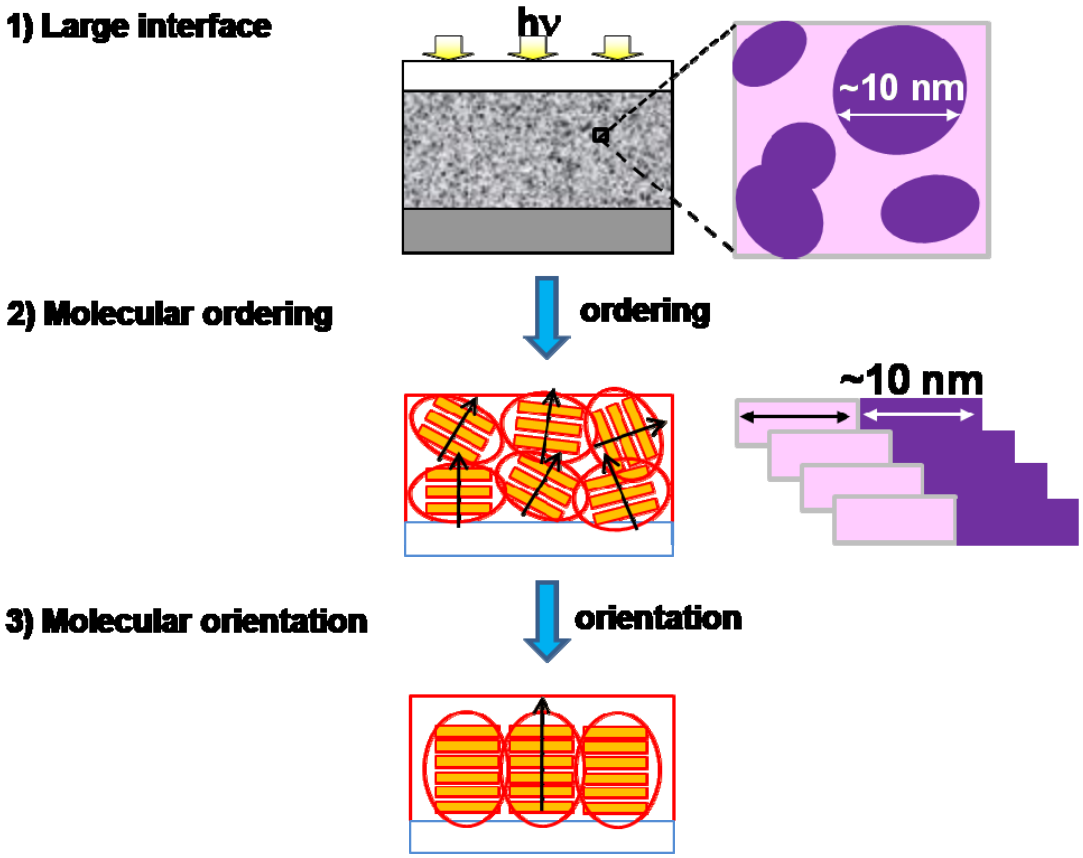

Figure 1.1.4. The aiming nanostructures in this study.

dyad can also be a model molecule for controlling molecular ordering in molecular level and thus for achieving the efficient charge transport. In chapter 5, ordering of crystalline donor materials is investigated to form percolated carrier pathways in bulk heterojunction structure with PCBM introduced as an acceptor. The design of novel donor materials that securely forms such pathways is of great desire and interest in the bulk heterojunction system.

In chapter 6, amphiphilic donor materials are introduced to control the orientation of the molecules. The π-π interaction and polar/nonpolar interactions of the molecules are utilized to spontaneously achieve anisotropic orientation of the molecules. Therefore such amphiphilic molecules can be a model for controlling the orientation of the molecules.

In the following sections, brief reviews are given on organic thin film solar cells, especially focusing on nanostructure formation and molecular designs.

1.2. Introduction of organic thin film solar cells

In this section, investigation and formation of the nanostructure and its importance in the organic thin film solar cells are described. First of all, background and brief history of organic thin film solar cells are described, which also includes discovery of photovoltaic effect and development of inorganic solar cells. Through many researches on investigation of the nanostructure in recent decade, influence of nanostructure of the components (i.e. donor and acceptor) in the thin film on the efficiency of the solar cells and its importance have been demonstrated. 10 nm scale phase separation of the components, which corresponds to their exciton diffusion lengths is of high importance for efficient charge separation. Interpenetrating network (mutually percolated carrier pathways throughout the thin film) of the components as well as local molecular conformation (i.e. π-π staking and thus crystallinity) is of high importance for efficient charge transport. In this section, some representative work on molecular designs for seeking formation of such nanostructure is also briefly reviewed.

1.2.1. Background and brief history of solar cells

1.2.1.1. Background

After the industrial revolution, human beings have started to utilize fossil fuels and their consumption has been increasing as economical activities are growing. It is said that all the existing fossil fuels will be consumed near future if we keep consuming them as we do now and do not reduce the consumption. Furthermore, consumption of fossil fuels emits the greenhouse effect gases such as carbon dioxide to cause global warming which has been one of the biggest issues in the world these days. Therefore, utilization of sustainable and environmentally-clean alternative energy sources has recently drawn much attention as one of the solutions for aforementioned problems. There have been several alternative energy sources proposed such as wind power, geothermal power, biomass, and solar cell. Solar cell has recently attracted much attention since it can convert solar energy (light) which is inexhaustible to electricity and thus is clean and sustainable. Silicon based solar cells have been widely used so far and achieved an

efficiency of approximately 25% in single crystal type solar cells [55]. However, such solar cells based on inorganic materials are expensive and repay of installation fee by energy gain requires a long time. Moreover, places for installation of inorganic solar cells are limited due to their heavy weight and rigidity. The solar cells based on organic materials such as polymers thus are attractive alternatives with their advantageous features over inorganic ones such as low fabrication cost, light weight, and flexibility.

1.2.1.2. Brief history of solar cells [56, 57]

The origin of solar cells is the observation of photocurrent by Becquerel in 1893. Becquerel discovered current generation in between the electrodes coated with silver chloride in an electrolyte solution under light irradiation and this is the first observation of photovoltaic effect (photo electrochemical effect) [58]. In 1870s, Adam and Day also observed the current generation in selenium in the solid, and the first solar cells were fabricated with selenium in the end of 18th century. The efficiency of the cell was however quite low (lower than 1%) at that time. In 1953, Chapin in Bell Laboratory developed silicon-based solar cells and the efficiency of the solar cells significantly improved up to 6% [59]. Until recently tremendous work has been done on silicon-based solar cells by many researchers and the highest efficiency of approximately 25% has achieved so far in single crystal type solar cells.

1.2.2. Background of organic thin film solar cells [56, 57]

1.2.2.1. Basic structure and working principle

The basic structure of the organic thin film solar cells is already introduced in former section (see Figure 1.1.1). The organic layer, which composes light absorber such as π-conjugated polymers, is sandwiched between the two different kinds of electrodes. For one side, a transparent electrode such as indium tin oxide (ITO) is used, and light is irradiated from this side. For the other side, a metal electrode such as aluminum is used.

The working principle is as follows, and schematic image is depicted in Figure 1.2.1. When

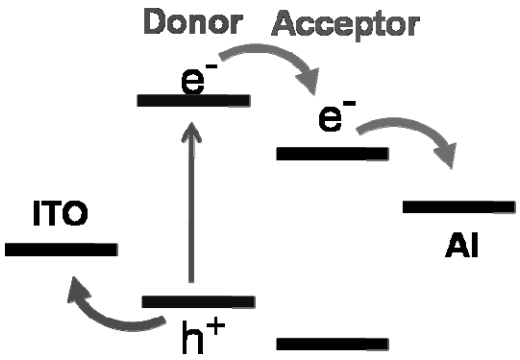

Figure 1.2.1. The schematic image of the working principle.

the light is irradiated, the molecules in the organic layer or active layer absorb light and an electron at the highest occupied molecular orbital (HOMO) excited to the lowest unoccupied molecular orbital (LUMO) (π-π* transition in general π-conjugated materials) to generate a bounded hole and electron pair by Coulombic force, called an exciton. In the case of single layer cell, the generated excitons are dissociated to free carriers (i.e. hole and electron) at the interface of the organic layer and the electrode by the potential difference of the ionization potential of the molecule and the work function of the metal electrode. In the case of heterojunction devices with electron donor and acceptor, the dissociation occurs at the interface of the donor and the acceptor by the potential offset of their LUMO levels. The generated carriers are transported to the electrodes by built-in potential; holes for the electrode with the higher work function, electrons for the one with the lower work function. As a result, current flows when the two electrodes are connected by the external circuit.

1.2.2.2. Evaluation methodology

Organic thin film solar cells are generally evaluated with power conversion efficiency (PCE) and external quantum efficiency (EQE).

Power Conversion Efficiency (PCE) is calculated from the *I-V* characteristic of the cells under light irradiation. Schematic *I-V* characteristics of the cell in the dark and under irradiation

are depicted in Figure 1.2.2. When the light is irradiated, photocurrent is generated and the curve is shifted to downward. The current obtained at zero voltage is called short circuit current, I_{SC} and the voltage obtained at zero current is called open circuit voltage, V_{OC}. It is noteworthy that V_{OC} is known to be related to the work function difference of the electrodes and the offset of the HOMO of the donor and LUMO of the acceptor [60-65]. The maximum output is the area which is the product of V_{max} and I_{max}, depicted in Figure 1.2.2. The ratio of the maximum output and the product of V_{OC} and I_{SC} is called fill factor (FF).

$$FF = \frac{I_{\max} \times V_{\max}}{I_{SC} \times V_{OC}}$$

PCE is then defined as the ratio of the maximum output of the energy of the irradiated light (P_{in}).

$$PCE = \frac{I_m \times V_m}{P_{in}} \times 100 = \frac{FF \times I_{SC} \times V_{OC}}{P_{in}} \times 100$$

PCE is generally evaluated under simulated solar light (Air Mass 1.5, A.M. 1.5, depicted in Figure 1.2.3) irradiation.

External quantum efficiency (EQE) is evaluated under monochromatic light irradiation and defined as the ratio of number of electrons extracted ($n_{electron}$) from the cell and number of photons irradiated (n_{photon}).

$$EQE = \frac{n_{electron}}{n_{photon}} = \frac{I_{SC}}{P_{in}} \frac{hc}{\lambda e}$$

h is Planck constant, c is speed of light, λ is the wavelength of the irradiated light, and e is elementary charge.

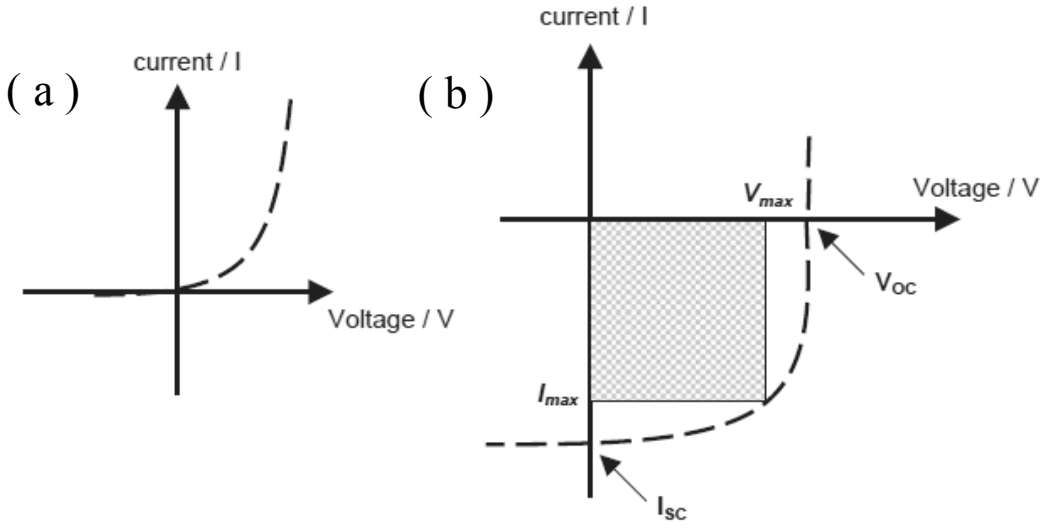

Figure 1.2.2. Schematic *I-V* characteristics (a) in the dark and (b) under the light irradiation. (**ref.56**)

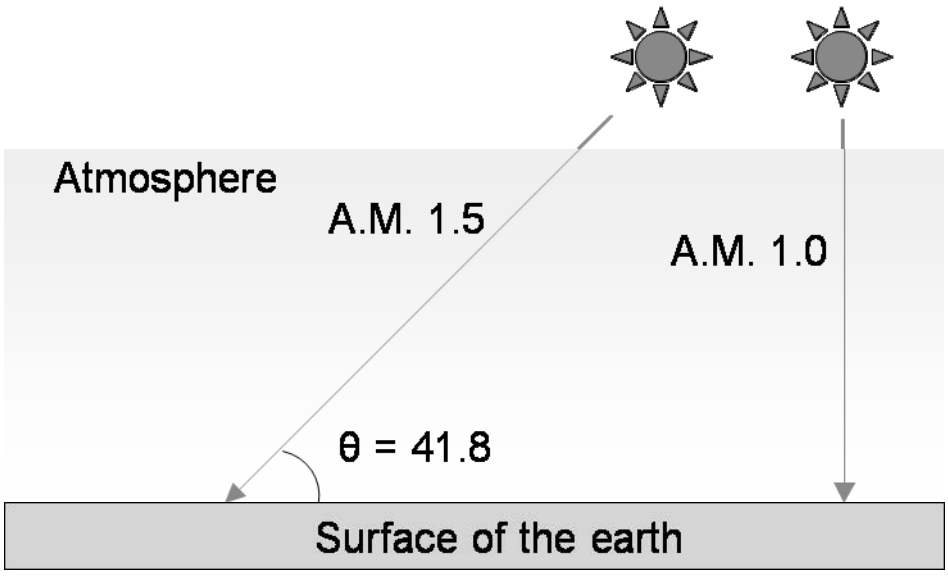

Figure 1.2.3. Schematic representation of air mass 1.5 (A.M. 1.5).

1.2.2.3. Historical change in structures and efficiencies

Efficiencies of organic thin film solar cells have improved dramatically as new conceptual structures are introduced such as p-n junction (i.e. heterojunction of donor and acceptor) and bulk heterojunction (i.e. randomly dispersed structures of donor and acceptor). In this section, the improvement of the efficiency of the organic thin film solar cells is reviewed in terms of changes in the device structures.

Monolayer device

The simplest structure is a monolayer device that is composed of just one material such as π-conjugated polymers in the organic layer. In a monolayer device, the generated excitons by light irradiation can be dissociated only at the interface of the organic layer and the electrodes (Figure 1.2.4). Since exciton diffusion length is within approximately 10 nm, the limited number of excitons can reach the interface to generate carriers and thus charge separation efficiency is quite low. Moreover, the generated carriers have to be transferred a long distance from one electrode to the other, which causes charge recombination and exciton annihilation. As a result, the efficiency of a monolayer device is limited below 0.1% [66-69].

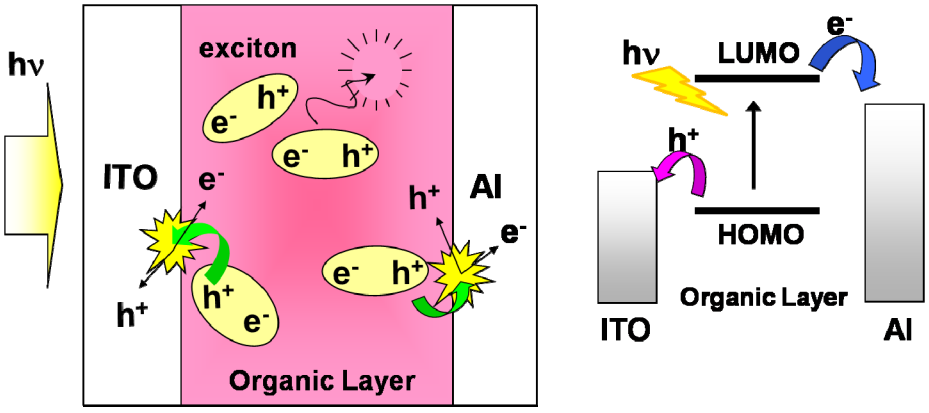

Figure 1.2.4. Schematic representation of monolayer device.

Bilayer device *(Heterojunction device)*

In 1986, Tang reported a new conceptual structure whose organic layer was composed of two laminated layers of donor and acceptor, depicted in Figure 1.2.5 [70]. In such a bilayer device, the heterojunction formed by the donor and acceptor layers is the exciton dissociation interface. Tang proposed that the local electric field is produced at the heterojunction interface of the two materials with different ionization potential and electron affinity and it enhances the exciton dissociation. Indeed photocurrent generation was dramatically increased in a bilayer device, resulting in an enhanced efficiency of approximately 1% (Figure 1.2.6). In a bilayer device, carrier transport is also improved compared to that in a monolayer device since holes and electrons are transported in different layers, which reduces possibility of charge recombination.

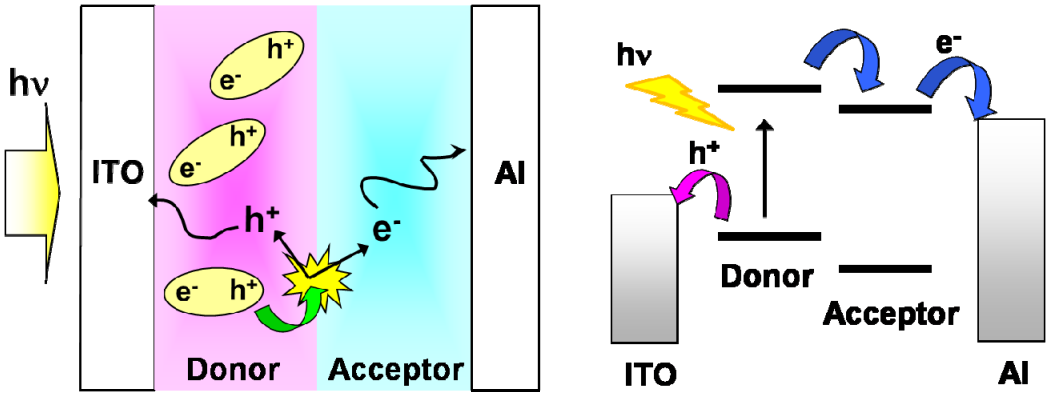

Figure 1.2.5. Schematic representation of bilayer device.

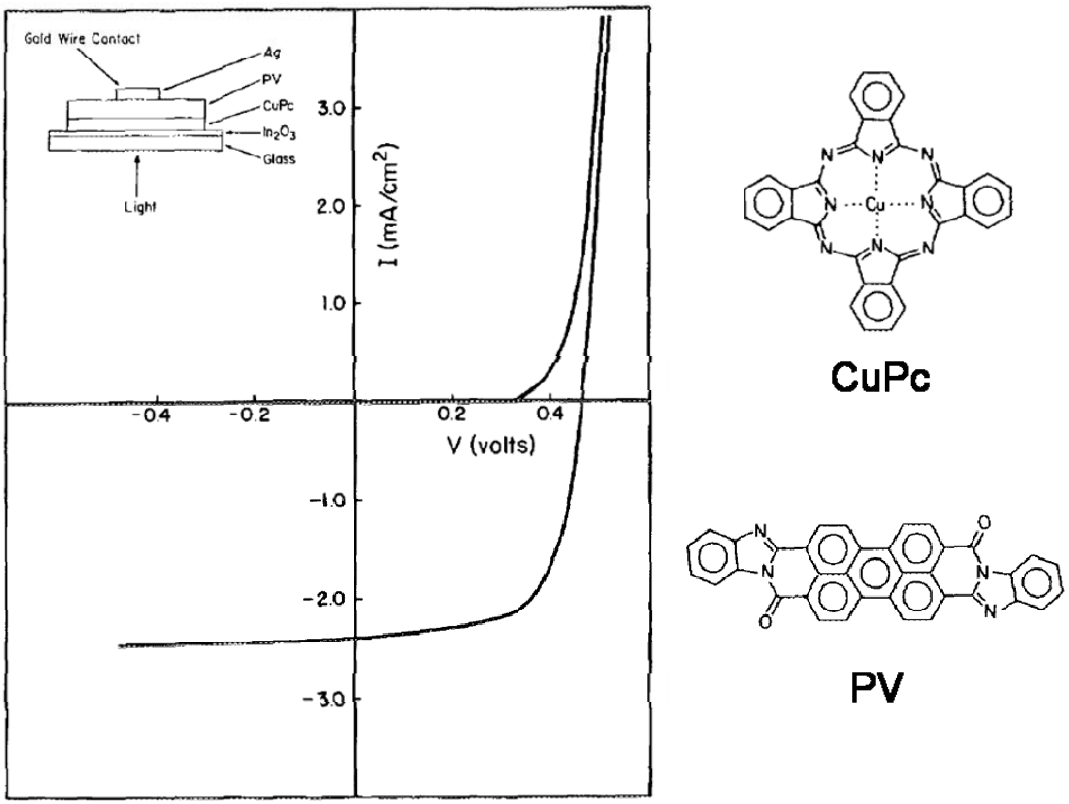

Figure 1.2.6. Configuration and current-voltage characteristics of an ITO/CuPc (250 Å)/PV (450 Å)/Ag cell, and the chemical structures of copper phthalocyanine (CuPc) and a perylene tetracarboxylic derivative (PV). (**ref.70**)

Bulk heterojunction device *(Randomly dispersed structures of donor and acceptor)*

To efficiently dissociate the generated excitons at the heterojunction interface, the total thickness of the organic layer should be usually thinner than 20 nm since the exciton diffusion length of general organic materials is limited to be 10 nm [41-54]. However, such a thin film cannot efficiently absorb the irradiated light. Usually, the thickness of approximately 100 nm is required for the organic films to efficiently absorb the light. With such a thick film, however, the exciton dissociation efficiency decreases in a bilayer device. To solve this dilemma, a new conceptual structure called bulk heterojunction (BHJ) was introduced [71-73]. The schematic representation of the BHJ structure is depicted in Figure 1.1.3. In the BHJ structure, domains of donor and acceptor are randomly dispersed in the organic layer and thus even in the thick film, large interface of the donor and acceptor can be formed. As a result, photocurrent generation significantly improves in a bulk heterojunction device [71-73].

The concept of bulk heterojunction was firstly introduced by Hiramoto et al [71]. In their report, co-evaporated layer (BHJ layer) of phthalocyanine (donor) and a perylene derivative (acceptor) was introduced in between donor layer and acceptor layer (Figure 1.2.7), and such 3-layered structure improved the photocurrent by order of 2, compared to the corresponding donor and acceptor bilayer device without BHJ layer (Figure 1.2.8). For polymer-based solution-processed solar cells, Yu et al, firstly reported a BHJ device in 1994 [72]. In their report, the BHJ device was fabricated by mixing poly(2-methoxy-5-(2'-ethyl-hexyloxy)-1,4-phenylenevinylene) (MEH-PPV) with fullerene (acceptor) (10% in weight), and improved the photocurrent by one order of magnitude, compared to the monolayer device with the polymer (Figure 1.2.9). However, insufficient content of a fullerene due to its low solubility in organic solvent used for device fabrication process limited the efficiency even though it possesses a superior electron acceptability which was discovered individually by Yoshino et al[74] and Sariciftci et al[75]. Hummelen et al, thus developed a soluble fullerene derivative, phenyl-C_{61}-butyric acid methyl ester (PCBM) in 1995[76]. Later in the same year, Yu et al, reported the BHJ device with MEH-PPV and PCBM (1:4 in weight), and the efficiency of the device significantly improved to 2.9% under monochromatic light irradiation (430 nm) (Figure 1.2.10)[73].

Donor and acceptor heterojunction concept by Tang and superior electron acceptability of fullerene by Yoshino and Sariciftci are considered as the two significant discoveries in the field of organic solar cells. Introduction of bulk heterojunction concept and a soluble fullerene derivative (PCBM) further developed organic solar cell. Since then, the most studied solution-processed solar cells have been based on the bulk heterojunction structure with PCBM and π-conjugated polymers.

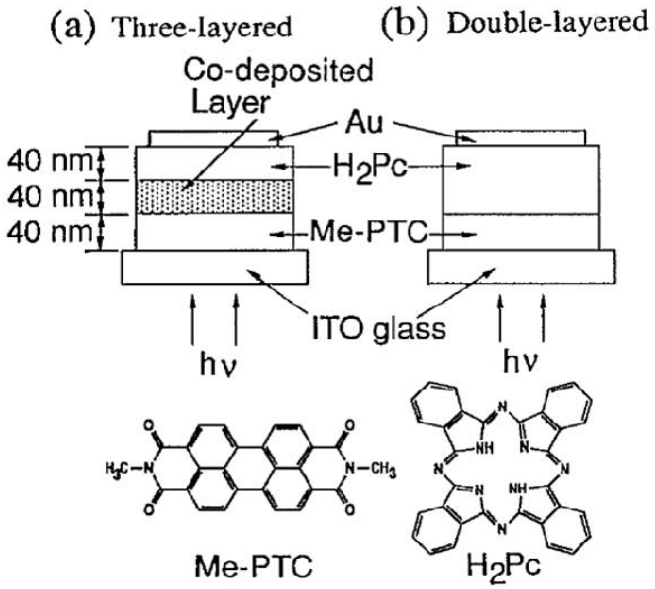

Figure 1.2.7. Structure of (a) three-layered and (b) double-layered organic solar cells, and the chemical structures of the pigments used. (**ref.71**)

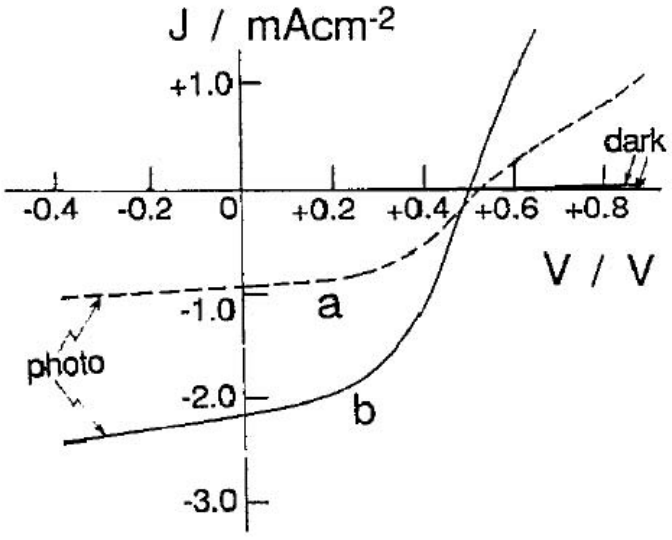

Figure 1.2.8. Typical current-voltage (*J*-*V*) characteristics. (a) double-layered cell, ITO/Me-PTC (40 nm)/H_2Pc (80 nm)/Au, and (b) three-layered cell, ITO/Me-PTC (40 nm)/codeposited layer (40 nm)/H_2Pc (40 nm)/Au. The pigment ratio of Me-PTC and H_2Pc in the codeposited layer is 1:2. White light (100 mW cm^{-2}) was irradiated through ITO. (**ref.71**)

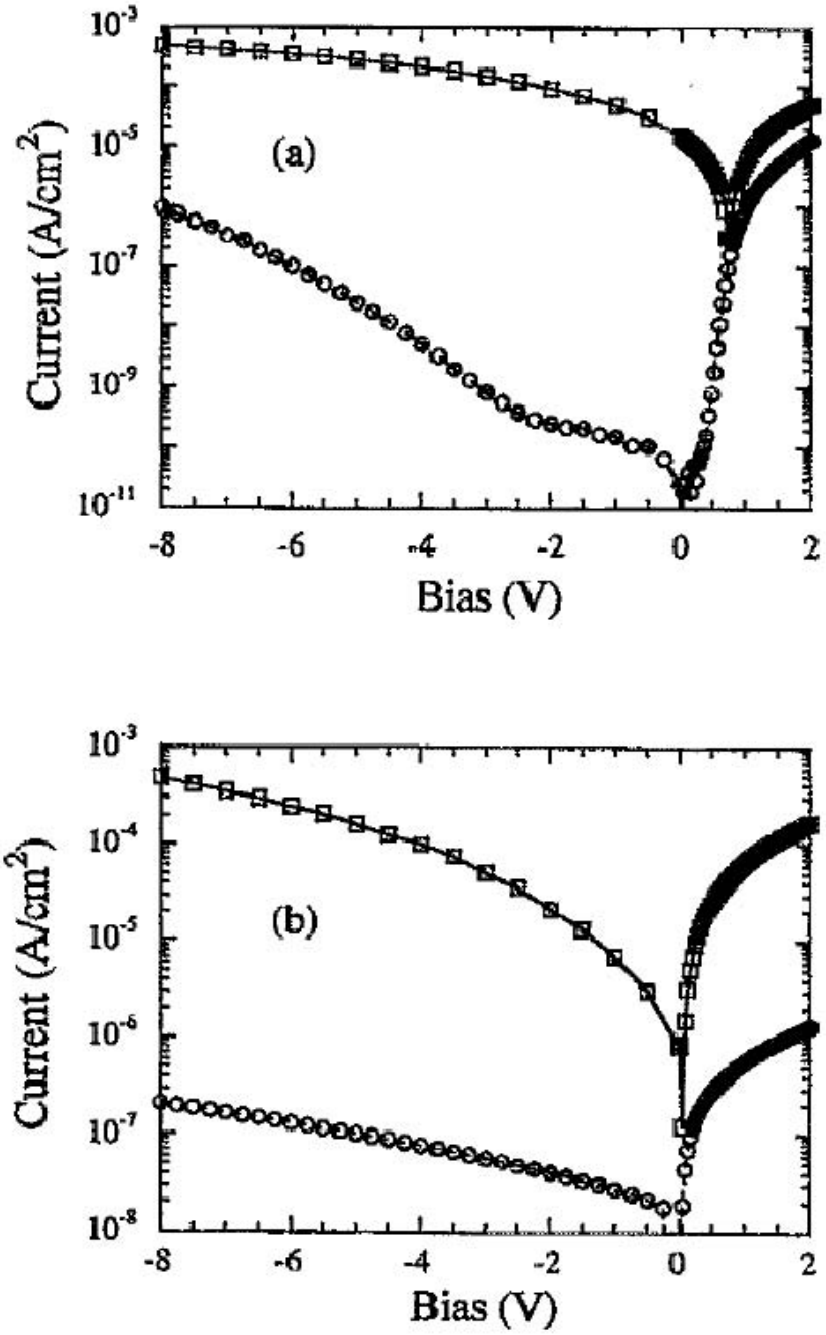

Figure 1.2.9. (a) *I-V* characteristics of an ITO/MEH-PPV:C_{60}/Ca diode in the dark (open circles), and illuminated under 2.8 mW/cm^2 at 500 nm (open squares). (b) *I-V* characteristics of an ITO/P3OT/Au diode in the dark (open circles), and illuminated under ~10 mW/cm^2 at 633 nm (open squares). (**ref.72**)

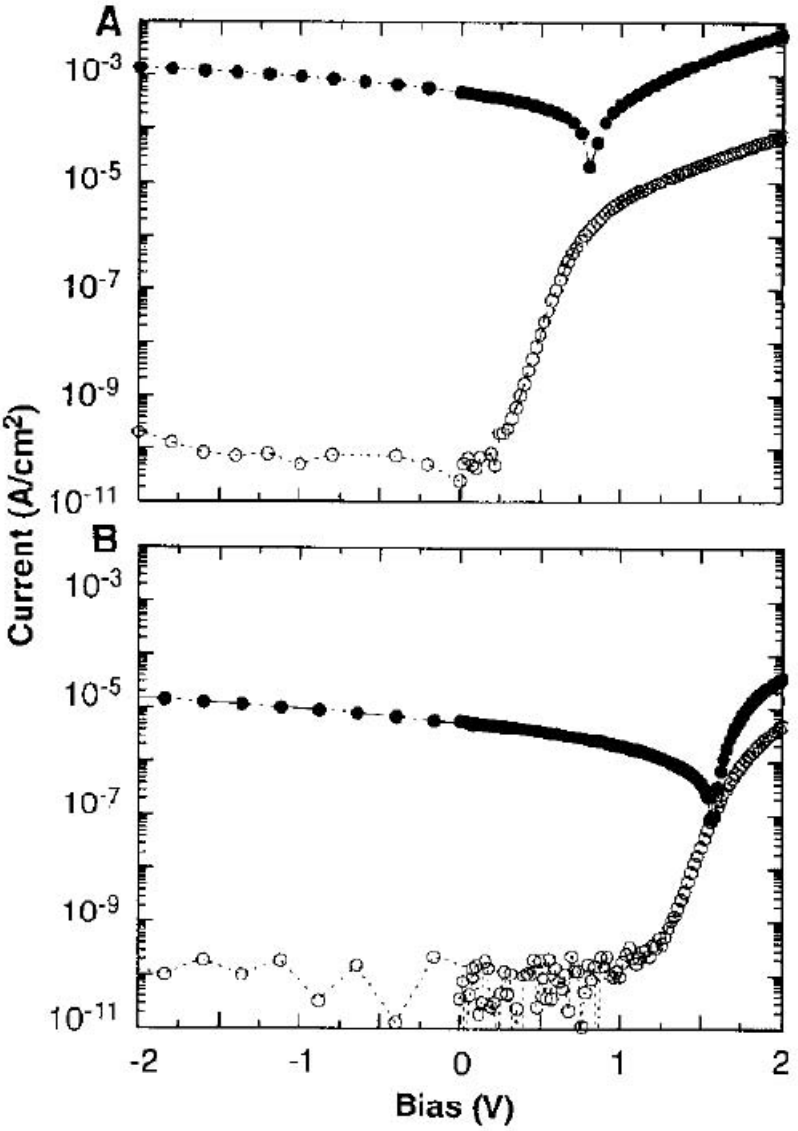

Figure 1.2.10. (A) *I-V* characteristics of an Ca/MEH-PPV:[6,6]PCBM/ITO device in the dark (open circles) and under 20 mW/cm^2 of illumination at 430 nm (solid circles). (B) The corresponding data from a Ca/MEH-PPV/ITO device. Currents were plotted as absolute values. (**ref.73**)

1.2.3. Nanostructure formation, investigation, and importance

The bulk heterojunction (BHJ) structure of the donor and acceptor has been widely accepted as a promising structure to achieve efficient charge separation since it provides the large interface of the donor and the acceptor. Although the large interface is expected to be achieved in the BHJ structure, it is of great importance for securing efficient charge separation to achieve the small domains of donor and acceptor with the size of approximately 10 nm which corresponds to the exciton diffusion length [41-54]. Therefore, investigation as well as formation of the nanostructure is of high significance.

The first investigation of such nanometer-scaled structures by transmission electron microscopy (TEM) was reported by Yang et al in 1996 [77]. They observed the BHJ films of MEH-PPV and fullerene, and found that the dark small areas with the dimension of approximately 10 nm were dispersed in the bright area. By electron diffraction measurement (observation of Debye ring), those dark areas were confirmed to be clusters of fullerenes. From their TEM observation they also claimed that bicontinuous network of the polymer and fullerene was formed in the blend films. However, their claim was not fully proven at that time since the resolution of the TEM images was quite poor. In the case of a polymer:polymer blend film, such bicontinuous network was firstly observed by Halls et al [78].

The importance of nanometer-scaled structures on the efficiency in the BHJ devices was firstly reported by Shaheen et al in 2001 [79]. In their report, the BHJ structures were fabricated with poly((2-methyl,5-(3,7,dimethyloctyloxy))-*p*-phenylene vinylene) (MDMO-PPV) and PCBM by spin-coating the toluene or chlorobenzene solutions. Atomic force microscopy (AFM) investigation revealed that large aggregated domains with the horizontal dimensions on the order of approximately 500 nm were formed in the BHJ structure formed by toluene (Figure 1.2.11a). In contrast, the smaller domains with the horizontal dimensions on the order of approximately 100 nm were observed in the BHJ structure by chlorobenzene (Figure 1.2.11b). The solar cells fabricated with those structures revealed that the higher EQE of 50% was achieved in the cell fabricated by chlorobenzene, nearly two-fold increase compared to that in the cell by toluene (Figure 1.2.12). At that time they explained this enhancement by increased

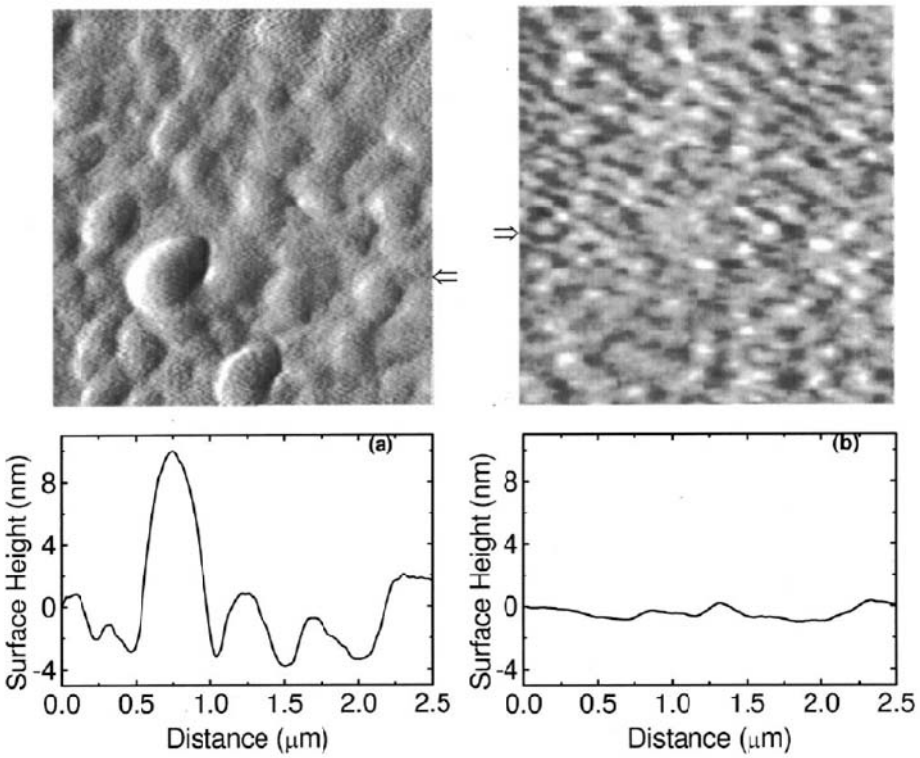

Figure 1.2.11. AFM images showing the surface morphology of MDMO-PPV:PCBM (1:4 by wt.) blend films with a thickness of approximately 100 nm and the corresponding cross sections. (a) Film spin coated from a toluene solution. (b) Film spin coated from a chlorobenzene solution. The images show the first derivative of the actual surface heights. The cross sections of the true surface heights for the films were taken horizontally from the points indicated by the arrow. (**ref.79**)

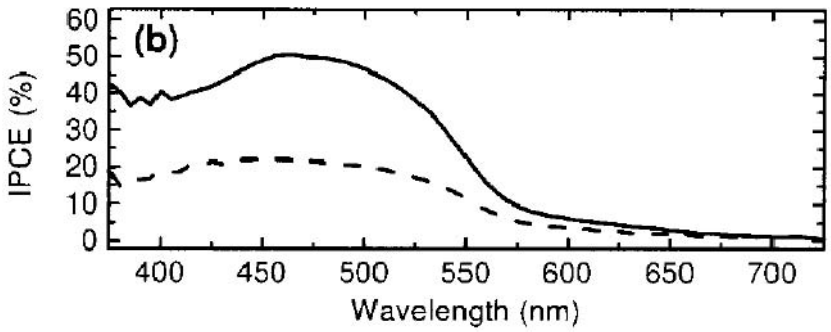

Figure 1.2.12. IPCE spectra for photovoltaic devices using 100-nm-thick MDMO-PPV:PCBM (1:4 by wt.) films spin coated from either toluene (dashed line) or chlorobenzene (solid line) solutions as the active layer. (**ref.79**)

charge carrier mobility for both holes and electrons since the voids between the PCBM clusters which can hinders electron hopping were reduced and the better interchain interaction of the polymers were achieved in the BHJ structure by chlorobenzene. Further investigation with cross section scanning electron microscope (SEM) revealed that the structure by chlorobenzene formed percolated carrier pathways of the donor and the acceptor to improve carrier transport in addition to efficient charge separation due to the large interface (Figure 1.2.13) [80]. For the structure by toluene, it was also confirmed that the large clusters were formed by pure PCBM and those clusters were covered with polymer skin layers [81]. What is worse, the skin layer between the PCBM and electron-collecting aluminum electrode can be recombination sites. The schematic representation of those structures is depicted in Figure 1.2.14.

In addition to the nanometer-scaled morphology of the donor and the acceptor described above, it is also of high importance to achieve a good molecular packing of the components in the film in order to achieve efficient charge transport.

Padinger et al, firstly reported the effect of post-production treatment of the devices on the crystallinity of the polymer (donor) as well as the efficiency of the device [82]. They fabricated the BHJ devices with poly(3-hexylthiophene-2,5-diyl) (P3HT) and PCBM, and found that the devices thermally annealed at 75 ºC which is higher than the glass transition temperature of the P3HT significantly improves the efficiency to 2.5%, compared to that of the untreated devices (PCE: 0.4%). Furthermore, simultaneous exertion of electric field of 2.7 V, together with the thermal annealing further improved the efficiency up to 3.5%. They attributed this enhancement in the efficiency to the enhanced carrier mobility due to the enhanced crystallinity of P3HT and the beneficial effect of molecular orientation induced by thermal annealing and electric field.

In fact the enhancement in mobility by thermal annealing was reported by several authors [83, 84]. Savenije et al, reported the one order of magnitude enhancement in mobility in P3HT:PCBM blend film annealed at 80 ºC (0.044 $cm^2 V^{-1} s^{-1}$) by flash-photolysis time-resolved microwave conductivity technique (FP-TRMC), compared to that of the untreated film (0.0056 $cm^2 V^{-1} s^{-1}$) [83]. Mihailetchi et al, also reported the enhancement in both hole and electron mobilities as well as their dependency on annealing temperature in P3HT:PCBM blend film[84]. Space charge limited current (SCLC) method was used to measure the mobilities, and revealed that the

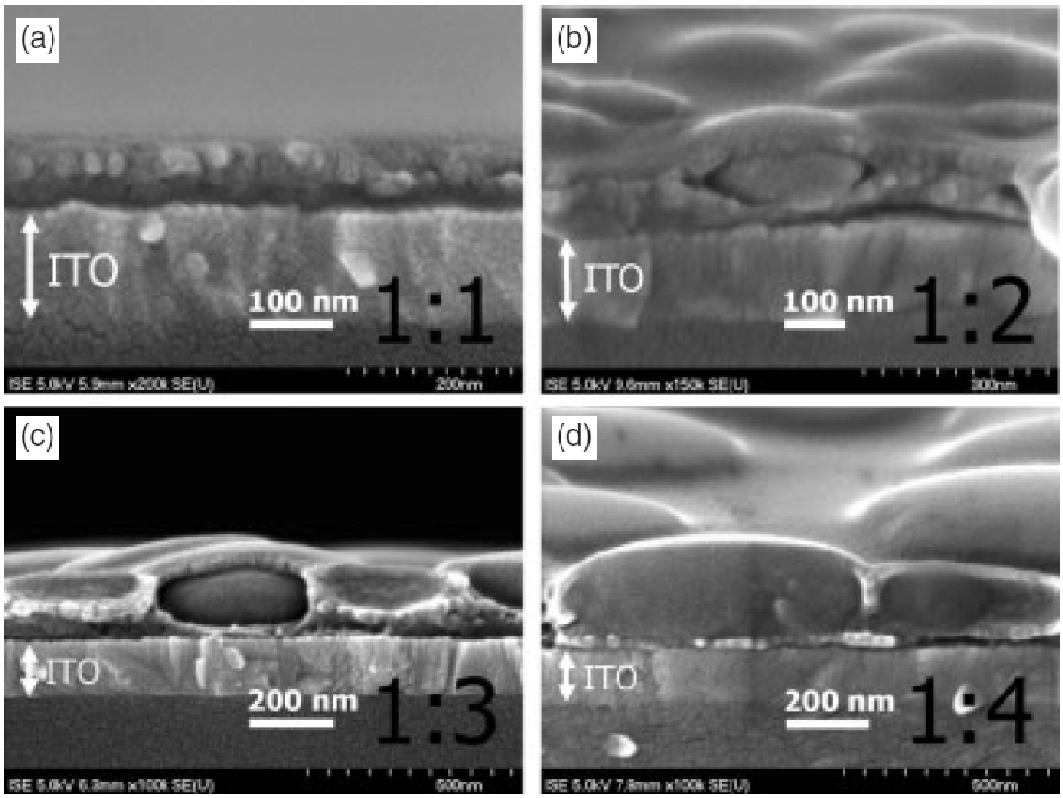

Figure 1.2.13. SEM side views (cross-sections) of MDMO-PPV/PCBM blend films cast from toluene with various weight ratios of MDMO-PPV and PCBM. For the ratios 1:4, 1:3, and 1:2 (b-d) the nanoclusters, in the form of discs, are surrounded by another phase, called the skin, that contains smaller spheres of about 20-30 nm diameter. For the 1:1 film, only these smaller spheres are found. The magnifications used are 100000 (d,d), 150000 (b), and 200000 (a). (**ref.80**)

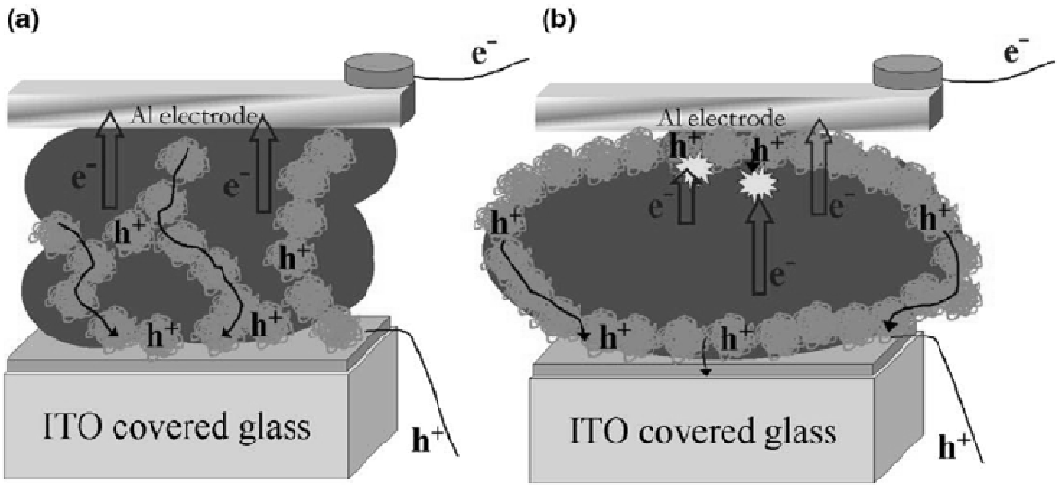

Figure 1.2.14. Schematic of (a) chlorobenzene and (b) toluene cast MDMO-PPV:PCBM blend layers as active layer in the solar cell. In (a) holes and electrons find percolated pathways to reach the respective electrode. In (b) electrons and holes suffer recombination due to missing percolation. (**ref.81**).

electron mobility increased from 10^{-4} cm^2 V^{-1} s^{-1} in as-cast film to 3×10^{-3} cm^2 V^{-1} s^{-1} after annealing and the hole mobility dramatically increased by more than three orders of magnitude, to reach a value of up to 2×10^{-4} cm^2 V^{-1} s^{-1} after annealing (Figure 1.2.15).

The enhancement by thermal annealing was studied from a view point of nanostructure by Yang et al [85]. In their report, TEM technique was utilized to visualize the nanometer-scale morphology of the blend film of P3HT and PCBM to reveal that the phase separation and crystallization of the two components were enhanced after thermal annealing. Interestingly, they also found that P3HT formed the nanofiber network in the film, which prevented PCBM from clustering in a large scale (Figure 1.2.16 and 17).

Further optimization on thermal annealing condition enhanced the efficiency up to 5%, reported by Reyes-Reyes et al [27] and Ma et al [26] at the same time in 2005. Both authors fabricated the devices in almost the same configuration with P3HT:PCBM (mixing ratio of 1:0.8 in weight). Interestingly, however their optimized annealing conditions were quite different each other. Reyes-Reyes et al, reported the maximum efficiency was achieved after a short time annealing such as 5 min at 155 ºC (Figure 1.2.18) [27]. They observed a decrease in the efficiency when the device was annealed for a longer time. They attributed this decrease to large aggregation of PCBM. In contrast, Ma et al, reported that the highest efficiency was achieved after annealing the device for 30 min at 150 ºC [26]. Moreover the efficiency kept almost constant even after a long time annealing up to 1 hour (Figure 1.2.19). From this remarkable stability of the device, they insisted on the formation of thermally stable nanoscale, interpenetrating donor-acceptor networks. They also claimed that suppression of the overgrowth of PCBM aggregates is of high importance to achieve thermally stable devices by using chlorobenzene as the solvent, which dissolves PCBM well, and reducing the P3HT:PCBM ratio and concentration. Indeed, TEM images of the blend film revealed the stability of the interpenetrating donor-acceptor networks with a typical feature size of approximately 10 nm (Figure 1.2.20). The enhanced crystallinity of P3HT after annealing was also confirmed by X-ray diffraction (XRD) measurement of the blend film (Figure 1.2.21).

These results above suggested that formation of the crystalline network of P3HT is of importance to prevent PCBM aggregation and thus to achieve a stable nanostructure as well as

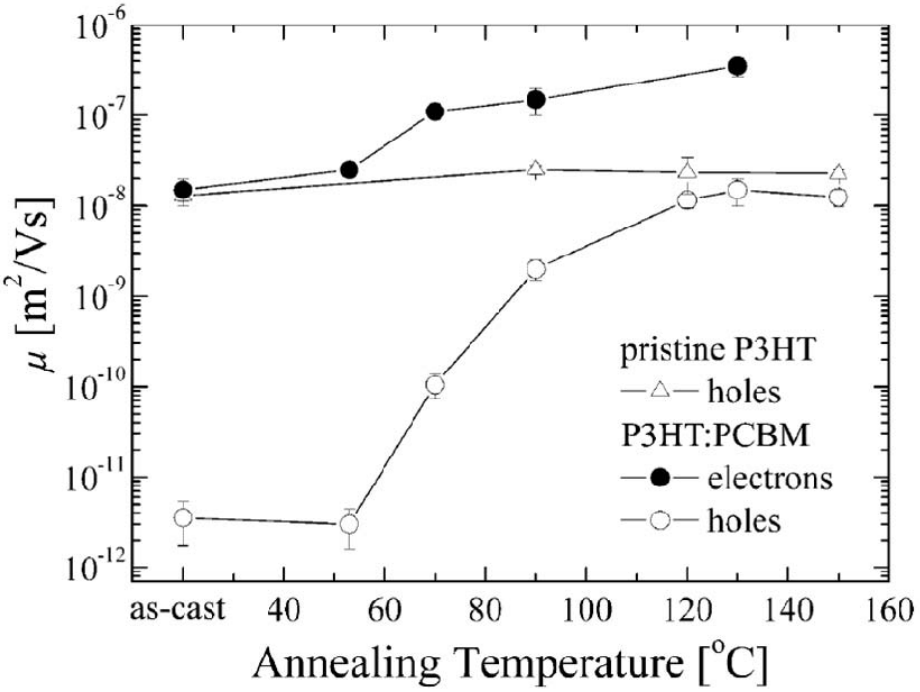

Figure 1.2.15. Room-temperature electron (●) and hole (○) zero-field mobilities in 50:50 wt.-% blends of P3HT:PCBM as a function of postproduction annealing temperature of the completed devices. For comparison, the hole mobility measured in pristine P3HT devices (Δ) is also shown. The mobilities were calculated from the SCL current measured using the electron- and hole-only device configuration. (**ref.84**)

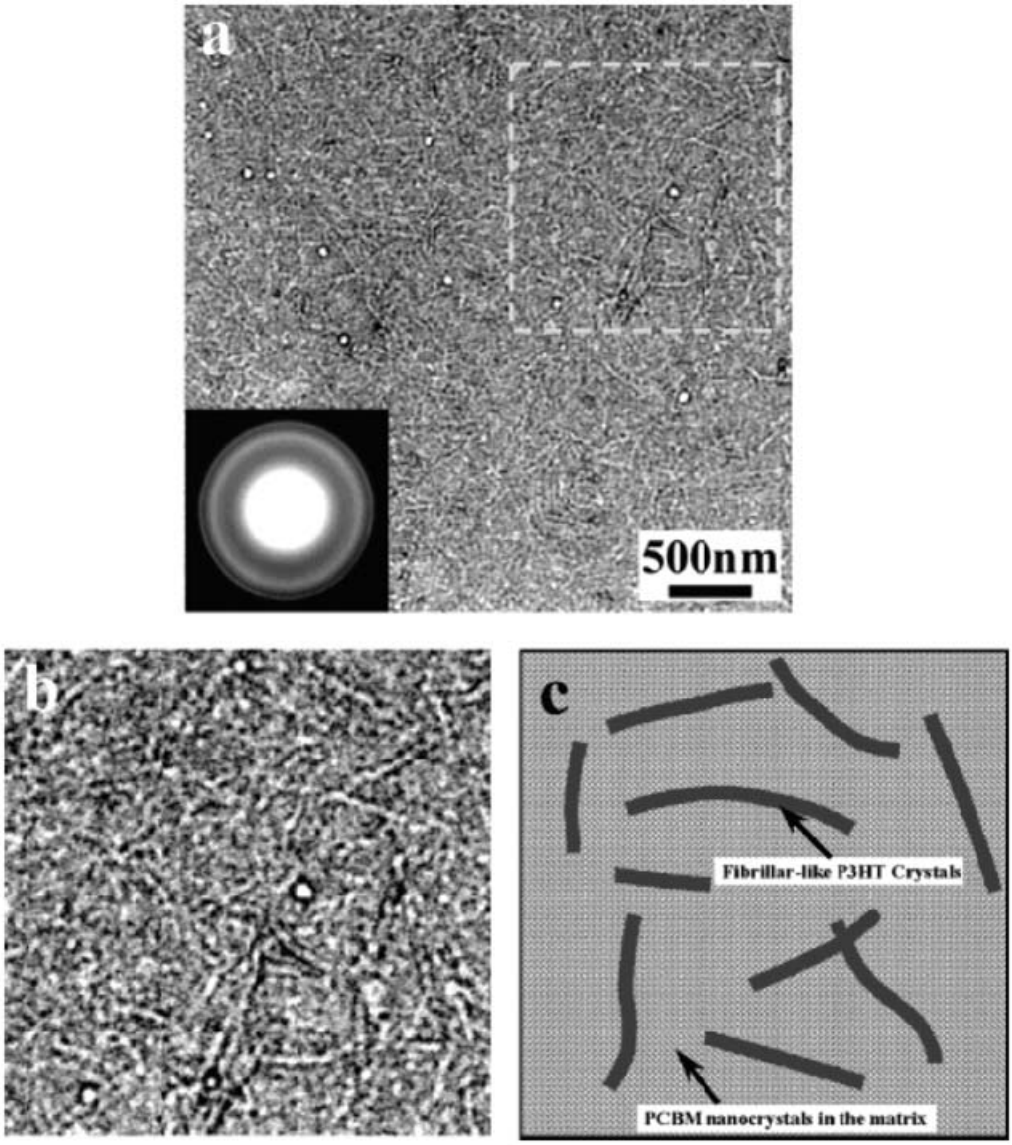

Figure 1.2.16. BF TEM images show the overview (a) and the zoom in (b), and the corresponding schematic representation (c) of the pristine photoactive layer of a P3HT/PCBM plastic solar cell. The inset in Figure 1.2.16a is the corresponding SAED pattern. The TEM images were recorded on a JEOL JEM-2000FX transmission electron microscope operated at 80 kV. (**ref.85**)

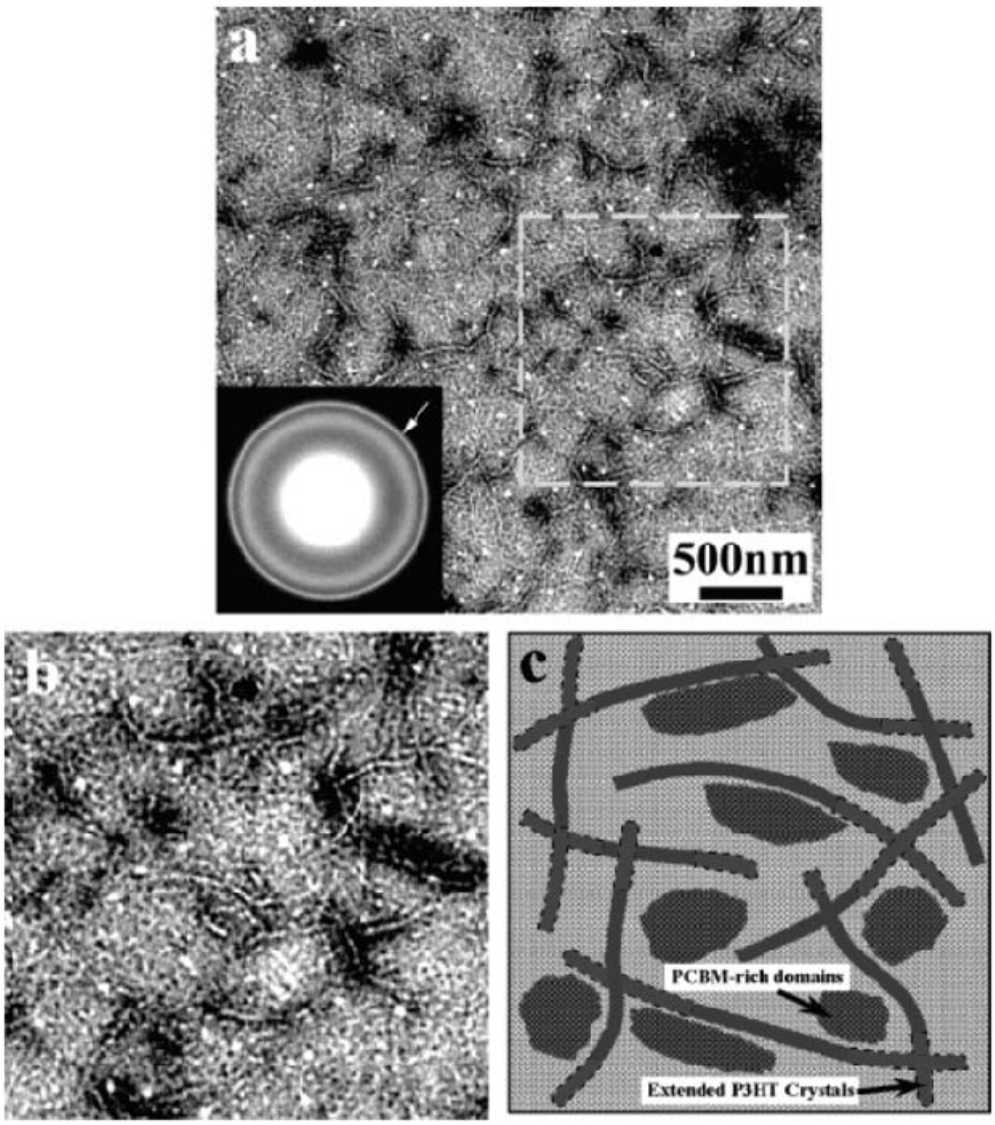

Figure 1.2.17. BF TEM images show the overview (a) and the zoom in (b), and the corresponding schematic representation (c) of the thermal annealed photoactive layer. The inset in Figure 1.2.17a is the corresponding SAED pattern. The arrow is to indicate the increased intensity of (020) Debye-Scherrer ring from P3HT crystals compared to the SAED pattern shown in the inset of Figure 1.2.16.a. Note: for Figure 1.2.17c, the dash line boardered regions represent the extension of existing P3HT crystals in the pristine film (Figure 1.2.16) or newly developed PCBM-rich domains during the annealing step. The TEM images were recorded on a JEOL JEM-2000FX transmission electron microscope operated at 80 kV. (**ref.85**)

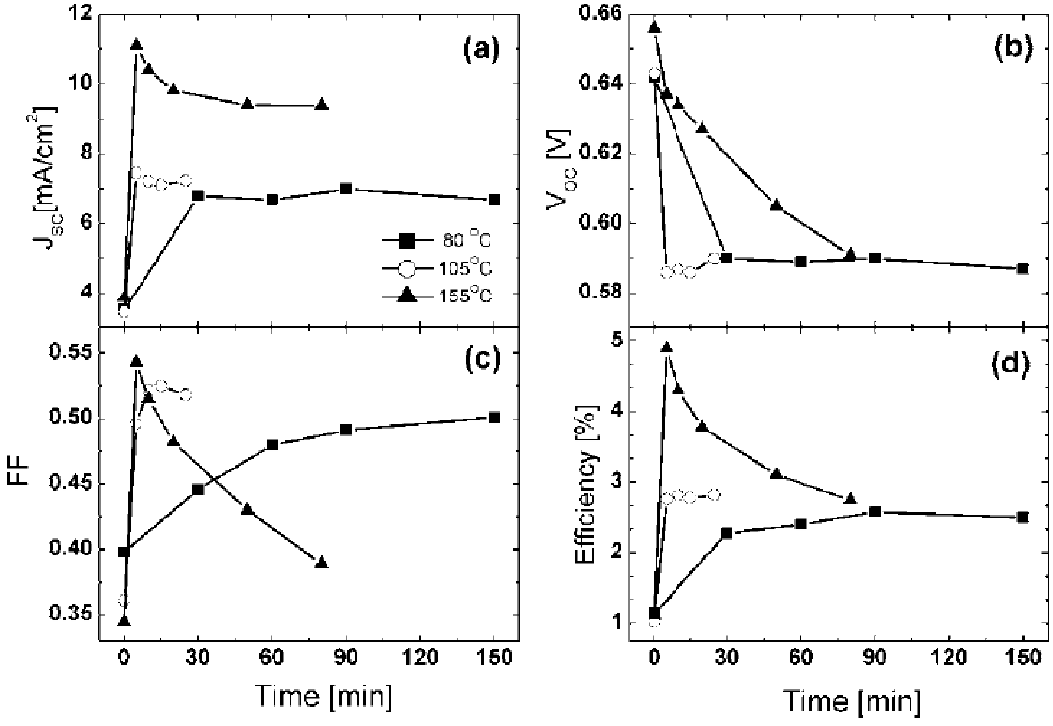

Figure 1.2.18. Influence of the duration of the annealing on (a) the short-circuit current density, (b) open-cirsuit voltage, (c) FF, and (d) power conversion efficiency for different temperatures. (**ref.27**)

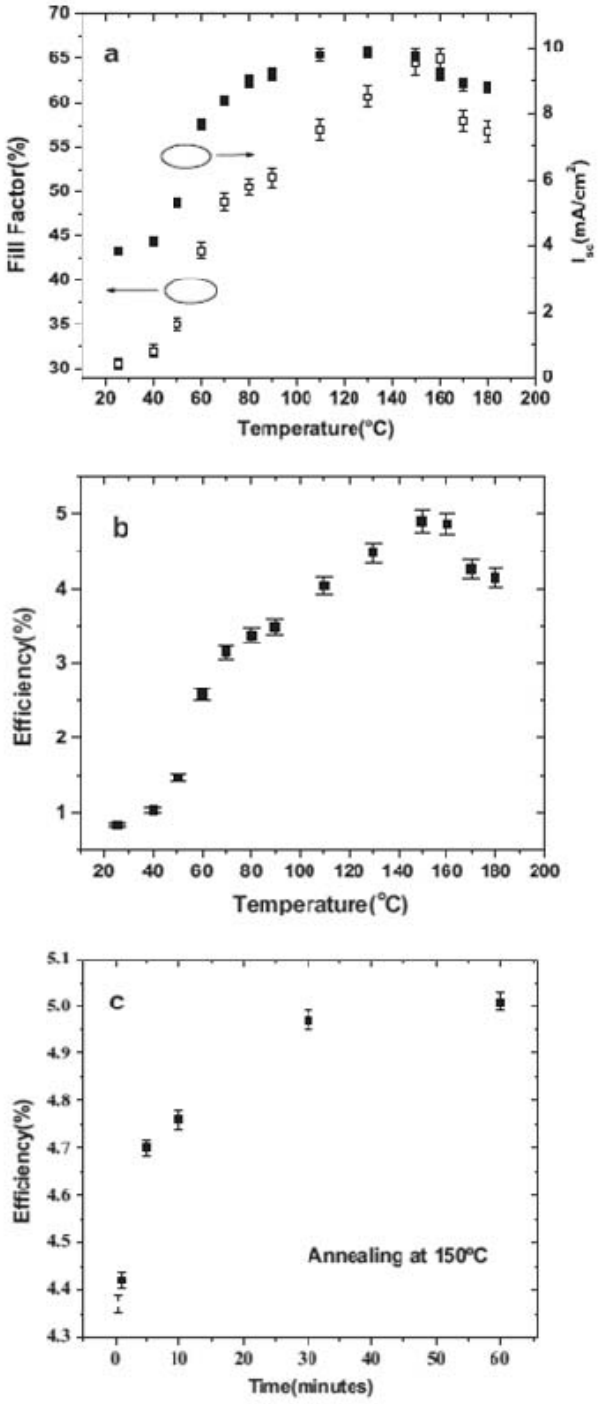

Figure 1.2.19. a) Variation of fill factor (open squares) and short-circuit current (filled squares) with annealing temperature (AM 1.5, 80 mW cm^{-2}). B) Device efficiency versus annealing temperature. For these data, the annealing time was 15 min. c) Evolution of device efficiency (filled squares) with thermal annealing time at 150 ºC. (**ref.26**)

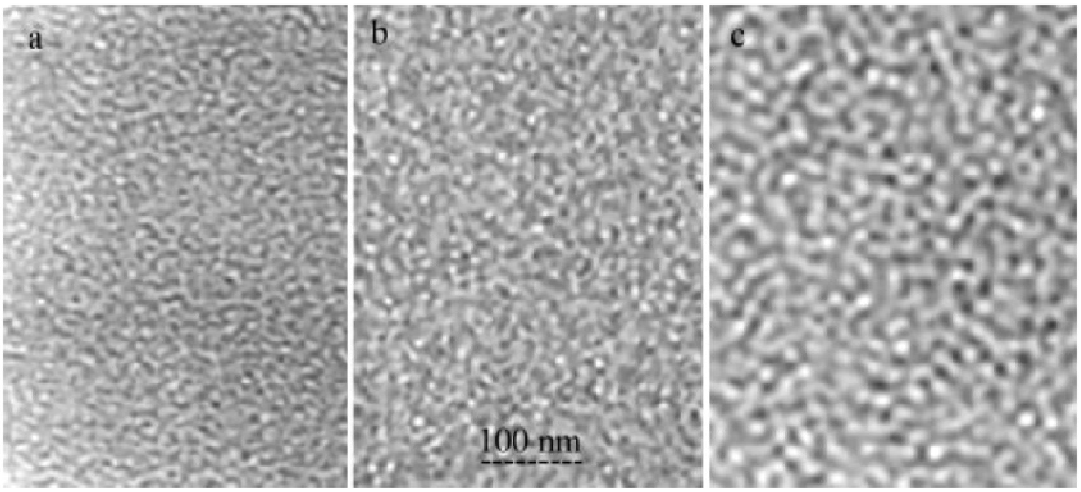

Figure 1.2.20. TEM images of P3HT:PCBM film bulk morphology before thermal annealing (a), after thermal annealing at 150 ºC for 30 minutes (b), and after thermal annealing at 150 ºC for 2h (c). (**ref.26**)

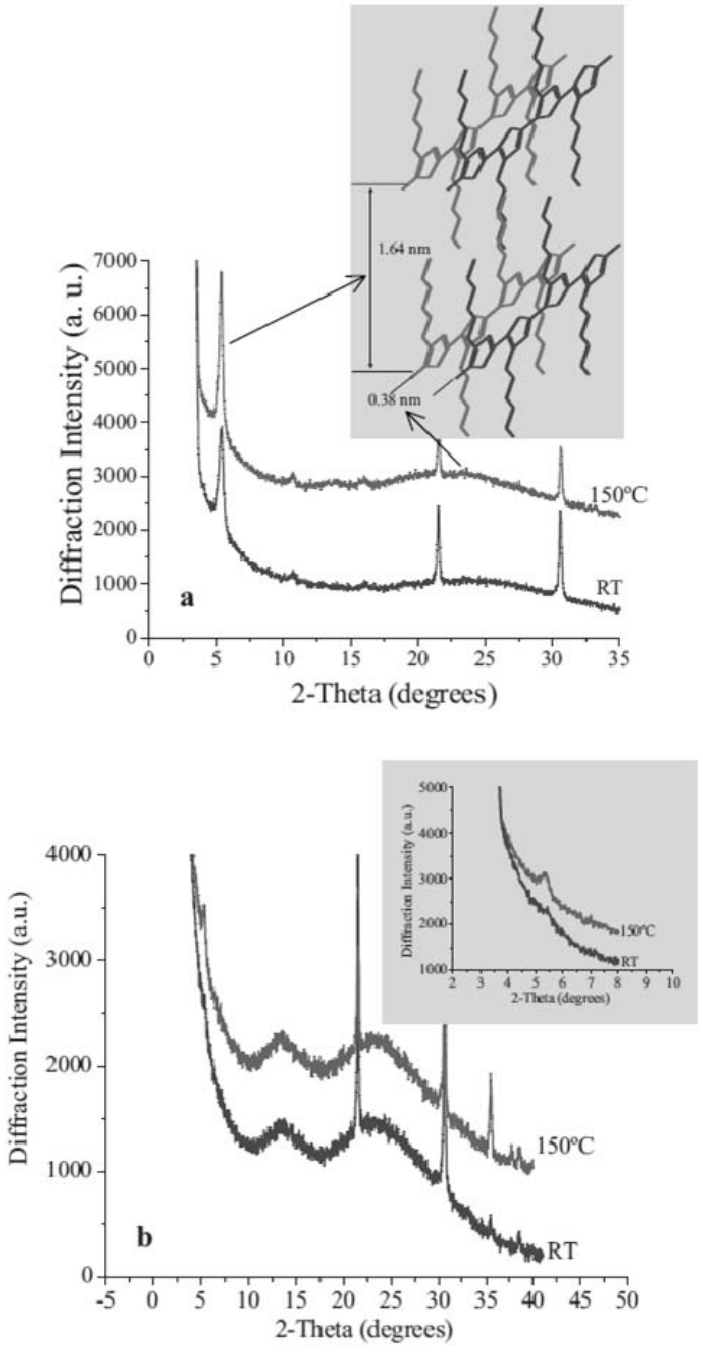

Figure 1.2.21. a) XRD spectra of a P3HT:PCBM film drop-cast onto a PEDOT/ITO substrate with and without thermal annealing at 150 ºC for 30 min. The inset shows the P3HT crystal structure. B) XRD spectra obtained from completed solar cells (with Al electrode) before and after annealing at 150 ºC for 30 min (RT = room temperature). The inset shows the region around 2θ ≈ 13º arises from the PEDOT layer and the peaks at 2θ ≈ 22º and 31º are from ITO. (**ref.26**)

to form percolated carrier pathways for efficient charge transport. In fact, several authors reported the importance of the P3HT crystallinity [25, 29, 86, 87]. Li et al, reported that slow evaporation of the solvent during the spin-coating process enhanced the crystallinity of the P3HT and self-organized P3HT ordered nanostructure was formed in the film [25]. The formation of P3HT nanocrystals was confirmed by the strong shoulder peaks in the absorption spectra, which suggested the strong interchain π-π staking (Figure 1.2.22). They also observed the much rougher surface in the "slow-grown" film than the "fast-grown" film by AFM investigation (Figure 1.2.23). From these result, together with the higher carrier mobility and efficiency (I_{SC}: 10.6 mA cm^{-2}, V_{OC}: 0.61 V, FF: 67.4, PCE: 4.4%) in the slow-grown film, they claimed the formation of self-organized P3HT crystalline network in the blend film with PCBM.

Kim et al, investigated the effect of regioregularity (RR) of P3HT on the crystallinity in the blend film with PCBM [29]. The absorption spectra of the thin film revealed that P3HT with the higher RR showed the stronger absorption with a shoulder, indicating the better crystallinity of P3HT with the higher RR in the blend film. Further investigation with grazing-incidence XRD measurement using a synchrotron X-ray beam (Figure 1.2.24) showed that the stronger out-of-plane diffraction peaks were observed in the blend film with the higher regioregular P3HT at 2 theta of 5.3º, 10.7º which corresponded for the primary (100) and secondary (200) peaks, indicating a well-organized intraplane structure of P3HT with lamellae oriented normal to the substrate. They also confirmed such P3HT crystalline network by TEM. As a result, the higher Time-of-Flight (TOF) carrier mobility was achieved in the film with a highly regioregular P3HT, resulting in a high efficiency of 4.4%.

The effect of RR of PPV on the nanostructure was also reported by Tajima and coworkers [86, 87]. They developed a new synthetic route with a novel anisotropic monomer to successfully synthesize a fully regioregular MDMO-PPV for the first time, and revealed the strong π-π interaction and the high crystallinity of the regioregular PPV in solid state which were confirmed by absorption spectra as well as powder XRD measurement [86]. They also reported that regioregular PPV prevented PCBM large aggregation which was revealed by AFM observation of the blend film (Figure 1.2.25). As a result, the solar cells fabricated with regioregular PPV showed the enhanced FF and I_{SC}, resulting in the highest efficiency of 3.1%

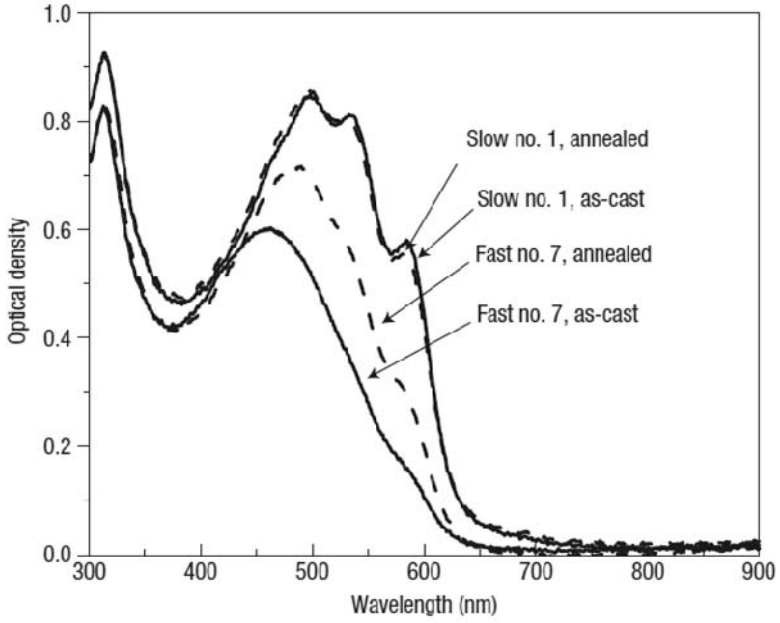

Figure 1.2.22. Effect of film growth rate and thermal annealing on the absorbance of the P3HT/PCBM films. Ultraviolet-visible absorption spectra for films of P3HT/PCBM (in 1:1 wt/wt ratio), for both slow-grown (no. 1) and fast-grown (no. 7) films, before (solid line) and after (dashed line) annealing. The films were spun cast at 600 r.p.m. for 60 s (film thickness ~ 210 nm) and the annealing was done at 100 ºC for 20 min. (**ref.25**)

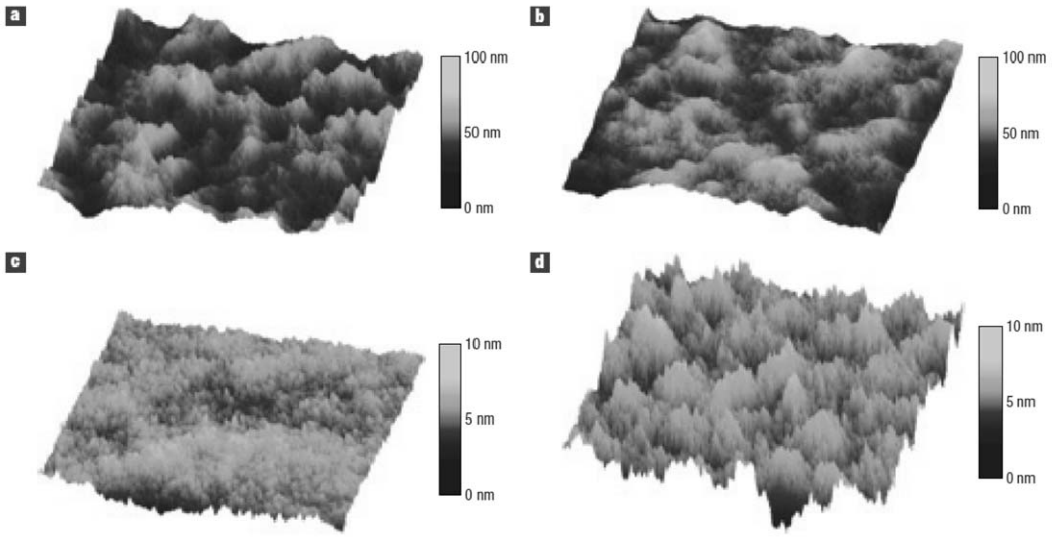

Figure 1.2.23. Effect of growth rate and thermal annealing on the morphology of the active layer. AFM height images of the P3HT/PCBM composite films (PCBM concentration = 50 wt%) showing a 5 μm × 5 μm surface area. a, Slow-grown film (no. 1) before thermal annealing. b, Slow-grown film (no. 1) after thermal annealing at 110 C for 10 min. c, Fast-grown film (no. 7) before thermal annealing. d, Fast-grown film (no. 7) after thermal annealing at 110 C for 20 min. Note that the colour scale for the films a and b is 0-100 nm, whereas for films c and d it is 0-10 nm. (**ref.25**)

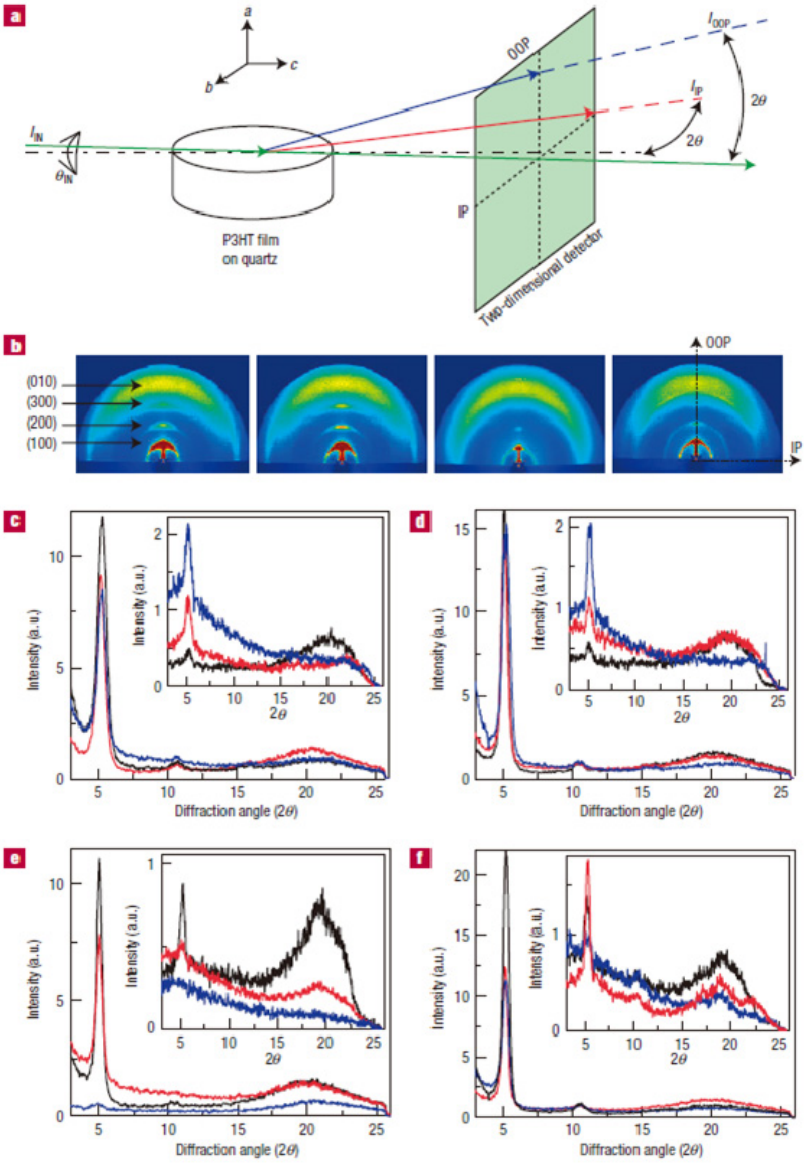

Figure 1.2.24. GIXRD setup and results for pristine and blend films. a,b, Schematic illustration 8a) of the two-dimensional GIXRD measurement (incident X-ray angle θ_{IN} = 0.2º) and representative two-dimensional images (b) of pristine P3HT film (no-annealed in first from left; annealed in second from left) and P3HT:PCBM (1:1) blend films (not-annealed in third from left; annealed in fourth from left). I_{IN}, incident X-ray intensity; I_{OOP}, diffracted X-ray intensity in the OOP direction; I_{IP}, diffracted X-ray intensity in the IP direction. c-f, OOP GIXRD diffractograms of pristine P3HT films (c, not-annealed; d, annealed) and P3HT:PCBM (1:1) blend films (e, not-annealed; f, annealed; approximately 200 nm thick): insets show corresponding IP GIXRD patterns. Black, red and blue colours represent 95.2%, 93% and 90.7% RR, respectively. (**ref.29**)

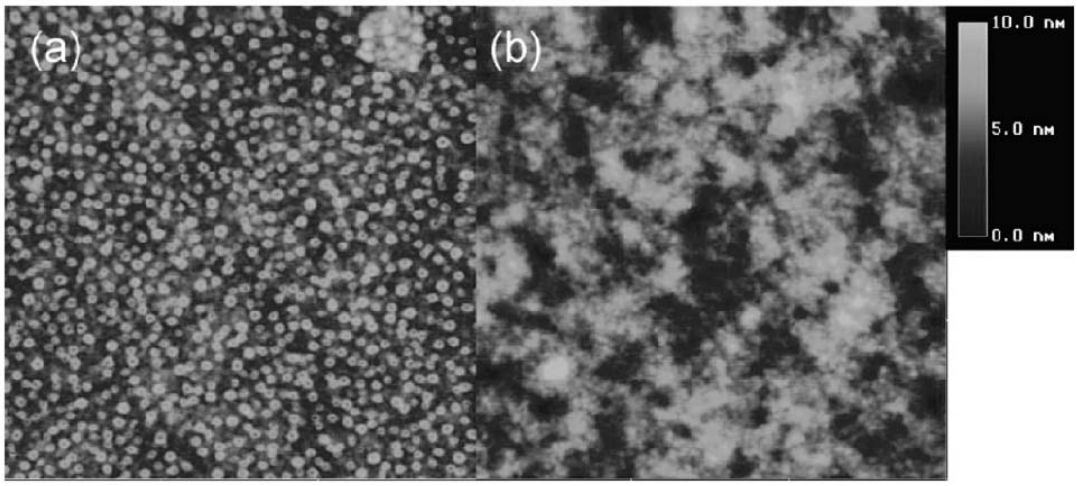

Figure 1.2.25. Atomic force microscopy height images of the spin-coated films from the mixtures of 67 wt% PCBM and (a) random-PPV (rms roughness, 1.2 nm) and (b) regular-PPV (rms roughness, 1.6 nm) (image size, 3 μm × 3 μm). (**ref.87**)

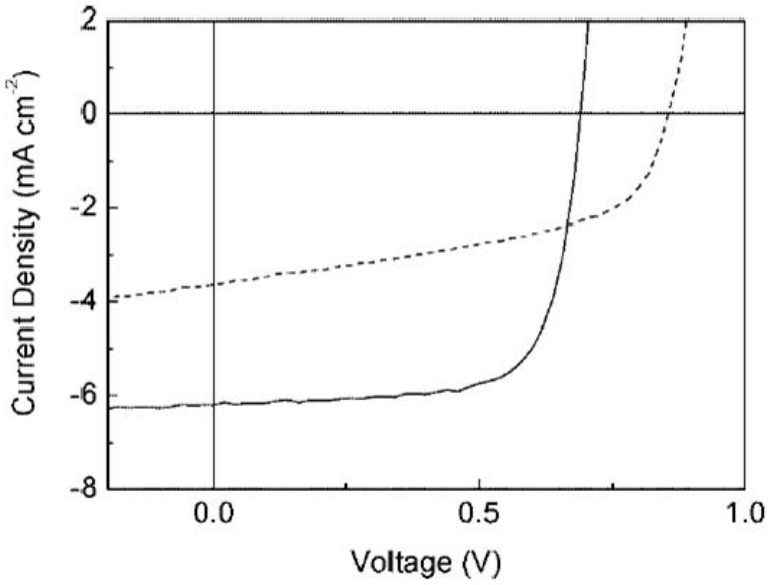

Figure 1.2.26. Atomic force microscopy height images of the spin-coated films from the mixtures of 67 wt% PCBM and (a) random-PPV (rms roughness, 1.2 nm) and (b) regular-PPV (rms roughness, 1.6 nm) (image size, 3 μm × 3 μm). (**ref.87**)

among the PPV-based solar cells (Figure 1.2.26) [87]. They also measured the SCLC hole mobility to reveal that regioregular PPV achieved 3.1×10^{-6} cm^2 V^{-1} s^{-1}, which was one order of magnitude higher than that of regiorandom PPV. All these results suggest that RR and resulting strong intermolecular π-π interactions of polymers are of great importance to form crystalline polymer network and prevent PCBM aggregation, and thus to form the interpenetrating network of the donor and acceptor in the film.

Interestingly, however, Sivula et al, reported that a small decrease in the effective RR of P3HT appeared to confer more thermal stability to the BHJ of P3HT and PCBM with implications on long-term performance [88]. They reduced the effective RR of P3HT by randomly incorporating a thiophene monomer with n-hexyl chains at both the 3 and 4 positions (poly(1-*co*-2) in Figure 1.2.27). TEM images revealed that a thermally stable interpenetrating network was formed with vermicular features on the order of 20 nm in width in poly(1-co-2) with RR of 91% and PCBM blend film while the large-scale phase segregation of the PCBM was formed in regioregular P3HT (RR: > 96%) and PCBM blend film after annealing at 150 ºC for 30 min (Figure 1.2.28). They also investigated the thermal stability of the device efficiency and found that the efficiency of the poly(1-co-2) device was almost the same even after annealing 300 min (Figure 1.2.29). Very recently, they further investigated the effect of RR of P3HT on the stability of the nanostructure of the BHJ structure with PCBM [89]. Optical microscopy images clearly showed that large PCBM aggregation in the BHJ film with the highly regioregular P3HT (RR = 96%) after thermal annealing for a long time (Figure 1.2.30), leading to the deterioration in the device efficiency. In contrast, P3HT with low RR of 86% prevented such large PCBM aggregation and stabilized the device efficiency. These results above suggest that a small decrease in RR is effective to prevent PCBM large aggregation and stabilize the BHJ nanostructure.

In section 1.2.3, the investigation and formation of the nanostructures and its importance in the BHJ structure of donor and acceptor was described to reveal that following factors are of importance for forming a proper nanostructure of donor and acceptor (i.e. 10-nm-scale phase separation, interpenetrating network) as well as its stability; a solvent for a blend solution, annealing condition, evaporation speed of a solvent during the spin-coat process, and

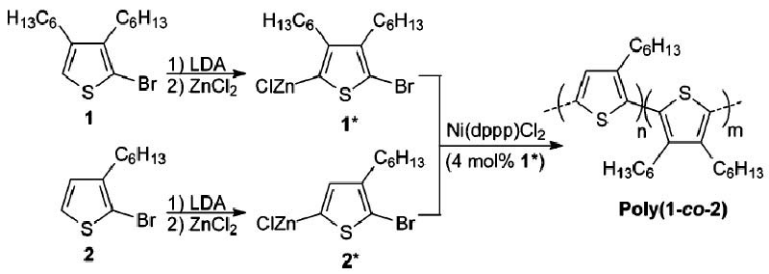

Figure 1.2.27. Synthetic scheme and molecular structure of poly(1-*co*-2). (**ref.88**)

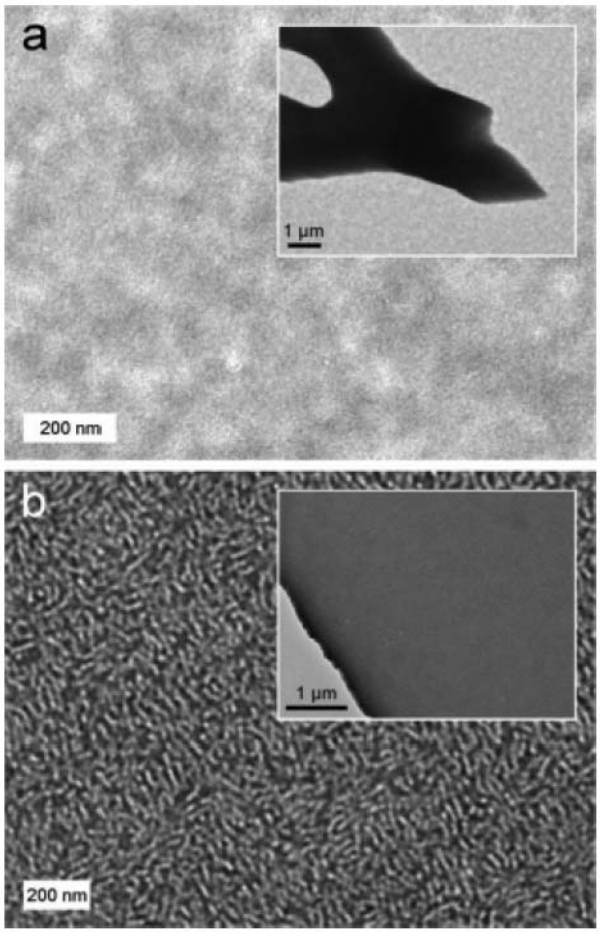

Figure 1.2.28. Transmission electron micrographs of annealed BHJ thin films containing 1:1 by weight RR-P3HT:PCBM (a) and poly(1-*co*-2):PCBM (b) An interpenetrating network of polymer and fullerene is observed with poly(1-*co*-2) (b), while no obvious features are seen in the polymer region of the control case (a). The insets show a wider view of the films and the micron-scale phase segregation of PCBM (dark region) from the RR-P3HT in the control case. No micron-scale features are observed when poly(1-*co*-2) is used in the BHJ. The film edge is shown to confirm focus in the inset of (b). (**ref.88**).

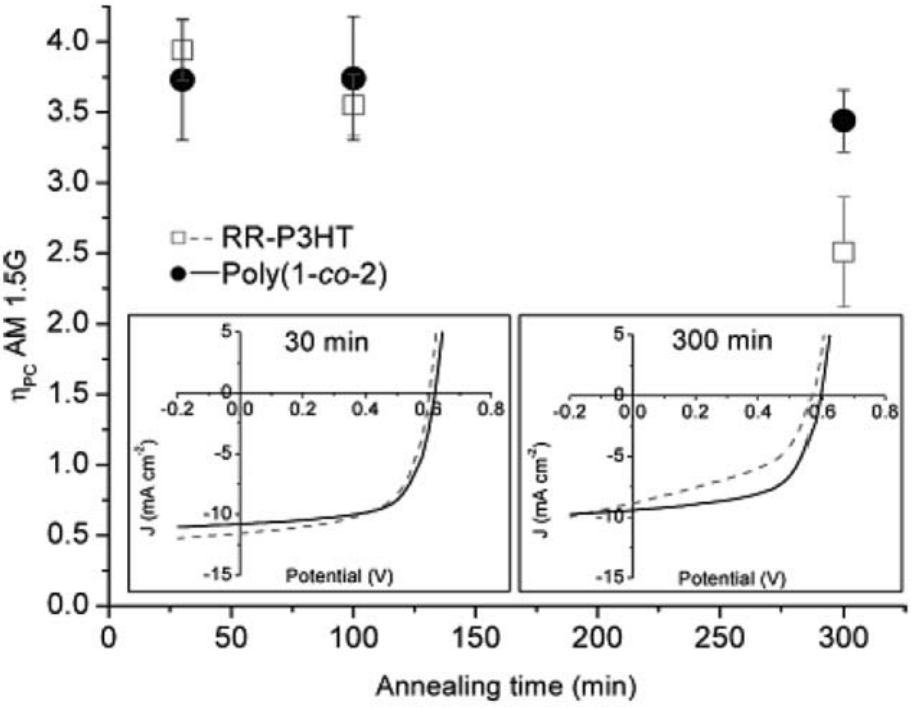

Figure 1.2.29. Performance of photovoltaic devices fabricated with the control RR-P3HT or poly(1-*co*-2). The eight-device average power conversion efficiency (η_{PC}) at standard conditions as a function of annealing time at 150 ºC and typical *J-V* behavior (insets) observed after 30 and 300 min of annealing illustrate the difference between the materials. The error bars represent the 95% confidence interval of the average values. (**ref.88**).

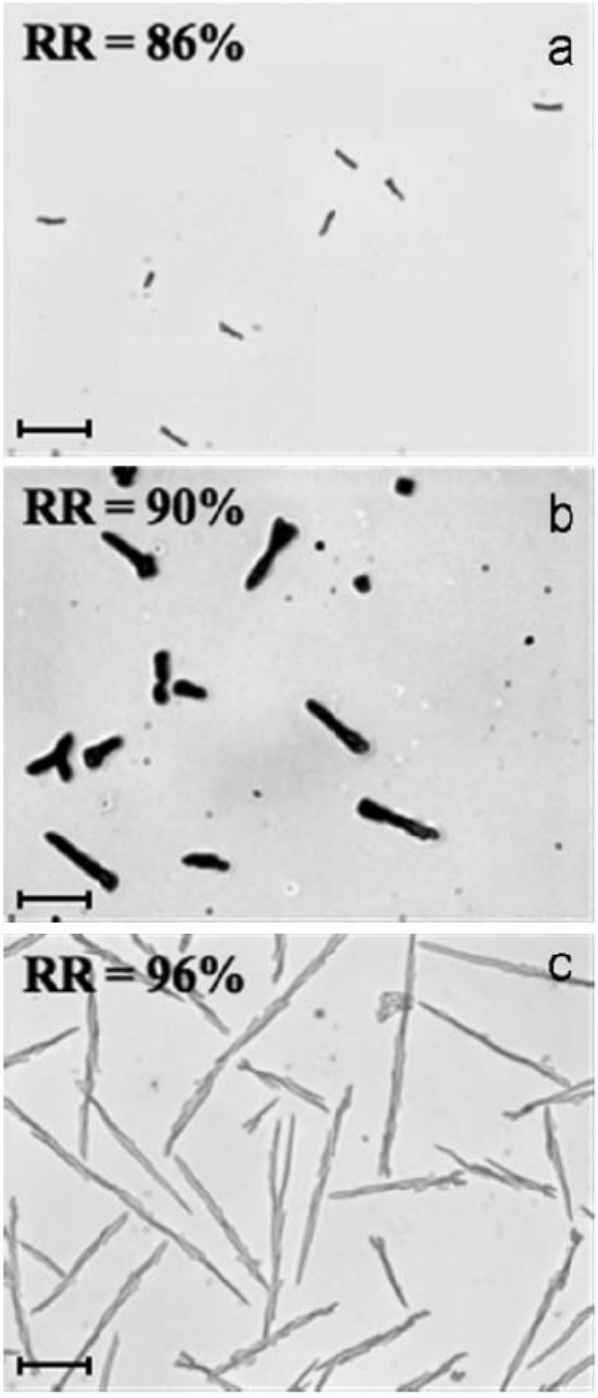

Figure 1.2.30. Optical microscopy images of (1) 86, (b) 90, and (c) 96% RR-P3HT:PCBM blends at a 55:45 weight ratio after 3 h of annealing at 150 ºC. Dar areas are PCBM-rich regions. Scale bar = 50 μm. (**ref.89**)

regioregularity of polymers. The nanostructure in BHJ system is generally formed simply by self-organization of the components during the coating and thermal annealing processes and thus formation of the nanostructure strongly depends on characters of the materials used and the conditions of the fabrication processes. Although the nanostructure formation is highly important, these things are just empirically optimized through trial and error and not well-controlled, resulting in the aforementioned large difference in optimized conditions among research groups as well as low reproducibility of the results. In fact, the most studied polymer and PCBM based solar cells often suffer from such problems. In addition, polymer based solar cells also suffer from batch-to-batch difference in polymer characters such as regioregularity, molecular weight, purity, etc, which leads to low reproducibility problem. For example, influence of the polymer molecular weight on the blend nanostructure with PCBM as well as the efficiency of the device was reported by Ma et al [90-92]. Therefore, nanostructure control, or elaborate nanostructure formation must be considered.

1.2.4. Nanostructure formation by molecular designs

1.2.4.1. π-conjugated oligomers

In the previous sections, it is suggested that polymer-based solar cells often suffers low reproducibility on formation of a proper nanostructure of donor and acceptor, and one possible reason is batch-to-batch difference in characters of polymers since it is difficult to always obtain polymers with the exactly same properties (RR, molecular weight, polydispersity, etc). In this respect, solution-processable small molecules such as π-conjugated oligomers have attracted much attention with their advantage over polymeric counterparts such as ease in synthesis and purification, monodispersity (there exists no RR or polydispersity in oligomers) as well as high carrier mobility. Moreover, characters of oligomers can be controlled more easily by molecular design in a way to form a proper nanostructure, compared to polymeric counterparts. Yet, the nanostructure investigation has not been well explored in the oligomer-based solar cells, and thus in this short section, recent achievement of a high efficiency over 1% by means of molecular design is briefly reviewed.

Lloyd et al, reported a synthesis of a novel anthradithiophene derivative (ethyl-TES-ADT in Figure 1.2.31) with an excellent charge carrier mobility 0.11 $cm^2 V^{-1} s^{-1}$, and fabricated the BHJ devices with PCBM [93]. Solvent vapor annealing formed spherulites which consist of a network of anthradithiophene crystallites dispersed in an amorphous matrix composed primarily of fullerene (Figure 1.2.32), and the devices with 82% spherulites coverage achieved a PCE of 1%. Valentini et al, also reported a novel soluble anthracene-based derivative (Figure 1.2.33) and its BHJ device with PCBM, resulting in a PCE of 1.12% [94].

Roquet et al, introduced a three-dimensional conjugated architecture to solve the problem of low-dimensional nature of π-conjugated oligomers which strongly reduces the absorption cross section for the incident light as well as the efficiency of charge transport [95]. They synthesized novel star-shaped triphenylene (TPD)-thienylenevinylene donors (Figure 1.2.34) and fabricated the BHJ devices with PCBM. Relatively high V_{OC} of 0.89 V and I_{SC} of 3.65 mA cm^{-2} were observed in the device with compound 4 (Figure 1.2.34) and the maximum PCE of 1.17% was obtained. He et al, also reported novel TPD-based star-shaped molecules (Figure 1.2.35) and

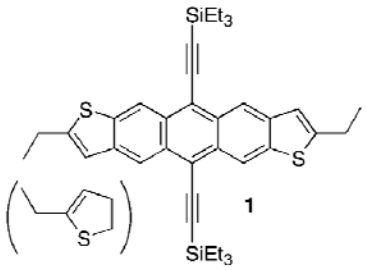

Figure 1.2.31. Molecular structure of Ethyl-TES-ADT. (**ref.93**)

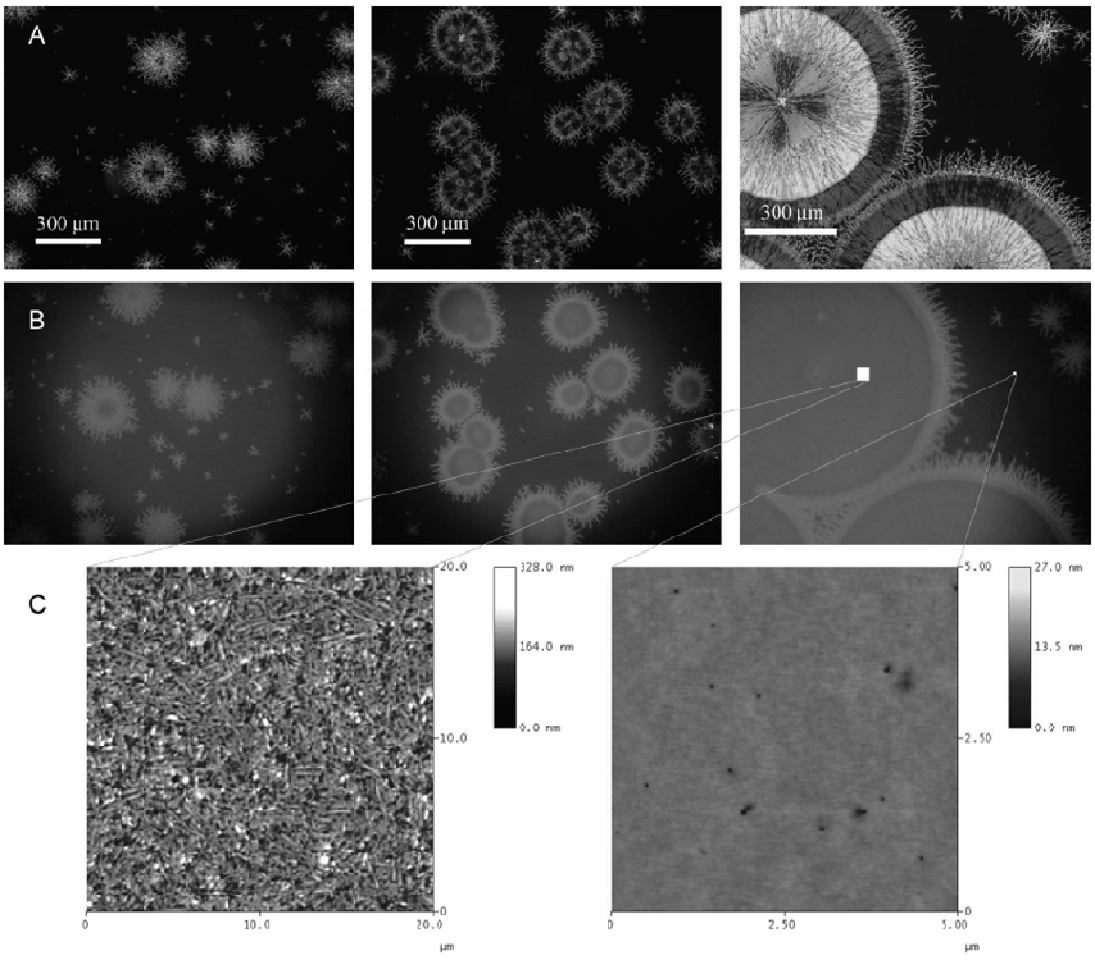

Figure 1.2.32. Optical micrographs of spherulites growth as seen through crossed polarizers (A) and by fluorescence (B). Spherulite growth induced by annealing with residual solvent vapor after 1 min (first column), 2 min (second column), and 3 min (third column). (C) AFM images inside and outside of a spherulites. (**ref.93**)

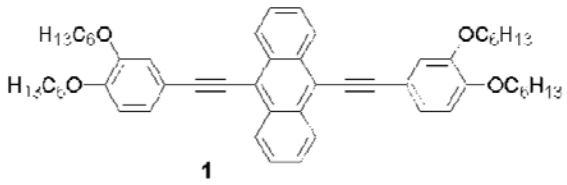

Figure 1.2.33. A novel diarylanthracene with hexyloxy groups in the benzene rings. (**ref.94**)

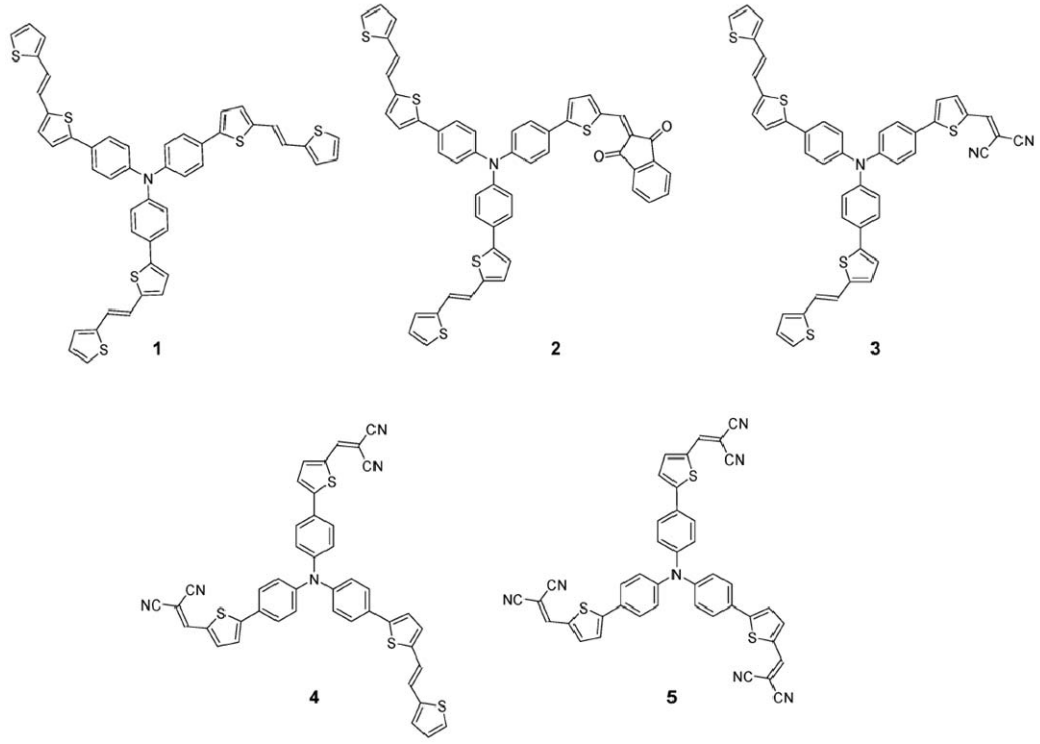

Figure 1.2.34. A novel star-shaped triphenylene (TPD)-thienylenevinylene donors. (**ref.95**)

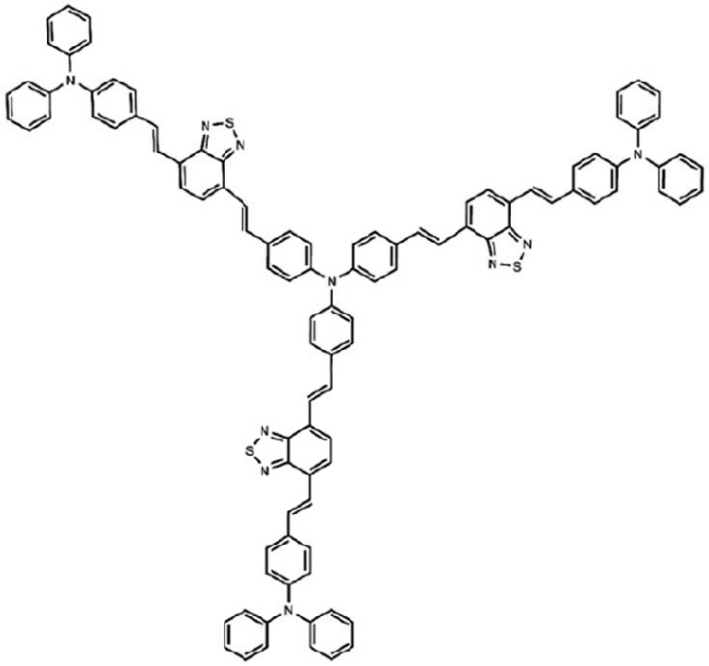

Figure 1.2.35. A novel TPD-based star-shaped molecule, S(TPA-BT). (**ref.96**)

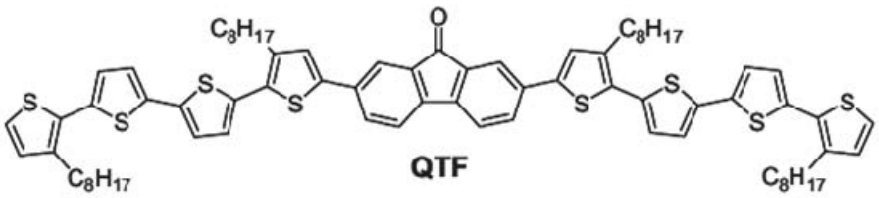

Figure 1.2.36. A novel fluorenone-based oligomer, QTF. (**ref.97**)

achieved the maximum PCE of 1.33% in its BHJ device with PCBM [96].

Very recently, low band-gap concept was introduced to π-conjugated oligomer based solar cells and high efficiencies have been achieved by several authors [97-100].

Lincker et al, synthesized novel fluorenone-based oligomers (Figure 1.2.36) to extend the wavelength region of the absorption by utilizing an intramolecular charge transfer band transition [97]. As a result, a relatively high I_{SC} of 3.61 mA cm^{-2} was achieved, resulting in a PCE of 1.19% in the QTF:PCBM BHJ device.

Tamayo et al, introduced a highly absorbing chromophore, diketopyrrolopyrrole into the oligothiophene backbone (α,α-DH6TDPP in Figure 1.2.37) to narrow the band gap of the molecule by a donor-acceptor approach [98]. The band gap was successfully reduced and the absorption edge reached up to 820 nm in the thin film (Figure 1.2.38). Such advantageous extension of absorption range leads to a large increase in I_{SC} up to 8.42 mA cm^{-2}, resulting in a high efficiency of 2.33% in the BHJ device with PCBM, which is the highest efficiency in the solution processed small molecules based solar cells (Figure 1.2.39).

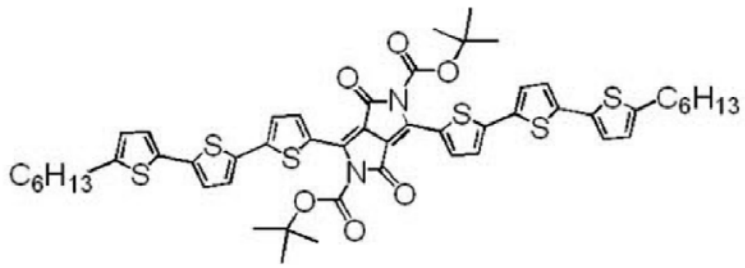

Figure 1.2.37. Molecular structure of α,α-DH6TDPP. (**ref.97**)

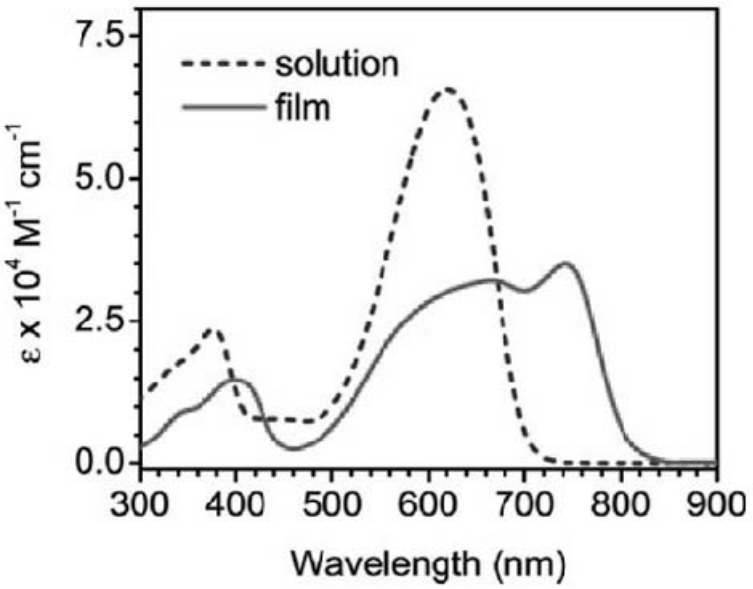

Figure 1.2.38. Solution and film absorption of α,α-DH6TDPP in chloroform and on a quartz substrate. (**ref.97**)

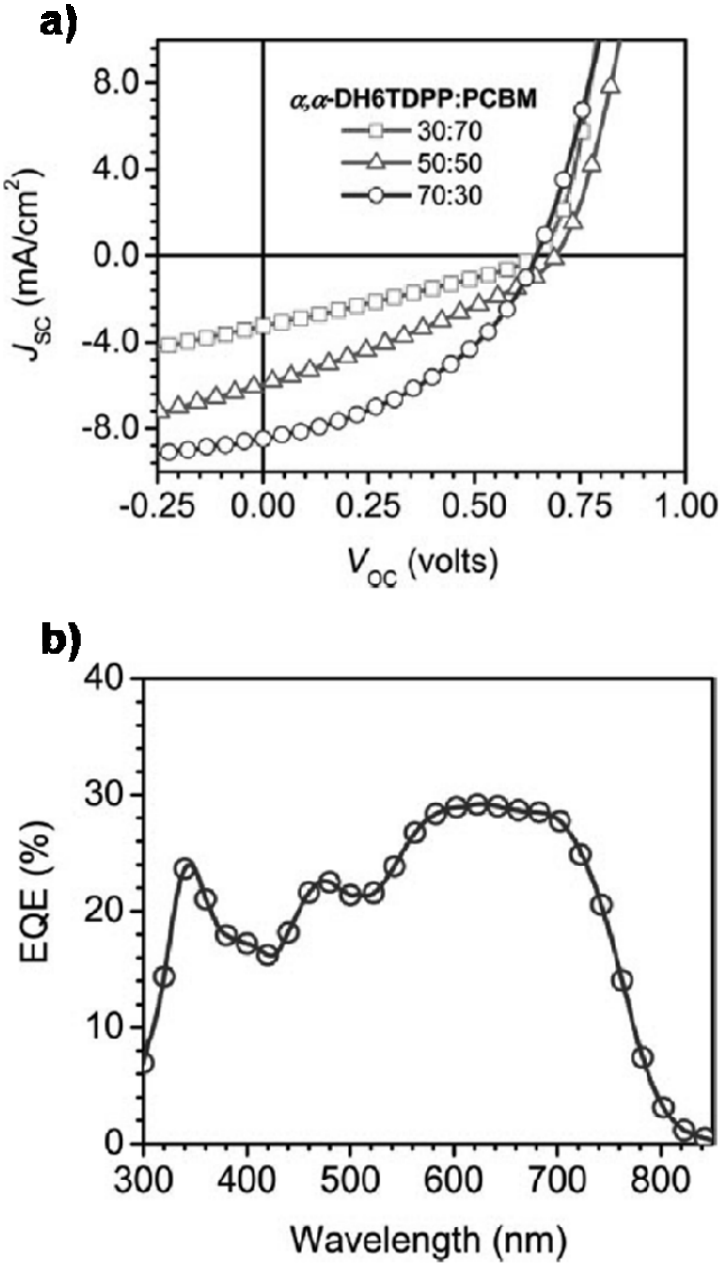

Figure 1.2.39. a) *J-V* characteristics of organic solar cells prepared fromα,α-DH6TDPP:PCBM blends: 30:70 (red squares), 50:50 (green triangles), and 70:30 (blue circles) under AM 1.5 irradiation (100 mW/cm^2). b) External quantum efficiency (EQE) curve for device using 70:30 blend of α,α-DH6TDPP (**ref.97**).

1.2.4.2. Nanostructure formation supramolecular approach

Self-assembly or –organization of organic molecules is one of the powerful tools used to control the nanostructures and to fine-tune the electronic interactions between the molecules [101-116]. There have been several intriguing reports on nanostructure formation in BHJ solar cells by such supramolecular approach. In this short section, some representative work is briefly reviewed.

The first report based on this idea reported by Schmidt-Mende et al in 2001 [117]. They utilized a discotic liquid crystal (LC) hexa-peri-hexabenzocoronene (HBC-PhC_{12}, Figure 1.2.40) as a donor which is discotic LC with columnar structure at room temperature and allows quasi-1D transport of charge carriers and excitons along the columns with high carrier mobility of as high as $\Sigma\mu_{1D} = 0.22\ cm^2\ V^{-1}\ s^{-1}$ [118]. As for an acceptor introduced was perylene diimides which possess high electron mobilities (Figure 1.2.40) [119]. They introduced those materials to enhance the charge transport through the spontaneous nanostructure formation in the BHJ device. In the blend film, vertical segregation of perylene (top) and HBC-PhC_{12} (bottom) was observed by AFM and SEM (Figure 1.2.41). The device with this blend film showed a reasonably high EQE of 34% and a PCE of 1.95% under monochromatic light irradiation. They attributed this result to efficient charge transfer through the HBC-PhC_{12} columns and crystalline network of the segregated perylene.

Another interesting study on utilization of a discotic LC molecule was reported by Hirota et al [120]. They introduced liquid crystalline 1,7,13-triheptanoyldecacyclene (C_7DC) (Figure 1.2.42) as an acceptor for the first time into a BHJ device with MEH-PPV in order to construct the charge carrier pathway through hexagonal columnar structure formed by self-organization of C_7DC [121]. AFM investigation (Figure 1.2.43) revealed that the square-shaped crystal-like structures were formed in the blend film of C_7DC and MEH-PPV after annealing at the LC transition temperature, suggesting the formation of crystalline network of C_7DC. As a result, the BHJ device fabricated such film improved the EQE by more than two-fold and resulted in an improved PCE of 0.3% under monochromatic light irradiation (500 nm), compared to the those of the as-cast device. They attributed this result to the enhanced electron mobility through the

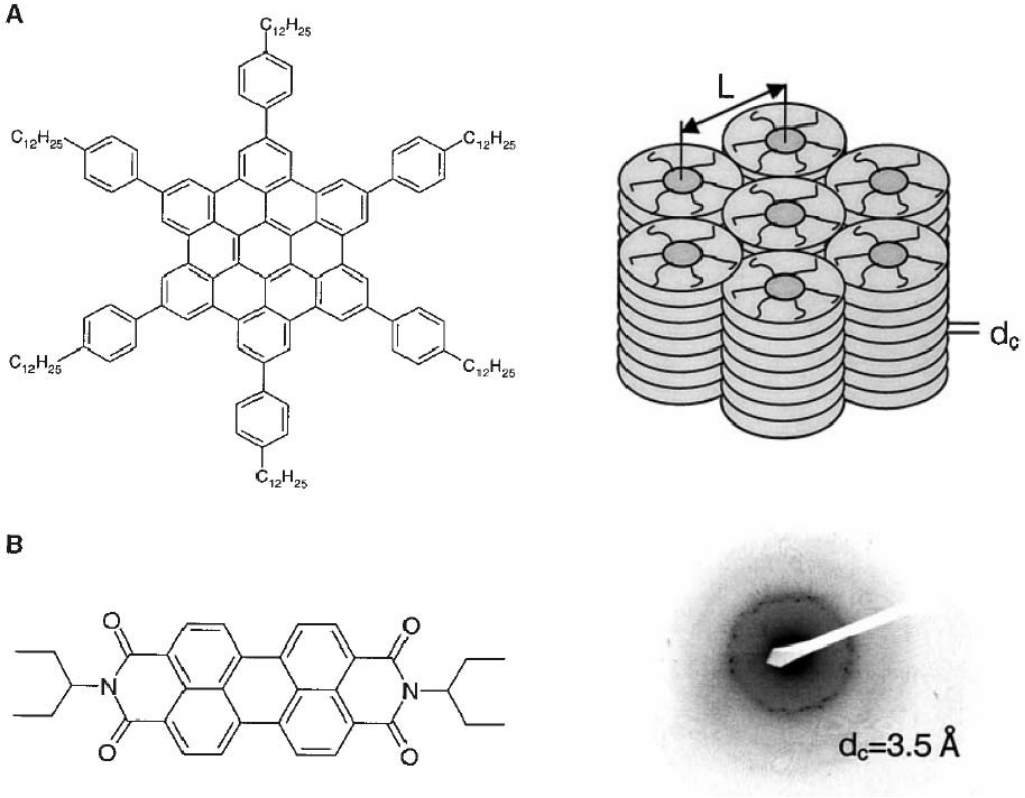

Figure 1.2.40. (A) The molecular structure of HBC-PhC_{12}, along with a simplified diagram of the π-π stacking configuration. The intercolumnar distance L = 34 Å and the cofacial distance d_c = 3.5 Å. (B) The structure of the perylene molecule and an electron diffraction image taken from a spin-coated xylene film. The densest ring of diffraction spots from perylene diimide crystallites corresponds to a spacing of approximately 3.5 Å. (**ref.117**)

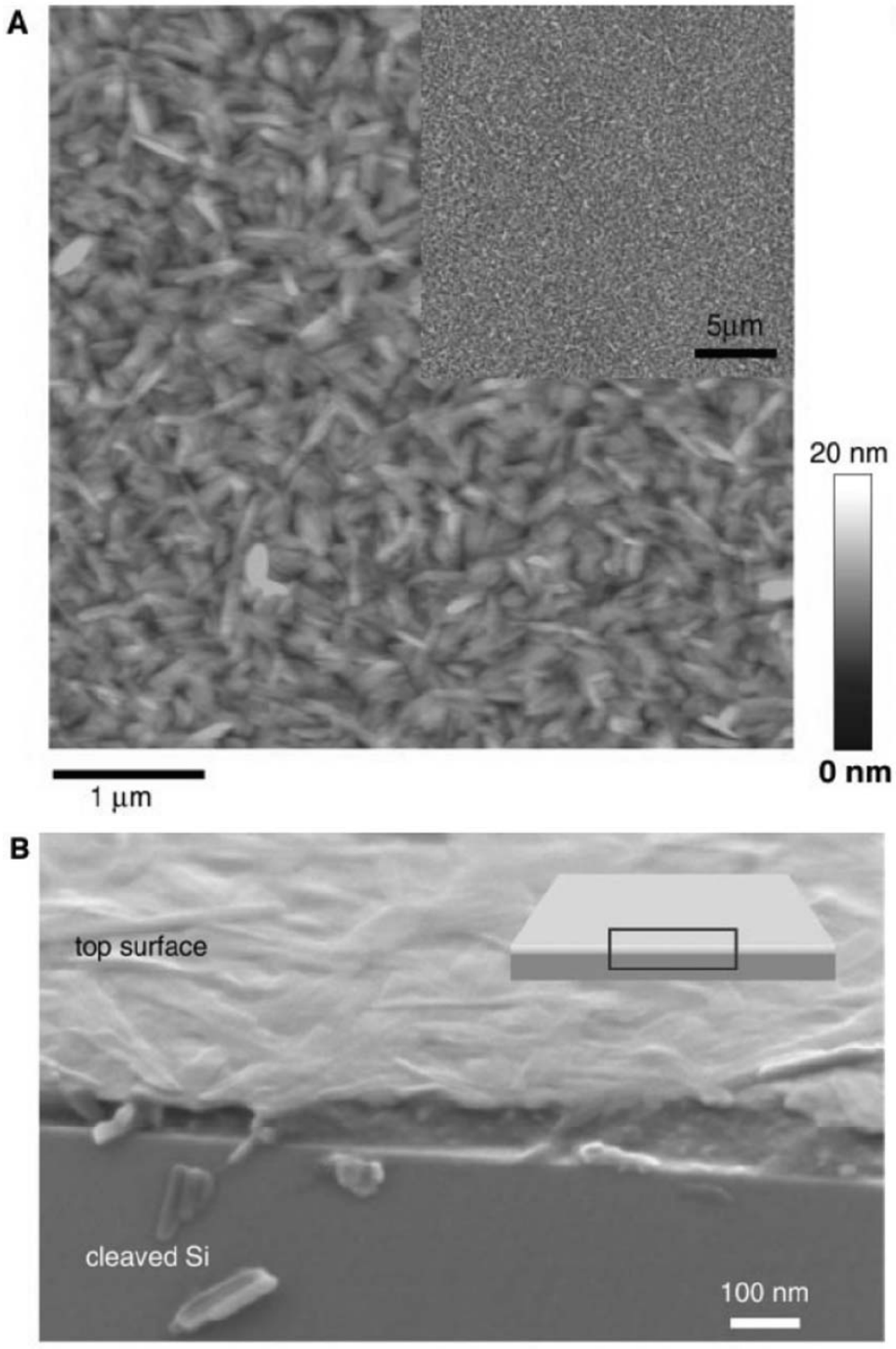

Figure 1.2.41. (A) Tapping-mode AFM image of a film spin-coated from a 40:60 blend solution of HBC-PhC_{12} and perylene diimide. (B) Field-emission SEM image of a 40% HBC-PhC_{12} blend sample, imaged with the cleaved surface tilted 15º from normal to the incident electron beam (1 kV). (**ref.117**).

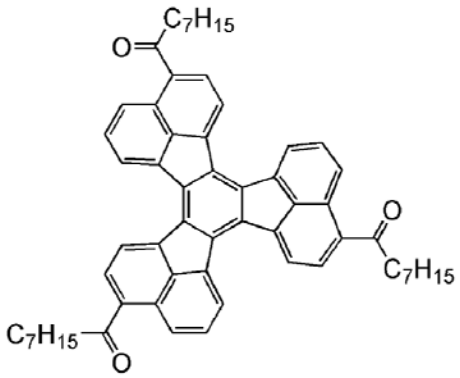

Figure 1.2.42. (A) Molecular structure of 1,7,13-triheptanoyldecacyclene (C_7DC). (**ref.120**)

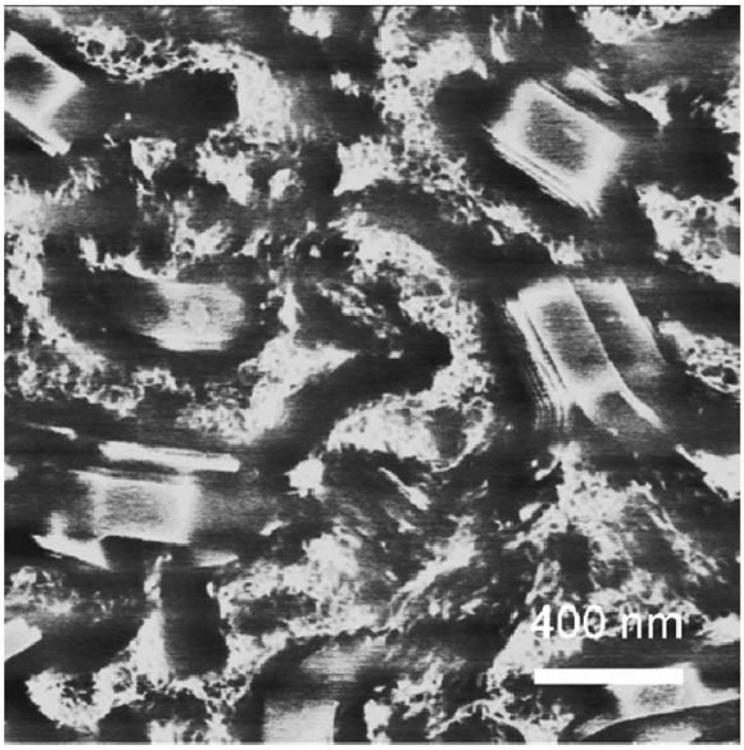

Figure 1.2.43. AFM phase image for MEH-PPV/C_7DC device surface after annealing at 100 ºC for 30 min (2 μm × 2 μm). (**ref.120**)

C_7DC crystalline network. Interestingly they also achieved one of the highest V_{OC} in the solar cells of 1.3V.

O'Neill and coworker reported a very interesting approach to control the nanostructure by utilizing a LC get as a template [122, 123]. They used a new electron-donating, visible-light absorbing, LC gel to form a surface with nanometer-sized grooves where electron acceptor materials are filled in to form the large interface as well as interpenetrating network (Figure 1.2.44). Such structure was constructed by following steps; at first a homogeneous mixture film of a reactive mesogen (**1** in Figure 1.2.45) and a non-polymerizable LC (**2** in Figure 1.2.45) was irradiated by UV light to polymerize **1**, resulting in controlled phase separation of the two components and the formation of a polymer network matrix around the nematic droplets [124]. Then a sponge-like surface with empty nanometer-sized grooves was formed by the removal of the soluble LC droplets by washing with an organic solvent, followed by filling the grooves with a novel acceptor, perylene incorporated with fluorene groups (**3** in Figure 1.2.45). The cross section of the surface morphology of thin films obtained using AFM (Figure 1.2.46) revealed formation of the grooves and refilling them by acceptor materials. As a result, an EQE of 5.3% and an improved PCE of 0.6% under monochromatic light irradiation (45 mW cm^{-2}, 500 nm) were achieved, compared to the control device with bilayer configuration.

Jonkheijm et al, utilized hydrogen-bonding (H-bonding) to control film morphology [125]. They synthesized oligo(*p*-phenylenevinylene) (OPV) with ureido-*s*-triazine H-bonding group, and found that the OPV derivative formed the columnar stacks in dodecane as well as concentrated toluene solutions, observed by neutron scattering experiment (Figure 1.2.47). This structure was successfully transferred to the thin solid film, which was confirmed by AFM, and the BHJ devices were fabricated with PCBM (Figure 1.2.48). Unfortunately, in the blend film, such structure was not clearly observed but instead large PCBM aggregation was observed (Figure 1.2.49). As a result, the maximum EQE was limited to 12% (430 nm) and a PCE of 0.25% was obtained under a white light irradiation (100 mW cm^{-2}, 400-800 nm).

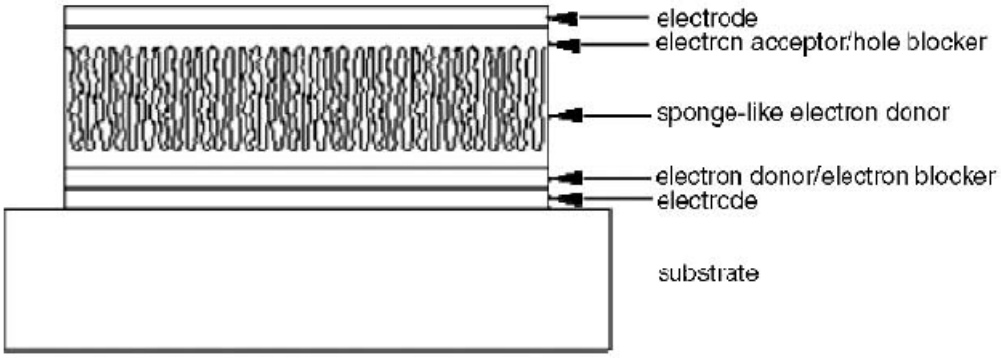

Figure 1.2.44. An illustration of an ideal LC composite photovoltaic containing three distinct organic layers deposited by spin-casting sandwiched between two electrodes. The first organic layer consists of an insoluble electron-blocking polymer network formed by crosslinking of an electron-donating reactive mesogen. The next layer has a spongelike surface with empty nanometer-sized grooves formed by the removal of the soluble LC droplets by washing a phase-separated LC gel in an appropriate solvent. The gel is created by photopolymerization of a homogeneous thin-film blend of an electron-donating reactive mesogen and its corresponding nonpolymerizable analogue. The third layer consisting of an electron-accepting, hole-blocking material is deposited by the same solution process on top of the honeycomb polymer network to fill the empty grooves. A vertically separated and large-area interface between electron-donating and electron-accepting layers provides complete and separate pathways for transport of holes and electrons to the bottom and top electrode, respectively. Trapped nonopolymerizable LC residues in the second layer will not disrupt hole transport because they have the same electronic properties as the liquid-crystalline polymer network. (**ref.122**)

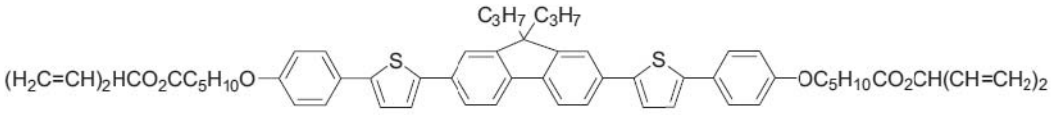

Compound **1**. T_g = 39 ºC; Cr-N = 92 ºC; N-I = 108 ºC.

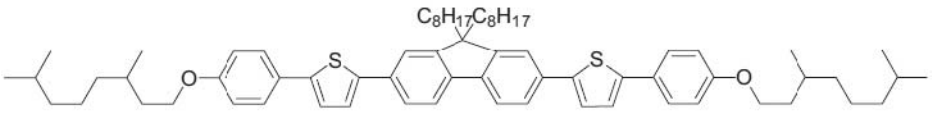

Compound **2**. T_g = -4 ºC; Cr-I = 72 ºC; N-I = 61 ºC.

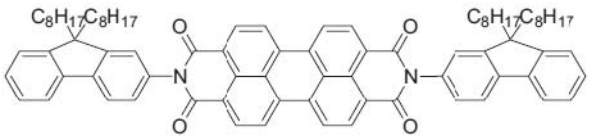

Compound **3**. Cr-I = 274 ºC (glass forms on rapid quenching in thin films).

Figure 1.2.45. The molecular structures and transition temperatures of the reactive mesogen **1**, the non-polymerizable LC **2**, and the electron-accepting material **3**. Cr-N and Cr-I represents the melting of the crystalline state of a compound to form the liquid-crystalline nematic phase and liquid phase, respectively. N-I represents the transition from the nematic phase into the isotropic liquid. The glass transition temperature is represented by T_g. (**ref.122**)

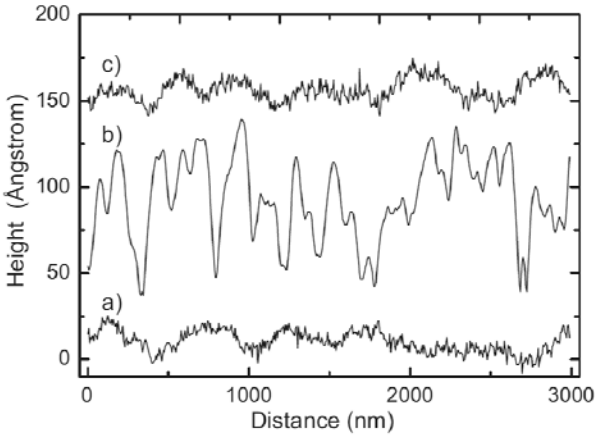

Figure 1.2.46. A cross section of surface morphology obtained using AFM of the thin-film gel following a) photopolymerization, b) washing of the photopolymerized gel, and c) deposition of the electron-accepting glassy layer of 3. The plots are displaced upwards for clarity. (**ref.122**)

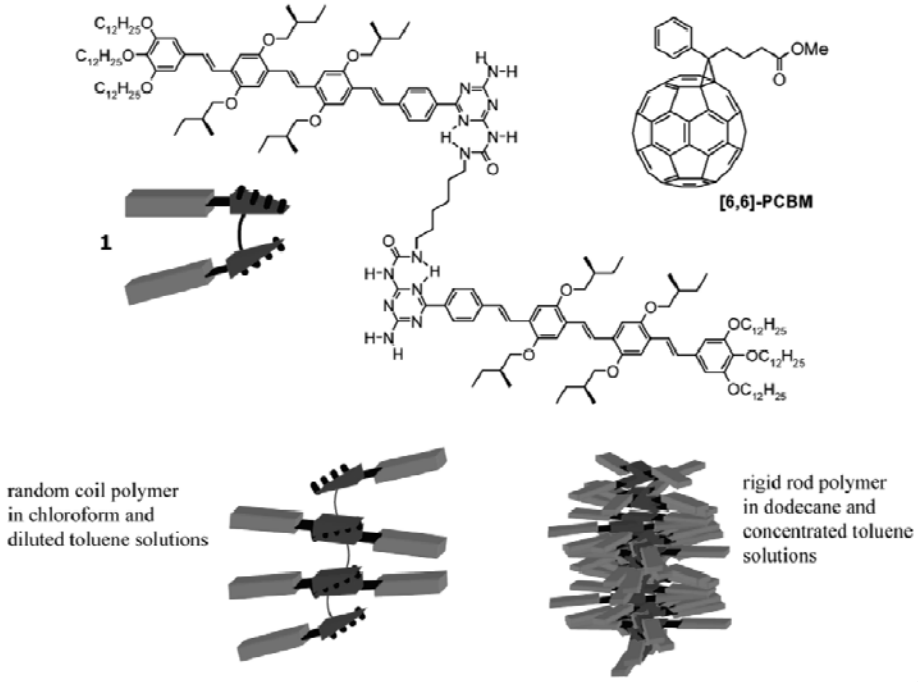

Figure 1.2.47. Molecular structure of oligo(*p*-phenylenevinylene) (OPV) with ureido-*s*-triazine H-bonding group (**1**). The blue blocks represent OPV parts, and the red triangles represent the quadruple hydrogen-bonding ureido-s-triazine units. The self-assembly process of **1** into random coiled and rigid rod polymer is depicted. The random coiled polymer of **1** is present in chloroform and dilute toluene solutions. Folded rigid-rod polymer of 1 exists in dodecane and concentrated toluene solution. (**ref.125**)

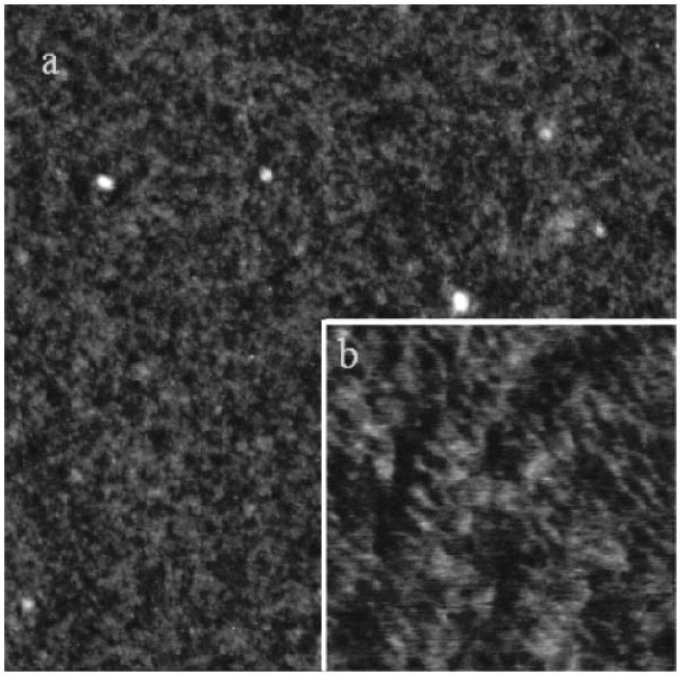

Figure 1.2.48. (a) Height image (a) 10 × 10 μm^2, z-scale 10 nm and (b) close-up phase image, 200 × 200 nm^2, z-scale of spin-cast films of **1** from toluene onto glass. (**ref.125**)

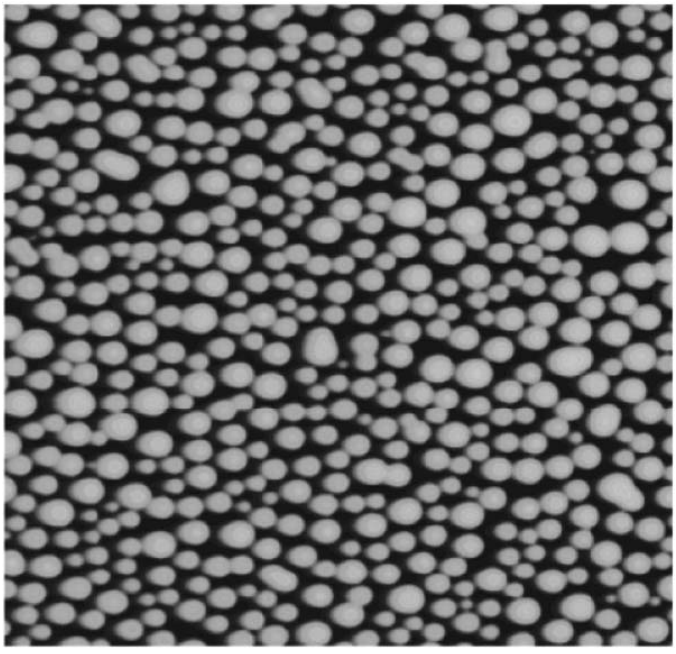

Figure 1.2.49. TM-AFM height image (z-scale is 90 nm, 10 × 10 μm^2) on blend films of 1 and PCBM spin-cast from toluene. (**ref.125**)

1.3.4.3. Nanostructure Stabilization and Formation by Block Copolymers

Block copolymers which compose immiscible polymeric parts (blocks) are well known to spontaneously form the segregated structures of each part with the dimensions of 5-20 nm, and have attracted much attention as a powerful tool to control the nanostructure [126-128]. In fact, several authors have reported the utilization of block copolymer to organic solar cells for stabilizing the nanostructure [129, 130], constructing the nanostructure as active materials [131, 132].

Sivula et al, reported the synthesis of a diblock copolymer incorporated with P3HT macromonomer and fullerene (poly(1)-block-poly(2) in Figure 1.2.50) for increasing the miscibility of P3HT and PCBM in the blend films and thus for stabilizing the nanostructure [129]. TEM images clearly revealed that the large phase separation and formation of PCBM clusters were suppressed in the blend film after annealing at 140 ºC for 1 hour by adding 17 wt.-% poly(1)-block-poly(2) (Figure 1.2.51). As a result, the efficiency of the device was stabilized even after a long time annealing (Figure 1.2.52). Similar study was also reported recently by Zhou et al [130].

de Boer et al, firstly reported the introduction of a donor-acceptor block polymer as the active material into solar cells[131]. They synthesized a novel diblock copolymer (PPV-*b*-P(S-*stat*-C_{60}MS) in Figure 1.2.53) which composes PPV as one block and C_{60}-functionalized polystyrene (PS) as the other, and investigated its nanostructure in the film as well as photovoltaic property. To their disappointment, the AFM image revealed that no highly ordered structure was formed but instead the elongated fiber like structure was observed (Figure 1.2.54). The diblock copolymer showed the higher photocurrent and resulted in the better PCE of 0.07% under monochromatic light irradiation (1 mW cm^{-2} at 458 nm), compared to those of the corresponding blend device with the donor homopolymer and the acceptor polymer. Similar diblock polymers grafting donor and acceptor materials, aiming at application to solar cells were also reported recently by several authors [132-135].

Another interesting approach for formation of nanostructure is utilization of all-conjugated block copolymers since they can reduce opto-electronically inactive (insulating) parts which donor-acceptor grafting type block copolymer contains such as PS part [127]. Several authors

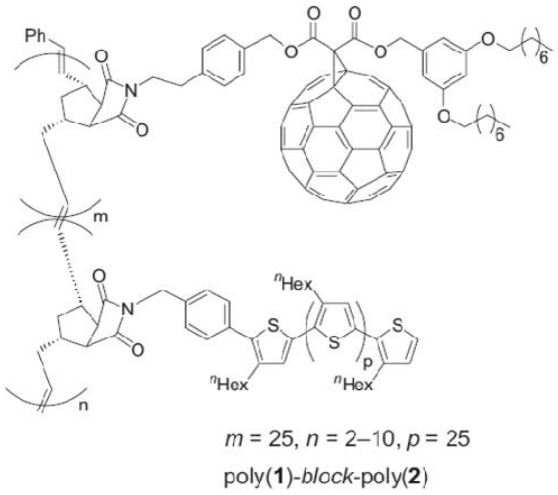

Figure 1.2.50. Molecular structure of poly(**1**)-*block*-poly(**2**). (**ref.129**)

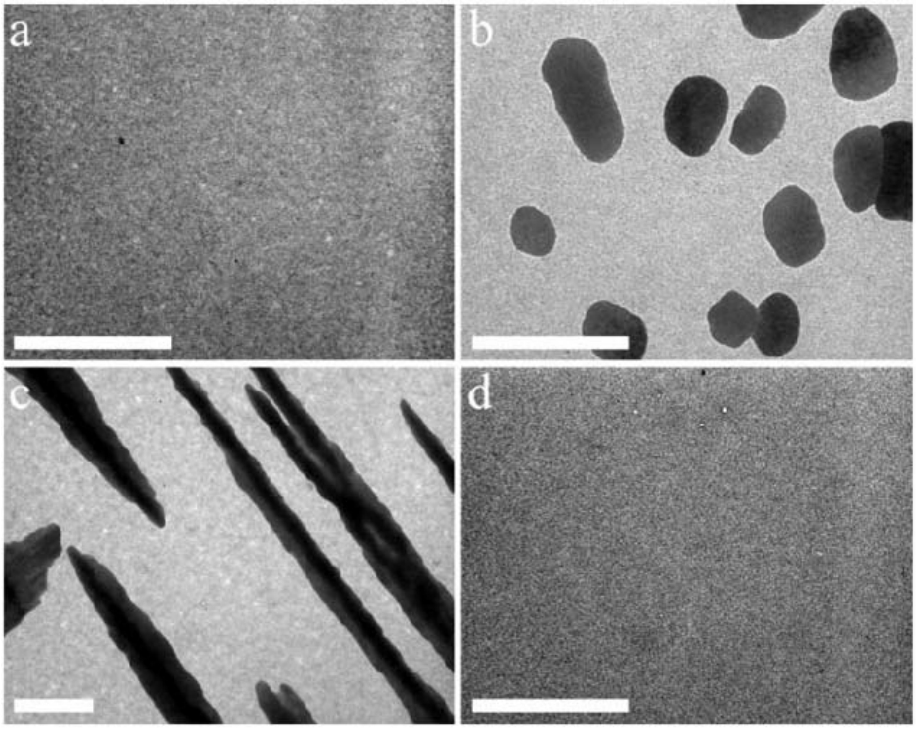

Figure 1.2.51. TEM image of a thin film of a) 1:1 P3HT/PCBM blend before annealing, and b) after annealing for 1 h at 140 C. c) 1:1 P3HT/PCBM + 5 wt.-% poly(**1**)-*block*-poly(**2**) after annealing (140 ºC). d) 1:1 P3HT/PCBM +17 wt.-% poly(**1**)-*block*-poly(**2**) after annealing (1 h, 140 ºC). The white scale bars are 2 μm. Solutions of the blends were spin-cast onto NaCl. After annealing, the films were floated onto water and placed on a 400-mesh copper grid. Images were obtained without stain; dark areas indicate fullerene-rich regions. (**ref.129**)

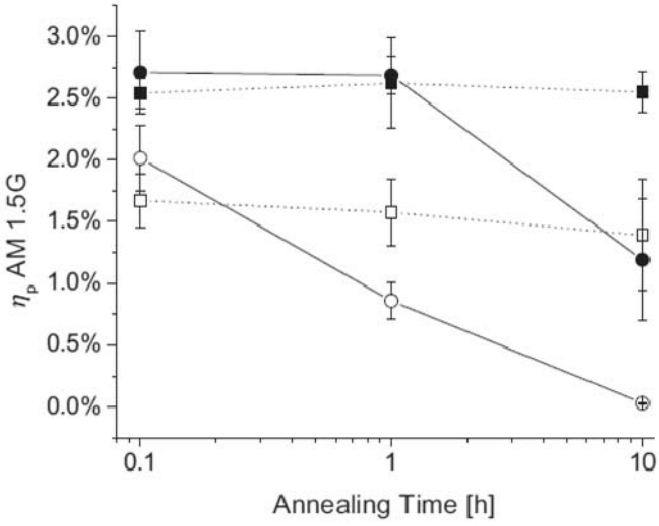

Figure 1.2.52. Average power conversion efficiency (AM 1.5G, 100 mW cm^{-2}) of 1:1 P3HT/PCBM solar cell as a function of annealing time before (open marks: ○, □) and after (closed marks: ●, ■) deposition of the aluminum electrode. Round marks (○, ●) represent standard P3HT:PCBM devices, while square marks (□, ■) represent devices made with 17 wt.-% poly(**1**)-*block*-poly(**2**) included in the active layer. Eight separate devices on one substrate were compared to give the average and standard deviation. (**ref.129**)

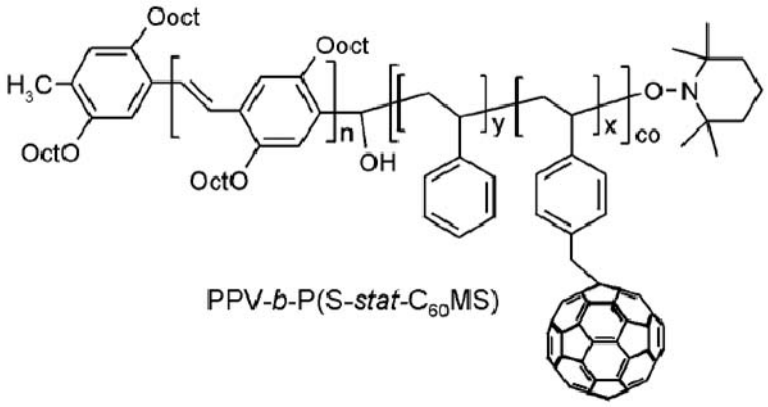

Figure 1.2.53. Molecular structure of PPV-*b*-P(S-*stat*-C_{60}MS). (**ref.131**)

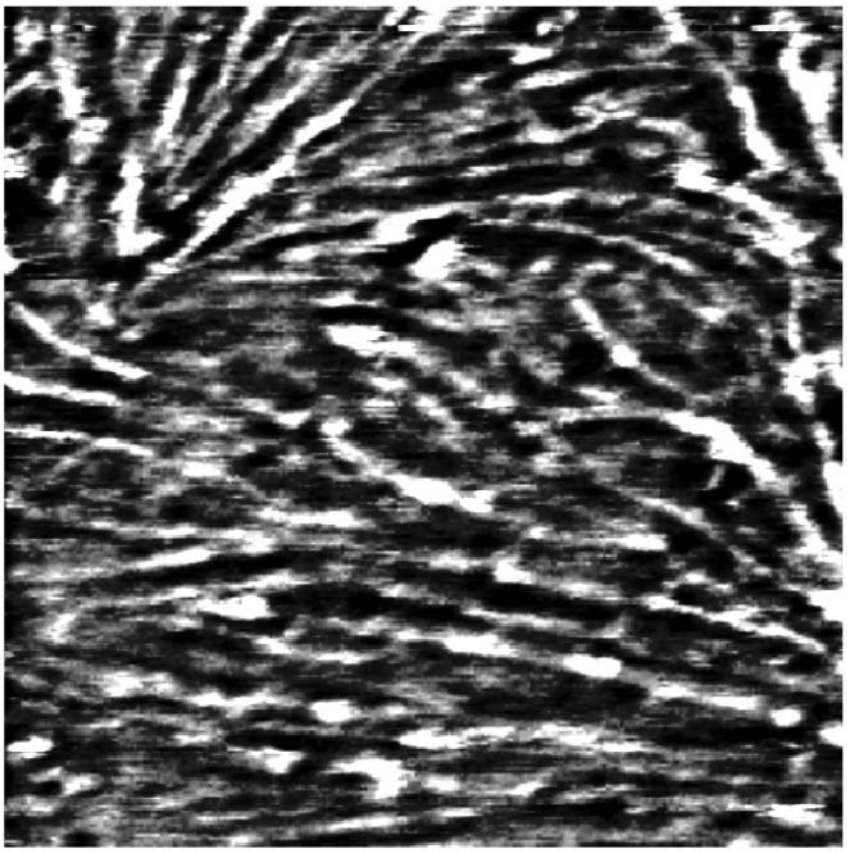

Figure 1.2.54. The morphology of PPV-*b*-P(S-*stat*-C_{60}MS) film spin-cast from a solution in *o*-dichlorobenzene, as imaged by tapping-mode AFM. (**ref.131**).

reported this kind of polymers, containing only donor blocks [136-138] or donor and acceptor blocks [139]. However, only limited number of studies on solar cells with such block copolymers has been reported. Barber Jr. et al, reported the synthesis of [MEH-PPV]-co-[biphenylene vinylene] block copolymer (the inset of Figure 1.2.55) and its application to solar cell with PCBM as an acceptor [140]. The best performance was obtained a device with PCBM molar ratio of 0.57, resulting in a PCE of 2.4% under AM1.5 (92 mW cm^{-2}) irradiation (Figure 1.2.55).

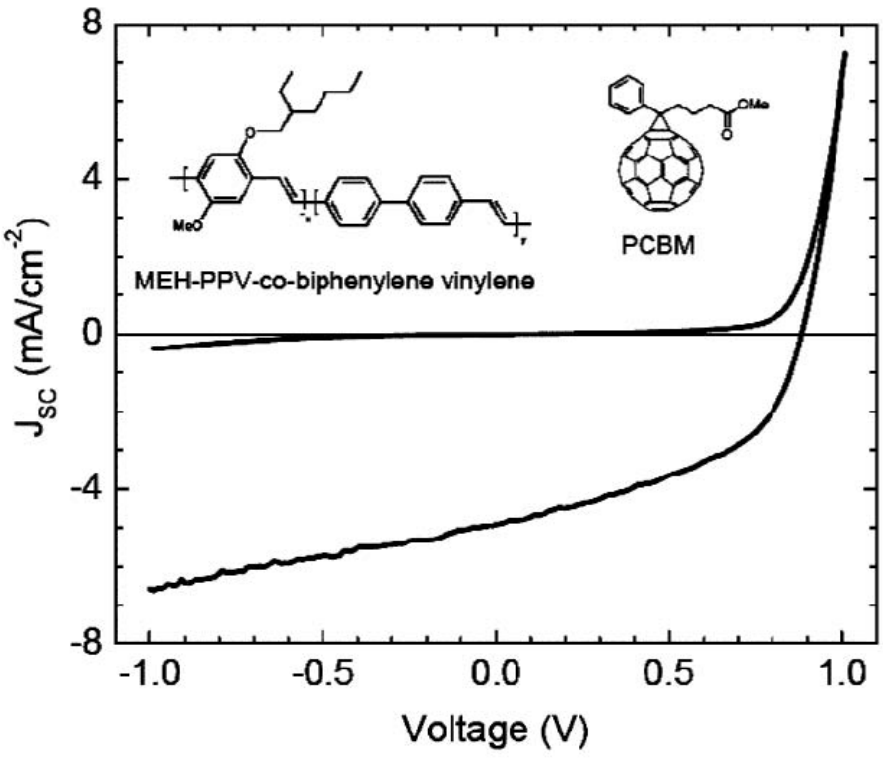

Figure 1.2.55. Comparison of the dark and illuminated current versus voltage characteristics for a device with x = 0.57 C_{60} molar fraction. The photovoltaic characteristics of this device are: V_{OC} = 0.88 V, J_{SC} = 4.92 mA cm^{-2}, FF = 0.47, η^{P}_{ext} = 2.4% using AM1.5 direct solar simulator with P_{in} = 92 mW cm^{-2}. The inset shows the chemical structures of MEH-PPV-co-biphenylene vinylene and PCBM molecules investigated in this work. (**ref.140**)

1.2.4.4. Nanostructure formation by covalently linked donor-acceptor molecules in solar cells

All the studies described above are fundamentally based on bulk heterojunction structure of donor and acceptor materials. In the case of BHJ structure, miscibility of the donor and acceptor materials and resulting phase separation are always the big issue since the photo-induced charge separation occurs at the interface of those two components. In this point of view, covalently linked donor and acceptor molecules such as double-cable polymers and donor-acceptor dyads are attractive materials since no phase separation occurs, and moreover, efficient charge separation is expected due to the close existence of donor and acceptor. Designs and photovoltaic properties of those materials are review in this section.

Double-cable polymer [141]

The first double-cable polymer bearing C_{60} side groups was reported by Benincori et al in 1996 [142]. They first synthesized a monomer by directly grafting C_{60} at the bridging carbon of cyclopentadithiophene (Figure 1.2.56) and subsequently polymerized it by electrochemical oxidation. Followed by this report, several authors synthesized double-cable polymers by electropolymerization (Figure 1.2.57) [143, 144]. However those polymers were not soluble in organic solvents. The first soluble double-cable polymer was synthesized by Ferraris et al in 1998 [145]. At first they synthesized a soluble polythiophene derivative bearing an azide group by Grignard metathesis method, catalyzed by nickel and then adducted C_{60} (Figure 1.2.58).

By such a chemical polymerization method, soluble double-cable polymers were successfully synthesized and applied to solar cells. Ramos et al, fabricated the first solar cell based on a double-cable polymer in 2001 [146]. They introduced a hybrid polymer of PPV and poly(p-phenylene ethynylene) bearing a C_{60} (C_{60} loading of 31.5 wt%) (Figure 1.2.59) as an active material in the device, and a preliminary result on the photovoltaic property showed the maximum EQE of 6% at 480 nm and a PCE of 0.1% under AM 1.5 irradiation (100 mW cm^{-2}).

Another solar cell based on a double-cable polymer was reported by Zhang et al in the same year [147]. They synthesized thiophene copolymers bearing 7 mol% (14.5 wt%) or 14 mol% (24.2

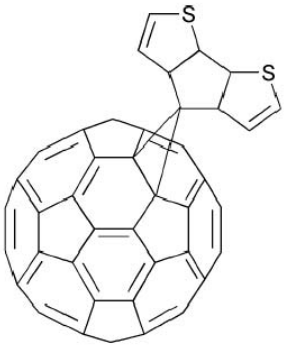

Figure 1.2.56. Molecular structure of cyclopentadithiophene fullerene adduct. (**ref.142**)

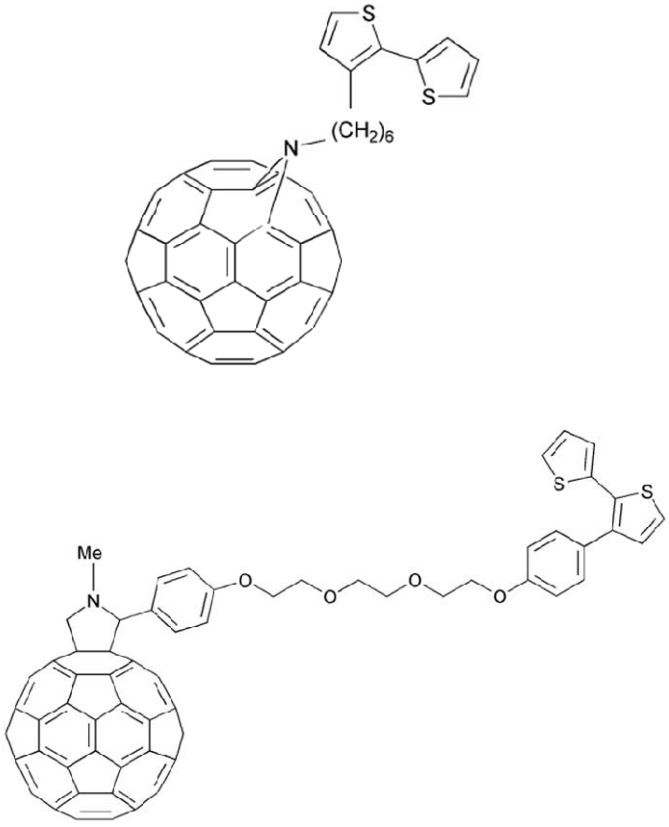

Figure 1.2.57. Other monomers for electropolymerised double-cable polymers . (**ref.143&144**)

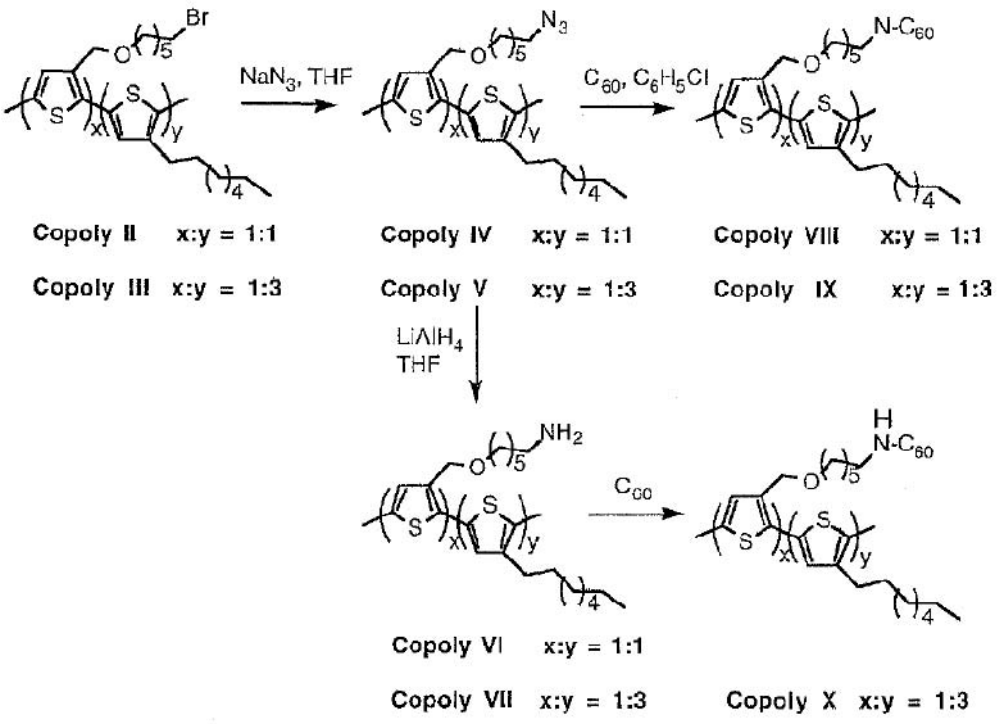

Figure 1.2.58. Molecular structure of cyclopentadithiophene fullerene adduct. (**ref.145**)

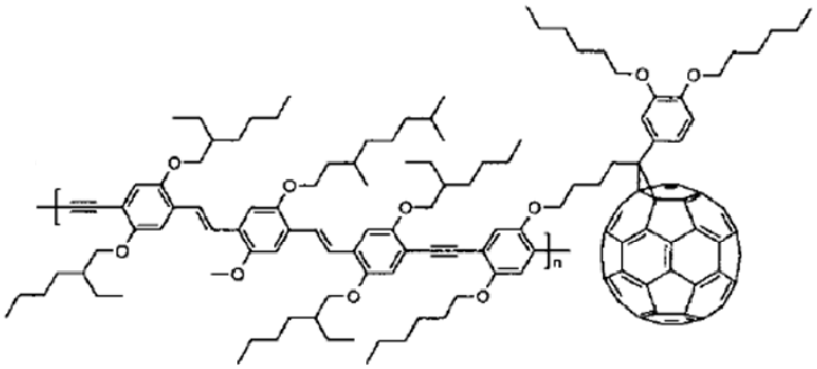

Figure 1.2.59. Molecular structure of a hybrid polymer of PPV and poly(p-phenylene ethynylene) bearing a C_{60}. (**ref.146**).

wt%) fulleropyrrolidine moieties by oxidative polymerization with $FeCl_3$ slurry (Figure 1.2.60). The higher efficiency of 0.6% was achieved in the device with the polymer with the higher C_{60} content under monochromatic light irradiation (0.1 mW cm^{-2}, 505 nm). Due to the solubility problem, these double-cable polymers above contained limited amount of C_{60} moieties (higher content of C_{60} seems to insolubilize the polymer) which could be below the percolation threshold for the formation of acceptor network, resulting in a relatively low efficiency.

Recently, Tan et al, successfully synthesized a double-cable polymer with a high C_{60} content with 56 wt% (Figure 1.2.61) [148]. As a result, the performance of the solar cell improved to achieve a high PCE of 0.52% under AM 1.5 irradiation (100 mW cm^{-2}), which is the highest efficiency in the double-cable polymer based solar cells (Figure 1.2.62). They also compared the performance with that of the blend device with the donor polymer and PCBM, and revealed that donor-acceptor linkage improved the I_{SC} by an order of 4. This result demonstrated the superiority of this class of materials although yet the efficiency of the solar cells based on double-cable polymers are still lower than polymer:PCBM BHJ devices.

Recently, a synthetic methodology so-called click chemistry has been well-developed and enable us to functionalize polymers with an excellently high yield, and synthesis of double-cable polymers by click chemistry have been reported, aiming at application to organic solar cells [149-151].

Donor-Acceptor Dyad [152-154]

Covalently linked donor and acceptor dyads have been studied for a long time as a model compound for natural photosynthetic center to investigate photo-induced energy and electron transfer in the solution [155-161]. In sharp contrast to the tremendous studies in solution, limited number of studied have has been done. Here some representative work on dyad-based solar cells is reviewed.

First example was reported by Nierengarten et al in 1999 [162]. They synthesized an oligophenylenevinylene (OPV)–fullerene dyad and fabricated the solar cell (Figure 1.2.63). They observed a photovoltaic effect and obtained a PCE of 0.01% under monochromatic

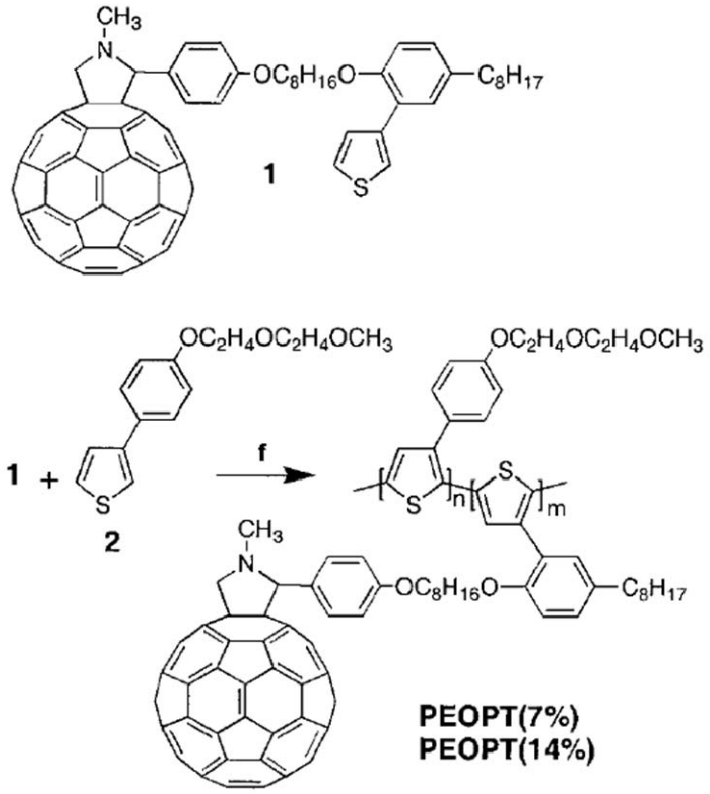

Figure 1.2.60. Molecular structures and synthetic scheme of the copolymers (PEOPT (7% and 14%)). The copolymers are denoted by the mole fractions of the fullerene repeating unit. *Reagents and condition:* f) $FeCl_3$ (1:6) (0.05 M), chloroform, 5 h. (**ref.147**).

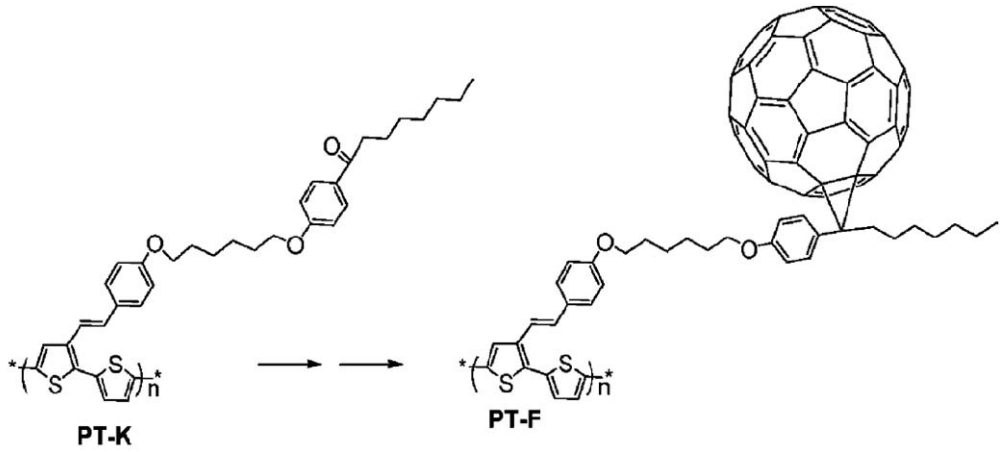

Figure 1.2.61. Molecular structures of the soluble double-cable polythiophene (PT-F) and its control polymer without C60 end group (PT-K). (**ref.148**).

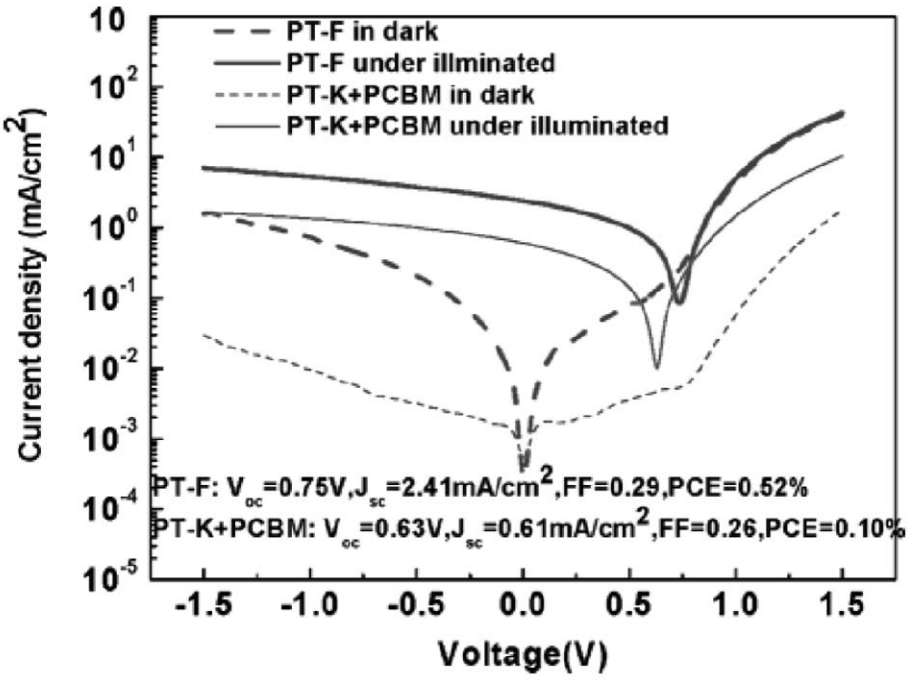

Figure 1.2.62. I-V curves of the polymer solar cells based on PT-F and PT-K blended with PCBM in dark and under the illumination of AM1.5, 100 mW/cm^2. (**ref.148**)

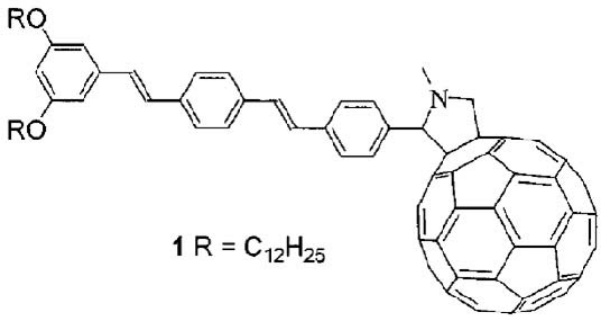

Figure 1.2.63. Molecular structures of an oligophenylenevinylene (OPV) – fullerene dyad. (**ref.162**)

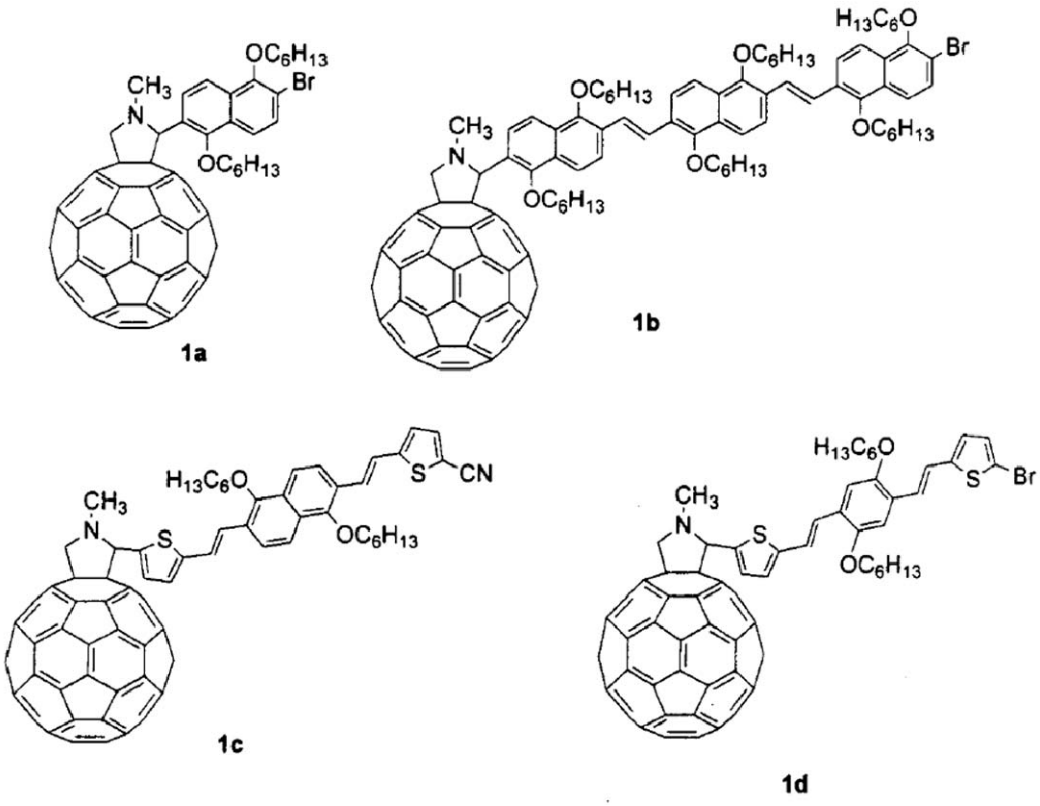

Figure 1.2.64. Molecular structures of dyads. (**ref.152**)

irradiation (12 mW cm^{-2}, 400 nm). They also synthesized a similar dyad with an elongated π-conjugation and achieved a better PCE of 0.03% under under monochromatic irradiation (12 mW cm^{-2}, 400 nm) [163].

Guldi et al, synthesized several kinds of dyads and also reported the photovoltaic property as well as their photochemical investigation in solution (Figure 1.2.64) [152]. The device fabricated with **1d** (Figure 1.2.64) achieved an EQE of 10% at 440 nm and a PCE of 0.2% under AM 1.5 irradiation (80 mW cm^{-2}).

Negishi et al, introduced oligothiophene-C_{60} dyads with different π-conjugation length of oligothiophene into solar cells, and clearly demonstrated that the dyad with longer showed the higher EQE (Figure 1.2.65) [164]. The device with the dyad with the longest oligothiophene π-conjugation length achieved the maximum EQE of 9.7% at 456 nm and a PCE of 0.41% under monochromatic light irradiation (10 μW cm^{-2}, 456 nm). They also reported two C_{60} adducted oligothiophene triads (Figure 1.2.66) and further improved the efficiency, resulting in the maximum EQE of 25% at 466 nm and the PCE of 0.65% under monochromatic light irradiation [165].

Maggini et al, successfully fabricated a relatively high efficiency dyad-based solar cell by introducing an azothiophene as a donor group which has an absorption maximum at 570 nm (Figure 1.2.67) [166]. By optimizing the active layer thickness, they achieved the maximum PCE of 0.37% under white light irradiation (80 mW cm^{-2}).

In these reports above, together with several other reports on dyad-based solar cells, there was no clear comparison with their corresponding donor and acceptor BHJ devices in order to confirm the superiority on charge separation in dyads. Moreover, few studies on their nanostructures were reported despite of their high importance on the efficiency of the solar cells, and furthermore for understanding the correlation between the nanostructure and intra- and intermolecular photo-induced energy and electron transfer and subsequent charge transport (charge carrier hopping) in the thin solid film.

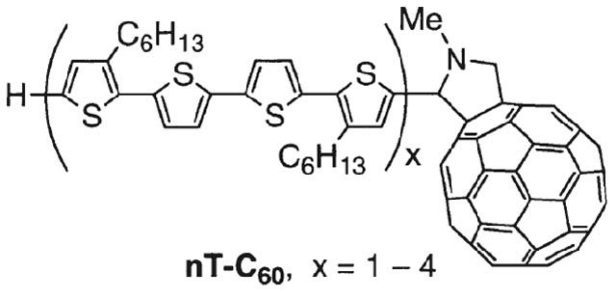

Figure 1.2.65. Molecular structure of an oligothiophene-fullerene dyad. (**ref.164**)

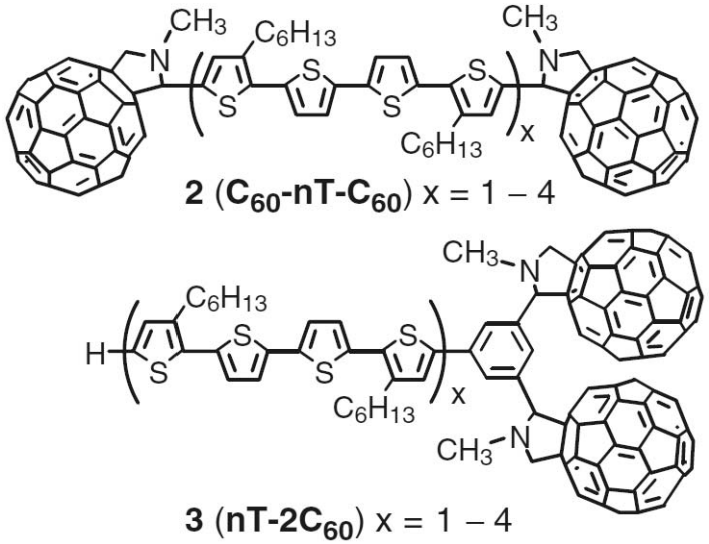

Figure 1.2.66. Molecular structures of oligothiophene-fullerene dyads. (**ref.165**)

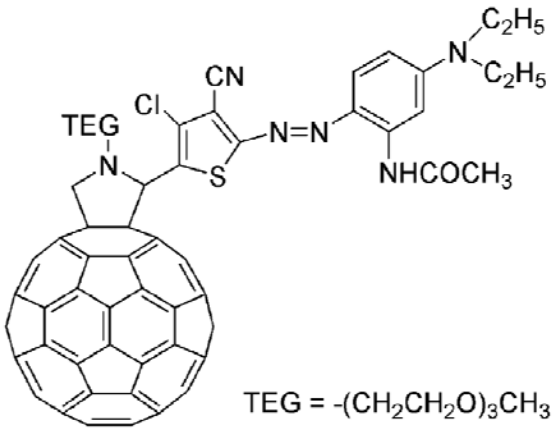

Figure 1.2.67. Molecular structure of fullerene-azothiophene dyad. (**ref.166**).

References

1. M. R. Wasielewski, *Chem. Rev.*, 1992, **92**, 435.
2. D. Gust, T. A. Moore and A. L. Moore, *Acc. Chem. Res.*, 1993, **26**, 198.
3. R. A. Marcus, *Angew. Chem. Int. Ed.*, 1993, **32**, 1111.
4. S. Speiser, *Chem. Rev.*, 1996, **96**, 1953.
5. M. D. Ward, *Chem. Soc. Rev.*, 1997, **26**, 365.
6. P. Piotrowiak, *Chem. Soc. Rev.*, 1999, **28**, 143.
7. J. L. Bredas, D. Beljonne, V. Coropceanu and J. Cornil, *Chem. Rev.*, 2004, **104**, 4971.
8. A. C. Benniston and A. Harriman, *Chem. Soc. Rev.*, 2006, **35**, 169.
9. J. W. Verhoeven, *J. Phtochem. Photobio., C*, 2006, **7**, 40.
10. M. R. Wasielewski, *J. Org. Chem.*, 2006, **71**, 5051.
11. B. Albinsson and J. Martensson, *J. Phtochem. Photobio., C*, 2008, **9**, 138.
12. Y. Araki and O. Ito, *J. Phtochem. Photobio., C*, 2008, **9**, 93.
13. Y. M. Sun, Y. Q. Liu and D. B. Zhu, *J. Mater. Chem.*, 2005, **15**, 53.
14. S. Allard, M. Forster, B. Souharce, H. Thiem and U. Scherf, *Angew. Chem. Int. Ed.*, 2008, **47**, 4070.
15. A. R. Murphy and J. M. J. Frechet, *Chem. Rev.*, 2007, **107**, 1066.
16. H. E. Katz and Z. Bao, *J. Phys. Chem. B*, 2000, **104**, 671.
17. F. Garnier, *Acc. Chem. Res.*, 1999, **32**, 209.
18. C. D. Dimitrakopoulos and P. R. L. Malenfant, *Adv. Mater.*, 2002, **14**, 99.
19. J. Y. Lee, S. Roth and Y. W. Park, *Appl. Phys. Lett.*, 2006, **88**.
20. T. Fujiwara, J. Locklin and Z. N. Bao, *Appl. Phys. Lett.*, 2007, **90**.
21. S. C. B. Mannsfeld, J. Locklin, C. Reese, M. E. Roberts, A. J. Lovinger and Z. Bao, *Adv. Funct. Mater.*, 2007, **17**, 1617.
22. C. Reese and Z. Bao, *Adv. Mater.*, 2007, **19**, 4535.
23. S. Gunes, H. Neugebauer and N. S. Sariciftci, *Chem. Rev.*, 2007, **107**, 1324.
24. B. C. Thompson and J. M. J. Frechet, *Angew. Chem. Int. Ed.*, 2008, **47**, 58.
25. G. Li, V. Shrotriya, J. S. Huang, Y. Yao, T. Moriarty, K. Emery and Y. Yang, *Nat. Mater.*, 2005, **4**, 864.
26. W. L. Ma, C. Y. Yang, X. Gong, K. Lee and A. J. Heeger, *Adv. Funct. Mater.*, 2005, **15**, 1617.
27. M. Reyes-Reyes, K. Kim and D. L. Carroll, *Appl. Phys. Lett.*, 2005, **87**, 83506.
28. J. Y. Kim, S. H. Kim, H. H. Lee, K. Lee, W. L. Ma, X. Gong and A. J. Heeger, *Adv. Mater.*, 2006, **18**, 572.
29. Y. Kim, S. Cook, S. M. Tuladhar, S. A. Choulis, J. Nelson, J. R. Durrant, D. D. C.

Bradley, M. Giles, I. McCulloch, C. S. Ha and M. Ree, *Nat. Mater.*, 2006, **5**, 197.

30. A. Hayakawa, O. Yoshikawa, T. Fujieda, K. Uehara and S. Yoshikawaa, *Appl. Phys. Lett.*, 2007, **90**.
31. J. Y. Kim, K. Lee, N. E. Coates, D. Moses, T. Q. Nguyen, M. Dante and A. J. Heeger, *Science*, 2007, **317**, 222.
32. S. S. Kim, S. I. Na, J. Jo, G. Tae and D. Y. Kim, *Adv. Mater.*, 2007, **19**, 4410.
33. J. Peet, J. Y. Kim, N. E. Coates, W. L. Ma, D. Moses, A. J. Heeger and G. C. Bazan, *Nat. Mater.*, 2007, **6**, 497.
34. C. P. Chen, S. H. Chan, T. C. Chao, C. Ting and B. T. Ko, *J. Am. Chem. Soc.*, 2008, **130**, 12828.
35. M. D. Irwin, B. Buchholz, A. W. Hains, R. P. H. Chang and T. J. Marks, *Proc. Natl. Acad. Sci. U.S.A.*, 2008, **105**, 2783.
36. J. K. Lee, W. L. Ma, C. J. Brabec, J. Yuen, J. S. Moon, J. Y. Kim, K. Lee, G. C. Bazan and A. J. Heeger, *J. Am. Chem. Soc.*, 2008, **130**, 3619.
37. A. J. Moule and K. Meerholz, *Adv. Mater.*, 2008, **20**, 240.
38. M. M. Wienk, M. Turbiez, J. Gilot and R. A. J. Janssen, *Adv. Mater.*, 2008, **20**, 2556.
39. H. Xin, F. S. Kim and S. A. Jenekhe, *J. Am. Chem. Soc.*, 2008, **130**, 5424.
40. H. L. Yip, S. K. Hau, N. S. Baek, H. Ma and A. K. Y. Jen, *Adv. Mater.*, 2008, **20**, 2376.
41. J. J. M. Halls, K. Pichler, R. H. Friend, S. C. Moratti and A. B. Holmes, *Appl. Phys. Lett.*, 1996, **68**, 3120.
42. A. Haugeneder, M. Neges, C. Kallinger, W. Spirkl, U. Lemmer, J. Feldmann, U. Scherf, E. Harth, A. Gugel and K. Mullen, *Phys. Rev. B*, 1999, **59**, 15346.
43. M. Theander, A. Yartsev, D. Zigmantas, V. Sundstrom, W. Mammo, M. R. Andersson and O. Inganas, *Phys. Rev. B*, 2000, **61**, 12957.
44. M. A. Stevens, C. Silva, D. M. Russell and R. H. Friend, *Phys. Rev. B*, 2001, **63**, 18.
45. T. Stubinger and W. Brutting, *J. Appl. Phys.*, 2001, **90**, 3632.
46. J. E. Kroeze, T. J. Savenije, M. J. W. Vermeulen and J. M. Warman, *J. Phys. Chem. B*, 2003, **107**, 7696.
47. L. Luer, H. J. Egelhaaf, D. Oelkrug, G. Cerullo, G. Lanzani, B. H. Huisman and D. de Leeuw, *Org. Electron.*, 2004, **5**, 83.
48. D. E. Markov, E. Amsterdam, P. W. M. Blom, A. B. Sieval and J. C. Hummelen, *J. Phys. Chem. A*, 2005, **109**, 5266.
49. D. E. Markov, C. Tanase, P. W. M. Blom and J. Wildeman, *Phys. Rev. B*, 2005, **72**, 6.
50. A. J. Lewis, A. Ruseckas, O. P. M. Gaudin, G. R. Webster, P. L. Burn and I. D. W. Samuel, *Org. Electron.*, 2006, **7**, 452.
51. D. E. Markov and P. W. M. Blom, *Phys. Rev. B*, 2006, **74**, 5.

52. S. R. Scully and M. D. McGehee, *J. Appl. Phys.*, 2006, **100**, 5.
53. I. G. Scheblykin, A. Yartsev, T. Pullerits, V. Gulbinas and V. Sundstrom, *J. Phys. Chem. B*, 2007, **111**, 6303.
54. P. E. Shaw, A. Ruseckas and I. D. W. Samuel, *Adv. Mater.*, 2008, **20**, 3516.
55. M. A. Green, K. Emery, D. L. King, S. Igari and W. Warta, *Prog. Photovoltaics*, 2005, **13**, 49.
56. H. Spanggaard and F. C. Krebs, *Sol. Energy Mater. Sol. Cells*, 2004, **83**, 125.
57. S.-S. Sun and N. S. Sariciftci, *Organic Photovoltaics*, CRC Press, 2005.
58. G. Calzaferri, D. Bruhwiler, S. Glaus, D. Schurch, A. Currao and C. Leiggener, *J. Imaging Sci. Technol.*, 2001, **45**, 331.
59. D. M. Chapin, C. S. Fuller and G. L. Pearson, *J. Appl. Phys.*, 1954, **25**, 676.
60. R. N. Marks, J. J. M. Halls, D. D. C. Bradley, R. H. Friend and A. B. Holmes, *J. Phys.: Condens. Matter*, 1994, **6**, 1379.
61. C. J. Brabec, A. Cravino, D. Meissner, N. S. Sariciftci, T. Fromherz, M. T. Rispens, L. Sanchez and J. C. Hummelen, *Adv. Funct. Mater.*, 2001, **11**, 374.
62. C. J. Brabec, A. Cravino, D. Meissner, N. S. Sariciftci, M. T. Rispens, L. Sanchez, J. C. Hummelen and T. Fromherz, *Thin Solid Films*, 2002, **403**, 368.
63. C. M. Ramsdale, J. A. Barker, A. C. Arias, J. D. MacKenzie, R. H. Friend and N. C. Greenham, *J. Appl. Phys.*, 2002, **92**, 4266.
64. V. D. Mihailetchi, P. W. M. Blom, J. C. Hummelen and M. T. Rispens, *J. Appl. Phys.*, 2003, **94**, 6849.
65. P. Peumans, A. Yakimov and S. R. Forrest, *J. Appl. Phys.*, 2003, **93**, 3693.
66. S. Karg, W. Riess, V. Dyakonov and M. Schwoerer, *Synth. Met.*, 1993, **54**, 427.
67. H. Antoniadis, B. R. Hsieh, M. A. Abkowitz, S. A. Jenekhe and M. Stolka, *Synth. Met.*, 1994, **62**, 265.
68. G. Yu, C. Zhang and A. J. Heeger, *Appl. Phys. Lett.*, 1994, **64**, 1540.
69. E. Frankevich, A. Zakhidov, K. Yoshino, Y. Maruyama and K. Yakushi, *Phys. Rev. B*, 1996, **53**, 4498.
70. C. W. Tang, *Appl. Phys. Lett.*, 1986, **48**, 183.
71. M. Hiramoto, H. Fujiwara and M. Yokoyama, *Appl. Phys. Lett.*, 1991, **58**, 1062.
72. G. Yu, K. Pakbaz and A. J. Heeger, *Appl. Phys. Lett.*, 1994, **64**, 3422.
73. G. Yu, J. Gao, J. C. Hummelen, F. Wudl and A. J. Heeger, *Science*, 1995, **270**, 1789.
74. S. Morita, A. A. Zakhidov and K. Yoshino, *Solid State Commun.*, 1992, **82**, 249.
75. N. S. Sariciftci, L. Smilowitz, A. J. Heeger and F. Wudl, *Science*, 1992, **258**, 1474.
76. J. C. Hummelen, B. W. Knight, F. Lepeq, F. Wudl, J. Yao and C. L. Wilkins, *J. Org. Chem.*, 1995, **60**, 532.

77. C. Y. Yang and A. J. Heeger, *Synth. Met.*, 1996, **83**, 85.
78. J. J. M. Halls, C. A. Walsh, N. C. Greenham, E. A. Marseglia, R. H. Friend, S. C. Moratti and A. B. Holmes, *Nature*, 1995, **376**, 498.
79. S. E. Shaheen, C. J. Brabec, N. S. Sariciftci, F. Padinger, T. Fromherz and J. C. Hummelen, *Appl. Phys. Lett.*, 2001, **78**, 841.
80. H. Hoppe, M. Niggemann, C. Winder, J. Kraut, R. Hiesgen, A. Hinsch, D. Meissner and N. S. Sariciftci, *Adv. Funct. Mater.*, 2004, **14**, 1005.
81. H. Hoppe, T. Glatzel, M. Niggemann, W. Schwinger, F. Schaeffler, A. Hinsch, M. C. Lux-Steiner and N. S. Sariciftci, *Thin Solid Films*, 2006, **511**, 587.
82. F. Padinger, R. S. Rittberger and N. S. Sariciftci, *Adv. Funct. Mater.*, 2003, **13**, 85.
83. T. J. Savenije, J. E. Kroeze, X. N. Yang and J. Loos, *Adv. Funct. Mater.*, 2005, **15**, 1260.
84. V. D. Mihailetchi, H. X. Xie, B. de Boer, L. J. A. Koster and P. W. M. Blom, *Adv. Funct. Mater.*, 2006, **16**, 699.
85. X. N. Yang, J. Loos, S. C. Veenstra, W. J. H. Verhees, M. M. Wienk, J. M. Kroon, M. A. J. Michels and R. A. J. Janssen, *Nano. Lett.*, 2005, **5**, 579.
86. Y. Suzuki, K. Hashimoto and K. Tajima, *Macromolecules*, 2007, **40**, 6521.
87. K. Tajima, Y. Suzuki and K. Hashimoto, *J. Phys. Chem. C*, 2008, **112**, 8507.
88. K. Sivula, C. K. Luscombe, B. C. Thompson and J. M. J. Frechet, *J. Am. Chem. Soc.*, 2006, **128**, 13988.
89. C. H. Woo, B. C. Thompson, B. J. Kim, M. F. Toney and J. M. J. Frechet, *J. Am. Chem. Soc.*, 2008, **130**, 16324.
90. W. Ma, J. Y. Kim, K. Lee and A. J. Heeger, *Macromol. Rapid. Commun.*, 2007, **28**, 1776.
91. R. C. Hiorns, R. de Bettignies, J. Leroy, S. Bailly, M. Firon, C. Sentein, A. Khoukh, H. Preud'homme and C. Dagron-Lartigau, *Adv. Funct. Mater.*, 2006, **16**, 2263.
92. A. M. Ballantyne, L. Chen, J. Dane, T. Hammant, F. M. Braun, M. Heeney, W. Duffy, I. McCulloch, D. D. C. Bradley and J. Nelson, *Adv. Funct. Mater.*, 2008, **18**, 2373.
93. M. T. Lloyd, A. C. Mayer, S. Subramanian, D. A. Mourey, D. J. Herman, A. V. Bapat, J. E. Anthony and G. G. Malliaras, *J. Am. Chem. Soc.*, 2007, **129**, 9144.
94. L. Valentini, D. Bagnis, A. Marrocchi, M. Seri, A. Taticchi and J. M. Kenny, *Chem. Mater.*, 2008, **20**, 32.
95. S. Roquet, A. Cravino, P. Leriche, O. Aleveque, P. Frere and J. Roncali, *J. Am. Chem. Soc.*, 2006, **128**, 3459.
96. C. He, Q. G. He, Y. P. Yi, G. L. Wu, F. L. Bai, Z. G. Shuai and Y. F. Li, *J. Mater. Chem.*, 2008, **18**, 4085.
97. F. Lincker, N. Delbosc, S. Bailly, R. De Bettignies, M. Billon, A. Pron and R.

Demadrille, *Adv. Funct. Mater.*, 2008, **18**, 3444.

98. A. B. Tamayo, B. Walker and T. Q. Nguyen, *J. Phys. Chem. C*, 2008, **112**, 11545.
99. N. M. Kronenberg, M. Deppisch, F. Wurthner, H. W. A. Lademann, K. Deing and K. Meerholz, *Chem. Commun.*, 2008, 6489.
100. F. Silvestri, M. D. Irwin, L. Beverina, A. Facchetti, G. A. Pagani and T. J. Marks, *J. Am. Chem. Soc.*, 2008, **130**, 17640.
101. F. S. Schoonbeek, J. H. van Esch, B. Wegewijs, D. B. A. Rep, M. P. de Haas, T. M. Klapwijk, R. M. Kellogg and B. L. Feringa, *Angew. Chem. Int. Ed.*, 1999, **38**, 1393.
102. A. M. Ramos, S. C. J. Meskers, E. H. A. Beckers, R. B. Prince, L. Brunsveld and R. A. J. Janssen, *J. Am. Chem. Soc.*, 2004, **126**, 9630.
103. J. van Herrikhuyzen, A. Syamakumari, A. Schenning and E. W. Meijer, *J. Am. Chem. Soc.*, 2004, **126**, 10021.
104. F. J. M. Hoeben, P. Jonkheijm, E. W. Meijer and A. Schenning, *Chem. Rev.*, 2005, **105**, 1491.
105. A. Schenning and E. W. Meijer, *Chem. Commun.*, 2005, 3245.
106. X. Q. Li, V. Stepanenko, Z. J. Chen, P. Prins, L. D. A. Siebbeles and F. Wurthner, *Chem. Commun.*, 2006, 3871.
107. V. K. Praveen, S. J. George, R. Varghese, C. Vijayakumar and A. Ajayaghosh, *J. Am. Chem. Soc.*, 2006, **128**, 7542.
108. S. J. George, A. Ajayaghosh, P. Jonkheijm, A. Schenning and E. W. Meijer, *Angew. Chem. Int. Ed.*, 2004, **43**, 3422.
109. P. Leclere, M. Surin, P. Viville, R. Lazzaroni, A. F. M. Kilbinger, O. Henze, W. J. Feast, M. Cavallini, F. Biscarini, A. Schenning and E. W. Meijer, *Chem. Mater.*, 2004, **16**, 4452.
110. S. J. George and A. Ajayaghosh, *Chem. Eur. J.*, 2005, **11**, 3217.
111. A. Ajayaghosh, R. Varghese, V. K. Praveen and S. Mahesh, *Angew. Chem. Int. Ed.*, 2006, **45**, 3261.
112. O. Henze, W. J. Feast, F. Gardebien, P. Jonkheijm, R. Lazzaroni, P. Leclere, E. W. Meijer and A. Schenning, *J. Am. Chem. Soc.*, 2006, **128**, 5923.
113. T. Nishizawa, K. Tajima and K. Hashimoto, *J. Mater. Chem.*, 2007, **17**, 2440.
114. T. Kato, N. Mizoshita and K. Kishimoto, *Angew. Chem. Int. Ed.*, 2006, **45**, 38.
115. P. Leclere, M. Surin, P. Brocorens, M. Cavallini, F. Biscarini and R. Lazzaroni, *Materials Science & Engineering R-Reports*, 2006, **55**, 1.
116. C. H. Huang, N. D. McClenaghan, A. Kuhn, G. Bravic and D. M. Bassani, *Tetrahedron*, 2006, **62**, 2050.
117. L. Schmidt-Mende, A. Fechtenkotter, K. Mullen, E. Moons, R. H. Friend and J. D.

MacKenzie, *Science*, 2001, **293**, 1119.

118. A. M. Van De Craats, J. M. Warman, A. Fechtenkotter, J. D. Brand, M. A. Harbison and K. Mullen, *Adv. Mater.*, 1999, **11**, 1469.
119. C. W. Struijk, A. B. Sieval, J. E. J. Dakhorst, M. van Dijk, P. Kimkes, R. B. M. Koehorst, H. Donker, T. J. Schaafsma, S. J. Picken, A. M. van de Craats, J. M. Warman, H. Zuilhof and E. J. R. Sudholter, *J. Am. Chem. Soc.*, 2000, **122**, 11057.
120. K. Hirota, K. Tajima and K. Hashimoto, *Synthetic Metals*, 2007, **157**, 290.
121. E. Keinan, S. Kumar, R. Moshenberg, R. Ghirlando and E. J. Wachtel, *Adv. Mater.*, 1991, **3**, 251.
122. M. Carrasco-Orozco, W. C. Tsoi, M. O'Neill, M. P. Aldred, P. Vlachos and S. M. Kelly, *Adv. Mater.*, 2006, **18**, 1754.
123. W. C. Tsoi, M. O'Neill, M. P. Aldred, S. P. Kitney, P. Vlachos and S. M. Kelly, *Chem. Mater.*, 2007, **19**, 5475.
124. I. Dierking, L. L. Kosbar, A. Afzali-Ardakani, A. C. Lowe and G. A. Held, *Appl. Phys. Lett.*, 1997, **71**, 2454.
125. P. Jonkheijm, J. K. J. van Duren, M. Kemerink, R. A. J. Janssen, A. Schenning and E. W. Meijer, *Macromolecules*, 2006, **39**, 784.
126. S. Sakurai, *Polym.*, 2008, **49**, 2781.
127. U. Scherf, A. Gutacker and N. Koenen, *Acc. Chem. Res.*, 2008, **41**, 1086.
128. C. J. Hawker and T. P. Russell, *MRS Bull.*, 2005, **30**, 952.
129. K. Sivula, Z. T. Ball, N. Watanabe and J. M. J. Frechet, *Adv. Mater.*, 2006, **18**, 206.
130. Z. Zhou, X. Chen and S. Holdcroft, *J. Am. Chem. Soc.*, 2008, **130**, 11711.
131. B. de Boer, U. Stalmach, P. F. van Hutten, C. Melzer, V. V. Krasnikov and G. Hadziioannou, *Polym.*, 2001, **42**, 9097.
132. S. M. Lindner, S. Huettner, A. Chiche, M. Thelakkat and G. Krausch, *Angew. Chem. Int. Ed.*, 2006, **45**, 3364.
133. S. Barrau, T. Heiser, F. Richard, C. Brochon, C. Ngov, K. van de Wetering, G. Hadziioannou, D. V. Anokhin and D. A. Ivanov, *Macromolecules*, 2008, **41**, 2701.
134. M. Sommer, A. S. Lang and M. Thelakkat, *Angew. Chem. Int. Ed.*, 2008, **47**, 7901.
135. J. I. Lee, S. H. Cho, S.-M. Park, J. K. Kim, J. K. Kim, J.-W. Yu, Y. C. Kim and T. P. Russell, *Nano Lett.*, 2008, **8**, 2315.
136. Y. Zhang, K. Tajima, K. Hirota and K. Hashimoto, *J. Am. Chem. Soc.*, 2008, **130**, 7812.
137. U. Asawapirom, R. Guentner, M. Forster and U. Scherf, *Thin Solid Films*, 2005, **477**, 48.
138. G. Tu, H. Li, M. Forster, R. Heiderhoff, L. J. Balk, R. Sigel and U. Scherf, *Small*, 2007, **3**, 1001.

139. G. Tu, H. Li, M. Forster, R. Heiderhoff, L. J. Balk and U. Scherf, *Macromolecules*, 2006, **39**, 4327.
140. R. P. Barber, R. D. Gomez, W. N. Herman and D. B. Romero, *Org. Electron.*, 2006, **7**, 508.
141. A. Cravino and N. S. Sariciftci, *J. Mater. Chem.*, 2002, **12**, 1931.
142. T. Benincori, E. Brenna, F. Sannicolo, L. Trimarco, G. Zotti and P. Sozzani, *Angew. Chem. Int. Ed.*, 1996, **35**, 648.
143. A. Yassar, M. Hmyene, D. C. Loveday and J. P. Ferraris, *Synth. Met.*, 1997, **84**, 231.
144. A. Cravino, G. Zerza, H. Neugebauer, M. Maggini, S. Bucella, E. Menna, M. Svensson, M. R. Andersson, C. J. Brabec and N. S. Sariciftci, *J. Phys. Chem. B*, 2002, **106**, 70.
145. J. P. Ferraris, A. Yassar, D. C. Loveday and M. Hmyene, *Opt. Mater.*, 1998, **9**, 34.
146. A. M. Ramos, M. T. Rispens, J. K. J. van Duren, J. C. Hummelen and R. A. J. Janssen, *J. Am. Chem. Soc.*, 2001, **123**, 6714.
147. F. Zhang, M. Svensson, M. R. Andersson, M. Maggini, S. Bucella, E. Menna and O. Inganas, *Adv. Mater.*, 2001, **13**, 1871.
148. Z. a. Tan, J. Hou, Y. He, E. Zhou, C. Yang and Y. Li, *Macromolecules*, 2007, **40**, 1868.
149. T. L. Benanti, A. Kalaydjian and D. Venkataraman, *Macromolecules*, 2008, **41**, 8312.
150. F. Ouhib, A. Khoukh, J.-B. Ledeuil, H. Martinez, J. Desbrieres and C. Dagron-Lartigau, *Macromolecules*, 2008, **41**, 9736.
151. T. L. Benanti, A. Kalaydjian and D. Venkataraman, *Macromolecules*, 2008, **41**, 8312.
152. D. M. Guldi, C. P. Luo, A. Swartz, R. Gomez, J. L. Segura, N. Martin, C. Brabec and N. S. Sariciftci, *J. Org. Chem.*, 2002, **67**, 1141.
153. J. F. Nierengarten, *New J. Chem.*, 2004, **28**, 1177.
154. J. Roncali, *Chem. Soc. Rev.*, 2005, **34**, 483.
155. D. Hirayama, K. Takimiya, Y. Aso, T. Otsubo, T. Hasobe, H. Yamada, H. Imahori, S. Fukuzumi and Y. Sakata, *J. Am. Chem. Soc.*, 2002, **124**, 532.
156. E. E. Neuteboom, E. H. A. Beckers, S. C. J. Meskers, E. W. Meijer and R. A. J. Janssen, *Org. Biomol. Chem.*, 2003, **1**, 198.
157. H. Imahori and S. Fukuzumi, *Adv. Funct. Mater.*, 2004, **14**, 525.
158. C. C. You and F. Wurthner, *Org. Lett.*, 2004, **6**, 2401.
159. F. Langa, M. J. Gomez-Escalonilla, J. M. Rueff, T. M. F. Duarte, J. F. Nierengarten, V. Palermo, P. Samori, Y. Rio, G. Accorsi and N. Armaroli, *Chem. Eur. J.*, 2005, **11**, 4405.
160. G. X. Zhang, D. Q. Zhang, X. H. Zhao, X. C. Ai, J. P. Zhang and D. B. Zhu, *Chem. Eur. J.*, 2006, **12**, 1067.
161. H. Zhang, F. J. M. Hoeben, M. J. Pouderoijen, A. Schenning, E. W. Meijer, F. C. Schryver and S. De Feyter, *Chem. Eur. J.*, 2006, **12**, 9046.

162. J.-F. Nierengarten, J.-F. Eckert, J.-F. Nicoud, L. Ouali, V. Krasnikov and G. Hadziioannou, *Chem. Commun.*, 1999, 617.
163. J.-F. Eckert, J.-F. Nicoud, J.-F. Nierengarten, S.-G. Liu, L. Echegoyen, F. Barigelletti, N. Armaroli, L. Ouali, V. Krasnikov and G. Hadziioannou, *J. Am. Chem. Soc.*, 2000, **122**, 7467.
164. N. Negishi, K. Yamada, K. Takimiya, Y. Aso, T. Otsubo and Y. Harima, *Chem. Lett.*, 2003, **32**, 404.
165. N. Negishi, K. Takimiya, T. Otsubo, Y. Harima and Y. Aso, *Chem. Lett.*, 2004, **33**, 654.
166. M. Maggini, G. Possamai, E. Menna, G. Scorrano, N. Camaioni, G. Ridolfi, G. Casalbore-Miceli, L. Franco, M. Ruzzi and C. Corvaja, *Chem. Commun.*, 2002, 2028.

Chapter 2.

Supramolecular Formation of Fibrous Nanostructure in Donor-Acceptor Dyad Film

2.1. Introduction

Nanostructure formation in organic thin solid films is of high importance in intermolecular opto-electronic processes such as photo-induced energy and electron transfer. Self-assembly of organic molecules is one of the powerful tools to control such nanostructures and to fine-tune the electronic interactions between the molecules[1, 2]. π-Conjugated oligomers, often combined with hydrogen bonding moieties, have been known to achieve such supramolecular organization through their strong π-π interaction[1-12]. 1-D structures of the π-conjugated oligomers have been successfully formed in the films, resulting in efficient charge transport or energy transfer[3-6].

Moreover, supramolecular organization of donor-acceptor (D-A) multifunctional molecules is of great interest to achieve efficient photo-induced charge separation and subsequent transport of both holes and electrons in the film. However, only a limited number of studies have been done on supramolecular nanostructures of the D-A molecules in solid state[7, 13], compared to examples of their self-assembly in solution[14-20].

In this chapter, syntheses of a novel oligothiophene and its fullerene derivative (**1** and **2** in Figure 2.1, respectively) are described. The oligothiophene and the fullerene groups in the dyad **2** were introduced as a donor and an acceptor, respectively. It was also designed that the fullerene group works as another driving force to form a supramolecular self-assembly via its strong self-aggregation tendency in additon to the π-π interaction of the oligothiophene group. The long, flexible oligo(ethyleneoxide) spacer connected the lateral position of the oligothiophene group to the fullerene group to effectively separate each group and thus to enhance the interactions of their own. As a result, fiber-like nanostructures were successfully fabricated by self-assembly of the

molecules in the films. Theri photo-physical and photovoltaic properties were also investigated.

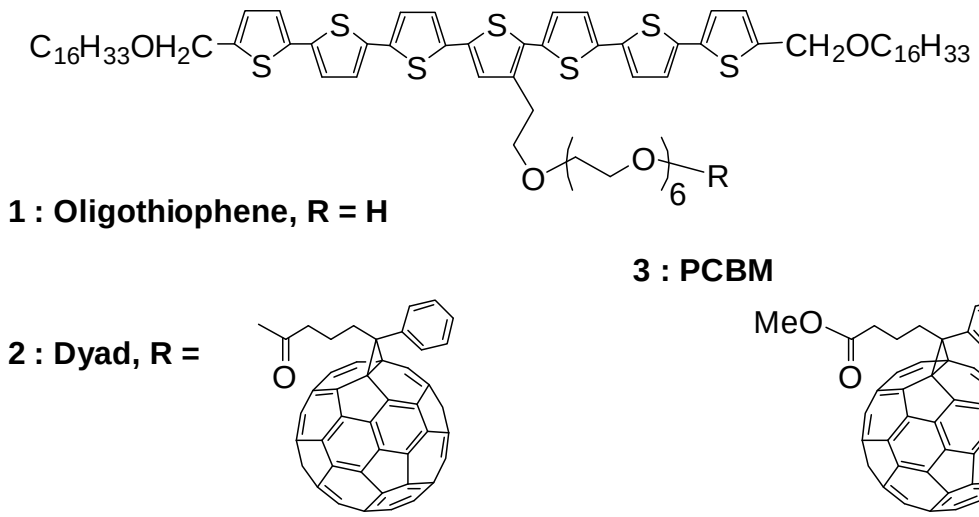

Figure 2.1. Molecular structures of oligothiophene **1**, dyad **2**, and PCBM **3**

2.2. Experimental

2.2.1. Materials and synthesis

1-(2H-Tetrahydropyran-2-yloxy)-17-{2,5-bis(trimethylstannyl)thiophene-3-ethoxy}-3,6,9,12,15-pentaoxaheptadecane **4**, 5-Bromo-5"-hexadecyloxymethyl-2,2':5',2"-terthiophene **5**, 1-(3-carboxypropyl)-1-phenyl[6,6]C_{61} were synthesized based on the literature procedures. Tetrakis(triphenylphosphine) palladium(0) was purchased from Tokyo Kasei Kogyo. Pyridinium *p*-toluenesulfonate, thienyl chloride, sodium hydride, and all organic solvents were purchased from Wako Chemicals. All the chemicals were used as received unless otherwise mentioned.

The oligothiophene **1** was synthesized via Pd^0 catalyzed Stille cross coupling reaction, followed by cleavage of tetrahydropyranyl ether (THP) (Scheme 2.1). The 2,5-bis stannyl thiophene derivative **4** and 2 equimolar of the terthiophene derivative with long alkyl chains **5** were employed in the coupling reaction. The toluene solution of the mixture of **4** and **5** with 5 mol % of $Pd^0(PPh_3)_4$ was refluxed over night, resulting in the oligothiophene derivative with THP group (**6** in Scheme 2.1). The product **6** and pyridinium *p*-toluenesulfonate were dissolved in $CHCl_3$/EtOH. The mixture solution was stirred at 60 ºC for 19 h, yielding oligothiophene **1**. The dyad **2** was synthesized via subsequent esterification reaction with the fullerene derivative bearing carboxylic chloride group **7** (scheme 2.2). The products were characterized by ^{1}H-NMR and MALDI-TOF-MS. The detail of the synthetic schemes is shown in Appendix.

2.2.2. Measurement instruments.

Differential scanning calorimetry (DSC) traces were obtained at a scan rate of 10 °C min^{-1} on a Rigaku Thermo plus DSC8230 after the first heating process to remove the thermal history of the samples. Atomic force microscopy (AFM) images were obtained by Digital Instrumental Nanoscope31 operated in the tapping mode. The X-ray diffraction (XRD) pattern of the liquid crystalline phase of **1** was measured using a RINT TTRII at Rigaku Corporation with Cu Kαoperated at 50 kV voltage and 300 mA current. The XRD pattern of dyad **2** was measured

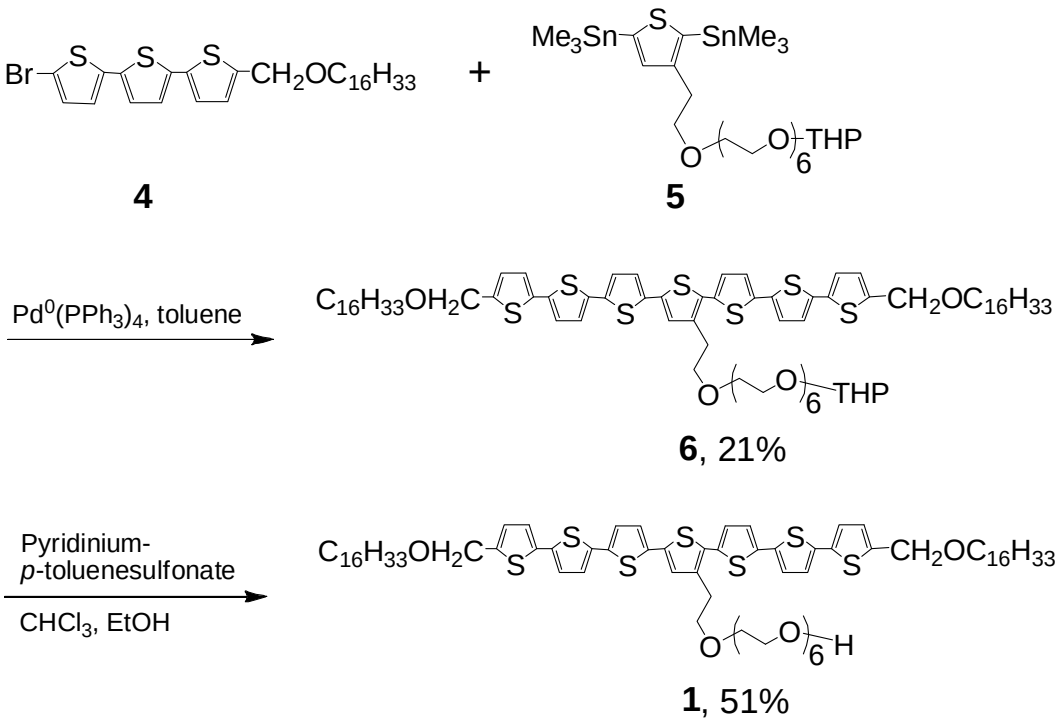

Scheme 2.1. Synthesis of oligothiophene **1**

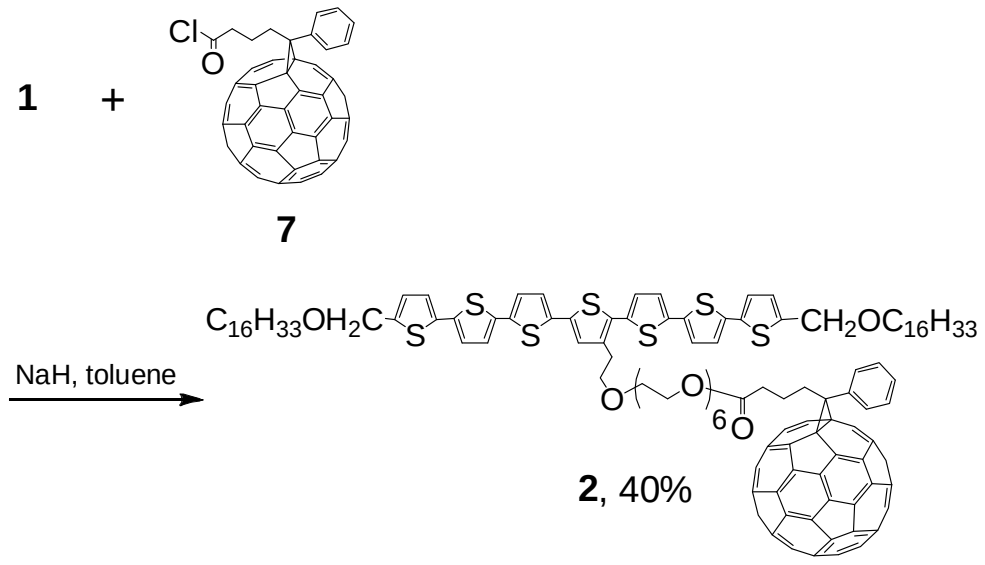

Scheme 2.2. Synthesis of dyad **2**

using a Rigaku RINT 2400 with Cu Kα operated at 40 kV voltage and 100 mA current. Absorption spectra were measured using a SHIMADZU spectrophotometer MPC-3100. Fluorescence spectra were measured using a HITACHI F-4500 fluorescence spectrophotometer.

2.2.3. Photovoltaic device preparation and measurement.

Photovoltaic devices were prepared as follows. Indium tin oxid (ITO) coated glass substrates (R_s = 10 Ω square^{-1}, Kuramoto Japan) were cleaned by ultra-sonication in detergent, water, acetone, and 2-propanol. After drying the substrate, poly(3,4-ethylenedioxythiophene):poly(styrene sulfonic acid) (PEDOT:PSS) (Baytron P) was spin-coated (4000 rpm) on ITO. The film was dried at 140 ºC under N_2 for 10 min. After cooling down the substrate, $CHCl_3$ solution of the dyad **2** (16 mg mL^{-1}) was spin-coated (2000 rpm). The film was dried with N_2 flow for 30 min. For the mixture device, the solution was prepared by dissolving 16 mg of the oligothiophene **1** and 1 equimolar (10.5 mg) of [6,6]-phenyl-C_{61}-butyric acid methyl ester (PCBM **3** in Figure 2.1) in 1 mL of $CHCl_3$, and the film was fabricated in the same manner. Finally, the Al electrode was evaporated on the organic layer under high vacuum (6×10^{-4} Pa) to complete a device in a structure of ITO/PEDOT:PSS/**2** (or **1**/**3**) /Al.

A HAYASHI LA-210UV xeon lamp and a USHIO SX-UID501CMQ xeon lamp with an AM 1.5 filter were used for external quantum efficiency (EQE) and power conversion efficiency (PCE) measurement, respectively. PCE of the devices were estimated at 100 mW cm^{-2}. The light intensity was adjusted with a silicon standard solar cell (Bunkoh-Keiki BS520).

2.3. Results and Discussion

2.3.1. Thermal behavior

Thermal behavior of the oligothiophene **1** and the dyad **2** were investigated by DSC and polarized optical microscopy (POM). Figure 2.2 showed the DSC chart of the oligothiophene **1** at the scan rate of 10 ºC min^{-1}. Upon heating two endothermic peaks were observed at 73 ºC and 105 ºC. POM observation revealed that at 73 ºC the crystalline phase turned to the liquid crystalline phase, and at 105 ºC to isotropic phase. The POM picture of the liquid crystalline phase of **1** (Figure 2.3) showed a focal-conic fan texture. An XRD pattern at around 80 ºC (Figure 2.4) showed a diffraction peak at 48.5 Å and the secondary order diffraction peak at 24.7 Å, which could be corresponding to the layer distance of the oligothiophenes with the alkyl side chains interdigitated. From the POM and XRD results, the liquid crystalline phase of **1** can be assigned to a smectic A phase.

In contrast to liquid crystal formation of the oligothiophene **1**, the dyad **2** did not show any liquid crystalline phases but simply melted at 52 ºC (See Appendix; Note that in chapter 3, it was found that dyad **2** also showed a liquid crystalline phase after further purification). The bulkiness and/or the strong aggregation tendency of the fullerene groups might weaken the π-π interaction of the oligothiophene groups, resulting in distrubing the liquid crystal formation.

2.3.2. Surface morphology

Surface morphology of the thin films of the oligothiophene **1** and the dyad **2** were investigated by AFM. Thin films of **1** and **2** were prepared by spin-coating on ITO/ PEDOT:PSS substrates from $CHCl_3$ solution. AFM phase images of the oligothiophene **1** showed bundles of fibers aggregated in a random orientation (Figure 2.5a). To enhance molecular alignment in the film, thermal annealing was conducted at a liquid crystalline temperature (80 ºC) for 5 minutes under N_2. As the result, the molecular alignment was expectedly enhanced and oligothiophene **1** formed fiber-like nanostructures in the film (Figugure 2.5b). This kind of feature has been reported in several liquid crystalline molecules[21]. Thus the molecular alignment in the oligothiophene film

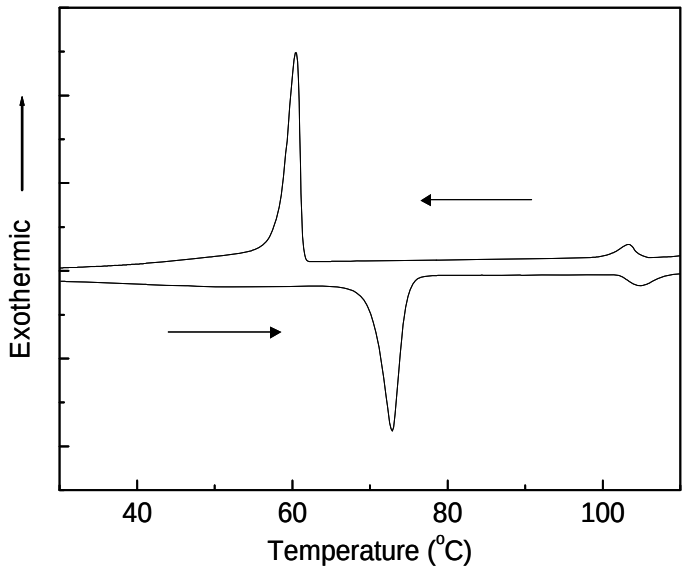

Figure 2.2. DSC Chart of the oligothiophene **1**, obtained at the scan rate of 10 ºC min^{-1}.

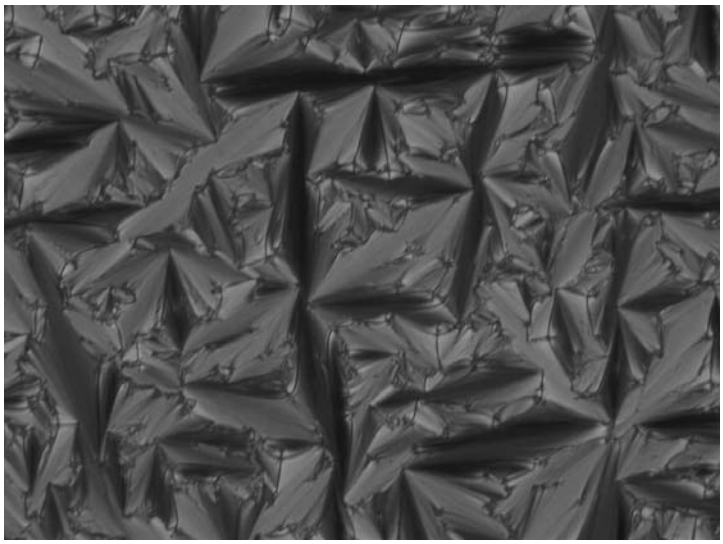

Figure 2.3. Polarized optical microscope picture of the liquid crystalline texture of the oligothiophene **1** at 100 ºC taken during the cooling process.

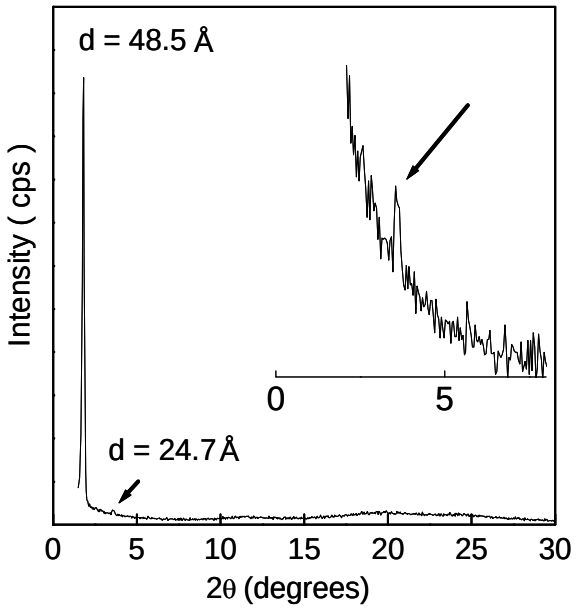

Figure 2.4. The XRD pattern of the liquid crystalline phase of the oligothiophene **1**, measured during the cooling process (82.6 ºC – 79.2 ºC).

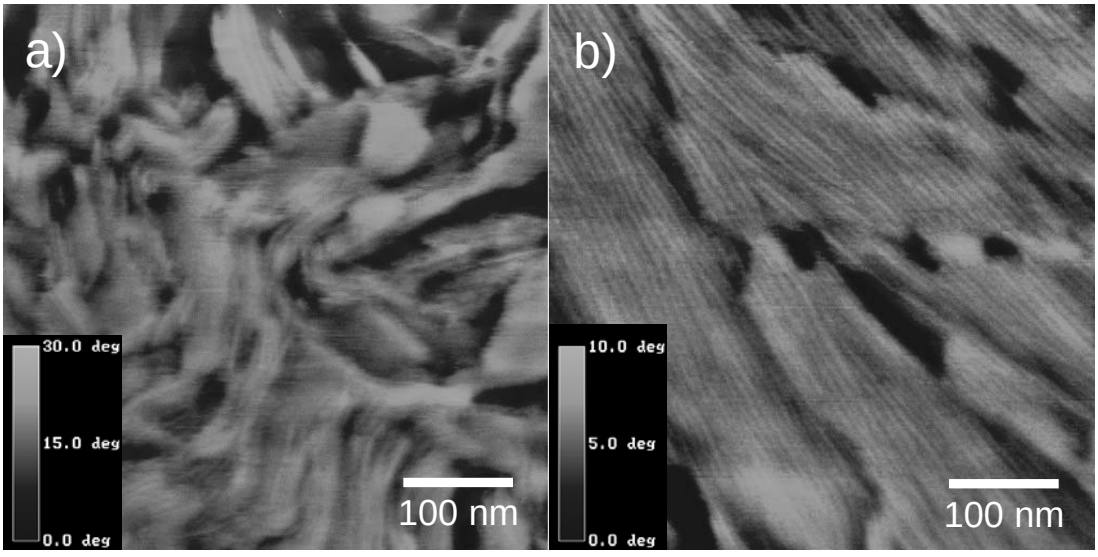

Figure 2.5. AFM phase images of the oligothiophene **1** in a) as-coated and b) thermally annealed (at 80 ºC for 5 min) films on ITO/PEDOT:PSS substrates.

observed by AFM was attributed to the self-assembly of the liquid crystalline molecules.

AFM images of as-cast film of **2** were shown in Figure 2.6. Both height (Figure 2.6a) and phase (Figure 2.6b) images clearly showed the formation of the fiber-like nanostructures. Thermal annealing at 50 ºC for 5 minutes under N_2 enhanced the structural order. A high resolution AFM phase image (Figure 2.7) revealed long, partially aligned fibers with the width of around 10 nm and the length as long as 200 nm. As for the width, however, the broadening effect by the AFM tip should be taken into account, since the width of the fiber is comparable to the curvature radius of the tip (2 nm)[22]. The corrected fiber width was calculated to be around 7 nm.

XRD of the bulk **2** in powder form was also investigated at 20 ºC (Figure 2.8). The XRD pattern showed a peak at 50.2 Å and the secondary order diffraction peak at 25.1 Å, which is quite similar to the XRD pattern of the smectic A phase of the oligothiophene **1** shown in Figure 2.4. This result suggests that the layered structure of the oligothiophene groups can be formed in the same manner even when the bulky fullerene groups are attached. Similarity of the fiber-like nanostructures in the dyad film to those in the oligothiophene film also suggests supramolecular self-assembly of the molecule driven by π-π interaction of the oligothiophene groups. Considering the covalent attachment of both the oligothiophene and the fullerene groups, the formation of the fiber-like nanostrucutre in the dyad **2** film also implies spontaneous anisotropic organization of the fullerene group in the ordered structures. Possible molecular alignment is schematically shown in the inset of Figure 2.8.

2.3.3. Photophysical properties

Optical absorption spectra of the thin films of the oligothiophene **1** and the dyad **2** on quartz/PEDOT:PSS substrates are shown in Figure 2.9. The thin films were fabricated in the same manner as the films for AFM measurement except quartz substrates were used instead of ITO substrates. A film of a 1:1 molar ratio mixture of **1** and PCBM **3** was also investigated as a control. Both the films of **1** and the **1**/**3** mixture showed π-π* absorption of the oligothiophene chromophore around 420 nm, which was blue-shifted compared to those

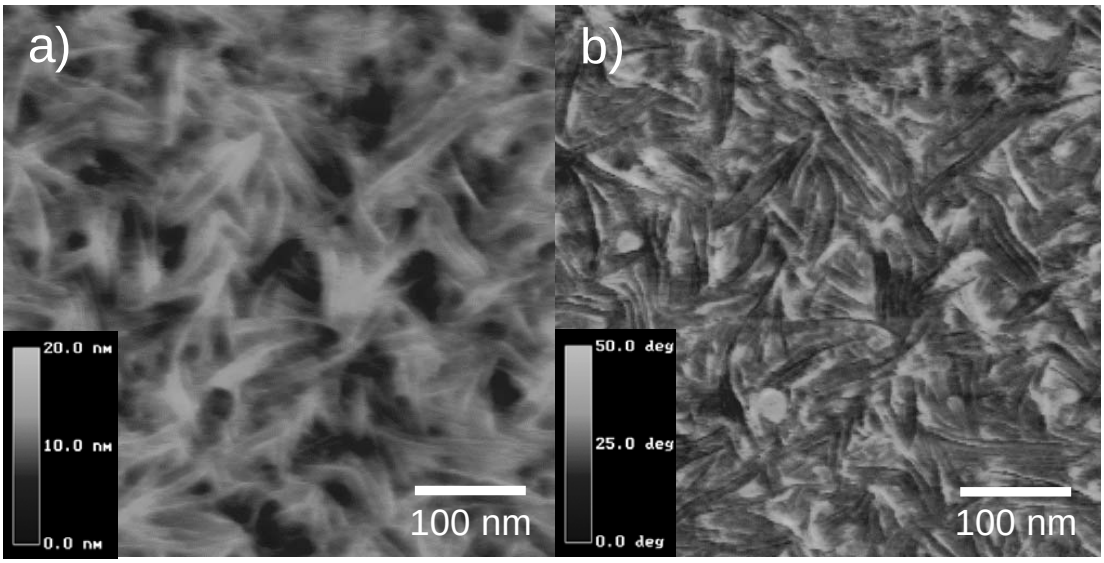

Figure 2.6. AFM a) height and b) phase images of the dyad **2** film on ITO/PEDOT:PSS substrate.

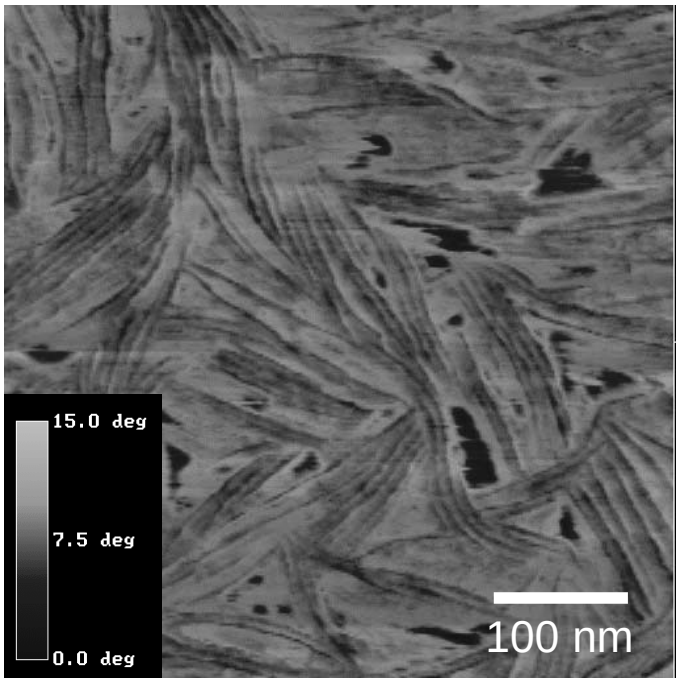

Figure 2.7. AFM phase image of the dyad **2** film annealed at 50 ºC for 5 min, observed with a super-sharp silicon probe.

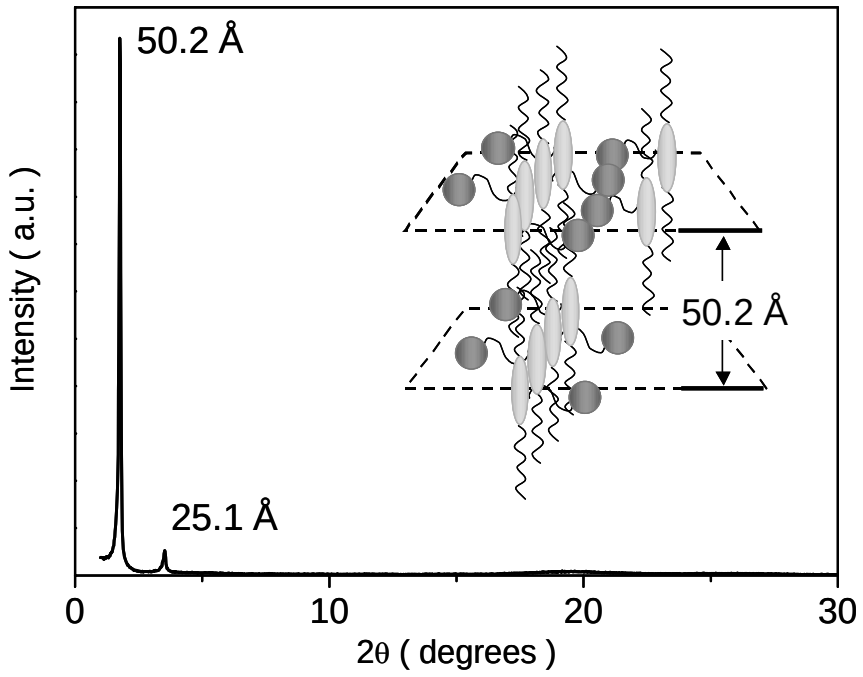

Figure 2.8. The powder XRD pattern of the dyad **2** in the bulk measured at 20 ºC. Inset: schematic representation of the proposed structure for the dyad molecules in the films.

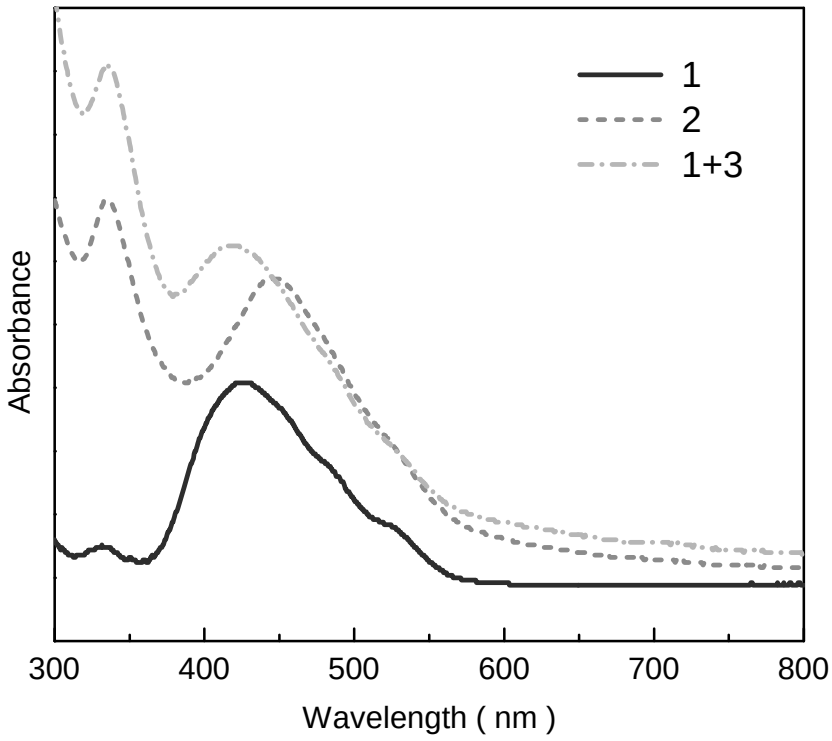

Figure 2.9. Absorption spectra of the thin films of **1** (solid), **2** (dashed), and the mixture of **1** and **3** (dash-dotted).

in $CHCl_3$ solution (440 nm, not shown). This could be attributed to the formation of H-aggregation of the oligothiophene groups in those films. This also implies that the oligothiophene and PCBM exist separately in the mixture films. Indeed, AFM image of the **1**/**3** mixture film in Figure 2.10 shows two different regions of domains with fiber-like features and featureless domains sized around 100-200 nm, indicating the phase separation of **1** and **3** in the film. In contrast, the dyad **2** film showed absorption peak around 447 nm, which was slightly red-shifted compared to that in $CHCl_3$ solution. This result suggests that strong interaction and bulky characteristics of the fullerene groups change the aggregation manner of the oligothiophene groups in the dyad **2** film, possibly into a J-aggregation type.

To investigate photo-induced electron transfer process in the films of the oligothiophene **1**, the mixture of **1**/**3** and the dyad **2**, fluorescence spectra were observed (Figure 2.11). The dyad **2** film showed almost complete quenching of the fluorescence from the oligothiophene chromophore at around 610 nm when excited at 430 nm. In contrast, partial quenching was observed with the film of the **1**/**3** mixture. These results suggest that the electron transfer from the oligothiophene to the fullerene takes place more efficiently in the dyad **2** film than in the **1**/**3** mixture film. This enhancement could be explained mainly by the enlargement of the D-A interface in the dyad **2** film suggested by the AFM images (Figure 2.6 and 2.10).

2.3.4. Photovoltaic devices

Photovoltaic devices were fabricated with the configuration of ITO/PEDOT:PSS/**2**/Al. For in the comparison, a photovoltaic device of the mixture of **1** and **3** (1:1 molar ratio) was also fabricated same manner. Figure 2.12 shows the I-V characteristics of the devices. Under simulated solar light (A.M.1.5, 100 mW cm^{-2}) the dyad device showed I_{SC} = 0.93 mA cm^{-2}, V_{OC} = 0.70 V, FF = 0.23, resulting in a higher PCE of 0.15% compared to that of the mixturedevice (PCE = 0.09%, I_{SC} = 0.53 mA cm^{-2}, V_{OC} = 0.61 V, and FF = 0.28). As expected from the fluorescence quenching measurement in the films, the photocurrent was increased in the dyad **2** device. However, the relatively poor FF of the device limits the power conversion efficiency. This might be attributed to inefficient charge transport in the

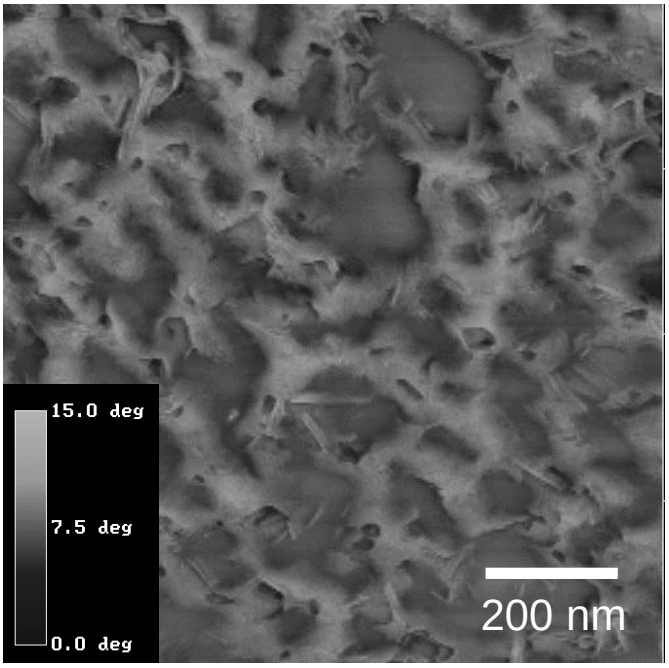

Figure 2.10. AFM phase image of the thin film of the mixture **1** and **3** on ITO/PEDOT:PSS substrate.

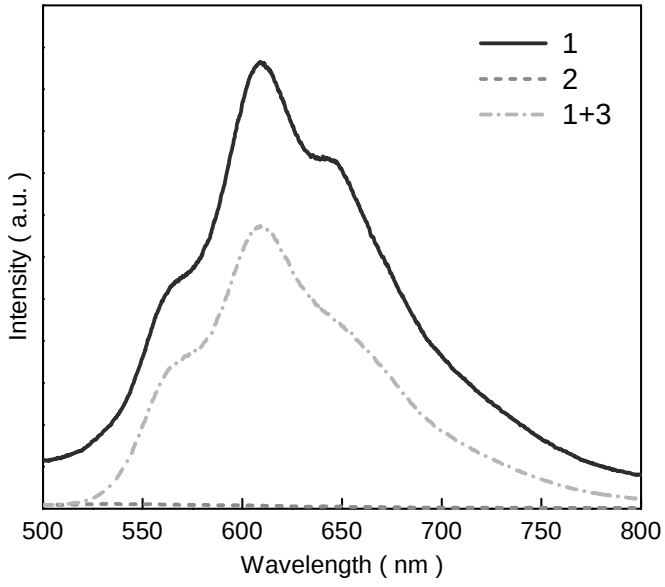

Figure 2.11. Fluorescence spectra of the thin films of **1** (solid), **2** (dashed), and the mixture of **1** and **3** (dash-dotted).

films because of unsuitable molecular packing of the oligothiophene and/or the fullerene groups or low alignment of their domains in the films. Figure 2.13 shows the EQE of the devices under monochromatic light irradiation. The dyad **2** device resulted in an improved EQE of 31% (440 nm), compared to EQE of 12% (420 nm) for the mixture device. The observed EQE is, to the best of knowledge, the highest value reported so far for dyad-based photovoltaic devices[23-27]. The improved quantum efficiency could be attributed to the large interface of the small domains of the oligothiophene and the fullerene groups formed in the dyad film, leading to enhanced charge separation. Furthermore, it is possible that the fibrous aggregation of the dyad molecules observed by AFM could facilitate intermolecular hopping of the separated charges and thus suppress charge recombination.

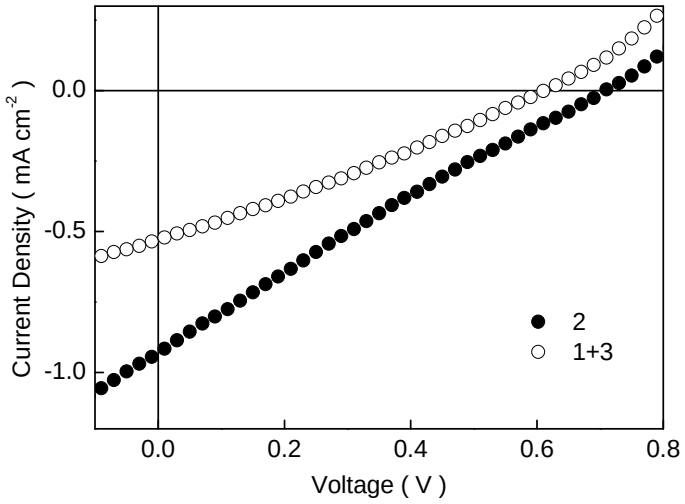

Figure 2.12. *I-V* characteristics of the photovoltaic devices of **2** (closed) and the mixture of **1** and **3** (open).

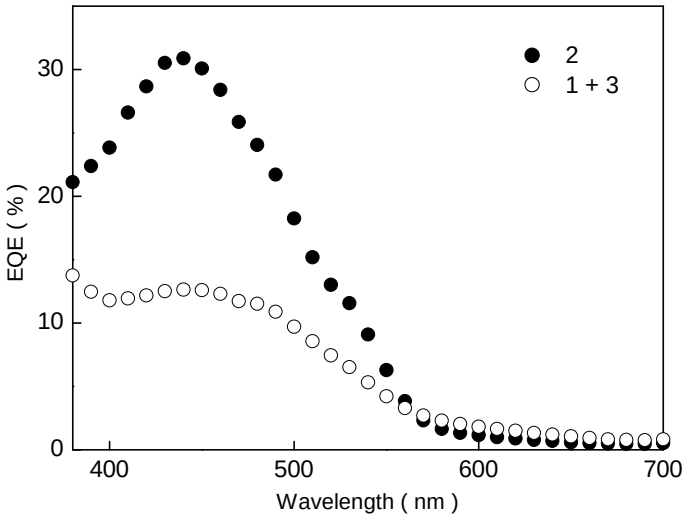

Figure 2.13. External quantum efficiencies of the photovoltaic devices with **2** (closed) and the mixture of **1** and **3** (open).

2.4. Conclusions

A novel liquid crystalline oligothiophene and an oligothiophene-fullerene dyad were synthesized to form supramolecular nanostructures in the solid film. The preliminary result on the application for photovoltaic devices clearly demonstrated that donor-acceptor dyad is promising design to form the large donor/acceptor interface and thus to achieve the efficient charge separation. It also suggested that optimization of the molecular structure and alignment of this supramolecular structure could provide us a strategy to achieve high performance opto-electronic devices through spontaneous formation of nanostructures.

Appendix

Synthetic Schemes

Oligothiophene **1** (**S11**) was synthesized via Stille cross coupling reaction of a terthiophene derivative (**S5**) and a 2, 5-bis (trimethylstannyl) thiophene derivative (**S9**). Subsequently, esterification reaction with a fullerene derivative with a carboxylic chloride group (**S14**) yielded oligothiophene-fullerene dyad **2** (**S15**). The synthetic schemes and the detail of the synthetic procedures are described below.

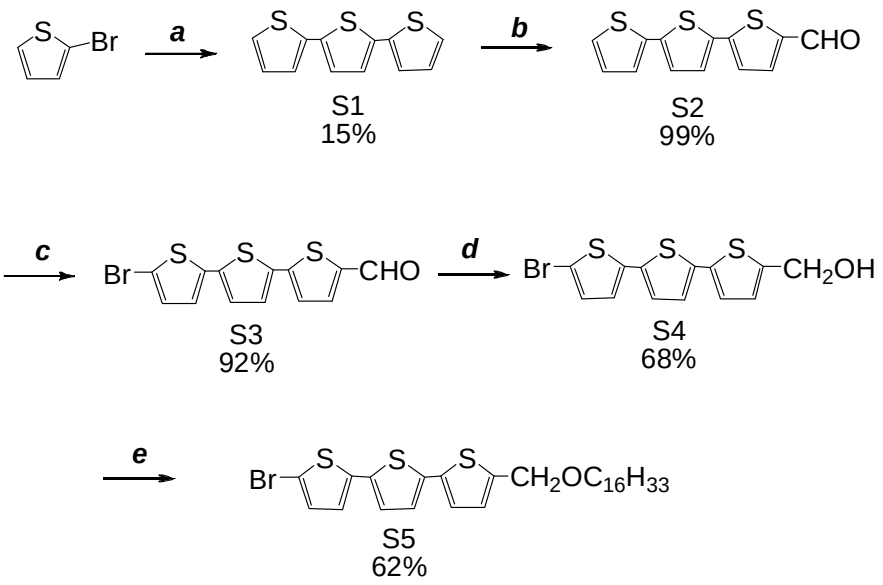

Scheme S2.1. Synthesis of the side unit of oligothiophene ***(a)*** 1. Mg, THF; 2. 2, 5-Dibromothiophene, Ni(dppp)Cl_2, THF ***(b)*** DMF, CH_2Cl_2, $POCl_3$ ***(c)*** CH_2Cl_2/AcOH, NBS ***(d)*** MeOH/THF, $NaBH_4$ ***(e)*** NaH, DMF, 1-Bromohexadecane

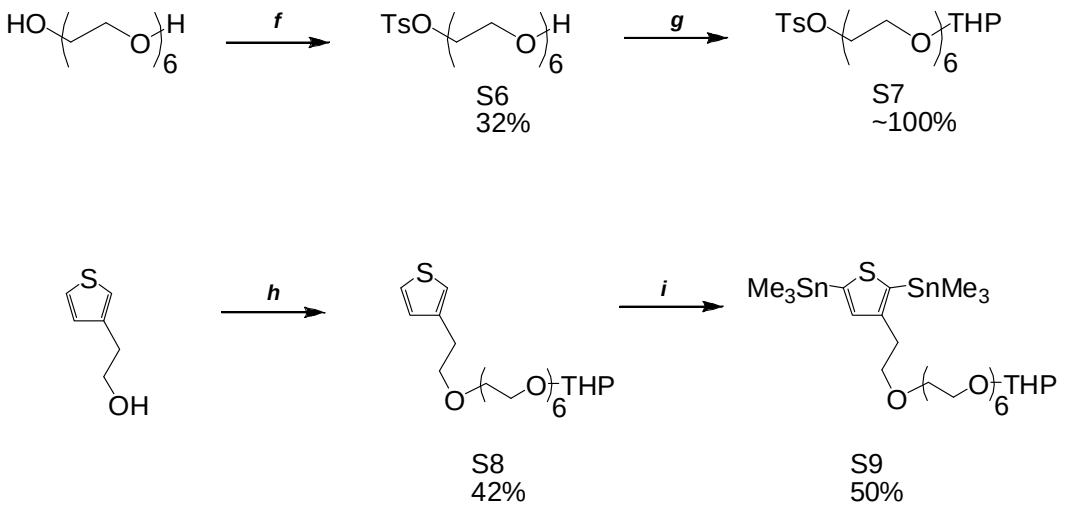

Scheme S2.2. Synthesis of the central unit of oligothiophene ***(f)*** NaOH, THF/H_2O, TsCl ***(g)*** CH_2Cl_2, PPTS, DHP ***(h)*** NaH, THF, S7 ***(i)*** LDA, Me_3SnCl

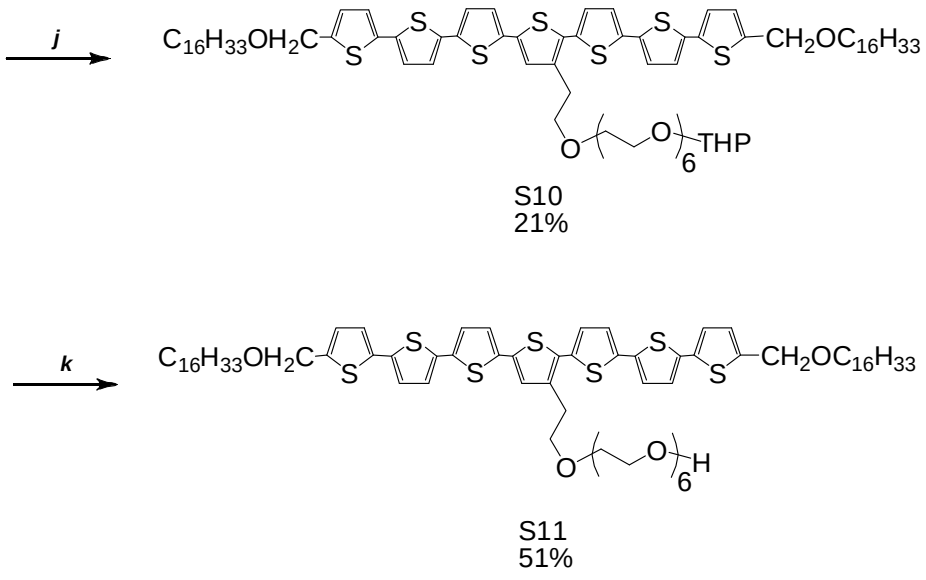

Scheme S2.3. Synthesis of oligothiophene ***(j)*** S5, S9, $Pd^0(PPh_3)_4$, toluene ***(k)*** PPTS, EtOH/$CHCl_3$

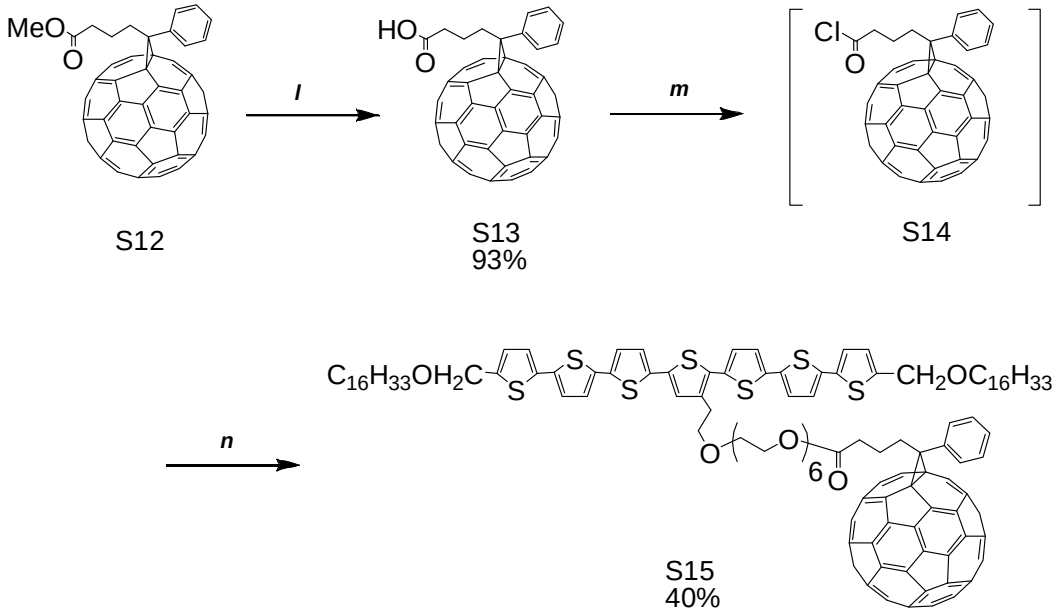

Scheme S2.4. Synthesis of oligothiophene-fullerene dyad ***(l)*** toluene, AcOH, HCl, reflux ***(m)*** CS_2, $SOCl_2$, reflux ***(n)*** S11, NaH, toluene

2,2':5',2''-Terthiophene (S1) [28]

To a solution of 2-bromothiophene (67 g, 0.41 mol) and Mg (powder, 12 g, 0.49 mol) in 100 mL of dry THF was added a little amount of I_2 at 0 ºC, then the solution was stirred intermittently. The solution was stirred at rt for an additional 1 h after it turned dark color. The synthesized Grignard reagent was added dropwise to a stirred solution of 2, 5-dibromothiophene (31g, 0.13 mol) and 1, 3-bis(diphenylphosphino)propane nickel (II) chloride (1.1 g, 0.64 mmol) in 300 ml of dry THF at -30 ºC. After stirring 23 h, the reaction was quenched by adding H_2O at 0 ºC and the product was extracted with CH_2Cl_2. The organic layer was washed with H_2O, dried over $MgSO_4$, and evaporated. The crude product was then recrystallized from hexanes, yielding 15.4 g (15 %) of **S1**. ^{1}H NMR (400 MHz, $CDCl_3$), δ (ppm): 7.22 (d, J = 2.8 Hz, 2H), 7.17 (d, J =

2.8 Hz, 2H), 7.08 (s, 2H), 7.03 (d, J = 4.8 Hz, 1H), 7.02 (d, J = 5.2 Hz, 1H).

5-Formyl-2,2':5',2"-terthiophene (S2) [29]

To a stirred solution of DMF (6.8 g, 93 mmol) in 35 mL of CH_2Cl_2 was added $POCl_3$ at 0 ºC and the solution was stirred for 30 min at 40 ºC. The synthesized Vilsmeier reagent was added dropwise to a solution of **S1** (15.4 g, 62 mmol) in 70 mL of CH_2Cl_2 at 0 ºC. After stirring 28 h at rt, the solvent was evaporated, 200 mL of cold 1M NaOH aq was added, and the solution was stirred overnight. The orange precipitate was washed with H_2O and filtrated. The filtrate was recrystallized from CH_2Cl_2/hexanes, yielding 17 g (~100%) of **S2**. ^{1}H NMR (400 MHz, $CDCl_3$), δ (ppm): 9.88 (s, 1H), 7.67 (d, J = 4.0 Hz, 1H), 7.29-7.26 (m, 2H), 7.24-7.22 (m, 2H), 7.13 (d, J = 4.0 Hz, 2H), 7.05 (d, J = 4.0 Hz, 1H), 7.03 (d, J = 3.2 Hz, 1H).

5-Bromo-5"-formyl-2,2':5',2"-terthiophene (S3) [29]

N-Bromosuccinimide (11 g, 62 mmol) was added portionwise to a stirred solution of **S2** (17 g, 62 mmol) in 600 mL of CH_2Cl_2/acetic acid (1:1), and the solution was stirred at rt for 25 h. Then the precipitate was filtrated, washed with H_2O and extracted with $CHCl_3$. The organic layer was washed with H_2O, dried over $MgSO_4$, and evaporated. The crude product was recrystallized from CH_2Cl_2/hexanes, yielding 20 g (92%) of **S3**. ^{1}H NMR (400 MHz, $CDCl_3$), δ (ppm): 9.86 (s, 1H), 7.67 (d, J = 4.0 Hz, 1H), 7.25 (d, J = 4.0 Hz, 1H), 7.24 (d, J = 4.0 Hz, 1H), 7.06 (d, J = 3.6 Hz, 1H), 7.00 (d, J = 4.0 Hz, 1H), 6.96 (d, J = 3.6 Hz, 1H).

5-Bromo-5"-hydroxymethyl-2,2':5',2"-terthiophene (S4) [29]

$NaBH_4$ (25 g, 661 mmol) was added to a solution of **S3** (20 g, 55 mmol) in 800 mL of dry methanol/THF (1:1) at 0 ºC. After stirring 10 h, the solution was neutralized with diluted HCl aq and the product was extracted with $CHCl_3$. The organic layer was washed with H_2O and evaporated. The crude product was recrystallized from $CHCl_3$, yielding 13.3 g (68%) of **S4**. ^{1}H NMR (500 MHz, $CDCl_3$), δ (ppm): 7.03 (d, J = 3.5 Hz, 1H), 7.02 (d, J = 4.0 Hz, 1H), 7.00 (d,

J = 4.5 Hz, 1H), 6.96 (d, J = 4.5 Hz, 1H), 6.91 (d, J = 4.5 Hz, 1H), 6.90 (d, J = 3.5 Hz, 1H), 4.80 (d, J = 6.0 Hz, 2H), 1.72 (t, J = 6.0 Hz, 1H).

5-Bromo-5"-hexadecyloxymethyl-2,2':5',2"-terthiophene (S5) [29]

NaH (1.2 g, 50 mmol) was added to a solution of **S4** (4.5 g, 13 mmol) in 300 mL of dry DMF at 0 ºC. After stirring 3 h at 0 ºC, 1-Bromohexadecane (4.2 g, 14 mmol) was added dropwise to the solution at rt. After stirring for 16 h, the reaction was quenched by adding H_2O, and the product was extracted with $CHCl_3$. The organic layer was washed with H_2O, dried over $MgSO_4$, and evaporated. The crude product was purified by silica column chromatography eluting with $CHCl_3$. Further purification was done by recrystallization from $CHCl_3$/hexanes, yielding 4.5 g (62%) of **S5**. ^{1}H NMR (400 MHz, $CDCl_3$), δ (ppm): 7.03 (d, J = 4.4 Hz, 1H), 7.02 (d, J = 3.2 Hz, 1H), 7.00 (d, J = 3.2 Hz, 1H), 6.97 (d, J = 4.0 Hz, 1H), 6.90 (d, J = 4.0 Hz, 1H), 6.88 (d, J = 3.6 Hz, 1H), 4.62 (s, 2H), 3.49 (t, J = 6.8 Hz, 2H), 1.61 (p, J = 7.0 Hz, 2H), 1.45-1.20 (m, 26H), 0.88 (t, J = 6.6, 3H).

17-Tosyloxy-3,6,9,12,15-pentaoxaheptadecane-1-ol (S6) [30]

A solution of hexa(ethyleneglycol) (15 g, 53 mmol) in 50 mL of THF and a solution of NaOH (5 g, 125 mmol) in 50 mL of H_2O were mixed and stirred at 0 ºC for 30 min. *p*-Toluenesulfoyl chloride (11g, 58 mmol) dissolved in 200 mL of THF was added dropwise to the mixed solution at 0 ºC. After stirring 4 h, cold water was added and the product was extracted with CH_2Cl_2. The organic layer was washed with H_2O, dried over $MgSO_4$, and evaporated. The product was purified by silica column chromatography eluting with ethyl acetate, yielding 7.4 g (32%) of **S6**. ^{1}H NMR (400 MHz, $CDCl_3$) δ (ppm): 7.77 (d, J = 8.4 Hz, 2H), 7.32 (d, J = 8.4 Hz), 4.13 (t, J = 4.8 Hz, 1H), 3.72-3.54 (m, 22H), 2.76 (br, 1H), 2.43 (s, 3H).

1-(2H-Tetrahydropyran-2-yloxy)-17-tosyloxy-3,6,9,12,15-pentaoxaheptadecane (S7) [30]

Pyridinium *p*-toluenesulfonate (0.85 g, 3.4 mmol) and 3,4-dihydro-2H-pyran (2.1 g, 25

mmol) were added to a solution of **S6** (7.4 g, 17 mmol) in 40 mL of CH_2Cl_2, and the solution was stirred 5 h at rt. The solution of the product was then washed with H_2O, dried over $MgSO_4$, and evaporated, yielding 9.0 g (~100%) of **S7**. ^{1}H NMR (400 MHz, $CDCl_3$) δ (ppm): 7.78 (d, J = 8.4 Hz, 2H), 7.32 (d, J = 7.6 Hz, 2H), 4.61 (t, J = 3.6 Hz, 1H), 4.14 (t, 4.8 Hz, 2H), 3.89-3.80 (m, 2H), 3.69-3.44 (m, 22H), 2.43 (s, 3H), 1.88-1.44 (m, 6H).

1-(2H-Tetrahydropyran-2-yloxy)-17-(thiophene-3-ethoxy)-3,6,9,12,15-pentaoxaheptadecane (S8)

3-Thiopheneethanol (2.4 g, 19 mmol) was added to a solution of NaH (1.6 g, 67 mmol) in 300 mL of dry THF, and the solution was stirred for 15 h at rt. **S7** (8.8 g, 17 mmol) was added dropwise to the stirred solution. After 7 h, the reaction was quenched by adding H_2O and the product was extracted with $CHCl_3$. The organic layer was washed with H_2O, dried over $MgSO_4$, and evaporated. The product was purified by silica column chromatography eluting with ethyl acetate, yielding 3.4 g (42%) of **S8**. ^{1}H NMR (400 MHz, $CDCl_3$), δ (ppm): 7.26-7.23 (m, 1H), 7.02 (d, J = 2.4 Hz, 1H), 6.98 (d, J = 4.8 Hz, 1H), 4.63 (t, J = 3.6 Hz, 1H), 3.91-3.83 (m, 2H), 3.72-3.47 (m, 26H), 2.93 (t, J = 7.2 Hz, 2H), 1.90-1.46 (m, 6H).

1-(2H-Tetrahydropyran-2-yloxy)-17-{2,5-bis(trimethylstannyl)thiophene-3-ethoxy}-3,6,9,12,15-pentaoxaheptadecane (S9)

Butyl lithium (1.6 M hexanes solution, 44 ml, 70 mmol) was added dropwise to a solution of diisopropylamine (7.16 g, 71 mmol) in 60 mL of dry THF at -84 ºC, and the solution was stirred for 30 min at rt. The solution containing LDA was cooled -84 ºC and added dropwise to a stirred solution of **S8** (3.4 g, 7.1 mmol) in 30 mL of dry THF. After stirring 1 h, trimethyltin chloride (1 M THF solution, 72 mL, 72 mmol) was added dropwise, and the solution was stirred for additional 7 h. Saturated aq NH_4Cl was added to the solution, and the product was extracted with $CHCl_3$. The organic layer was washed with H_2O, dried over $MgSO_4$, and evaporated. The product was purified by silica column chromatography eluting with ethyl acetate, yielding 2.9 g (50%) of **S9**. ^{1}H NMR (400 MHz, $CDCl_3$), δ (ppm): 7.20 (s, 1H), 4.63 (t, J = 3.4 Hz, 1H),

3.91-3.81 (m, 2H), 3.70-3.47 (m, 26H), 2.99 (t, J = 7.8 Hz, 2H), 1.87-1.46 (m, 6H), 0.38 (s, 9H), 0.34 (s, 9H).

Compound S10

S5 (4.0 g, 6.9 mmol), **S9** (2.8 g, 3.5 mmol), and tetrakis(triphenylphosphine) palladium(0) (1 g, 0.87 mmol) were dissolved in 100 mL of dry toluene. The solution was treated with N_2 bubbling for 5 min, and then heated to reflux for 22 h. The solution was filtrated to remove Pd catalysts and evaporated. The crude product was purified by silica column chromatography eluting with ethyl acetate/hexanes (4:1), yielding 1.1 g (21%) of **S10**. ^{1}H NMR (400 MHz, $CDCl_3$), δ (ppm): 7.12-7.03 (m, 11H), 6.85 (d, J = 3.6 Hz, 2H), 4.63 (s, 5H), 3.88-3.83 (m, 2H), 3.78-3.47 (m, 26H), 3.50 (t, J = 6.8Hz, 4H), 3.08 (t, J = 6.8Hz, 2H), 1.90-1.50 (m, 6H), 1.63-1.55 (m, 4H),1.45-1.10 (m, 56H), 0.88 (t, J = 6.8, 6H). MALDI TOF-MS m / z: 1478.28 (calc.), 1476.77 (found, M^+).

Oligothiophene 1 (S11)

S10 (1.1 g, 0.73 mmol) and pyridinium *p*-toluenesulfonate (0.24 g, 0.96 mmol) were dissolved in 70 mL of $CHCl_3$/EtOH (1:1), and the solution was heated at 60 ºC for 19 h. The solution was evaporated, and the crude product was purified by silica column chromatography eluting with $CHCl_3$/ethyl acetate/methanol (50:30:1), yielding 0.52 g (51%) of **S11**. ^{1}H NMR (500 MHz, $CDCl_3$), δ (ppm): 7.13-7.02 (m, 11H), 6.89 (d, J = 3.0 Hz, 2H), 4.63 (s, 4H), 3.78-3.58 (m, 26H), 3.50 (t, J = 6.4 Hz, 4H), 3.08 (t, J = 7.0 Hz, 2H), 1.61 (p, J = 7.0 Hz, 4H), 1.39-1.21 (m, 52H), 0.88 (t, 7.0 Hz, 6H). MALDI TOF-MS m / z: 1392.64 (calc.), 1392.1 (found).

Phenyl-C_{61}-butyricacid methyl ester (**PCBM**, **S12**) was synthesized according to the report of Hummelen et al[31].

^{1}H NMR (400 MHz, $CDCl_3$), δ (ppm): 7.93 (d, J = 7.6 Hz, 2H), 7.60-7.52 (m, 2H), 7.51-7.42

(m, 1H), 3.68 (s, 3H), 2.94-2.87 (m, 2H), 2.53 (t, J = 7.4, 2H), 2.24-2.14 (m, 2H). MALDI TOF-MS m / z: 911.11 (calc.), 910.10 (found, M^+).

Phenyl-C_{61}-buryric acid (S13) [31]

Acetic acid (250 mL) and HCl (100 mL) were added to a solution of **S12** (1.1 g, 1.2 mmol) in 250 ml of toluene, and the mixed solution was heated to reflux for 18 h. After the solution was evaporated, the crude product was treated with methanol, centrifuged to collect the suspension. This procedure was repeated with diethyl ether, toluene, and twice with diethyl ether, yielding 1.0 g (93%) of **S13**. ^{1}H NMR (400 MHz, $CDCl_3$), δ (ppm): 7.66 (d, J = 7.2 Hz, 2H), 7.31-7.22 (m, 2H), 7.22-7.16 (m, 1H), 2.72-2.62 (m, 2H), 2.67 (t, J = 7.2 Hz, 2H), 2.00-1.89 (m, 2H). MALDI TOF-MS m / z: 897.09 (calc.), 896.50 (found).

Dyad 2 (S15)

Thienyl chloride (0.98 g, 8.2 mmol) was added to a solution of **S13** (80 mg, 0.089 mmol) in 20 mL of freshly distilled CS_2, and the solution was heated to reflux for 21 h. After all the volatile components were removed in vacuo, sodium hydride (5 mg, 0.22 mmol), toluene (10 mL), and **S11** (62 mg, 0.045 mmol) dissolved in 10 mL of toluene were added to the residue (**S14**). The mixed solution was stirred for 3 days, and then the solution was evaporated. The product was purified by silica column chromatography eluting with ethyl acetate/hexanes (4:1), yielding 41 mg (40%) of **S15**. ^{1}H NMR (500 MHz, $CDCl_3$), δ (ppm): 7.90 (d, J = 7.5 Hz, 2H), 7.53 (t, J = 7.5 Hz, 2H), 7.49-7.42 (m, 1H), 7.13-7.02 (m, 11H), 6.89 (d, J = 3.0 Hz, 2H), 4.63 (s, 4H), 4.22 (t, J = 4.7 Hz, 2H), 3.77-3.60 (m, 24H), 3.50 (t, J = 6.6 Hz, 4H), 3.07 (t, J = 6.8 Hz, 2H), 2.91-2.86 (m, 2H), 2.53 (t, J = 7.5 Hz, 2H), 2.20-2.14 (m, 2H), 1.61 (p, J = 6.9 Hz, 4H), 1,38-1.23 (m, 52H), 0.88 (t, J = 6.6 Hz, 6H). MALDI TOF-MS m / z: 2270.71 (calc.), 2270.4 (found).

NMR and MALDI-TOF-MS Spectra of the Oligothiophene 1 (S11) and the Dyad 2 (S15)

^{1}H-NMR spectra were measured in $CDCl_3$ containing 0.03% v/v TMS by OXFORD Superconducting magnet system (500 MHz). MALDI-TOF-MS spectra were measured with a dithranol as a matrix by Applied Biosystems BioSpectrometry Workstaion model Voyager-DE STR spectrometer.

The NMR spectrum of the Oligothiophene 1

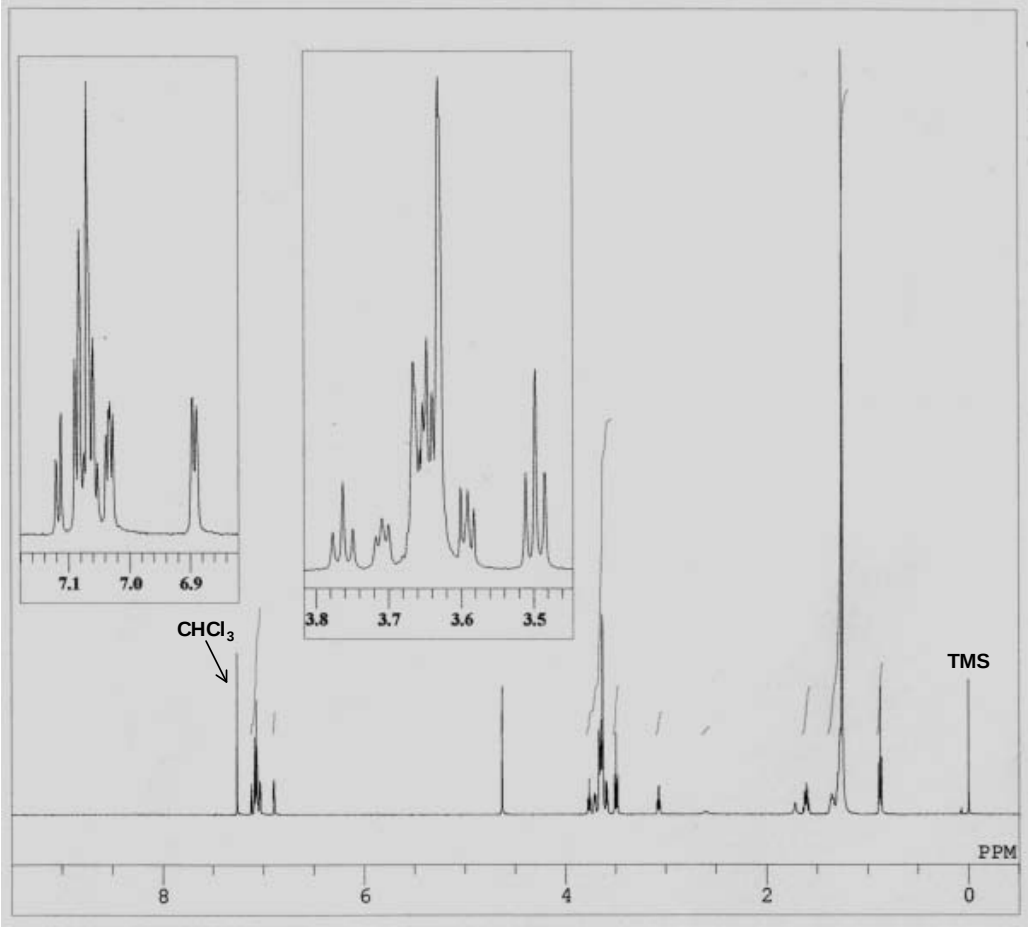

Figure S2.1. The NMR spectrum of the oligothiophene **1**

The MALDI-TOF-MS Spectrum of the Oligothiophene 1

m/z: 1392.64 (calculated), 1392.1 (measured). #(M-$OCH_2C_{16}H_{33}$ fraction): 1151.38 (calculated), 1151.17 (measured). **&**($M+Na^+$): 1415.62 (calculated), 1416.24 (measured).

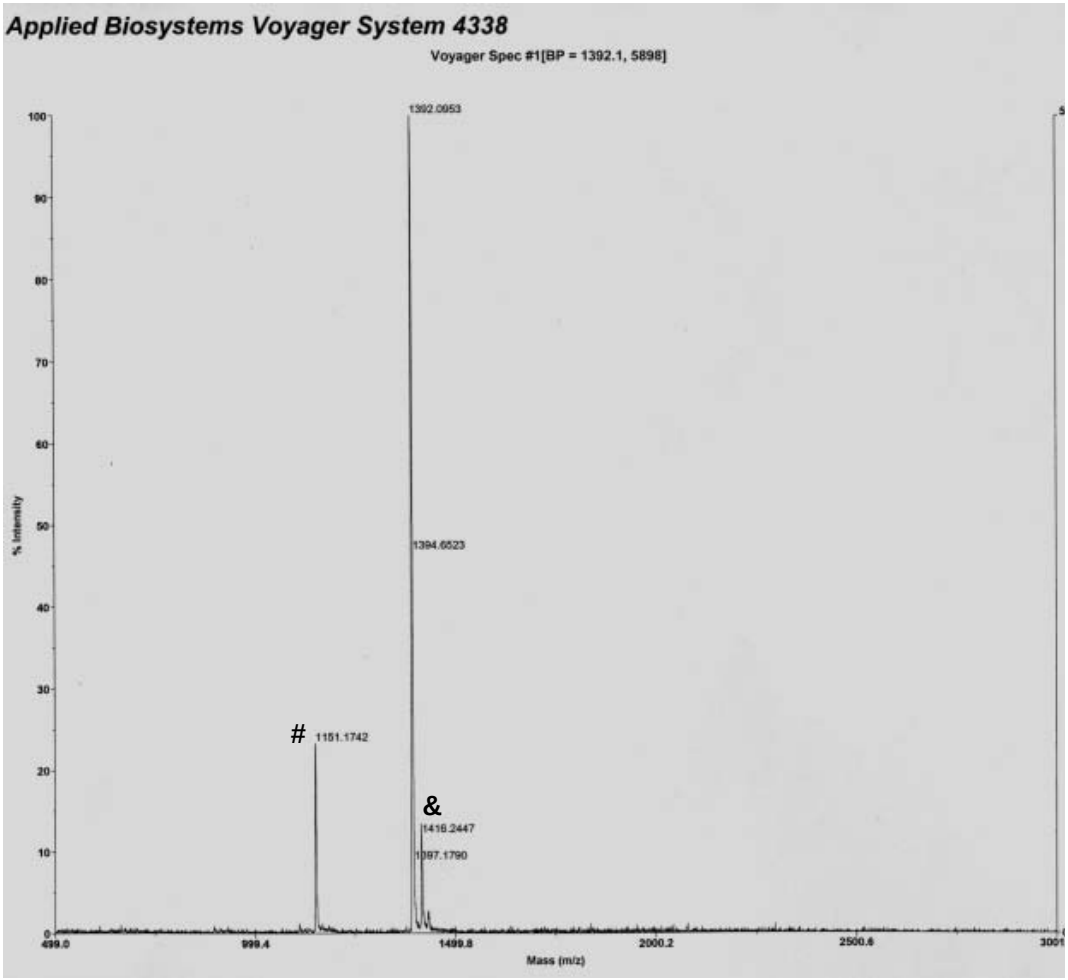

Figure S2.2. The MALDI-TOF-MS spectrum of the oligothiophene **1**

The NMR Spectrum of the Dyad 2

#: Ethyl acetate (The peak at around 1.3 ppm is superposed on the peak of dyad **2**.)

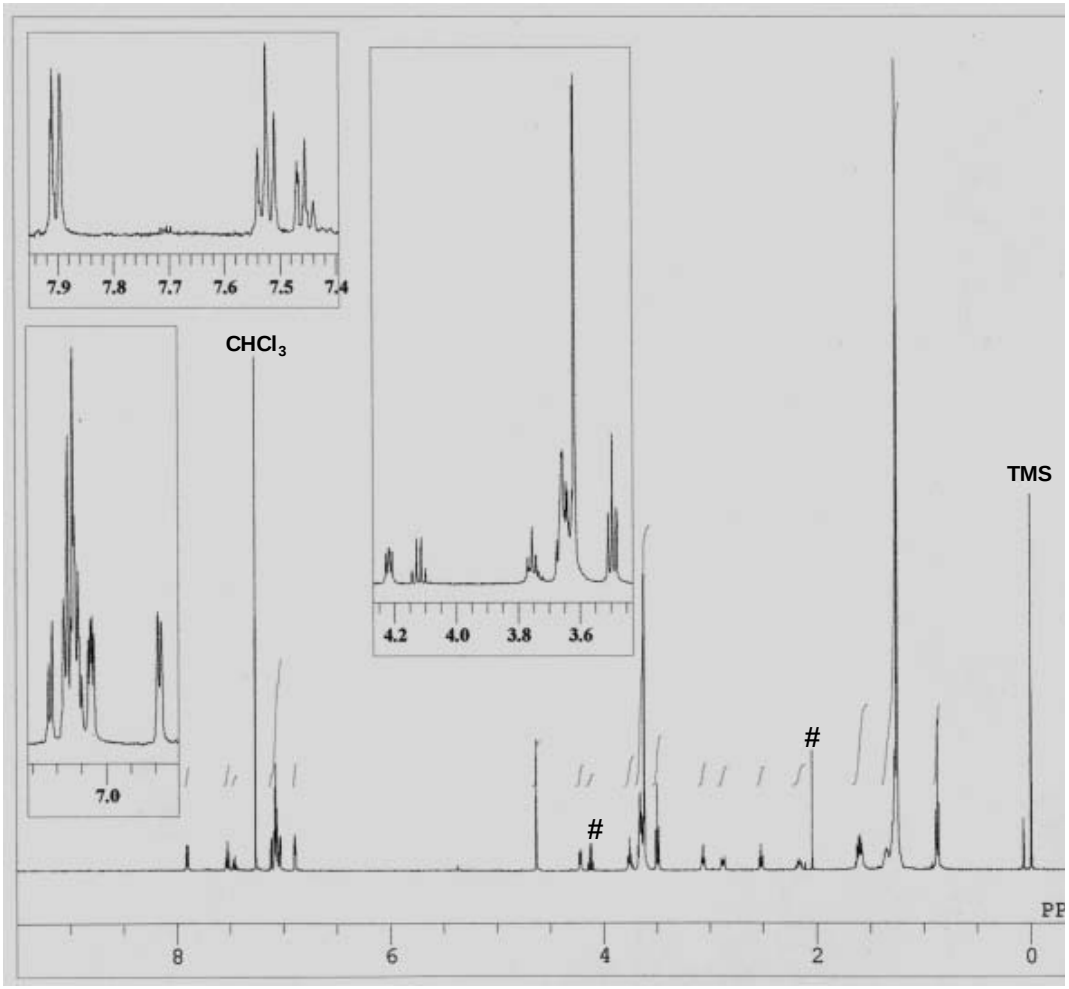

Figure S2.3. The NMR spectrum of the dyad **2**

The MALDI-TOF-MS Spectrum of the Dyad 2

m/z: 2270.71 (calculated), 2270.4 (measured). #(M-$OCH_2C_{16}H_{33}$ fraction): 2029.46 (calculated), 2029.89 (measured).

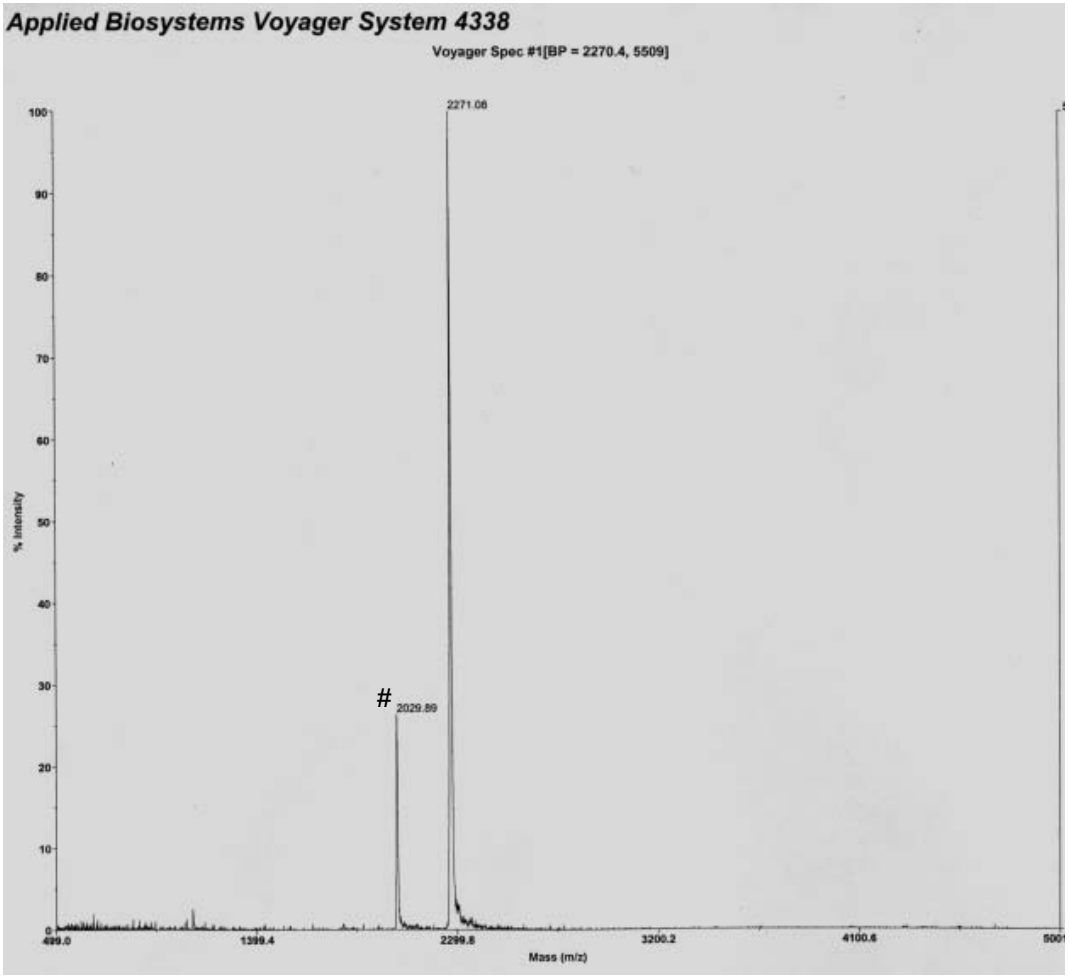

Figure S2.4. The MALDI-TOF-MS spectrum of the dyad **2**

The DSC Chart of the Dyad 2

The DSC chart (Figure S5) showed a broad endothermic peak at 52 ºC on heating, at which crystalline phase turned to isotropic phase, observed by a polarized optical microscope.

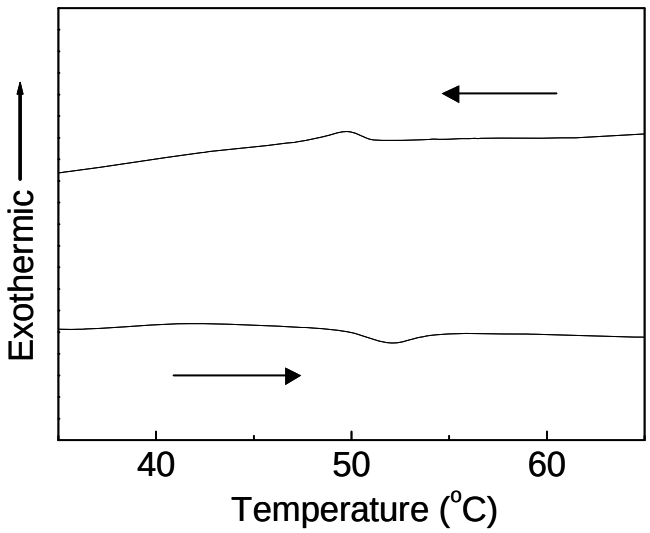

Figure S2.5. The DSC chart of the dyad **2**, measured at a heating/cooling rate of 10 ºC min^{-1}

References

1. F. J. M. Hoeben, P. Jonkheijm, E. W. Meijer and A. Schenning, *Chem. Rev.*, 2005, **105**, 1491-1546.
2. A. Schenning and E. W. Meijer, *Chem. Commun.*, 2005, 3245-3258.
3. F. S. Schoonbeek, J. H. van Esch, B. Wegewijs, D. B. A. Rep, M. P. de Haas, T. M. Klapwijk, R. M. Kellogg and B. L. Feringa, *Angew. Chem. Int. Ed.*, 1999, **38**, 1393-1397.
4. V. K. Praveen, S. J. George, R. Varghese, C. Vijayakumar and A. Ajayaghosh, *J. Am. Chem. Soc.*, 2006, **128**, 7542-7550.
5. X. Q. Li, V. Stepanenko, Z. J. Chen, P. Prins, L. D. A. Siebbeles and F. Wurthner, *Chem. Commun.*, 2006, 3871-3873.
6. J. van Herrikhuyzen, A. Syamakumari, A. Schenning and E. W. Meijer, *J. Am. Chem. Soc.*, 2004, **126**, 10021-10027.
7. A. M. Ramos, S. C. J. Meskers, E. H. A. Beckers, R. B. Prince, L. Brunsveld and R. A. J. Janssen, *J. Am. Chem. Soc.*, 2004, **126**, 9630-9644.
8. A. Ajayaghosh, R. Varghese, V. K. Praveen and S. Mahesh, *Angew. Chem. Int. Ed.*, 2006, **45**, 3261-3264.
9. S. J. George and A. Ajayaghosh, *Chem. Eur. J.*, 2005, **11**, 3217-3227.
10. S. J. George, A. Ajayaghosh, P. Jonkheijm, A. Schenning and E. W. Meijer, *Angew. Chem. Int. Ed.*, 2004, **43**, 3422-3425.
11. O. Henze, W. J. Feast, F. Gardebien, P. Jonkheijm, R. Lazzaroni, P. Leclere, E. W. Meijer and A. Schenning, *J. Am. Chem. Soc.*, 2006, **128**, 5923-5929.
12. P. Leclere, M. Surin, P. Viville, R. Lazzaroni, A. F. M. Kilbinger, O. Henze, W. J. Feast, M. Cavallini, F. Biscarini, A. Schenning and E. W. Meijer, *Chem. Mater.*, 2004, **16**, 4452-4466.
13. P. Jonkheijm, N. Stutzmann, Z. J. Chen, D. M. de Leeuw, E. W. Meijer, A. Schenning and F. Wurthner, *J. Am. Chem. Soc.*, 2006, **128**, 9535-9540.
14. D. Hirayama, K. Takimiya, Y. Aso, T. Otsubo, T. Hasobe, H. Yamada, H. Imahori, S. Fukuzumi and Y. Sakata, *J. Am. Chem. Soc.*, 2002, **124**, 532-533.
15. H. Imahori and S. Fukuzumi, *Adv. Funct. Mater.*, 2004, **14**, 525-536.
16. E. E. Neuteboom, E. H. A. Beckers, S. C. J. Meskers, E. W. Meijer and R. A. J. Janssen, *Org. Biomol. Chem.*, 2003, **1**, 198-203.
17. C. C. You and F. Wurthner, *Org. Lett.*, 2004, **6**, 2401-2404.
18. G. X. Zhang, D. Q. Zhang, X. H. Zhao, X. C. Ai, J. P. Zhang and D. B. Zhu, *Chem. Eur. J.*, 2006, **12**, 1067-1073.

19. F. Langa, M. J. Gomez-Escalonilla, J. M. Rueff, T. M. F. Duarte, J. F. Nierengarten, V. Palermo, P. Samori, Y. Rio, G. Accorsi and N. Armaroli, *Chem. Eur. J.*, 2005, **11**, 4405-4415.
20. H. Zhang, F. J. M. Hoeben, M. J. Pouderoijen, A. Schenning, E. W. Meijer, F. C. Schryver and S. De Feyter, *Chem. Eur. J.*, 2006, **12**, 9046-9055.
21. Y. Morikawa, S. Nagano, K. Watanabe, K. Kamata, T. Iyoda and T. Seki, *Adv. Mater.*, 2006, **18**, 883-+.
22. P. Samori, V. Francke, T. Mangel, K. Mullen and J. P. Rabe, *Opt. Mater.*, 1998, **9**, 390-393.
23. D. M. Guldi, C. P. Luo, A. Swartz, R. Gomez, J. L. Segura, N. Martin, C. Brabec and N. S. Sariciftci, *J. Org. Chem.*, 2002, **67**, 1141-1152.
24. N. Negishi, K. Takimiya, T. Otsubo, Y. Harima and Y. Aso, *Chem. Lett.*, 2004, **33**, 654-655.
25. F. S. Meng, J. L. Hua, K. C. Chen, H. Tian, L. Zuppiroli and F. Nuesch, *J. Mater. Chem.*, 2005, **15**, 979-986.
26. M. A. Loi, P. Denk, H. Hoppe, H. Neugebauer, C. Winder, D. Meissner, C. Brabec, N. S. Sariciftci, A. Gouloumis, P. Vazquez and T. Torres, *J. Mater. Chem.*, 2003, **13**, 700-704.
27. M. Narutaki, K. Takimiya, T. Otsubo, Y. Harima, H. Zhang, Y. Araki and O. Ito, *J. Org. Chem.*, 2006, **71**, 1761-1768.
28. R. C. Advincula, D. Phillips and S. Inaoka, *Abstracts of Papers of the American Chemical Society*, 1999, **217**, U445-U445.
29. J. P. Parakka and M. P. Cava, *Tetrahedron*, 1995, **51**, 2229-2242.
30. F. A. Loiseau, K. K. Hii and A. M. Hill, *J. Org. Chem.*, 2004, **69**, 639-647.
31. J. C. Hummelen, B. W. Knight, F. LePeq, F. Wudl, J. Yao and C. L. Wilkins, *J. Org. Chem.*, 1995, **60**, 532-538.

Chapter 3.

Effect of crystallinity in donor groups on performance of photovoltaic devices based on oligothiophene-fullerene dyad

3.1. Introduction

Organic photovoltaic devices with their advantages of low fabrication cost, light weight, flexibility, and large area have recently drawn much attention as a sustainable energy source [1, 2]. Breakthroughs such as the discoveries of the superior electron acceptability of fullerene [3, 4] and the donor/acceptor interpenetrating network "bulk heterojunction" [5-7] have improved the efficiency of the devices, and efficiencies of around 5% have been reported under simulated AM1.5 solar irradiation [8-16], Much recent work has been dedicated to the design of new materials with various properties such as low-band gap[10, 15, 17-25], modified crystallinity [12, 26-29], and self-assembly [30-38] in efforts to increase the absorption or to form suitable nanostructures for charge separation, transport, and collection, etc. Recent examples of the formation of self-assembled nanostructures using a block copolymer with donor and acceptor blocks [30] and hydrogen-bonded supramolecules [31] have demonstrated that self-assembly of the molecules is a powerful tool for controlling the nanostructure in photovoltaic devices.

In Chapter 2, the synthesis of a novel oligothiophene-fullerene dyad (**1** in Figure 3.1) for application to organic photovoltaic devices were described [34]. The covalent attachment of the donor and acceptor was expected to enhance photo-induced charge separation because these units were placed close to each other in the films. At the same time, supramolecular organization of the donor–acceptor multifunctional molecules would enable efficient charge transport of both holes and electrons in the film. It was showed that the dyad **1** spontaneously formed a fibrous supramolecular nanostructure in the film upon thermal annealing, induced by

π-π interaction of the oligothiophene parts [34]. Preliminary results of their application to the photovoltaic devices demonstrated that charge separation was enhanced in the dyad device, compared to the corresponding bulk heterojunction device from the donor/acceptor mixture. This could be attributed to the efficiency of the intramolecular charge separation in the dyad molecules. However, a relatively low fill factor (FF) limited the power conversion efficiency of the devices. This was probably due to the insufficiently connected carrier paths of the oligothiophene groups for holes and/or of the fullerene groups for electrons in the film. Further investigation of this system was therefore warranted in order to explore suitable nanostructures for both the charge separation and transport required to achieve higher photovoltaic performance.

In this chapter, a study of photovoltaic devices based on the oligothiophene-fullerene dyad **1** mixed with either the oligothiophene **2** or [6,6]-phenyl-C61-butyric acid methyl ester (PCBM) **3** (Figure 3.1) is described. Mixing of the donor or the acceptor into the dyad could lead to a better connection of each part, and thus improve carrier transport in the films. Investigation of the origin of the device performance dependence on the mixing ratios revealed that addition of the oligothiophene molecules improved the crystallinity of the donor groups in the films, resulting in a 20% increase in fill factor, while the addition of PCBM slightly lowered the crystallinity, thereby reducing the fill factor.

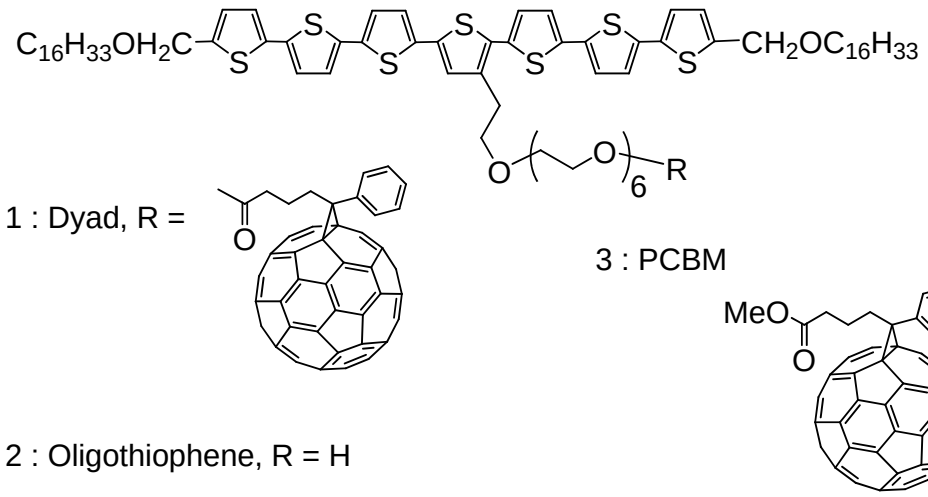

Figure 3.1. Molecular structures of oligothiophene-fullerene dyad **1**, oligothiophene **2**, and PCBM **3**.

3.2. Experimental

3.2.1 Synthesis and materials

1 and **2** were synthesized as shown previously in Chapter 2 [34]. **2** was further purified by recrystallization from ethyl acetate at room temperature. For the synthesis of **1**, anhydrous chlorobenzene was used instead of toluene to improve the yield from 40% to 70%. The synthesized dyad was also purified by reprecipitation in hexane. The fullerene derivative PCBM **3** was purchased from Frontier Carbon Corp., Japan and used as received.

3.2.2 Photovoltaic device fabrication and measurement

Photovoltaic devices were fabricated either with **1**, mixtures of **1** and **2**, or mixtures of **1** and **3**. The mixing ratios of **2** or **3** were 0.09, 0.23, 0.33, and 0.50 by weight. The device fabrication procedure was as follows. Indium tin oxide (ITO)-coated glass substrates (sheet resistance: 10 Ω sq^{-1}, Kuramoto Japan) were cleaned by ultrasonication in detergent, distilled water, acetone, and 2-propanol. The substrates were dried by air-blowing, and the poly(3,4-ethylenedioxythiophene):poly(styrene sulfonic acid) (PEDOT:PSS) (Baytron P) was spin-coated (4000 rpm, 30 s) on the ITO. The film was dried at 140 °C in air for 10 min and cooled down before spin-coating of the organic layer. The organic layer was prepared by spin-coating (2000 rpm, 30 s) the blend solutions of **1** and **2** or of **1** and **3** which were prepared by mixing the solution of **1** ($CHCl_3$, 16 mg mL^{-1}) with the solution of **2** or **3** ($CHCl_3$, 16 mg mL^{-1}). As a control, the dyad-only device was also fabricated from the $CHCl_3$ solution (16 mg mL^{-1}) of **1** in the same manner. After drying the organic layer, the ethanol solution of titanium tetraisopropoxide (TTIP) was spin-coated (2000 rpm, 30 s), and the film was dried in air for 20 min to form TiO_x hole-blocking layer [39]. Finally, the Al electrode was deposited under a high vacuum (3×10^{-4} Pa) to complete the devices. A 150 W xenon lamp (Peccell Technologies, Inc., solar simulator PEC-L11) equipped with band-pass filters with a maximum transmission wavelength of 430 or 440 nm (ASAHI SPECTRA, MX0430, MX0440; half width: 10 nm) was used as a light source. The *I-V* characteristics of the devices were measured using a Keithley

2400 source measurement unit. The devices were evaluated under monochromatic light irradiation with a 0.06 cm^2 photo mask. The 430 nm light with 1.05 mW cm^{-2} intensity and 440 nm light with 1.08 mW cm^{-2} intensity were applied for the **1**:**2** and the **1**:**3** mixture devices, respectively. The light intensities were calibrated with a standard silicon solar cell (Bunkoh-Keiki, BS520).

3.2.3 Atomic force microscopy (AFM) and UV-vis absorption spectra measurements

Thin films of the **1**:**2** and the **1**:**3** mixtures were prepared on the quartz/PEDOT:PSS substrates in the same manner as for the photovoltaic devices. The measurements were carried out without a TiO_x layer or an Al electrode. AFM images were obtained on a Digital Instrument Nanoscope31 operated in tapping mode. Absorption spectra were measured on a JASCO V-650 spectrophotometer.

3.2.4. Differential scanning calorimetry (DSC) measurement

The powder samples of **1**:**2** and the **1**:**3** mixtures for DSC were prepared by mixing the dyad solution with either the oligothiophene or the PCBM solution and then evaporating the solvents. The samples were dried in vacuo before the measurement. DSC traces were obtained at a scan rate of 10 °C min^{-1} on a Rigaku Thermo plus DSC8230. DSC traces after the first heating process were presented to remove the thermal history of the samples.

3.3. Results and discussion

3.3.1 Dyad and oligothiophene mixture

3.3.1.1 Photovoltaic performance.

One of the reasons for the low FF (0.23) of existing dyad-only photovoltaic devices in Chapter 2 [34] could be the insufficient connection of the carrier paths. The oligothiophene **2** (donor) was added to the dyad **1** to connect the hole transport path in the film and investigated the effect of the addition on the FF and other photovoltaic parameters. Photovoltaic devices of the mixture of **1** and **2** were fabricated with the configuration of ITO/PEDOT:PSS/**1**:**2**/TiO_x/Al and evaluated under monochromatic light irradiation at 430 nm. The averaged values of the device parameters over 30 devices for each data points with the standard deviations were plotted against the weight ratios of **2** in Figure 3.2. As expected, the FF increased from 0.31 to 0.37 as the ratio of **2** increased from 0 to 0.50. The open circuit voltage (V_{OC}) was also increased from 0.59 V to 0.66 V by the addition of **2**. On the other hand, the short circuit current (I_{SC}) stayed almost constant with the ratio of **2** up to 0.23, and decreased down to the half value at the ratio of 0.50. As a result, the power conversion efficiency under monochromatic light improved from 1.7% to 2.1% at the ratio of 0.23 and dropped to 1.1% at the ratio of 0.50, mainly due to the large decrease in I_{SC}.

3.3.1.2 AFM investigation of the thin films.

To clarify the origin of the above change in the photovoltaic device performance, the surface morphology of the thin films with the **1**:**2** mixtures was observed by AFM. In fact, recent studies have reported that the morphology significantly affects the device performance [1, 2, 40-42]. AFM images (Figure 3.3) revealed that the surface roughness increased as the ratio of **2** increased, and the calculated average roughness increased from 0.34 nm to 1.8 nm. The addition of **2** into **1** also gradually changed the size of the aggregation, and large aggregations over 100 nm were observed with the ratio of 0.50 (Figure 3.3e). These results suggest that the addition of the oligothiophene **2** enhanced the crystallinity of the components in the films. The similar

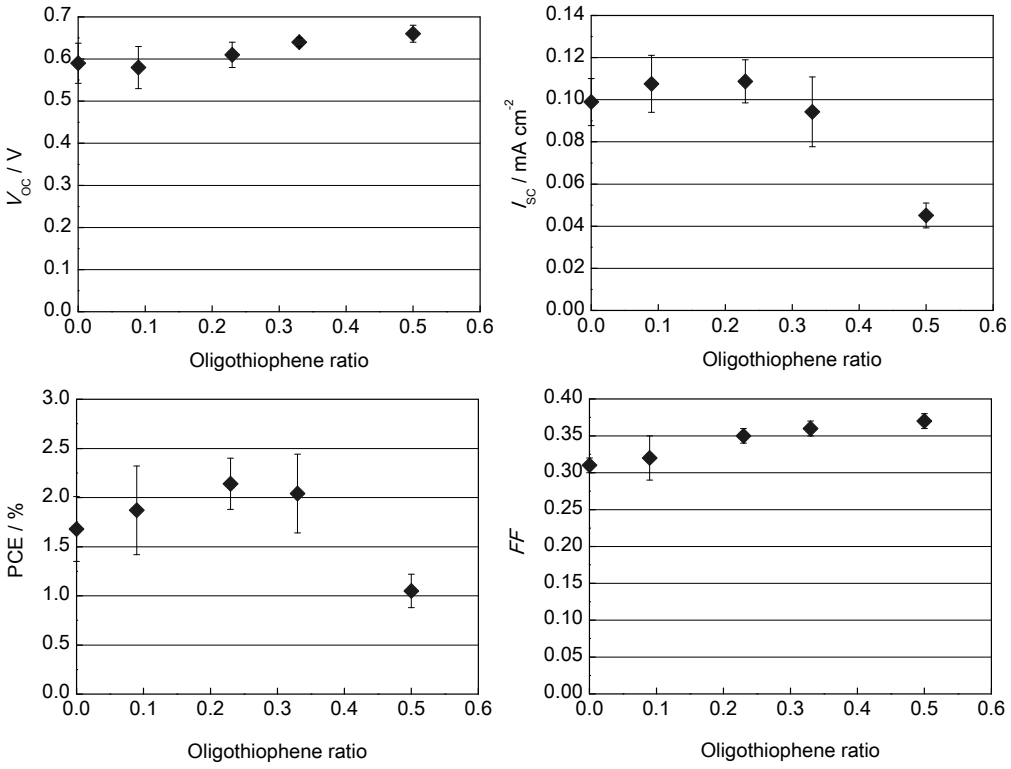

Figure 3.2. Photovoltaic parameters of the **1**:**2** mixture devices plotted against the ratio of **2** under monochromatic light irradiation at 430 nm.

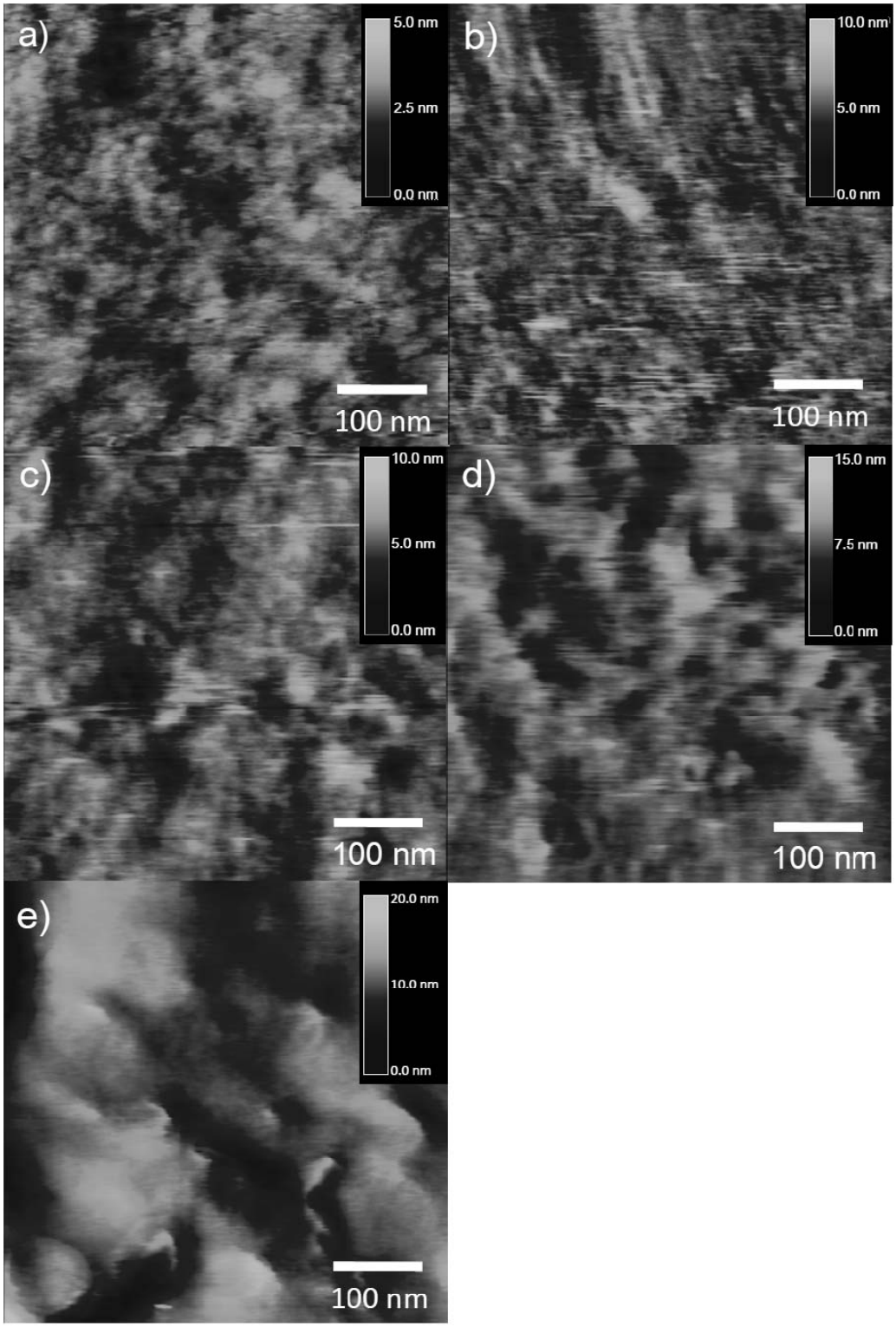

Figure 3.3. AFM height images of **1**:**2** mixture films with weight ratios of **2** of a) 0, b) 0.09, c) 0.23, d) 0.33, and e) 0.50. The calculated average roughnesses Ra of the films were a) 0.34 nm, b) 0.62 nm, c) 0.67 nm, d) 0.94 nm, and e) 1.8 nm.

morphological changes were observed previously for crystalline polythiophenes films [11, 12]. In Chapter 2, it was reported that the oligothiophene **2** has better crystallinity than the dyad **1** [34]. Since the crystallinity of the molecules has a close relationship with the carrier mobility in the films, and the enhancement of the molecular crystallinity in the films is reported to lead to higher FF in the photovoltaic devices [1, 2, 8, 9, 11, 12, 27], the observed improvement in FF in the **1**:**2** devices could be ascribed to improvement in hole mobility, derived from high crystallinity of the donor components in the film. At the same time, the addition of **2** (donor) reduced the relative content of the fullerene groups (acceptor) in the films. Thus the observed large drop in I_{SC} with the ratio of 0.50 could be attributed to the reduction in charge separation interface due to the insufficient acceptor content. Overall, the addition of the crystalline oligothiophene **2** was effective for improving the FF and the efficiency of the devices, whereas the power conversion efficiency did not improve with the higher content of **2** due to the reduction in I_{SC}.

3.3.1.3 UV-vis absorption spectra and DSC measurements.

The enhancement of the crystallinity in the above-mentioned AFM observation suggests that the addition of **2** changed the molecular interaction between the oligothiophene groups. To investigate the manner of interaction, UV-vis absorption spectra of the mixture films were measured. The spectra in Figure 3.4 show the two peaks characteristic of the fullerene and oligothiophene groups at around 330 nm and 440 nm, respectively. Interestingly, the gradual blue-shift of the peak at around 440 nm was observed as the ratio of **2** increased, while the other peak at 330 nm showed no shift but a decrease in the intensity. This blue-shift could be attributed to the formation of H-aggregation in the oligothiophene groups as observed in a film of **2** in Chapter 2 [34]. The gradual shift of the peaks also suggests that **2** intercalated into the oligothiophene group in **1**, leading to stronger interaction of the oligothiophene groups. To confirm this strengthened interaction, DSC measurement of the powder samples of **1**:**2** mixtures was carried out (Figure 3.5). Below the melting points, the mixtures showed complex thermal behaviors upon heating, possibly due to crystal-crystal or crystal-liquid crystal phase transitions. The melting points were confirmed by polarized optical microscope observation under crossed

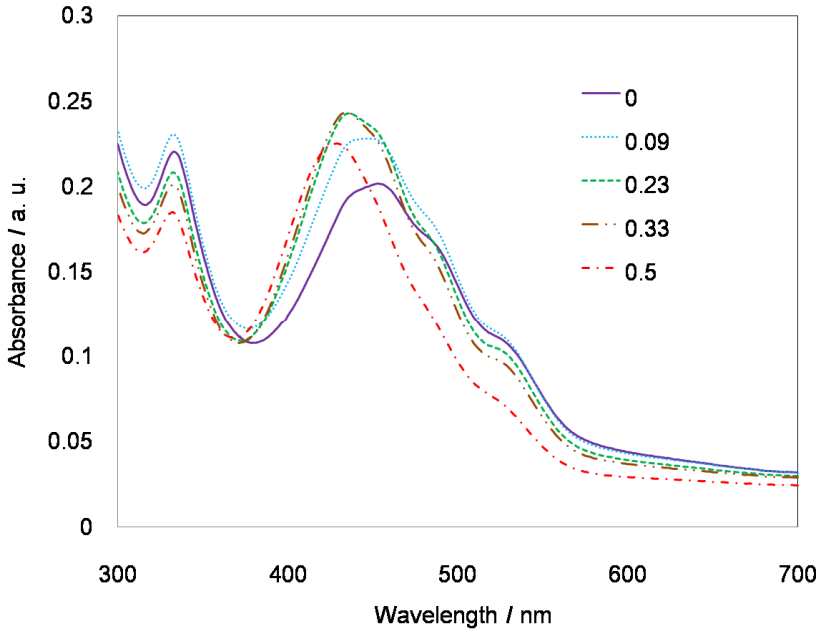

Figure 3.4. UV-vis absorption spectra of **1**:**2** mixture films with various ratios of **2**, as indicated in the key.

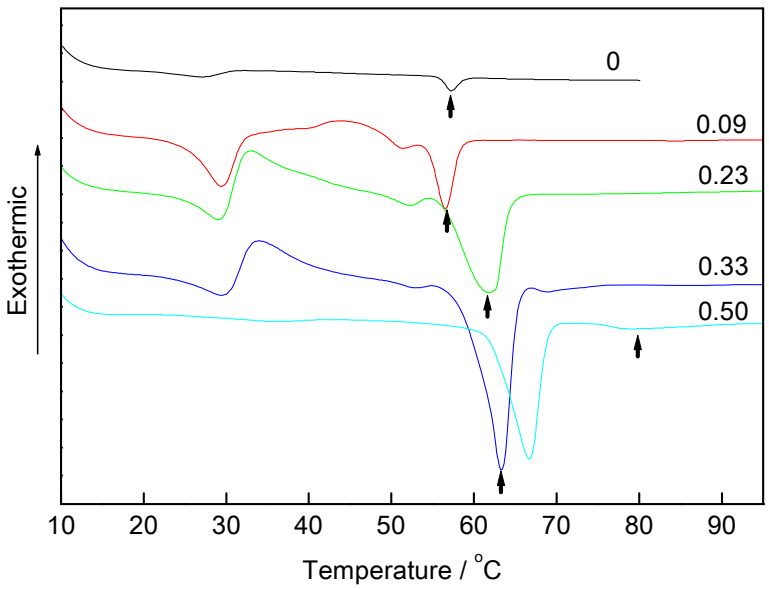

Figure 3.5. DSC traces of powder samples of **1**:**2** mixtures with various ratios of **2** upon heating, at a scan rate of 10 ºC min^{-1}. Numbers in the figure indicate the mixing ratios of **2**. Arrows indicate the melting points of the mixtures as confirmed by polarized optical microscope observation under crossed nicols.

nicols and are indicated by arrows in the figure. It was found that they were consecutively shifted to higher temperatures from 57 °C to 79 °C as the ratio of **2** increased from 0 to 0.5, indicating the enhanced crystallinity of the molecules, as also observed by AFM. Importantly, DSC traces of the mixtures were not a superposition of those of each component, indicating that **2** did not segregate from **1** but rather intercalated into the oligothiophene groups of **1** as suggested by the UV-vis absorption spectra. Combining these observations with the device results, it is concluded that the addition of **2** enhanced the crystallinity of the donor groups in the films due to stronger interaction between the oligothiophene groups. Although the obtained FF is still low compared to the polymer/fullerene solar cells possibly due to the still significant charge recombination nature of the dyad materials and/or the recombination at the organic/electrode interface, the enhancement of the FF in the **1**:**2** mixtures could result from the construction of better hole transport paths in the photovoltaic devices.

3.3.2 Dyad and PCBM mixture

3.3.2.1 Photovoltaic performance.

Analogous to the addition of the oligothiophene **2** described above, the addition of **3** (acceptor) can also be expected to improve the FF by connecting the electron transport paths. To investigate this notion, photovoltaic devices with the **1**:**3** mixtures were fabricated in the same manner as for the **1**:**2** mixture devices and evaluated under monochromatic light irradiation at 440 nm. The values of the device parameters were plotted against the weight ratios of **3** in Figure 3.6. In contrast to the **1**:**2** devices, in the **1**:**3** devices a slight decrease in FF was observed by the addition of **3**, while the other parameters were essentially independent of the mixing ratio. This opposite effect on FF suggests that the charge transport of the dyad device is not limited by the electron transport in the fullerene groups but occurs mainly by the hole transport in the oligothiophene groups.

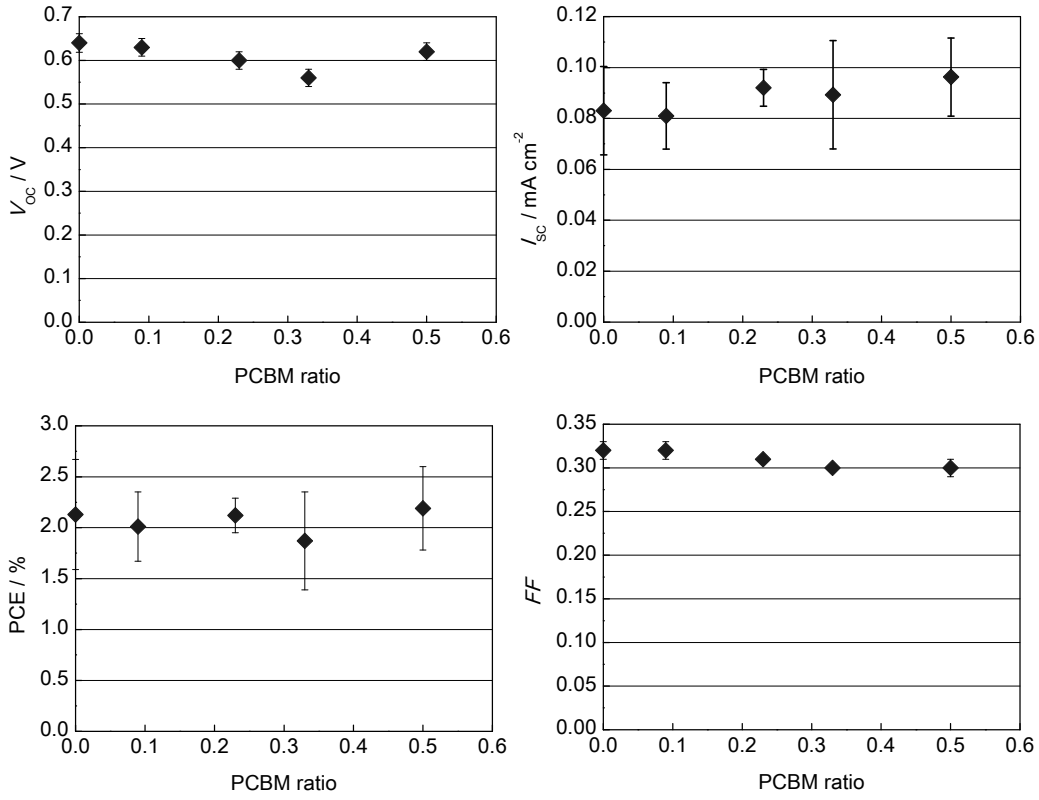

Figure 3.6. Photovoltaic parameters of the **1**:**3** mixture devices plotted against the ratio of **3** under monochromatic light irradiation at 440 nm.

3.3.2.2 AFM measurement.

AFM observation (Figure 3.7) of the **1**:**3** films with the various mixing ratios revealed that the morphologies of all the films were essentially unchanged by the addition of **3**; only the surface roughness gradually decreased. The calculated average roughness Ra decreased from 0.34 nm with the ratio of 0 (Figure 3.3a) to 0.22 nm with the ratio of 0.50 (Figure 3.7d). This result can be explained by the reduced crystallinity of the molecules in the film, which can be attributed to the slight decrease in FF in the **1**:**3** mixture devices. Interestingly, even at the high ratio of **3**, the morphology change was small and no large aggregation of **3** was observed in the **1**:**3** mixture films. This result suggests that mixed **3** intermingled with both the fullerene and the oligothiophene groups in the dyad.

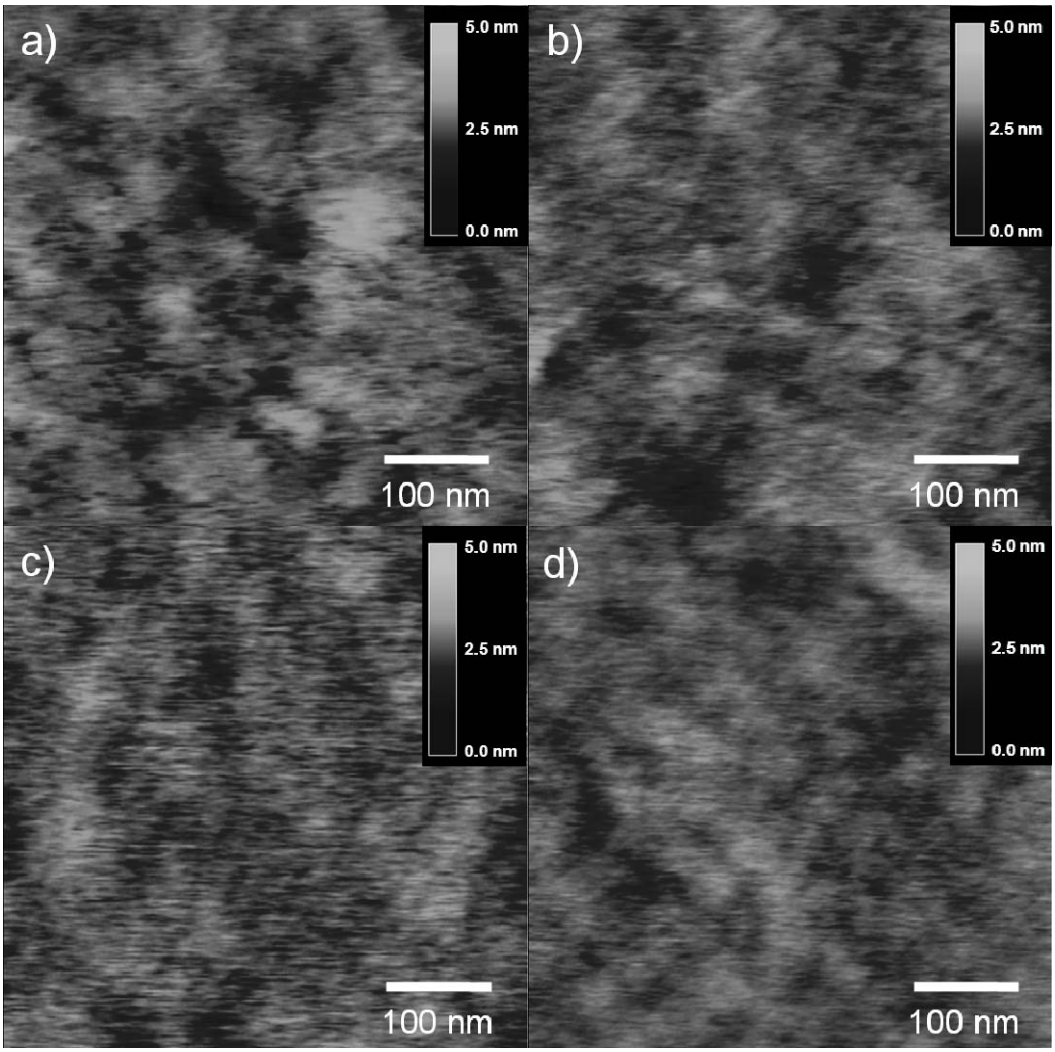

Figure 3.7. AFM height images of **1**:**3** mixture films with the ratio of **3** of a) 0.09, b) 0.23, c) 0.33, and d) 0.50. The calculated roughnesses Ra of the films were a) 0.27 nm, b) 0.23 nm, c) 0.25 nm, and d) 0.20 nm.

3.3.2.3 UV-vis absorption spectra and DSC measurements.

UV-vis absorption spectra of the **1**:**3** mixture films (Figure 3.8) showed the same two characteristic peaks as did the **1**:**2** mixture films. The spectra revealed that an absorption peak at around 440 nm, derived from the oligothiophene group, shifted from 457 nm to 445 nm as the ratio of **3** increased from 0 to 0.23, and remained at around 445 nm at the higher ratios. On the other hand, a peak at around 330 nm, derived from the fullerene group, showed no shift but did show an increase in the intensity. In Chapter 2, it was found that the absorption peak of the dyad film was red-shifted compared to that in solution at 440 nm, suggesting the formation of J-aggregation in the oligothiophene groups [34]. Thus, this peak shift suggests that the added PCBM molecules hindered the J-aggregation of the oligothiophene groups in **1** by weakening the interaction between them, which is consistent with the results of AFM observation. DSC measurement of the powder samples of the **1**:**3** mixtures (Figure 3.9) showed that the melting point of the mixture shifted to a lower temperature by the addition of **3**, and the peaks disappeared at the ratio of 0.33. This result also indicates that the addition of **3** weakened the interaction of the oligothiophene groups, thereby reducing the crystallinity. Consistent with the results for the **1**:**2** mixtures, the results for the **1**:**3** mixtures suggest that the crystallinity of the donor groups in the film is highly important to the improvement of the FF.

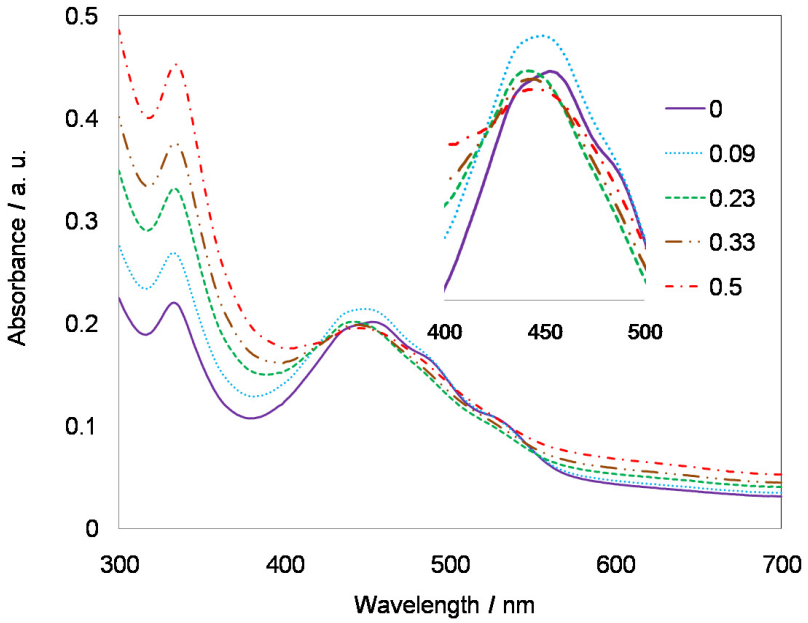

Figure 3.8. UV-vis absorption spectra of **1**: **3** mixture films with various ratios of **3**, as indicated in the key. Inset shows the enlarged spectra in the range of 400 to 500 nm.

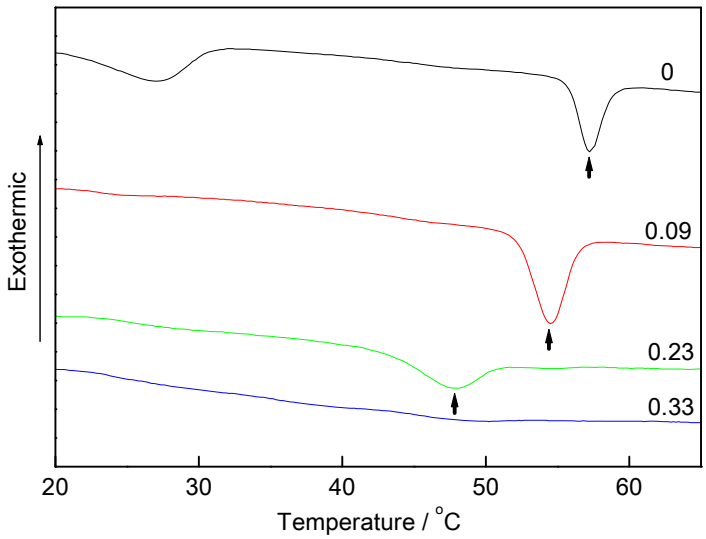

Figure 3.9. DSC traces of powder samples of **1**:**3** mixtures with various ratios of **3** upon heating, with a scan rate of 10 ºC min^{-1}. Numbers in the figure indicate the mixing ratios of **3**. Arrows indicate the melting points of the mixtures as confirmed by polarized optical microscope observation under crossed nicols.

3.4. Conclusion

Photovoltaic devices based on an oligothiophene-fullerene dyad mixed with either an oligothiophene or PCBM were fabricated. Analysis of the device performance by AFM and UV-vis absorption spectra and DSC measurements revealed that the addition of the oligothiophene molecules improved the crystallinity of the donor groups in the film, resulting in a 20% increase in FF. The obtained FF is still low compared to the polymer/fullerene solar cells possibly due to the fast charge recombination nature of the materials and/or the recombination at the organic/electrode interface. Nevertheless, the increase in FF suggests that introduction of highly crystalline donor groups with strong π-π interactions could be a promising design principle for dyad molecules so as to construct efficient hole transport paths and thus to further improve photovoltaic performance in combination with the efficient intramolecular charge separation of the dyad molecules.

References

1. S. Gunes, H. Neugebauer and N. S. Sariciftci, *Chem. Rev.*, 2007, **107**, 1324.
2. B. C. Thompson and J. M. J. Frechet, *Angew. Chem. Int. Ed.*, 2008, **47**, 58.
3. N. S. Sariciftci, L. Smilowitz, A. J. Heeger and F. Wudl, *Science*, 1992, **258**, 1474.
4. S. Morita, A. A. Zakhidov and K. Yoshino, *Solid State Commun.*, 1992, **82**, 249.
5. G. Yu and A. J. Heeger, *J. Appl. Phys.*, 1995, **78**, 4510.
6. G. Yu, J. Gao, J. C. Hummelen, F. Wudl and A. J. Heeger, *Science*, 1995, **270**, 1789.
7. M. Hiramoto, H. Fujiwara and M. Yokoyama, *Appl. Phys. Lett.*, 1991, **58**, 1062.
8. W. L. Ma, C. Y. Yang, X. Gong, K. Lee and A. J. Heeger, *Adv. Funct. Mater.*, 2005, **15**, 1617.
9. M. Reyes-Reyes, K. Kim and D. L. Carroll, *Appl. Phys. Lett.*, 2005, **87**, 83506.
10. J. Peet, J. Y. Kim, N. E. Coates, W. L. Ma, D. Moses, A. J. Heeger and G. C. Bazan, *Nat. Mater.*, 2007, **6**, 497.
11. G. Li, V. Shrotriya, J. S. Huang, Y. Yao, T. Moriarty, K. Emery and Y. Yang, *Nat. Mater.*, 2005, **4**, 864.
12. Y. Kim, S. Cook, S. M. Tuladhar, S. A. Choulis, J. Nelson, J. R. Durrant, D. D. C. Bradley, M. Giles, I. McCulloch, C. S. Ha and M. Ree, *Nat. Mater.*, 2006, **5**, 197.
13. S. S. Kim, S. I. Na, J. Jo, G. Tae and D. Y. Kim, *Adv. Mater.*, 2007, **19**, 4410.
14. J. Y. Kim, S. H. Kim, H. H. Lee, K. Lee, W. L. Ma, X. Gong and A. J. Heeger, *Adv. Mater.*, 2006, **18**, 572.
15. J. Y. Kim, K. Lee, N. E. Coates, D. Moses, T. Q. Nguyen, M. Dante and A. J. Heeger, *Science*, 2007, **317**, 222.
16. M. D. Irwin, B. Buchholz, A. W. Hains, R. P. H. Chang and T. J. Marks, *Proc. Natl. Acad. Sci. U.S.A.*, 2008, **105**, 2783.
17. F. L. Zhang, E. Perzon, X. J. Wang, W. Mammo, M. R. Andersson and O. Inganas, *Adv. Funct. Mater.*, 2005, **15**, 745.
18. C. J. Shi, Y. Yao, Y. Yang and Q. B. Pei, *J. Am. Chem. Soc.*, 2006, **128**, 8980.
19. M. M. Wienk, M. P. Struijk and R. A. J. Janssen, *Chem. Phys. Lett.*, 2006, **422**, 488.
20. W. Y. Wong, X. Z. Wang, Z. He, A. B. Djurisic, C. T. Yip, K. Y. Cheung, H. Wang, C. S. K. Mak and W. K. Chan, *Nat. Mater.*, 2007, **6**, 521.
21. Y. Yao, Y. Y. Liang, V. Shrotriya, S. Q. Xiao, L. P. Yu and Y. Yang, *Adv. Mater.*, 2007, **19**, 3979.
22. N. Blouin, A. Michaud, D. Gendron, S. Wakim, E. Blair, R. Neagu-Plesu, M. Belletete, G. Durocher, Y. Tao and M. Leclerc, *J. Am. Chem. Soc.*, 2008, **130**, 732.
23. N. Blouin, A. Michaud and M. Leclerc, *Adv. Mater.*, 2007, **19**, 2295.

24. K. Schulze, C. Uhrich, R. Schuppel, K. Leo, M. Pfeiffer, E. Brier, E. Reinold and P. Bauerle, *Adv. Mater.*, 2006, **18**, 2872.
25. E. Bundgaard and F. C. Krebs, *Macromolecules*, 2006, **39**, 2823.
26. K. Sivula, C. K. Luscombe, B. C. Thompson and J. M. J. Frechet, *J. Am. Chem. Soc.*, 2006, **128**, 13988.
27. A. J. Mozer, P. Denk, M. C. Scharber, H. Neugebauer and N. S. Sariciftci, *J. Phys. Chem. B*, 2004, **108**, 5235.
28. Y. Suzuki, K. Hashimoto and K. Tajima, *Macromolecules*, 2007, **40**, 6521.
29. K. Tajima, Y. Suzuki and K. Hashimoto, *J. Phys. Chem. C*, 2008, **112**, 8507.
30. S. M. Lindner, S. Huttner, A. Chiche, M. Thelakkat and G. Krausch, *Angew. Chem. Int. Ed.*, 2006, **45**, 3364.
31. P. Jonkheijm, J. K. J. van Duren, M. Kemerink, R. A. J. Janssen, A. Schenning and E. W. Meijer, *Macromolecules*, 2006, **39**, 784.
32. L. Schmidt-Mende, A. Fechtenkotter, K. Mullen, E. Moons, R. H. Friend and J. D. MacKenzie, *Science*, 2001, **293**, 1119.
33. T. Heiser, G. Adamopoulos, M. Brinkmann, U. Giovanella, S. Ould-Saad, C. Brochon, K. van de Wetering and G. Hadziioannou, *Thin Solid Films*, 2006, **511**, 219.
34. T. Nishizawa, K. Tajima and K. Hashimoto, *J. Mater. Chem.*, 2007, **17**, 2440.
35. K. Hirota, K. Tajima and K. Hashimoto, *Synth. Met.*, 2007, **157**, 290.
36. S. S. Sun, C. Zhang, A. Ledbetter, S. Choi, K. Seo, C. E. Bonner, M. Drees and N. S. Sariciftci, *Appl. Phys. Lett.*, 2007, **90**, 43117.
37. Q. S. Wei, T. Nishizawa, K. Tajima and K. Hashimoto, *Adv. Mater.*, 2008, **20**, 2211.
38. Y. Zhang, K. Tajima, K. Hirota and K. Hashimoto, *J. Am. Chem. Soc.*, 2008, **130**, 7812.
39. A. Hayakawa, O. Yoshikawa, T. Fujieda, K. Uehara and S. Yoshikawaa, *Appl. Phys. Lett.*, 2007, **90**, 163517.
40. H. Hoppe and N. S. Sariciftci, *J. Mater. Chem.*, 2006, **16**, 45.
41. P. Peumans, S. Uchida and S. R. Forrest, *Nature*, 2003, **425**, 158.
42. X. Yang and J. Loos, *Macromolecules*, 2007, **40**, 1353.

Chapter 4.

Efficient Dyad-based Organic Solar Cells with Highly Crystalline Donor Group

4.1. Introduction

Organic solar cells based on solution-processable materials such as π-conjugated oligomers, polymers, and fullerene derivatives have recently drawn much attention as an alternative energy source with low fabrication cost, light weight, and flexibility [1, 2]. In the state-of-the-art solution-processed organic solar cells, bulk heterojunction (BHJ) structure provides large interface between donor and acceptor materials by forming nanometer-scaled domains and interpenetrating network of the components (i.e. mutually percolated carrier pathways throughout the thin film). As a result, efficient charge separation and transport are achieved in the films, leading to high power conversion efficiency (PCE) of 4-5% with the combination of π-conjugated polymers such as poly(3-hexylthiophene-2,5-diyl) (P3HT) as a donor and fullerene derivative, [6,6]-phenyl-C_{61}-butyric acid methyl ester (PCBM) as an acceptor [3-10]. However, the formation of such nanostructures is not well-controlled in the BHJ films since it is simply achieved by optimizing the fabrication conditions of the devices including donor/acceptor mixing ratio [11, 12], solvent [5-7, 13, 14], evaporation speed of the solution during the coating processes [3, 5, 15], and thermal annealing conditions [6, 8, 16]. Therefore mixture BHJ systems often meet the low reproducibility of the appropriate nanostructure formation and sometimes suffers from unwanted structure change such as phase separation in large scale (e.g. micrometer-sized PCBM aggregation [17-20]), resulting in significant reduction of the performance.

Recently much work has been done to construct an appropriate donor/acceptor nanostructure in sophisticated ways such as introduction of inorganic nanostructure [21-26] or molecular design [27-36]. Covalent attachment of the donor and acceptor molecules as in dyads is promising

molecular design to prevent phase separation and thus to realize efficient charge separation. In fact, the close existence of the donor and acceptor in dyads assures the efficient charge separation and as a result, higher photocurrent has been achieved in the dyad based solar cells compared to the corresponding mixture BHJ counterpart [31]. However, low fill factor (FF) of the dyad-based devices has limited the PCEs, which is probably due to insufficient charge transport and resulting recombination of the charges. In Chapter 3, it was found that the addition of the donor component to the dyad increased the crystallinity in the films, resulting in improvement in FF of the devices [36]. This result suggests that introduction of the highly crystalline donor group with strong π-π interactions into the dyad would enhance intermolecular hopping of the charges and thus reduce the charge recombination, leading to the improvement in FF as well as the efficiency of the devices.

In this chapter, syntheses of oligo(*p*-phenylenevinylene)-fullerene dyads and their application to solar cells are described to investigate the influence of the donor crystallinity on performance of the solar cells. The chemical structures of the dyads are shown in Figure 4.1. Oligo(*p*-phenylenevinylene) (OPV) (Figure 4.2.) was introduced as a crystalline donor group with high planarity of π-conjugated plane and thus strong intermolecular π-π interactions to enhance intermolecular charge hopping. As for the acceptor introduced was a fullerene derivative which is well-known as an excellent electron acceptor and transporter [37-39]. A long and flexible spacer of oligo(ethylene oxide) connects the lateral position of the OPV group to the fullerene group in such a way that both groups are effectively apart to enhance their own interaction and thus to construct the efficient charge transport. As a result, FF of the device expectedly improved to achieve PCE of over 1% under simulated solar light irradiation (AM1.5, 100 mW cm^{-2}), indicating that the strong intermolecular interaction of the donor groups is of importance to achieve the efficient charge transport in the film.

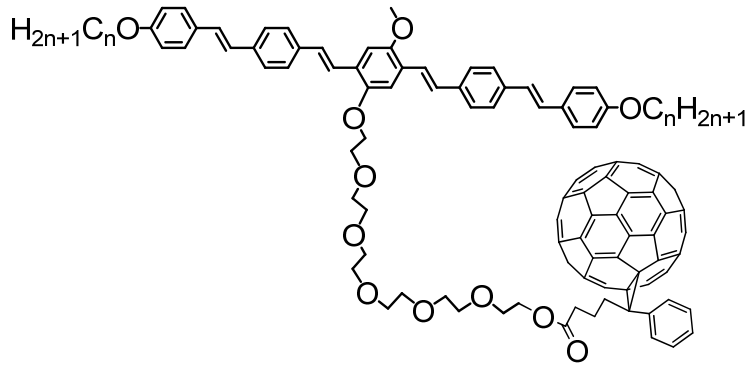

Figure 4.1. Molecular structures of oligo(*p*-phenylenevinylene)-fullerene dyads, **1** (n = 1), **2** (n = 6), and **3** (n = 12).

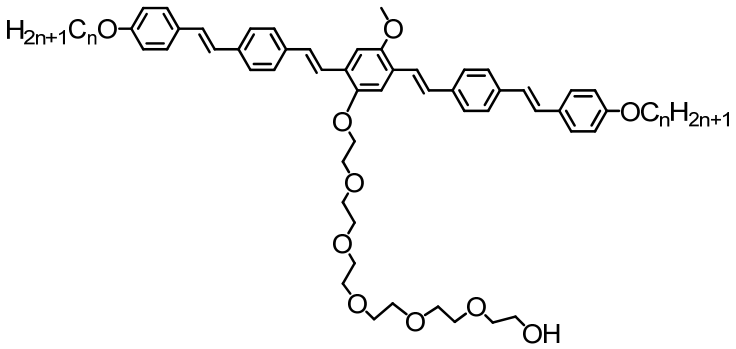

Figure 4.2. Molecular structures of oligo(*p*-phenylenevinylene)s, **4** (n = 1), **5** (n = 6), and **6** (n = 12).

4.2. Experimental

4.2.1. Synthesis

OPV-fullerene dyads were synthesized via esterification reaction of OPVs (**4**-**6** in Scheme 4.1) and a fullerene derivative with carboxylic chloride functional group (**7** in Scheme 4.1). After purification by column chromatography and HPLC, the products were identified by ^{1}H-NMR and MALDI-TOF-MS. The detail of the synthetic schemes is described in Appendix.

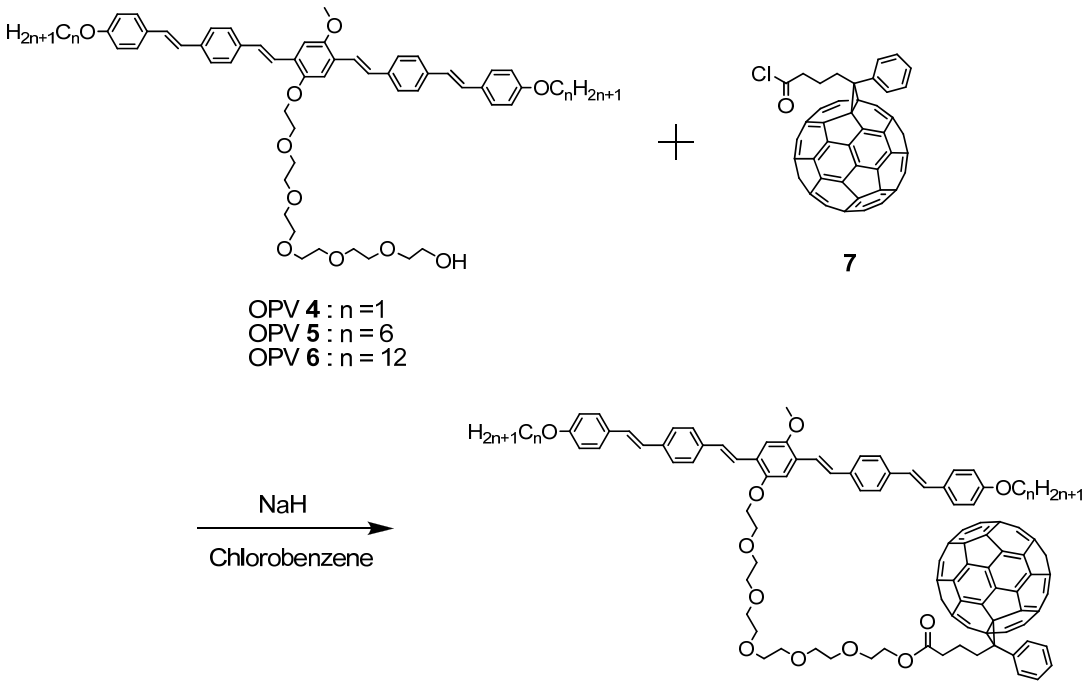

Scheme 4.1. Syntheses of dyads.

4.2.2. Measurement instruments

Powder X-ray diffraction (XRD) patterns were obtained on X-ray diffractometer RINT 2400 (Rigaku) with an X-ray source of Cu-Kα at 45 kV-200 mA.

Differential scanning calorimetry (DSC) traces were obtained at a scan rate of 10 ºC min^{-1} on a Rigaku Thermo plus DSC8230 after first heating process to eliminate the thermal history of the sample. Polarized optical microscope observations were conducted using Nikon ECLIPSE LV100POL equipped with a hotplate (MT-350, Collet-Kogyo, Japan).

Absorption spectra were measured on a JASCO V-650 spectrophotometer and fluorescence spectra were measured on a HITACHI F-4500 fluorescence spectrophotometer.

Atomic force microscopy (AFM) images were obtained on a Digital Instrument Nanoscope31 operated in tapping mode.

4.2.3. Solar cell fabrication and measurement

Solar cells were fabricated as follows. Indium tin oxide (ITO) coated glass substrates (sheet resistance: 10 Ω sq^{-1}, Geomatech, Japan) were cleaned by ultra-sonication in detergent, H_2O, acetone, and 2-propanol. PEDOT:PSS layer was formed on the ITO substrates by spin-coating (4000 rpm, 30s), followed by drying at 140 ºC for 15 minutes. After the substrates were cooled down to the room temperature, the organic layer was formed on the PEDOT:PSS layer by spin-coating (1000 rpm, 30s) $CHCl_3$ solutions containing 10 mg mL^{-1} of dyads **1-3**, and 0.4 mg mL^{-1} of poly(dimethyl siloxane-*b*-methyl methacrylate) (PDMS-*b*-PMMA) (M_n = 8000 for PDMS and M_n = 4000 for PMMA, M_w/M_n = 1.09, Polymer Source, Canada). Note that PDMS-*b*-PMMA spontaneously forms a buffer layer over the organic layer [40]. Finally, Al cathode electrode (80 nm) was deposited on the organic layer under a high vacuum (3×10^{-4} Pa).

I-V characteristics of the devices were measured under the irradiation of simulated solar light (AM 1.5, 100 mW cm^{-2}) from a 150 W xenon lamp (PEC-L11, Peccell Technologies, Inc., Japan) with an AM 1.5 filter. The light intensity was calibrated with a standard silicon solar cell (BS520, Bunkoh-Keiki, Japan). The active area of the devices was defined by the photo mask as

0.06 cm^2. External quantum efficiency (EQE) of the devices was measured on a Hypermonolight System SM-250F (Bunkoh-Keiki, Japan).

4.3. Results and Discussion

4.3.1. Physical property investigation

The crystallinity of the donor groups were investigated prior to introduction of the fullerene group. The powder XRD patterns (Figure 4.3) revealed that OPVs of **4** and **5** with shorter alkyl chains showed the strong diffraction peaks in the wide angle region (for **4**, 2θ of 19.72º (*d*-spacing of 4.50 Å), 21.32º (4.17 Å), and 23.45º (3.79 Å), and for **5**, 2θ of 20.07º (4.42 Å), 23.04º (3.86 Å)), which could be derived from π-π stacking of the molecules. In contrast, the XRD pattern of OPV **6** with the longest alkyl chain showed no such strong peaks in the wide angle region but instead distinctive peaks in the small angle region (2θ of 1.62º (54.5 Å), 3.15º (28.1 Å, 5.24º (16.9 Å)). These results indicated that the π-π interaction of the molecules enhanced by shortening the alkyl chain length. It is also noteworthy that the solubility of the molecules in common organic solvents such as $CHCl_3$ decreases as the alkyl chain length shortens, which also suggests the enhanced π-π interaction with the shorter alkyl chain length.

The crystallinity of the fullerene linked dyads was also investigated by DSC. DSC traces (Figure 4.4) revealed that dyad **1** showed sharp endothermic and exothermic peaks at 192 ºC (ΔH = -43.5 kJ mol^{-1}) on heating process and 152 ºC (ΔH = 36.0 kJ mol^{-1}) on cooling process, respectively. Optical microscope observation of the sample under crossed nicols revealed that the molecules melted at 192 ºC and recrystallized at 152 ºC, indicating the crystalline nature of the dyad **1**. The obtained enthalpy change is comparable with that of OPV **4** during its phase transition from crystal to isotropic liquid phase (ΔH = 33.7 kJ mol^{-1}, see Appendix), which could suggest the strong π-π interaction of OPV groups in the dyad despite of introduction of bulky fullerene groups. Similarly, the crystallinity of dyad **2** and **3** were also investigated. The DSC traces revealed the crystalline nature of both dyads with the enthalpy change of 20.5 kJ mol^{-1} and 39.4 kJ mol^{-1} for dyad 2 and 3, respectively, during their phase transition from crystal to isotropic liquid phase. Those enthalpy changes of the dyads were also comparable with those of corresponding OPVs for **5** (ΔH = 12.4 kJ mol^{-1}) and **6** (ΔH = 44.1 kJ mol^{-1}) (see Appendix). It is also noteworthy that dyad **2** showed liquid crystal phase, which was confirmed by optical microscope observation under crossed nicols (see Appendix).

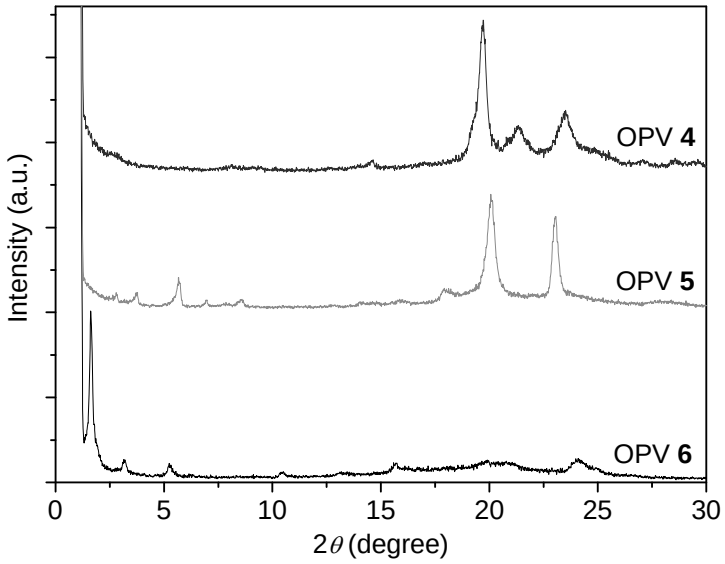

Figure 4.3. Powder XRD patterns of OPVs.

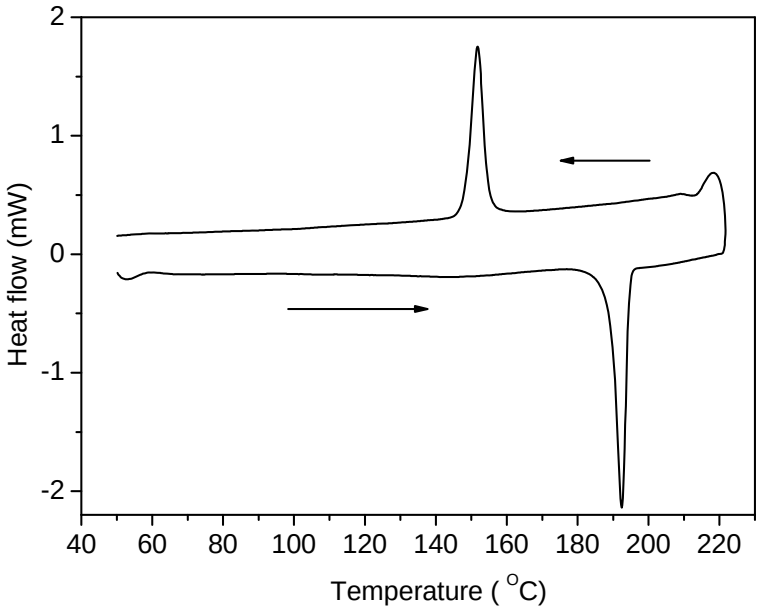

Figure 4.4. DSC trace of dyad **1**.

4.3.2. Photopysical property measurement

The photophysical properties of dyads were investigated in the thin film. Figure 4.5 shows the absorption spectra of dyads in the thin film. Two distinctive peaks were observed at 336 nm and around 430 nm, which were derived from the absorption of the fullerene groups and OPV groups, respectively. The peaks derived from OPV groups were red-shifted in the films of **1** and **2** and blue-shifted in the film of **3**, compared to those in solution which suggests that J-aggregation or H-aggregation formation in the films, respectively (see Appendix). This result also supports the strong π-π interaction of OPV groups in the film as shown in the aforementioned results.

The fluorescence spectra of the thin films of the dyads and OPVs are shown in Figure 4.6. The monochromatic light at 440 nm was used to excite the OPV groups and the spectra were normalized with the absorbance at that wavelength. In the OPV films, the fluorescence from the OPV groups was observed at 502 nm with shoulders at 532 nm and around 580 nm. In sharp contrast, almost complete quenching of the fluorescence was observed in the dyad films. This result suggests that the efficient electron transfer was occurred from the OPV groups to the fullerene groups in the dyad films.

4.3.3. Solar cells and AFM observation

From the results above, efficient charge separation and transport can be expected by applying the dyads to solar cells. The solar cells of the dyads were fabricated with the configuration of ITO/PEDOT:PSS/**1**, **2**, or **3**/PDMS-*b*-PMMA/Al, and *I*-*V* characteristics under AM 1.5 irradiation are shown in Figure 4.7. The FF of the devices increased as the alkyl chain length shortens, and the maximum FF of 0.41 was achieved in the device with dyad **1**. The short circuit current (I_{SC}) also increased from 1.56 mA cm^{-2} in the device with **3** to 3.20 mA cm^{-2} in the device with **1** while open circuit voltage (V_{OC}) in each device was comparable (0.88 V, 0.90 V, and 0.92 V for the device with **1**, **2**, and **3**, respectively). As a result, the power conversion efficiency (PCE) improved from 0.43% to 1.15%. Moreover, thermal annealing at 150 ºC for 1 minute under N_2 atmosphere further improved the efficiency of the device with **1** up to a

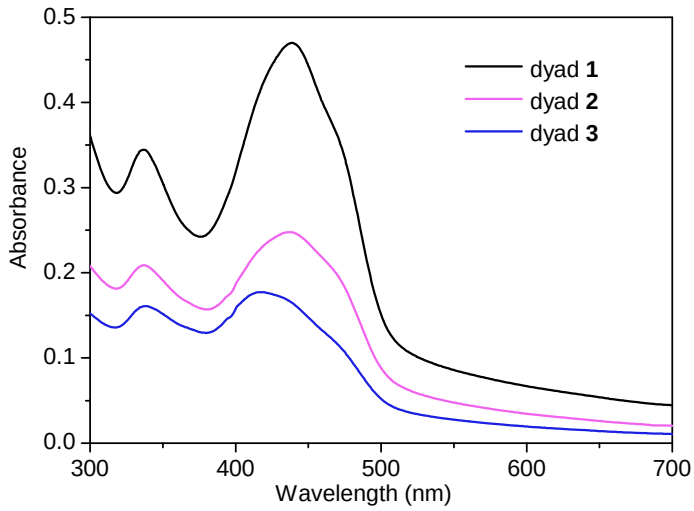

Figure 4.5. Absorption spectra of thin films of dyads.

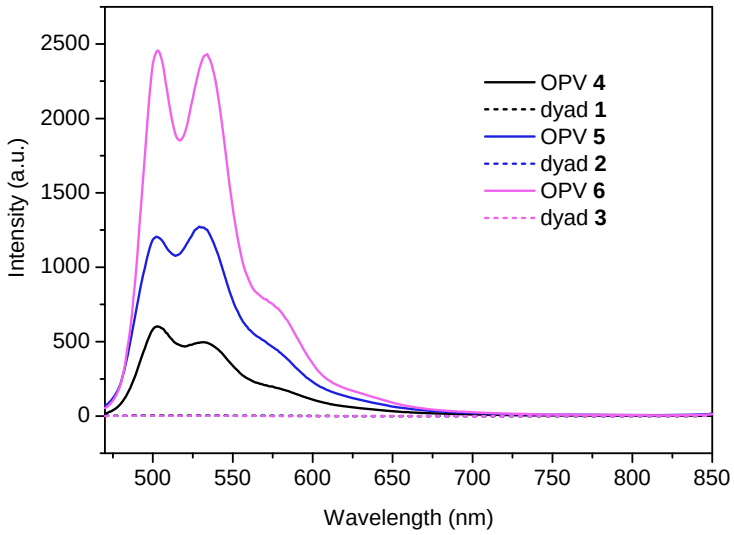

Figure 4.6. Fluorescence spectra of dyads and OPVs.

maximum PCE of 1.28% with V_{OC} of 0.88 V, I_{SC} of 3.3 mA cm^{-2}, and FF of 0.44 (dashed line in Figure 4.7), which is the highest efficiency among the dyad-based solar cells [27, 33, 41]. It is also noteworthy that FF of 0.44 is relatively high since the highest value reported in the dyad-based solar cells is 0.3 [27, 33], obtained under a similar condition (white light irradiation, 80 mW cm^{-2}).

The EQE of the annealed device with **1** was also evaluated under monochromatic light irradiation. The maximum EQE (Figure 4.8) reached 40% at 440 nm and the calculated I_{SC} with the EQE spectra resulted in 3.0 mA cm^{-2} which is good agreement with the observed value.

The surface morphologies of the thin films were also investigated by AFM. AFM height images revealed that the larger aggregation was formed in the films of the dyads with the shorter alkyl chains and the annealed film (Figure 4.9). The calculated average roughness increased from 0.19 nm in the film of **3** to 1.3 nm in the annealed film of **1**. These AFM results could suggest that the formation of the better network of the OPV groups and/or fullerene groups through the strong π-π interaction of the OPV groups, resulting in the improved FF and I_{SC}.

The observed improvement in FF and PCE in the solar cell with dyad **1** could be attributed to the enhanced carrier transport through the carrier pathways formed by the strong π-π interaction of the OPV groups. Although the observed FF is still lower than that of the polymer/fullerene BHJ devices, probably due to the disconnected network of the donor and acceptor and/or improper orientation of the molecules in the film, the results above clearly demonstrated that the importance of the crystallinity of the donor groups to improve the carrier transport in the dyad-based solar cells.

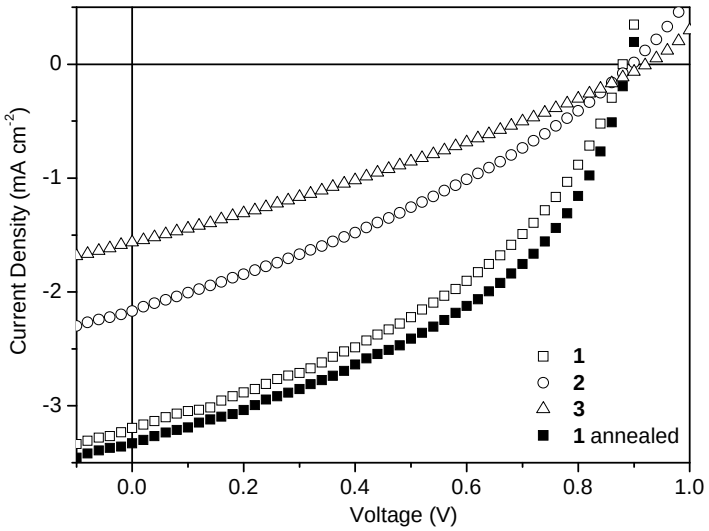

Figure 4.7. *I-V* characteristics of the devices with **1** (open squares), **2** (circles), **3** (triangles), and **1** after annealing (closed squares).

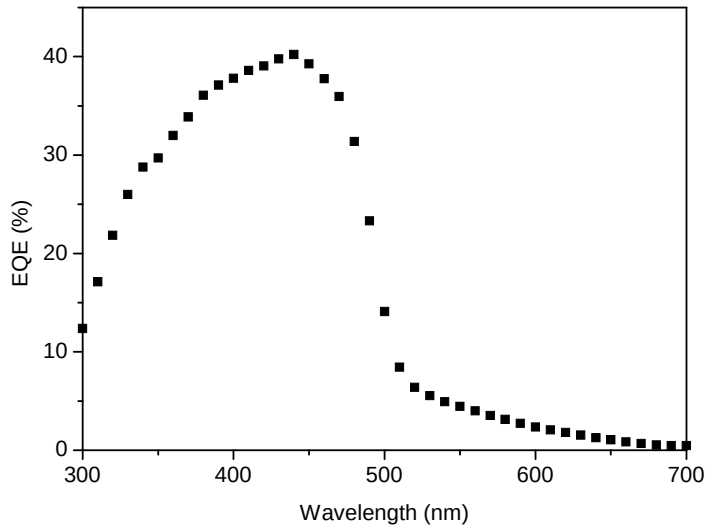

Figure 4.8. EQE spectrum of the dyad **1** device after annealing at 150 ºC for 1 minute.

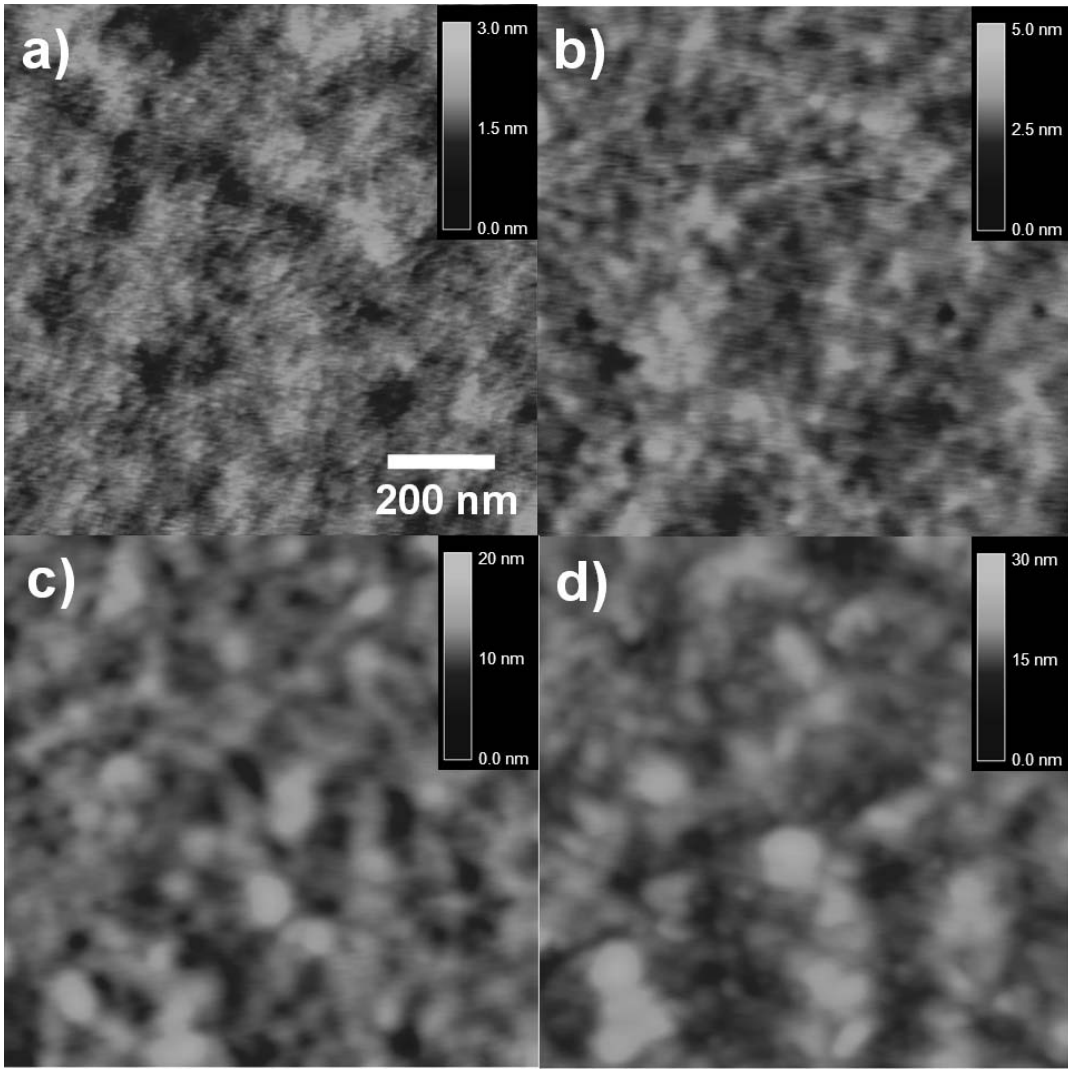

Figure 4.9. AFM height images of a) **3**, b) **2**, c) **1**, and d) **1** annealed films.

4.4. Conclusion

Novel oligo(*p*-phenylenevinylene)-fullerene dyads were synthesized, and the importance of the strong π-π interaction of the donor groups for achieving the efficient charge transport was demonstrated. The introduction of highly crystalline OPV donor into the dyad molecule improved FF up to 0.44, resulting in a high efficiency of 1.28%, which is the highest value among the dyad-based solar cells. This result revealed the high potential of donor-acceptor dyads as a photovoltaic material. Further optimization of the molecular design such as introduction of a low band gap donor or self-organization ability will be promising strategy to achieve highly efficient solar cells together with single component.

Appendix

Chemicals

4-cyanobenzyl bromide was purchased from Tokyo Chemical Industry Co. Ltd., Japan. Triethyl phosphite, hexaethyleneglycol, *p*-methoxy phenol and paraformaldehyde were purchased from Aldrich. The fullerene derivative PCBM was purchased from Frontier Carbon Corp., Japan. The rest of the chemicals and organic solvents were purchased from Wako Pure Chemicals Industries Ltd., Japan. All of these chemicals are used as received without further purification.

Instruments

^{1}H NMR spectra were measured in $CDCl_3$ containing 0.03% v/v TMS by OXFORD Superconducting magnet system (500 MHz) or JEOL JNM-LA400 spectrometer (400 MHz). MALDI-TOF MS spectra were measured on Applied Biosystems BioSpectrometry workstation Model Voyager-DE STR Spectrometer using dithranol as a matrix. High performance liquid chromatography was conducted using a SHIMADZU Preparative Liquid Chromotograph LC-8A

Synthetic Schemes [31, 42, 43]

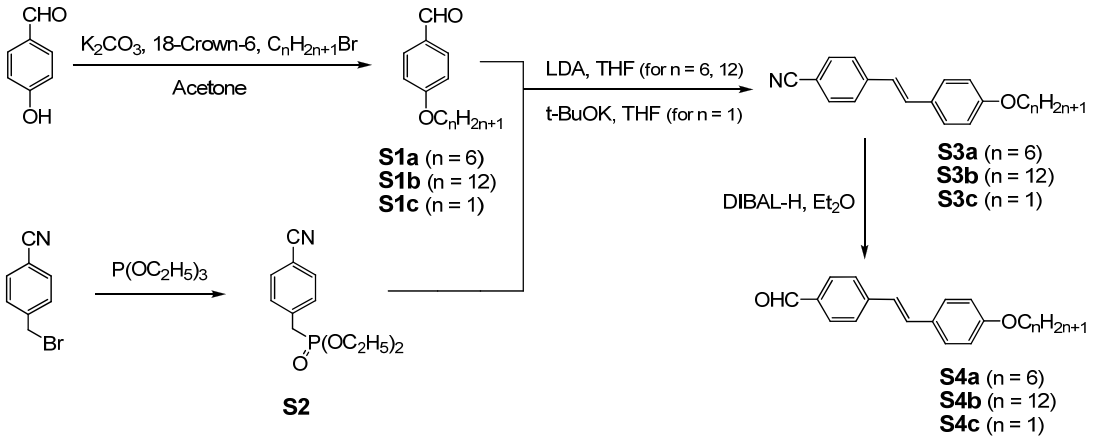

Scheme S4.1. Synthesis of the side parts.

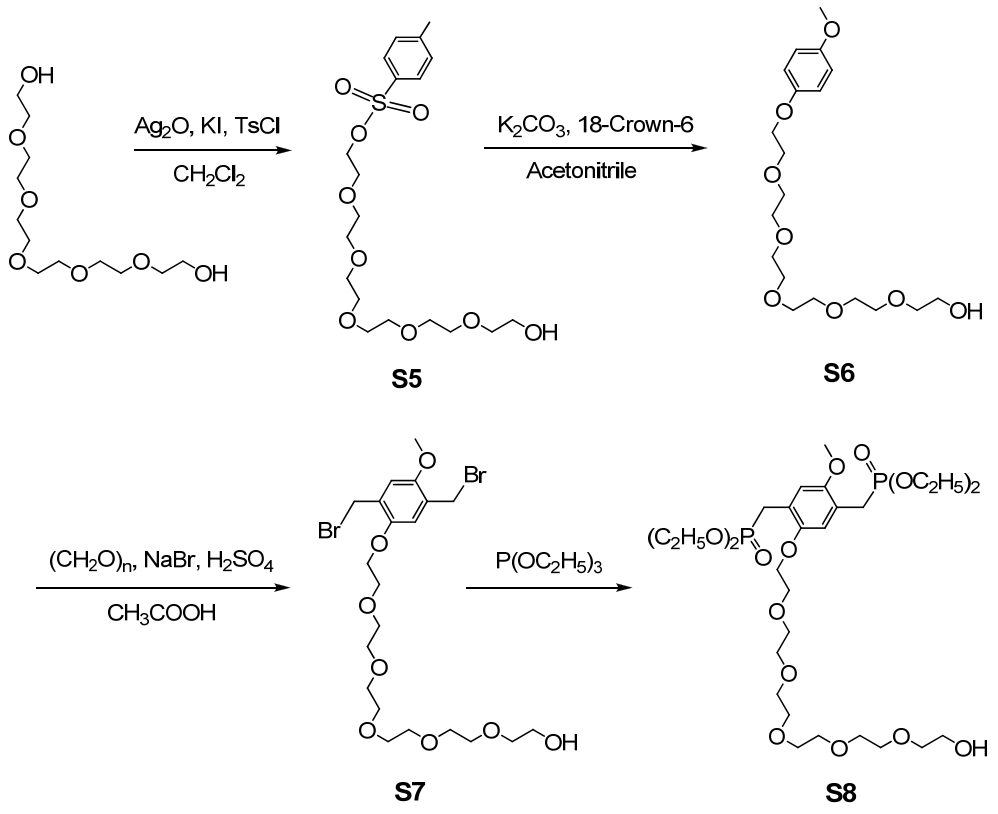

Scheme S4.2. Synthesis of the center part.

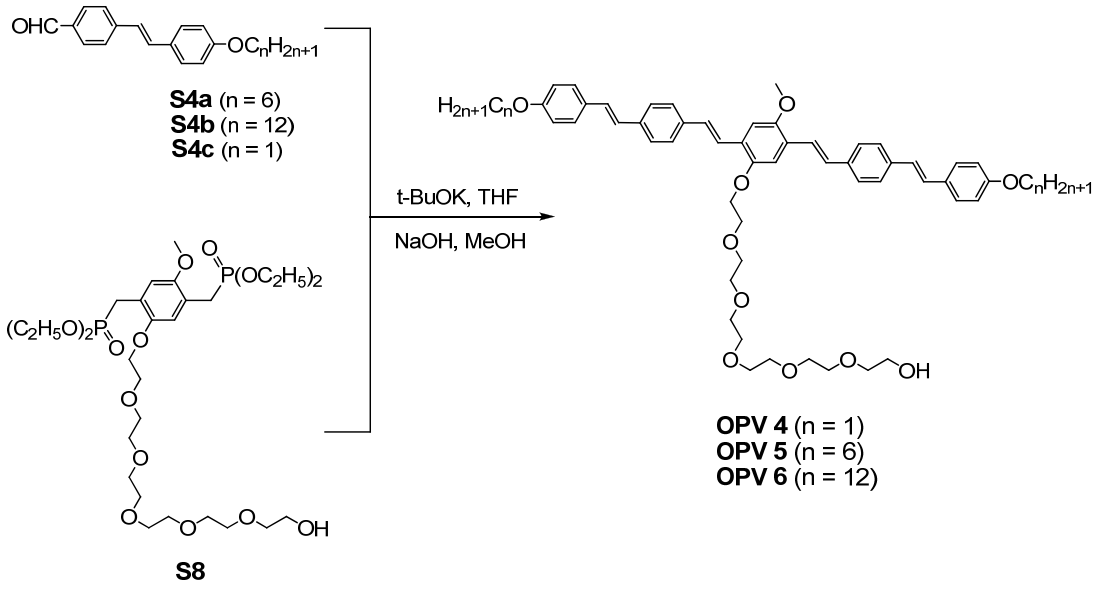

Scheme S4.3. The coupling reaction for OPVs.

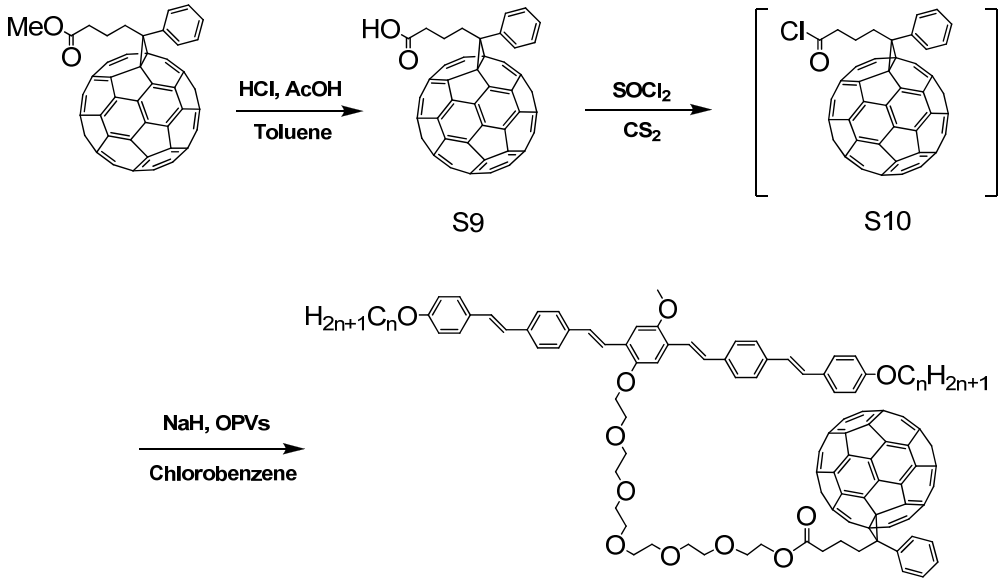

Scheme S4.4. The synthesis of dyads

4-(Hexyloxy)benzaldehyde (S1a)

p-Hydroxybenzaldehyde (4.9 g, 40 mmol), hexyl bromide(6.6 g, 40 mmol), potassium carbonate (8.3 g, 60 mmol) and 18-crown-6 (0.98 g, 4 mmol) were placed into a 200 mL rounded bottom flask and dissolved in 100 mL of acetone. The reaction mixture was refluxed for 24 hours. After the reaction mixture was cooled down to room temperature, the residue was filtered and the filtrate was concentrated by rotary evaporation. The crude product was subjected to a silica column chromatography first eluting with hexanes and then hexanes/ethyl acetate (1:1) to afford 6.6 g of the pure product (80% yield). ^{1}H NMR ($CDCl_3$, 500 MHz) δ : 9.88 (s, 1H, Ph-C*H*O), 7.83 (d, 2H, J = 8.5 Hz, ortho-*H* Ph), 6.99 (d, 2H, J = 8.5 Hz, meta-*H* Ph), 4.04 (t, 2H, J = 6.7 Hz, -OCH_2-), 1.78 – 1.84 (m, 2H, -OCH$_2$CH_2-), 1.50-1.44 (m, 2H, -CH_2CH$_3$), 1.37-1.33 (m, 4H, -OCH$_2$CH$_2$CH_2CH_2-), 0.91 (t, 3H, J = 7.3 Hz, -CH$_2$CH_3).

4-(Dodecyloxy) benzaldehyde (S1b)

The title compound was obtained by following; the same synthetic procedure as **S1a** except using dodecyl bromide instead of hexyl bromide (61% yield). ^{1}H NMR ($CDCl_3$, 500 MHz) δ : 9.88 (s, 1H, Ph-C*H*O), 7.83 (d, 2H, J = 8.5 Hz, ortho-*H* Ph), 6.99 (d, 2H, J = 8.5 Hz, meta-*H* Ph), 3.98 (t, 2H, J = 6.7 Hz, -OCH_2-), 1.83-1.76 (m, 2H, -OCH$_2$CH_2-), 1.49-1.42 (m, 2H, -CH_2CH$_3$), 1.36-1.22 (m, 16H, -OCH$_2$CH$_2$-(CH_2)$_8$-CH_3), 0.88 (t, 3H, J = 7.3 Hz, -CH$_2$CH_3).

Diethyl (4-cyanobenzyl)phosphonate (S2)

4-Cyanobenzyl bromide (6.9 g, 35 mmol) and triethylphosphite (7 g, 42 mmol) were placed in a 50 mL rounded bottom flask. A distillation apparatus was attached to collect poisonous ethyl bromide formed during the reaction. The reaction mixture was heated to 130 ˚C for 1 hour and then cooled down to room temperature. Remaining triethylphosphite was removed in vacuo by gradual heating from room temperature up to 130 ˚C for 4 hours. The product was used for the next step without further purification (8.8 g, ~100% yield). ^{1}H NMR ($CDCl_3$, 500 MHz) δ : 7.61 (d, 2H, J = 7.9 Hz, meta-*H* Ph), 7.42 (d, 2H, J = 8.2 Hz, ortho-*H* Ph), 4.07-4.01 (m, 4H,

-PO(OC*H*$_2$CH$_3$)$_2$), 3.20 (d, 2H, J = 22.6 Hz, Ph-C*H*$_2$-), 1.26 (t, 6H, J = 7.0 Hz, -PO(OCH$_2$C*H*$_3$)$_2$).

4-(4-(hexyloxy)styryl)benzonitrile (S3)

To a solution of diisopropyl amine (4.2 g, 42 mmol) in 40 mL of dry THF was added dropwise *n*-BuLi (1.6 M solution in hexane, 24 mL, 38 mmol) at -78 ˚C. After the reaction mixture was stirred for 1 h to form LDA, a solution of phosphonate **S2** (8.1 g, 32 mmol) in 30 mL of dry THF was added dropwise into the solution at -78 ˚C. The reaction mixture was then stirred for 30 minutes at 0 ˚C. A solution of aldehyde **S1a** (6.6 g, 32 mmol) in 30 mL of dry THF was added dropwise into the reaction mixture. The reaction mixture was stirred overnight at room temperature and quenched by adding 10% v/v aqueous solution of acetic acid, followed by rotary evaporation to remove THF. Precipitated yellowish-white solid was filtrated and washed with water. To remove the remaining acetic acid, the yellowish-white solid was dissolved in chloroform and the solution was washed with H_2O and a saturated aqueous solution of $NaHCO_3$. The organic layer was collected, dried over $MgSO_4$ and concentrated by rotary evaporation. The crude product was subjected to a silica column chromatography eluting with dichloromethane to afford the pure product (8.5 g, 87% yield). ^{1}H NMR ($CDCl_3$, 500 MHz) δ : 7.61 (d, 2H, J = 8.5 Hz, NC-*H*Ph), 7.54 (d, 2H, J = 8.5 Hz, Ph*H*-CH=CH-), 7.46 (d, 2H, J = 9.2 Hz, -CH=CH-*H*Ph), 7.18-6.92 (m, 2H, -*CH*=*CH*-), 6.90 (d, 2H, J = 8.5 Hz, Ph*H*-OCH$_2$), 3.98 (t, 2H, J = 6.7 Hz, -OC*H*$_2$-), 1.82-1.76 (m, 2H, -OCH$_2$C*H*$_2$-), 1.49-1.44 (m, 2H, -C*H*$_2$CH$_3$), 1.36-1.33 (m, 4H, -OCH$_2$CH$_2$C*H*$_2$C*H*$_2$-), 0.91 (t, 3H, J = 7.3 Hz, -CH$_2$C*H*$_3$).

4-(4-(dodecyloxy)styryl)benzonitrile (S3b)

The title compound was obtained by following; the same synthetic procedure as **S3a** except using **S1b** instead of **S1a** (84% yield). ^{1}H NMR ($CDCl_3$, 400 MHz) δ : 7.62 (d, 2H, J = 8.3 Hz, NC-*H*Ph), 7.55 (d, 2H, J = 8.3 Hz, Ph*H*-CH=CH-), 7.46 (d, 2H, J = 8.8 Hz, -CH=CH-*H*Ph), 7.19-6.92 (m, 2H, -*CH*=*CH*-), 6.91 (d, 2H, J = 8.8 Hz, Ph*H*-OCH$_2$), 3.98 (t, 2H, J = 6.3 Hz, -OC*H*$_2$-), 1.83-1.76 (m, 2H, -OCH$_2$C*H*$_2$-), 1.49–1.42 (m, 2H, -C*H*$_2$CH$_3$), 1.36-1.22 (m, 16H,

-OCH_2CH_2-(CH_2)$_8$), 0.88 (t, 3H, J = 6.3 Hz, -CH_2CH_3).

4-(4-(methoxy)styryl)benzonitrile (S3c)

To a solution of *p*-methoxybenzaldehyde (6.5 g, 48 mmol) and phosphonate **2** (12 g, 48 mmol) in 350 mL of dry THF was added dropwise *t*-BuOK (1.0 M in THF, 50 mL, 50 mmol) and the reaction mixture was stirred overnight at room temperature. After removal of THF by rotary evaporation, precipitated yellowish-white solid was filtrated and the product was extracted with chloroform. The organic layer was washed with H_2O, dried over $MgSO_4$, and concentrated by rotary evaporation to get the crude product. The pure product was afforded after recrystallization from chloroform several times (7.6 g, 67% yield). ^{1}H NMR ($CDCl_3$, 500 MHz) δ : 7.61 (d, 2H, J = 7.9 Hz, NC-*H*Ph), 7.55 (d, 2H, J = 8.5 Hz, Ph*H*-CH=CH-), 7.48 (d, 2H, J = 8.5 Hz, -CH=CH-*H*Ph), 7.18-6.94 (m, 2H, -*CH*=*CH*-), 6.92 (d, 2H, J = 8.5 Hz, Ph*H*-OCH_3), 3.84 (s, 3H, -OCH_3).

4-(4-(hexyloxy)styryl)benzadelhyde (S4a)

To a solution of nitrile **S3a** (8.5 g, 28 mmol) in 400 mL of dry diethyl ether was added dropwise diisobutylaluminum hydride (DIBAL-H 1.0 M solution in hexane, 42 mL, 42 mmol) at 0 ˚C. The solution was stirred at 0 ˚C for 1 hour and quenched by pouring 10% v/v aqueous solution of acetic acid into the reaction mixture. After the ether layer was removed by rotary evaporation, precipitated yellow solid was filtrated and washed with H_2O. To remove the remaining acetic acid, the yellow solid was dissolved in chloroform and the solution was washed with H_2O and a saturated aqueous solution of $NaHCO_3$. The organic layer was collected, dried over $MgSO_4$ and concentrated by rotary evaporation to get the crude product. The pure product was afforded by recrystallization from chloroform (8.3 g, 95% yield). ^{1}H NMR ($CDCl_3$, 500 MHz) δ : 9.98 (s, 1H, Ph-C*H*O), 7.85 (d, 2H, J = 7.9 Hz, OHC-*H*Ph), 7.62 (d, 2H, J = 8.5 Hz, Ph*H*-CH=CH-), 7.47 (d, 2H, J = 8.5 Hz, -CH=CH-*H*Ph), 7.23-6.98 (m, 2H, -C*H*=C*H*-), 6.91 (d, 2H, J = 8.5 Hz, Ph*H*-OCH_2), 3.98 (t, 2H, J = 6.7 Hz, -OCH_2-), 1.82-1.76 (m, 2H, -OCH_2CH_2-), 1.49-1.44 (m, 2H, -CH_2CH_3), 1.36-1.33 (m, 4H, -$OCH_2CH_2CH_2CH_2$-), 0.91 (t, 3H,

J = 7.3 Hz, -CH_2CH_3).

4-(4-(dodecyloxy)styryl)benzaldehyde (S4b)

The title compound was obtained by following; the same synthetic procedure as **S4a** except using **S3b** instead of **S3a**, and the crude product was purified by silica column chromatography eluting with chloroform (50% yield). ^{1}H NMR ($CDCl_3$, 400 MHz) δ : 9.98 (s, 1H, Ph-C*H*O), 7.86 (d, 2H, J = 7.8 Hz, OHC-*H*Ph), 7.63 (d, 2H, J = 8.3 Hz, Ph*H*-CH=CH-), 7.48 (d, 2H, J = 8.3 Hz, -CH=CH-*H*Ph), 7.24-6.99 (m, 2H, -C*H*=C*H*-), 6.91 (d, 2H, J = 8.3 Hz, Ph*H*-OCH_2), 3.99 (t, 2H, J = 6.3 Hz, -OCH_2-), 1.82-1.76 (m, 2H, -OCH_2CH_2-), 1.49-1.43 (m, 2H, -CH_2CH_3), 1.36-1.22 (m, 16H, -OCH_2CH_2-$(CH_2)_8$), 0.88 (t, 3H, J = 6.3 Hz, -CH_2CH_3).

4-(4-(methoxy)styryl)benzaldehyde (S4c)

The title compound was obtained by following; the same synthetic procedure as **S4a** except using **S3c** instead of **S3a**, and the crude product was purified by recrystallization from chloroform (80% yield). ^{1}H NMR ($CDCl_3$, 500 MHz) δ : 9.98 (s, 1H, Ph-C*H*O), 7.86 (d, 2H, J = 7.9 Hz, OHC-*H*Ph), 7.63 (d, 2H, J = 8.5 Hz, Ph*H*-CH=CH-), 7.50 (d, 2H, J = 8.5 Hz, -CH=CH-*H*Ph), 7.24-7.00 (m, 2H, -C*H*=C*H*-), 6.93 (d, 2H, J = 8.5 Hz, Ph*H*-OCH_2), 3.85 (s, 3H, -OCH_3).

17-tosyloxy-3n_{15}^{3}-pentaoxaheptadecan-1-ol (S5)

Silver oxide (12.2 g, 53 mmol) was added to a solution of hexaethyleneglycol (9.9 g, 35 mmol) in 100 mL of dry dichloromethane and the mixture was cooled to 0˚C. *p*-Toluenesulfoyl chloride (7.3 g, 39 mmol) and potassium iodide (1.2 g, 7 mmol) were added to the mixture and the reaction mixture was stirred overnight at room temperature. After filtration, the solvent was removed by rotary evaporation. The product was purified by silica column chromatography eluting with ethyl acetate to afford the pure product as pale yellow oil (8.2 g, 54% yield). ^{1}H NMR ($CDCl_3$, 500 MHz) δ : 7.80 (d, 2H, J = 7.9 Hz, -SO_2-*H*Ph), 7.34 (d, 2H, J = 7.9 Hz,

Ph*H*-CH_3), 4.16 (t, 2H, J = 4.9 Hz, TsOC*H*$_2$$CH_2$O-), 3.59 – 3.73 (m, 22H, TsO-CH_2C*H*$_2$O-(*CH*$_2$*CH*$_2$O)$_5$-) 2.45 (s, 3H, C*H*$_3$-Ph).

17-(4-methoxyphenoxy)-3n$_{15}$^{3}-pentaoxaheptadecan-1-ol (S6)

p-Methoxy phenol (2.8 g, 23 mmol), tosylate **S5** (8.2 g, 19 mmol), potassium carbonate (15.6 g, 113 mmol), and 18-Crown-6 (0.46 g, 1.9 mmol) were mixed in 300 mL acetonitrile and the reaction mixture was refluxed for 24 hours. After the reaction mixture was cooled down to room temperature, the residues were filtered and the filtrate was concentrated by rotary evaporation. To remove the remaining salt, the acquired oil was dissolved in chloroform and the solution was washed with water. The organic layer was collected, dried over $MgSO_4$ and concentrated by rotary evaporation. The crude product was subjected to a column chromatography eluting first with ethyl acetate to remove the first fraction, and then with ethyl acetate/methanol (9 : 1) to afford the pure product (6 g, 83% yield). ^{1}H NMR ($CDCl_3$, 500 MHz) δ : 6.81 – 6.87 (m, 4H, Ph-*H*), 4.08 (t, 2H, J = 4.9 Hz, Ph-OC*H*$_2$), 3.83 (t, 2H, J = 4.9 Hz, Ph-OCH_2C*H*$_2$O-), 3.76 (s, 3H, C*H*$_3$O-Ph), 3.59 – 3.73 (m, 20H, -CH_2CH_2O-(C*H*$_2$C*H*$_2$O)$_5$-H), 2.9 (t, 1H, J = 6.1 H, -OCH_2CH_2-*OH*).

17-(2,5-bis(bromomethyl)-4-methoxyphenoxy)-3n$_{15}$^{3}-pentaoxaheptadecyl acetate (S7)

S6 (9.8 g, 25 mmol), paraformaldehyde (7.6 g, 252 mmol), and sodium bromide (13 g, 126 mmol) were dissolved in 160 mL of acetic acid. Sulfuric acid (4.9 g, 50 mmol) diluted in 71 mL of acetic acid was added dropwise into the reaction mixture and the mixture was stirred at room temperature for 15 days. The product was extracted with chloroform, washed with water and then with a saturated aqueous solution of $NaHCO_3$. The organic layer was dried over $MgSO_4$ and concentrated by rotary evaporation. The crude product was subjected to a column chromatography eluting with ethyl acetate to afford the pure product (6.8 g, 44% yield). ^{1}H NMR ($CDCl_3$, 500 MHz) δ : 6.91 and 6.87 (s, 2H, Ph-*H*), 4.57 and 4.49 (s, 4H, BrC*H*$_2$-Ph-C*H*$_2$Br), 4.22 (t, 2H, J = 4.9 Hz, -CH_2C*H*$_2$O-$COCH_3$), 4.17 (t, 2H, J = 4.9 Hz, -Ph-OC*H*$_2$$CH_2$O-), 3.88 (t, 2H, J = 4.9 Hz, -Ph-OCH_2C*H*$_2$O-), 3.87 (s, 3H, C*H*$_3$O-Ph-), 3.65 –

3.75 (m, 18H, -CH_2CH_2O -(C*H*$_2$C*H*$_2$O)$_4$-C*H*$_2$$CH_2O$-$COCH_3$), 2.08 (s, 3H, -OCOC*H*$_3$).

17-(2,5-bis(diethylphosphonatemethyl)-4-methoxyphenoxy)-3n$_{15}^3$-pentaoxaheptadecyl acetate (S8)

Dimethyl bromide **S7** (1.1 g, 1.8 mmol) and triethylphosphite (1.8 g, 11 mmol) were placed in a 50 mL rounded bottom flask. A distillation apparatus was attached to collect poisonous ethyl bromide formed during the reaction. The reaction mixture was heated to 130 ˚C for 1.5 hour and then cooled down to room temperature. Remaining triethylphosphite was removed in vacuo by gradual heating from room temperature up to 130 ˚C for 4 hours. The product was used for the next step without further purification (1.3 g, ~100% yield). ^{1}H NMR ($CDCl_3$, 500 MHz) δ : 6.92 (s, 2H, Ph-*H*), 4.22 (t, 2H, J = 4.9 Hz, -CH_2C*H*$_2$O-$COCH_3$), 4.10 (t, 2H, J = 4.9 Hz, -Ph-OC*H*$_2$$CH_2O$-), 3.99 – 4.06 (m, 8H, (CH_3C*H*$_2$O)$_2$$POCH_2$-Ph-$CH_2PO$(OC*H*$_2$$CH_3$)$_2$), 3.82 (t, 2H, J = 4.9 Hz, -Ph-OCH_2*CH*$_2$O-), 3.80 (s, 3H, C*H*$_3$O-Ph), 3.65 – 3.71 (m, 18H, -CH_2CH_2O -(C*H*$_2$C*H*$_2$O)$_4$-C*H*$_2$$CH_2O$-$COCH_3$), 3.22 (t, 4H, J = 20.7 Hz, (CH_3CH_2O)$_2$POC*H*$_2$ -Ph-C*H*$_2$PO(OCH_2CH_3)$_2$), 2.08 (s, 3H, -OCOC*H*$_3$), 1.237 – 1.241 (t-t, 12H, J = 7.3 Hz, (C*H*$_3$$CH_2O$)$_2$$POCH_2$-Ph-$CH_2PO$($OCH_2$C*H*$_3$)$_2$).

OPV 4 (n = 1)

To a solution of Alkyloxy PV-2 **S4c** (2 g, 8.2 mmol) and diphosphonate **S8** (3 g, 4.1 mmol) in 300 mL of dry THF was added dropwise potassium t-BuOK (1.0 M in THF, 16.4 mL, 16.4 mmol), and the reaction mixture was stirred overnight at room temperature. After removal of THF by rotary evaporation, the product was extracted with chloroform, washed with H_2O, dried over $MgSO_4$, and concentrated by rotary evaporation. The crude product was purified by recrystallization from chloroform/methanol, reprecipitated from methanol and hexanes, and then by Soxlet extraction with methanol and chloroform, followed by column chromatography eluting first with chloroform, then chloroform/ethyl acetate (1:1), and finally chloroform/ethyl acetate/methanol (30:10:1) to afford the pure product (1 g, 28.5% yield). ^{1}H NMR ($CDCl_3$, 500 MHz) δ : 7.54-7.46 (m, 14H, Ph-*H*), 7.20-6.96 (m, 8H, -*CH*=*CH*- x 4), 6.91 (d, 4H, J = 8.5 Hz,

-CH_2O-*H*Ph, Ph*H*-OCH_2-), 4.25 (t, 2H, J = 4.9 Hz, -Ph-O*C*$H_2$$CH_2O$-), 3.96-3.93 (m, 5H, C$H_3$O-Ph-$OCH_2CH_2$O-), 3.84 (s, 6H, C$H_3$O-Ph-CH=CH-, -CH=CH-Ph-OCH_3), 3.80-3.57 (m, 20H, -OCH_2CH_2O -(CH_2CH_2O)$_5$H), 2.52 (s, 1H, -OH). Molecular weight (calc. for $C_{53}H_{60}O_{10}$, 857.04). MALDI-TOF MS m/z: (found $[M]^+$ 857.20, $[M+Na]^+$ 880.21). UV-vis ($CHCl_3$) λ_{max} (nm) : 424 nm

OPV 5 (n = 6)

To a solution of **S4a** (0.61 g, 2 mmol) and diphosphonate **S8** (0.66 g, 0.9 mmol) in 40 mL of dry THF was added dropwise potassium *t*-BuOK (1.0 M in THF, 3.6 mL, 3.6 mmol), and the reaction mixture was stirred overnight at room temperature. A methanol solution of NaOH was added to the reaction mixture and the mixture was stirred for one hour to hydrolyze the acetate group. After removal of THF by rotary evaporation, the product was extracted with chloroform, washed with H_2O, dried over $MgSO_4$, and concentrated by rotary evaporation. The crude product was purified by recrystallization from ethyl acetate several times and then by silica column chromatography eluting with chloroform several times to afford the pure product (50% yield). ^{1}H NMR ($CDCl_3$, 500 MHz) δ : 7.53-7.44 (m, 14H, Ph-*H*), 7.20-6.95 (m, 8H, -*CH*=*CH*- x 4), 6.89 (d, 4H, J = 8.5 Hz, -CH_2O-*H*Ph, Ph*H*-OCH_2-), 4.25 (t, 2H, J = 4.9 Hz, -Ph-O*C*$H_2$$CH_2O$-), 3.98 (t, 4H, J = 6.7 Hz, Ph-O*C*$H_2$$CH_2CH_2$-, - CH_2CH_2CH_2O-Ph), 3.96-3.93 (m, 5H, CH_3O-Ph-OCH_2CH_2O-), 3.80-3.56 (m, 20H, -OCH_2CH_2O -(CH_2CH_2O)$_5$H), 2.98 (s, 1H, -OH), 1.82-1.76 (m, 4H, Ph-OCH_2C$H_2$$CH_2$-, -$CH_2CH_2$$CH_2$O-Ph), 1.50-1.44 (m, 4H, -*C*$H_2$$CH_3$, CH_3*C*H_2-), 1.38-1.32 (m, 8H, -OCH_2CH_2CH_2CH_2-, -CH_2C$H_2$$CH_2CH_2O$-), 0.91 (t, 6H, J = 6.7 Hz, -CH_2CH_3, C$H_3$$CH_2$-). Molecular weight (calc. for $C_{63}H_{80}O_{10}$, 997.30). MALDI-TOF MS m/z: (found $[M]^+$ 996.22, $[M+Na]^+$ 1019.17, $[M+K]^+$ 1035.44). UV-vis ($CHCl_3$) λ_{max} (nm) : 425 nm

OPV 6 (n = 12)

OPV 6 was synthesized by following the same synthetic procedure as **OPV 5** except using **S4b** instead of **S4a**. The crude product was purified by recrystallization from ethyl acetate

several times and then by silica column chromatography eluting with chloroform several times to afford the pure product (50% yield). ^{1}H NMR ($CDCl_3$, 500 MHz) δ : 7.53-7.44 (m, 14H, Ph-*H*), 7.20-6.95 (m, 8H, -*CH*=*CH*- x 4), 6.89 (d, 4H, J = 8.5 Hz, -CH_2O-*H*Ph, Ph*H*-OCH_2-), 4.24 (t, 2H, J = 4.9 Hz, -Ph-O*C*$H_2$$CH_2$O-), 3.98 (t, 4H, J = 6.7 Hz, Ph-O*C*$H_2$$CH_2$$CH_2$-, -$CH_2$$CH_2$*C*$H_2$O-Ph), 3.95-3.93 (m, 5H, *C*H_3O-Ph-OCH_2*C*H_2O-), 3.80-3.56 (m, 20H, -$OCH_2$$CH_2$O -(*C*$H_2$*C*$H_2$O)$_5$H), 2.89 (s, 1H, -OH), 1.82-1.76 (m, 4H, Ph-OCH_2*C*$H_2$$CH_2$-, -$CH_2$*C*$H_2$$CH_2$O-Ph), 1.48-1.43 (m, 4H, -*C*$H_2$$CH_3$, CH_3*C*H_2-), 1.36-1.22 (m, 32H, -$OCH_2$$CH_2$(C*H*$_2$)$_8$-, -(C*H*$_2$)$_8$$CH_2$$CH_2$O-), 0.89 (t, 6H, J = 6.7 Hz, -CH_2*C*H_3, *C*$H_3$$CH_2$-). Molecular weight (calc. for $C_{75}H_{104}O_{10}$, 1165.62). MALDI-TOF MS m/z: (found $[M]^+$ 1164.25, $[M+Na]^+$ 1187.21, $[M+K]^+$ 1203.17). UV-vis ($CHCl_3$) λ_{max} (nm) : 424 nm

Phenyl-C_{61}-buryric acid (S9)

Acetic acid (250 mL) and HCl (100 mL) were added to a solution of phenyl-C61-buryric acid methyl ester (PCBM) (1.1 g, 1.2 mmol) in 250 mL of toluene, and the mixed solution was heated to reflux for 18 h. After the solution was evaporated, the crude product was treated with methanol, centrifuged to collect the suspension. This procedure was repeated with diethyl ether, toluene, and twice with diethyl ether, to afford the pure product (1.0 g, 93%). ^{1}H NMR (500 MHz, $CDCl_3$), δ (ppm): 7.86 (d, 2H, J = 7.3 Hz, *o*-H arom), 7.50 (m, 2H, *m*-H arom), 7.43 (m, 1H, *p*-H arom), 2.89 (m, 2H, PhC*CH*$_2$), 2.51 (t, 2H, J = 7.3 Hz, *CH*$_2$COOH), 2.16 (m, 2H, *CH*$_2$$CH_2$COOH). Molecular weight (calc. for $C_{71}H_{12}O_2$, 896.85). MALDI TOF-MS m / z: (found [M] 896.49).

Dyad 1

Thionyl chloride (4.9 g, 41 mmol) was added to a solution of **S9** (300 mg, 0.34 mmol) in 80 mL of freshly distilled CS_2, and the solution was heated to reflux for 17 h. After all the volatile components were removed in vacuo, sodium hydride (8 mg, 0.33 mmol) and chlorobenzene (50 mL) were added to the residue (**S10**). Then, separately prepared solution of **OPV 4** (150 mg, 0.18 mmol) dissolved in 100 mL of chlorobenzene was added to the reaction mixture. After the

reaction mixture was stirred at 60 ºC for 5 days, the solution was filtered and evaporated. The crude product was purified by silica column chromatography twice; first eluting with chloroform/ethyl acetate (1:1), then with chloroform/ethyl acetate(7:1). The obtained product was further purified by HPLC eluting with chloroform/ethyl acetate(9:1) to afford the pure product (81 mg, 26.3%). ^{1}H NMR ($CDCl_3$, 500 MHz) δ : 7.89 (d, 2H, J = 7.5 Hz, *o-H*PhC(C60)), 7.54 – 7.44 (m, 17H, Ph-H(OPV), *m-H*PhC(C60), *p-H*PhC(C60)), 7.19-6.96 (m, 8H, -*CH*=*CH*- x 4), 6.91 (d, 4H, J = 8.5 Hz, -CH_2O-*H*Ph, Ph*H*-OCH_2-), 4.24 (t, 2H, J = 5.0 Hz, -Ph-OC*H*$_2$$CH_2$O-), 4.21 (t, 2H, J = 4.8 Hz, -*CH*$_2$OCOCH2-), 3.94-3.93 (m, 5H, C*H*$_3$O-Ph-OCH_2C*H*$_2$O-), 3.84 (s, 6H, C*H*$_3$O-Ph-CH=CH-, -CH=CH-Ph-OC*H*$_3$), 3.79-3.61 (m, 18H, -(OC*H*$_2$C*H*$_2$O)$_4$C*H*$_2$$CH_2$OCO), 2.89 (m, 2H, PhC(C60)*CH*$_2$), 2.52 (t, 2H, J = 7.8 Hz, *CH*$_2$COO), 2.16 (m, 2H, *CH*$_2$$CH_2$COO). Molecular weight (calc. for $C_{124}H_{70}O_{11}$, 1735.88). MALDI TOF-MS m / z: (found $[M]^{2-}$ 1733.44).

Dyad 2 (n = 6)

Dyad 2 was synthesized by following the same synthetic procedure as **Dyad 1. OPV 5** was used instead of **OPV 4**, and for the esterification reaction the reaction was conducted at rt. The crude product was purified by silica column chromatography twice; first mounted with chloroform/ethyl acetate/hexanes (2:1:1) and eluting with ethyl acetate/hexanes (1:1), then with chloroform/ethyl acetate (5:1). The obtained product was further purified by HPLC eluting with chloroform/ethyl acetate (5:1) to afford the pure product (8%). ^{1}H NMR ($CDCl_3$, 500 MHz) δ : 7.89 (d, 2H, J = 7.5 Hz, *o-H*PhC(C60)), 7.53 – 7.44 (m, 17H, Ph-H(OPV), *m-H*PhC(C60), *p-H*PhC(C60)), 7.19-6.99 (m, 8H, -*CH*=*CH*- x 4), 6.89 (d, 4H, J = 8.5 Hz, -CH_2O-*H*Ph, Ph*H*-OCH_2-), 4.24 (t, 2H, J = 5.0 Hz, -Ph-OC*H*$_2$$CH_2$O-), 4.21 (t, 2H, J = 4.8 Hz, -*CH*$_2$OCOCH2-), 3.98 (t, 4H, J = 6.7 Hz, Ph-OC*H*$_2$$CH_2$$CH_2$-, -$CH_2$$CH_2$C*H*$_2$O-Ph), 3.96-3.92 (m, 5H, C*H*$_3$O-Ph-OCH_2C*H*$_2$O-), 3.79-3.61 (m, 18H, -(OC*H*$_2$C*H*$_2$O)$_4$C*H*$_2$$CH_2$OCO), 2.89 (m, 2H, PhC(C60)*CH*$_2$), 2.52 (t, 2H, J = 7.8 Hz, *CH*$_2$COO), 2.16 (m, 2H, *CH*$_2$$CH_2$COO), 1.82-1.76 (m, 4H, Ph-OCH_2C*H*$_2$$CH_2$-, -$CH_2$C*H*$_2$$CH_2$O-Ph), 1.50-1.44 (m, 4H, -*CH*$_2$$CH_3$, CH_3*CH*$_2$-), 1.38-1.32 (m, 8H, -$OCH_2$$CH_2$C*H*$_2$C*H*$_2$-, -C*H*$_2$C*H*$_2$$CH_2$$CH_2$O-), 0.91 (t, 6H, J = 6.7 Hz, -CH_2C*H*$_3$,

C*H*$_3$CH$_2$-). Molecular weight (calc. for $C_{134}H_{90}O_{11}$, 1876.14). MALDI TOF-MS m / z: (found $[M]^-$ 1875.44).

Dyad 3 (n = 12)

Dyad 3 was synthesized by following the same synthetic procedure as **Dyad 1. OPV 6** was used instead of **OPV 4**, and for the esterification reaction the reaction was conducted at rt. The crude product was purified by silica column chromatography, eluting with chloroform/ethyl acetate (15:1). The obtained product was further purified by HPLC eluting with chloroform/ethyl acetate (15:1) to afford the pure product (31%). ^{1}H NMR ($CDCl_3$, 500 MHz) δ : 7.89 (d, 2H, J = 7.5 Hz, *o-H*PhC(C60)), 7.53 – 7.43 (m, 17H, Ph-H(OPV), *m-H*PhC(C60), *p-H*PhC(C60)), 7.19-6.99 (m, 8H, -*CH*=*CH*- x 4), 6.89 (d, 4H, J = 8.5 Hz, -CH$_2$O-*H*Ph, Ph*H*-OCH$_2$-), 4.24 (t, 2H, J = 4.5 Hz, -Ph-OC*H*$_2$CH$_2$O-), 4.21 (t, 2H, J = 5.0 Hz, -*CH*$_2$OCOCH2-), 3.98 (t, 4H, J = 6.5 Hz, Ph-OC*H*$_2$CH$_2$CH$_2$-, - CH$_2$CH$_2$C*H*$_2$O-Ph), 3.95-3.92 (m, 5H, C*H*$_3$O-Ph-OCH$_2$C*H*$_2$O-), 3.79-3.61 (m, 18H, -(OC*H*$_2$C*H*$_2$O)$_4$C*H*$_2$CH$_2$OCO), 2.89 (m, 2H, PhC(C60)*CH*$_2$), 2.52 (t, 2H, J = 7.8 Hz, *CH*$_2$COO), 2.16 (m, 2H, *CH*$_2$CH$_2$COO), 1.82-1.76 (m, 4H, Ph-OCH$_2$C*H*$_2$CH$_2$-, -CH$_2$C*H*$_2$CH$_2$O-Ph), 1.48-1.43 (m, 4H, -*CH*$_2$CH$_3$, CH$_3$*CH*$_2$-), 1.36-1.22 (m, 32H, -OCH$_2$CH$_2$(C*H*$_2$)$_8$-, -(C*H*$_2$)$_8$CH$_2$CH$_2$O-), 0.89 (t, 6H, J = 6.7 Hz, -CH$_2$C*H*$_3$, C*H*$_3$CH$_2$-). Molecular weight (calc. for $C_{146}H_{114}O_{11}$, 2044.46). MALDI-TOF MS (found [M] 2043.81).

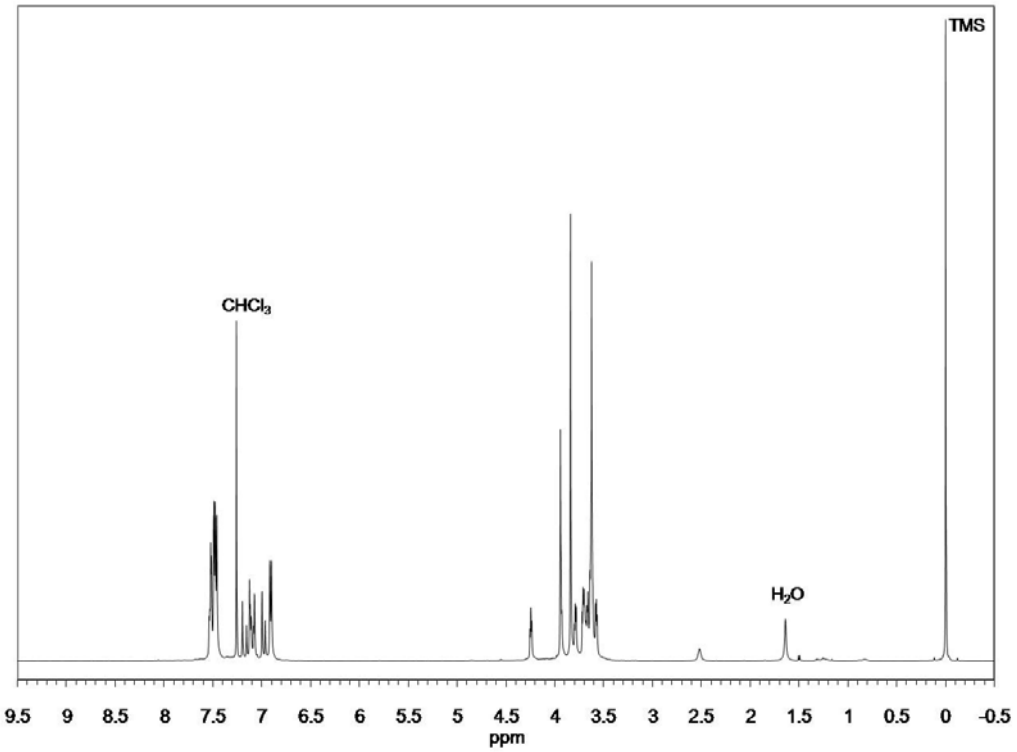

Figure S4.1. NMR chart of OPV **4** (n = 1).

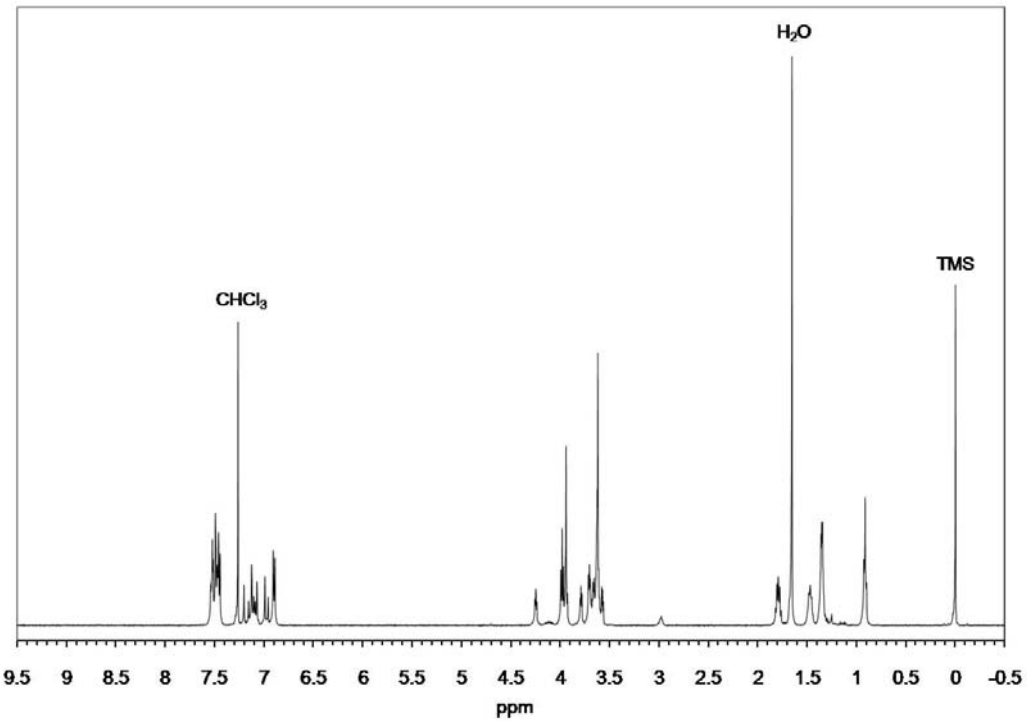

Figure S4.2. NMR chart of OPV **5** (n = 6).

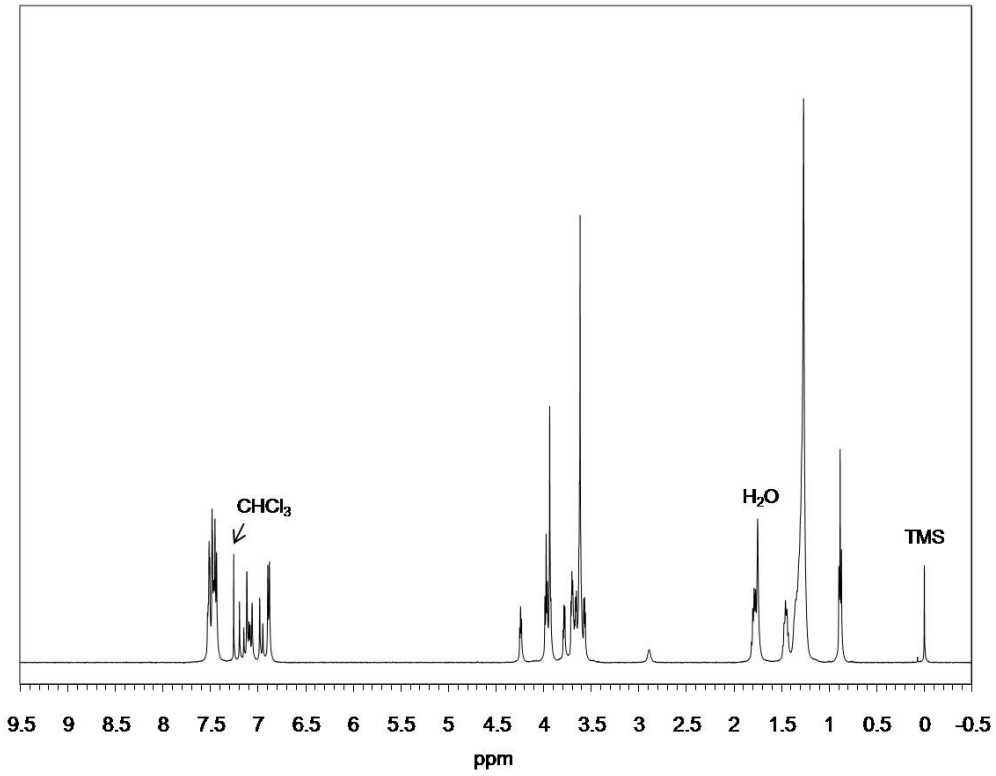

Figure S4.3. NMR chart of OPV **6** (n = 12).

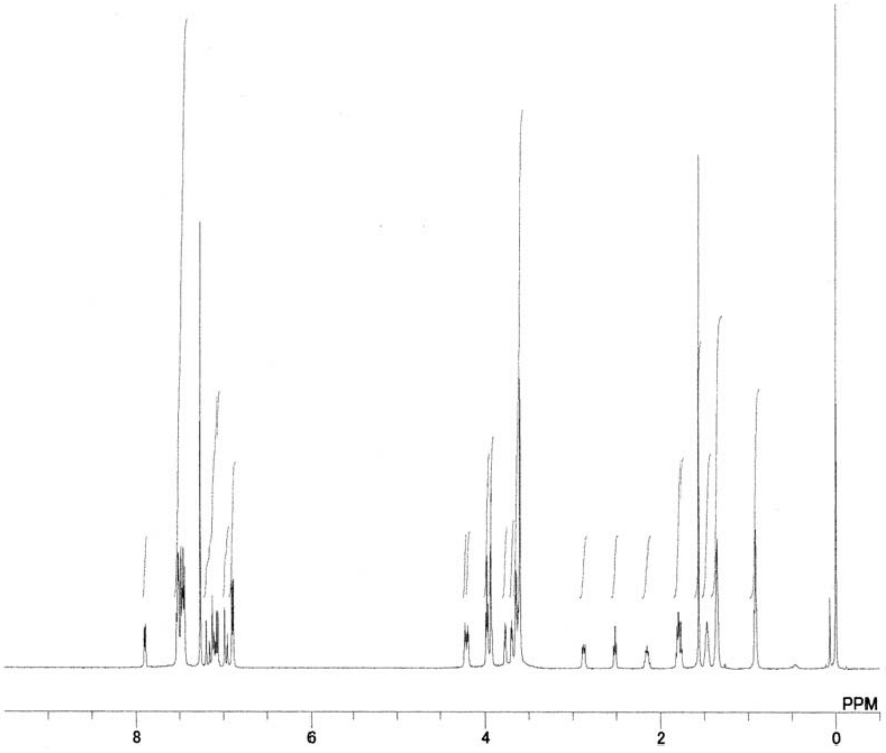

Figure S4.4. NMR chart of dyad **1** (n = 1).

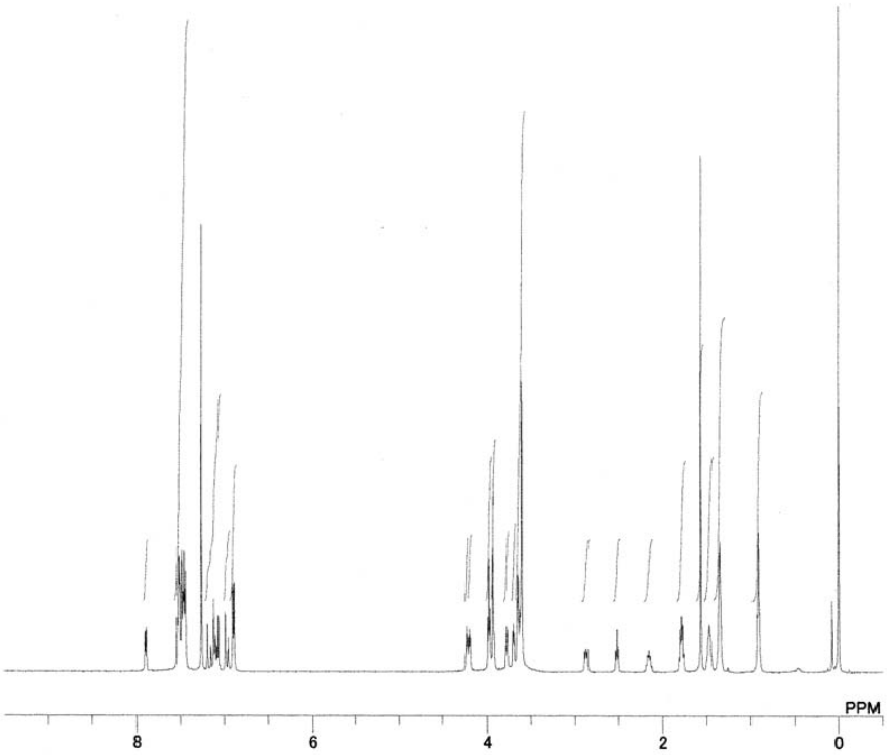

Figure S4.5. NMR chart of dyad **2** (n = 6).

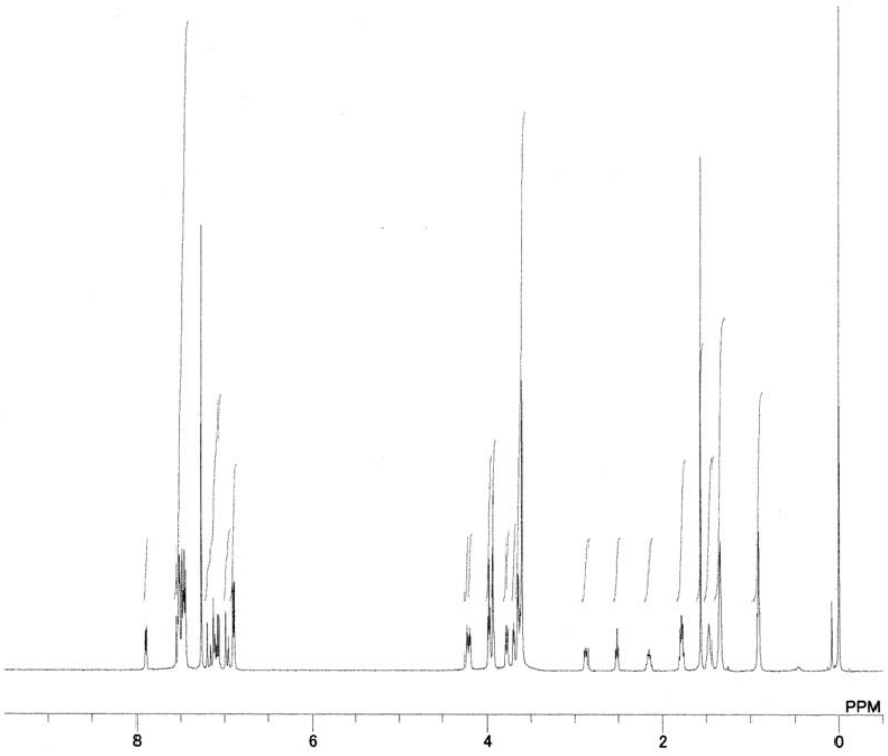

Figure S4.6. NMR chart of dyad **3** (n = 12).

Thermal behaviors

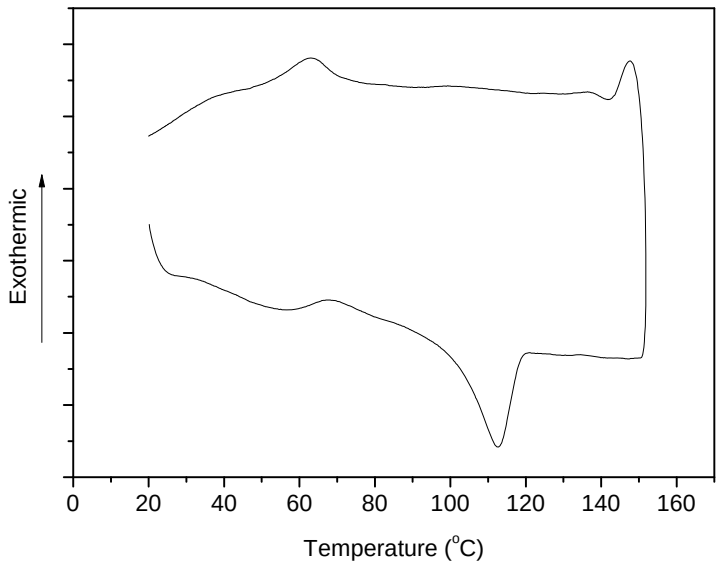

Figure S4.7. DSC trace of dyad **2**.

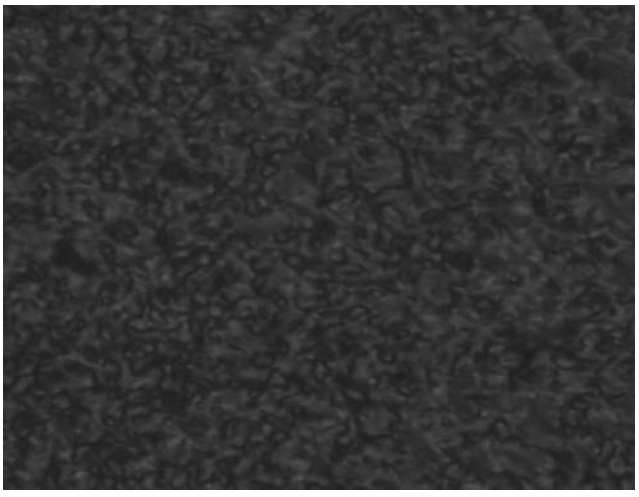

Figure S4.8. Polarized optical microscope image of LC state of dyad **2** under crossed nicols (90 ºC on cooling process).

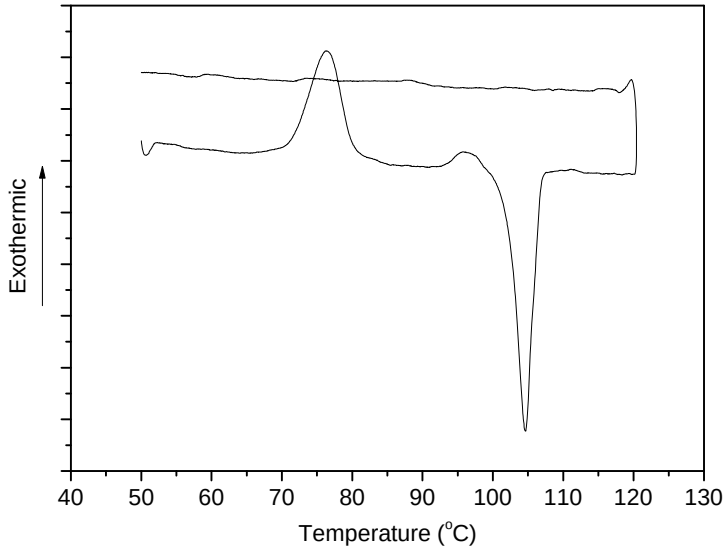

Figure S4.9. DSC trace of dyad **3**.

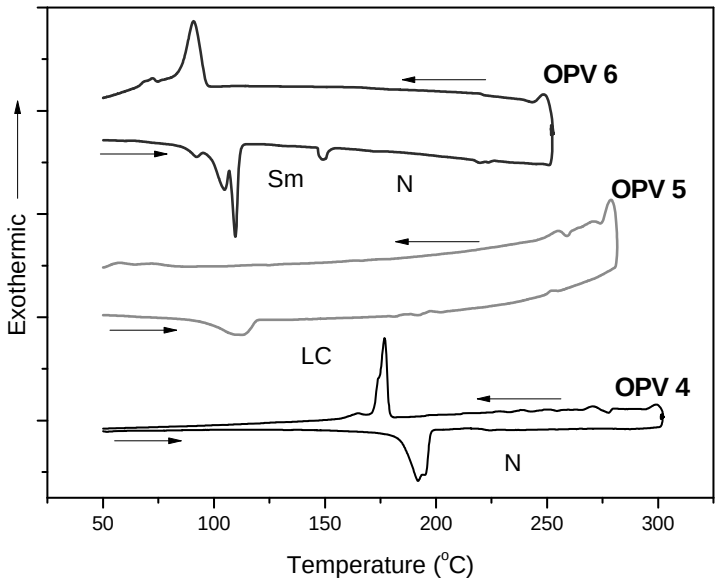

Figure S4.10. DSC traces of OPVs. Sm, N, and LC stand for Smectic, Nematic, and Liquid crystal phases, respectively.

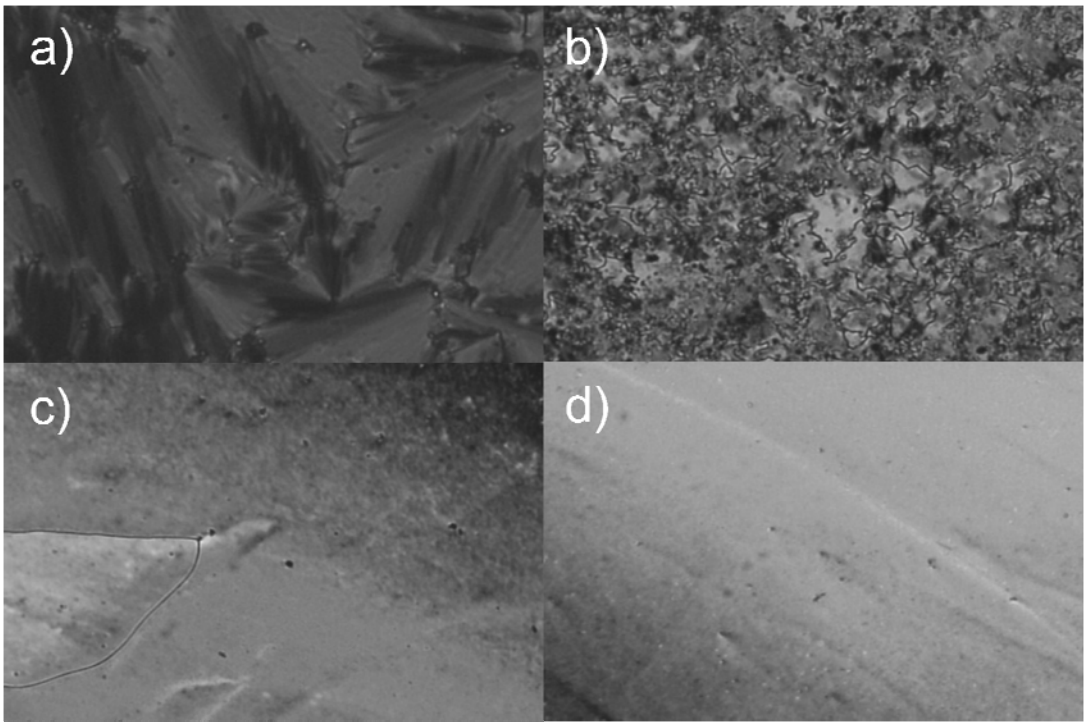

Figure S4.11. Polarized optical microscope images of a) Sm phase and b) N phase of OPV **6**, c) LC phase of OPV **5**, and d) N phase of OPV **4** under crossed nicols.

Absorption spectra of dyads in $CHCl_3$ solution (comparison).

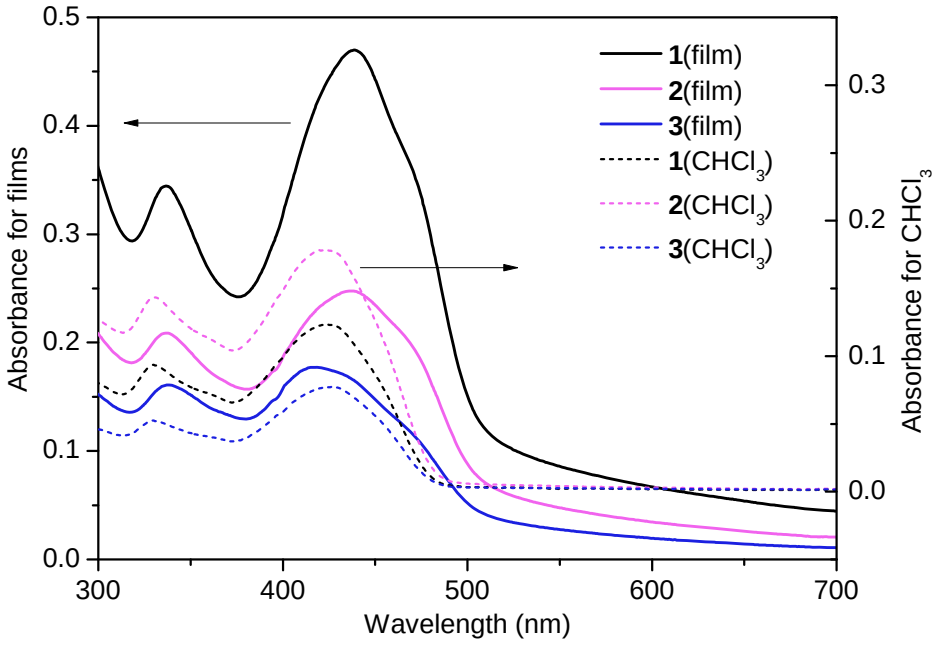

Figure S4.12. Absorption spectra of dyads in thin films (solid line) and $CHCl_3$ (dashed line).

References

1. S. Gunes, H. Neugebauer and N. S. Sariciftci, *Chem. Rev.*, 2007, **107**, 1324.
2. B. C. Thompson and J. M. J. Frechet, *Angew. Chem. Int. Ed.*, 2008, **47**, 58.
3. S. S. Kim, S. I. Na, J. Jo, G. Tae and D. Y. Kim, *Adv. Mater.*, 2007, **19**, 4410.
4. Y. Kim, S. Cook, S. M. Tuladhar, S. A. Choulis, J. Nelson, J. R. Durrant, D. D. C. Bradley, M. Giles, I. McCulloch, C. S. Ha and M. Ree, *Nat. Mater.*, 2006, **5**, 197.
5. G. Li, V. Shrotriya, J. S. Huang, Y. Yao, T. Moriarty, K. Emery and Y. Yang, *Nat. Mater.*, 2005, **4**, 864.
6. W. L. Ma, C. Y. Yang, X. Gong, K. Lee and A. J. Heeger, *Adv. Funct. Mater.*, 2005, **15**, 1617.
7. A. J. Moule and K. Meerholz, *Adv. Mater.*, 2008, **20**, 240.
8. M. Reyes-Reyes, K. Kim and D. L. Carroll, *Appl. Phys. Lett.*, 2005, **87**, 83506.
9. J. Y. Kim, S. H. Kim, H. H. Lee, K. Lee, W. L. Ma, X. Gong and A. J. Heeger, *Adv. Mater.*, 2006, **18**, 572.
10. A. Hayakawa, O. Yoshikawa, T. Fujieda, K. Uehara and S. Yoshikawaa, *Appl. Phys. Lett.*, 2007, **90**.
11. S. Berson, R. De Bettignies, S. Bailly and S. Guillerez, *Adv. Funct. Mater.*, 2007, **17**, 1377.
12. M. Reyes-Reyes, K. Kim, J. Dewald, R. Lopez-Sandoval, A. Avadhanula, S. Curran and D. L. Carroll, *Org. Lett.*, 2005, **7**, 5749.
13. S. E. Shaheen, C. J. Brabec, N. S. Sariciftci, F. Padinger, T. Fromherz and J. C. Hummelen, *Appl. Phys. Lett.*, 2001, **78**, 841.
14. F. L. Zhang, K. G. Jespersen, C. Bjorstrom, M. Svensson, M. R. Andersson, V. Sundstrom, K. Magnusson, E. Moons, A. Yartsev and O. Inganas, *Adv. Funct. Mater.*, 2006, **16**, 667.
15. V. D. Mihailetchi, H. X. Xie, B. de Boer, L. M. Popescu, J. C. Hummelen, P. W. M. Blom and L. J. A. Koster, *Appl. Phys. Lett.*, 2006, **89**.
16. R. C. Hiorns, R. de Bettignies, J. Leroy, S. Bailly, M. Firon, C. Sentein, A. Khoukh, H. Preud'homme and C. Dagron-Lartigau, *Adv. Funct. Mater.*, 2006, **16**, 2263.
17. A. Swinnen, I. Haeldermans, M. vande Ven, J. D'Haen, G. Vanhoyland, S. Aresu, M. D'Olieslaeger and J. Manca, *Adv. Funct. Mater.*, 2006, **16**, 760.
18. L. H. Nguyen, H. Hoppe, T. Erb, S. Gunes, G. Gobsch and N. S. Sariciftci, *Adv. Funct. Mater.*, 2007, **17**, 1071.
19. L. H. Slooff, J. M. Kroon, J. Loos, M. M. Koetse and J. Sweelssen, *Adv. Funct. Mater.*, 2005, **15**, 689.

20. X. N. Yang, J. K. J. van Duren, M. T. Rispens, J. C. Hummelen, R. A. J. Janssen, M. A. J. Michels and J. Loos, *Adv. Mater.*, 2004, **16**, 802.
21. K. M. Coakley, Y. X. Liu, M. D. McGehee, K. L. Frindell and G. D. Stucky, *Adv. Funct. Mater.*, 2003, **13**, 301.
22. K. Takanezawa, K. Hirota, Q. S. Wei, K. Tajima and K. Hashimoto, *J. Phys. Chem. C*, 2007, **111**, 7218.
23. K. Takanezawa, K. Tajima and K. Hashimoto, *Jpn. J. Appl. Phys.*, 2008, **47**, 8049.
24. Q. S. Wei, K. Hirota, K. Tajima and K. Hashimoto, *Chem. Mater.*, 2006, **18**, 5080.
25. D. C. Olson, J. Piris, R. T. Collins, S. E. Shaheen and D. S. Ginley, *Thin Solid Films*, 2006, **496**, 26.
26. G. K. Mor, K. Shankar, M. Paulose, O. K. Varghese and C. A. Grimes, *Appl. Phys. Lett.*, 2007, **91**.
27. D. M. Guldi, C. P. Luo, A. Swartz, R. Gomez, J. L. Segura, N. Martin, C. Brabec and N. S. Sariciftci, *J. Org. Chem.*, 2002, **67**, 1141.
28. S. M. Lindner, S. Huettner, A. Chiche, M. Thelakkat and G. Krausch, *Angew. Chem. Int. Ed.*, 2006, **45**, 3364.
29. M. Maggini, G. Possamai, E. Menna, G. Scorrano, N. Camaioni, G. Ridolfi, G. Casalbore-Miceli, L. Franco, M. Ruzzi and C. Corvaja, *Chem. Commun.*, 2002, 2028.
30. N. Negishi, K. Takimiya, T. Otsubo, Y. Harima and Y. Aso, *Chem. Lett.*, 2004, **33**, 654.
31. T. Nishizawa, K. Tajima and K. Hashimoto, *J. Mater. Chem.*, 2007, **17**, 2440.
32. Z. a. Tan, J. Hou, Y. He, E. Zhou, C. Yang and Y. Li, *Macromolecules*, 2007, **40**, 1868.
33. J. L. Segura, N. Martin and D. M. Guldi, *Chem. Soc. Rev.*, 2005, **34**, 31.
34. J. F. Nierengarten, *New J. Chem.*, 2004, **28**, 1177.
35. J. Roncali, *Chem. Soc. Rev.*, 2005, **34**, 483.
36. T. Nishizawa, K. Tajima and K. Hashimoto, *Nanotechnology*, 2008, **19**, 424017.
37. S. Morita, A. A. Zakhidov and K. Yoshino, *Solid State Commun.*, 1992, **82**, 249.
38. N. S. Sariciftci, L. Smilowitz, A. J. Heeger and F. Wudl, *Science*, 1992, **258**, 1474.
39. P. H. Wobkenberg, D. D. C. Bradley, D. Kronholm, J. C. Hummelen, D. M. de Leeuw, M. Colle and T. D. Anthopoulos, *Synth. Met.*, 2008, **158**, 468.
40. S. Yamakawa, K. Tajima and K. Hashimoto, *Org. Electron.*, doi:10.1016/j.orgel.2008.12.014.
41. A. Cravino and N. S. Sariciftci, *J. Mater. Chem.*, 2002, **12**, 1931.
42. F. A. Loiseau, K. K. Hii and A. M. Hill, *J. Org. Chem.*, 2004, **69**, 639.
43. J. F. Hulvat, M. Sofos, K. Tajima and S. I. Stupp, *J. Am. Chem. Soc.*, 2005, **127**, 366.

Chapter 5.

Effect of the Crystallinity on Morphology and Performance in Oligomer-Based Solar Cells

5.1. Introduction

Solution-processed organic solar cells have drawn much attention recently because of their applicability to flexible optoelectronic devices with low fabrication cost [1, 2]. Bulk heterojunction (BHJ) is a promising structure to fabricate the efficient devices since it can achieve the large interface and the interpenetrating network of the donor and acceptor, resulting in efficient charge separation and transport and thus high efficiency. The efficiencies of 4-5% have been achieved in bulk heterojunction devices with π-conjugated polymers and a fullerene derivative (PCBM) [3-18]. Besides polymers, π-conjugated oligomers have recently attracted attention as alternative donor materials with their advantages over polymeric counterparts [19-27]. For example, oligomers are easily purified and monodispersed to always secure the same characters such as crystallinity and solubility. Thus there is no batch to batch difference in the efficiency of solar cells, which polymeric counterparts often suffer since it is difficult to always obtain polymers with same characters (molecular weight, purity, etc) [28-30]. Moreover, oligomers also enable us to fine-tune their properties such as optical band gap, crystallinity, etc more easily by molecular designs compared to polymeric counterparts. In fact several authors have recently designed novel, functional oligomers for application to solar cells and demonstrated high efficiencies of over 1% [20-27]. In contrast to such advantages, the reported oligomer-based solar cells often suffer a low FF which limited the efficiency of the devices. The low fill factor of solution-processed oligomer-based solar cells is probably due to the insufficient percolation pathways of the carriers and resulting charge recombination. In the case of polymer:PCBM BHJ devices, it is reported that crystallinity of polymer are high significance to form the polymer network in the film and to achieve efficient carrier transport, resulting in a high FF [9, 31]. Therefore it is also

expected highly crystalline oligomers can also improve the FF of the oligomer:PCBM bulk heterojunction devices and worth investigating the effect of the crystallinity on the efficiency of the oligomer-based solar cells. However, there has been no such report up to now.

In this chapter, the effect of crystallinity of oligo(*p*-phenylenevinylene)s (OPVs) on the efficiency of the BHJ devices with PCBM is described. The chemical structures of the OPVs studied are shown in Figure 5.1. By changing the alkyl side chains, π-π interaction the molecules are tuned to realized a high crystallinity of the molecules. As a result, a high fill factor of 0.6 was achieved in the device with highly crystalline OPV. The surface morphology of the OPV:PCBM thin films were also investigated to clarify the effect of the crystallinity on the nanostructure in the blend films.

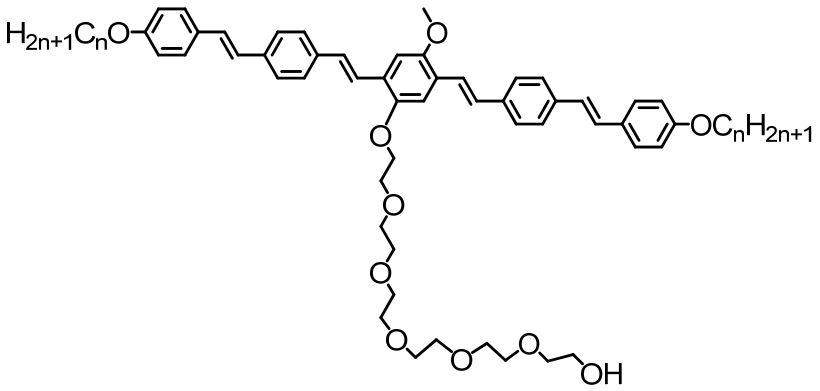

Figure 5.1. Molecular structures of oligo(*p*-phenylenevinylene)s, **1** (n = 1), **2** (n = 6), and **3** (n = 12).

5.2. Experimental

5.2.1. Synthesis and measurement instruments

OPV **1-3** were synthesized via a Horner-Emmons reaction and the detail of the syntheses was described in Chapter 4. A fullerene derivative PCBM was purchased from Frontier Carbon Corp., Japan, and used as received.

Cyclic voltammetry (CV) was measured on a HSV-100 (Hokuto Denko) electrochemical workstation. The experimental setup contains a Pt working electrode (BAS, Japan), a Pt wire counter electrode and a silver wire reference electrode. Anhydrous dichloromethane was used as an electrolyte containing 0.1 M Bu_4NPF_6 and approximately 5 mM OPVs. Powder X-ray diffraction (XRD) patterns were obtained on X-ray diffractometer RINT 2400 (Rigaku) with an X-ray source of Cu-Kα at 45 kV-200 mA. Absorption spectra were measured on a JASCO V-650 spectrophotometer. AFM images were obtained on a Digital Instrument Nanoscope31 operated in tapping mode.

5.2.2. Solar cell fabrication and measurement

Solar cell were fabricated and evaluated as follows; Indium tin oxide (ITO) coated glass substrates (sheet resistance: 10 Ω sq^{-1}, Geomatech, Japan) were cleaned by ultra-sonication in detergent, H_2O, acetone, and 2-propanol prior to spin-coating poly(3,4-ethylenedioxythiophene):poly(styrene sulfonic acid) (PEDOT:PSS) (Baytron P) at 4000 rpm for 30s to form a hole-transporting layer. After the films were dried at 140 ºC for 20 minutes, the organic layer was formed by spin-coating (3000 rpm, 5s). $CHCl_3$ was used as a solvent and the concentrations of the solutions were 7 mg mL^{-1} for OPV **1** and **2**, 6 mg mL^{-1} for **3** and all the solution contain equimolar ratio of PCBM and 0.4 mg mL^{-1} of poly(dimethyl siloxane-*b*-methyl methacrylate) (PDMS-*b*-PMMA) (M_n = 8000 for PDMS and M_n = 4000 for PMMA, M_w/M_n = 1.09, Polymer Source, Canada) which spontaneously forms the buffer layer at the organic/electrode interface [32]. To complete the device, Al cathode electrode (80 nm) was deposited on the organic layer under a high vacuum (3×10^{-4} Pa).

The devices were characterized under the irradiation of simulated solar light (AM 1.5, 100 mW cm^{-2}) calibrated its intensity with a standard silicon solar cell (BS520, Bunkoh-Keiki, Japan) and the active area of the devices was defined by the photo mask as 0.06 cm^2. External quantum efficiency (EQE) of the devices was measured on a Hypermonolight System SM-250F (Bunkoh-Keiki, Japan).

5.3. Results and Discussion

5.3.1. Cyclic voltammetry and XRD measurements

The highest occupied molecular orbital (HOMO) levels of the molecules were investigated by CV. The HOMO levels were calculated to be 5.06, 5.05, and 5.06 eV for **1**, **2**, and **3**, respectively, by assuming the half potential of ferrocenium/ferrocene at 4.8 eV relative to the vacuum level, which was used as an internal reference (see Appendix). This result indicated that the HOMO levels of the molecules are not changed with alkyl side chain lengths.

The crystallinity of the molecules in the bulk state was investigated by power XRD measurement and the results were already shown in Chapter 4 (Figure 4.2), indicating that the π-π interaction of the molecules enhanced by shortening the alkyl chain length.

5.3.2. Solar cells

Now it is expected that the crystalline OPVs form the crystalline network to achieve the efficient charge transport in the blended film with PCBM as reported in polymer:PCBM BHJ devices. To investigate this notion, the solar cells were fabricated with the configuration of ITO/PEDOT:PSS/**1**, **2**, or **3**/PDMS-*b*-PMMA/Al, and *I*-*V* characteristics under AM 1.5 irradiation are shown in Figure 5.2. As expected, FF of the devices improved as the alkyl chain length shortens. In the device with the shortest alkyl chain OPV **1**, the FF largely improved to 0.60, compared to FF of 0.47 in device with the longest alkyl chain OPV **3** while OPV **2** showed the a little improvement with FF of 0.48. I_{SC} in the OPV **1** device also improved to 1.38 mA cm^{-2} and thus leaded to the higher efficiency of 0.76% compared to those in the other two devices. Figure 5.3 shows the EQE spectra of the devices. The spectra showed broad photocurrent response, which nearly corresponded to the absorption spectra of the devices (Figure 5.4). Interestingly, OPV **1** device showed the EQE maximum around 350 nm. Considering that the absorption peak observed at 340 nm is attributed to the absorption of PCBM, this EQE maximum indicated that contribution of the PCBM absorption to the photocurrent increased in OPV **1** device, suggesting the enhanced dissociation of PCBM

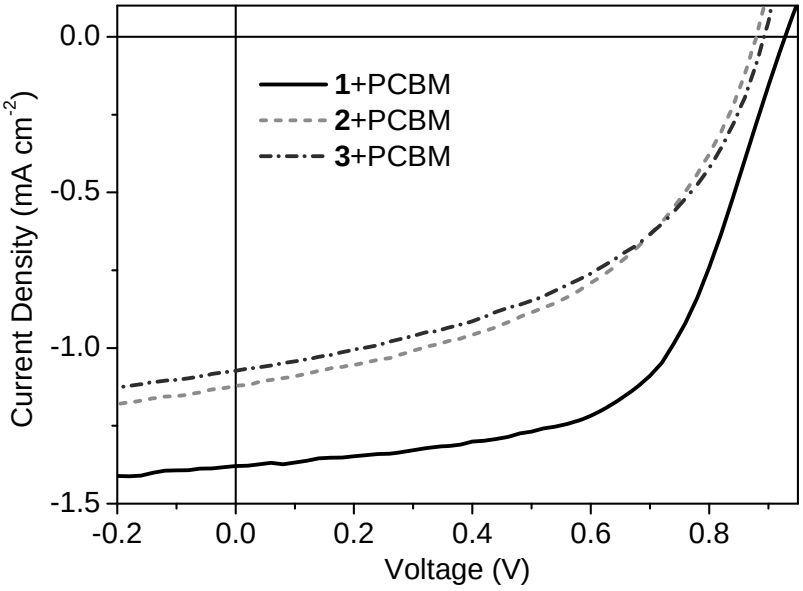

Figure 5.2. *I-V* characteristics of the BHJ devices of OPVs and PCBM under AM 1.5 irradiation.

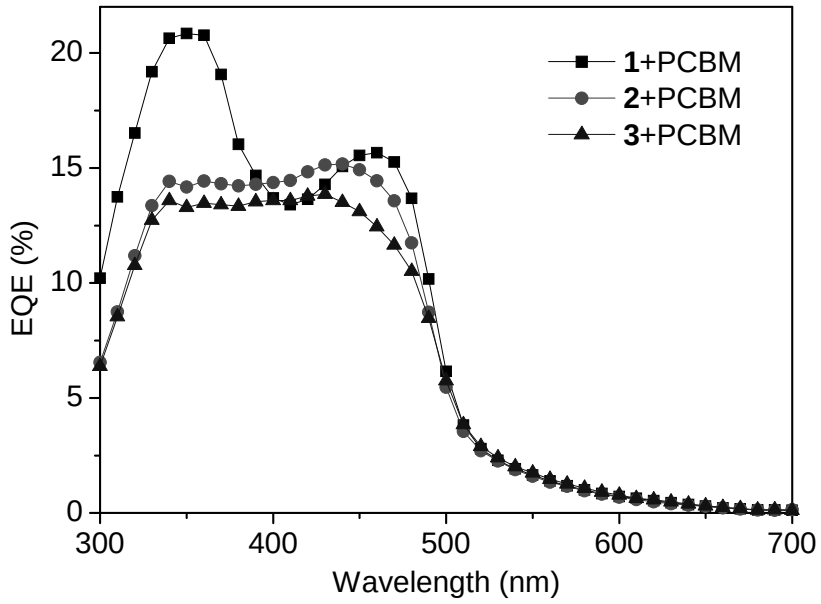

Figure 5.3. EQE spectra of the BHJ devices of OPVs and PCBM.

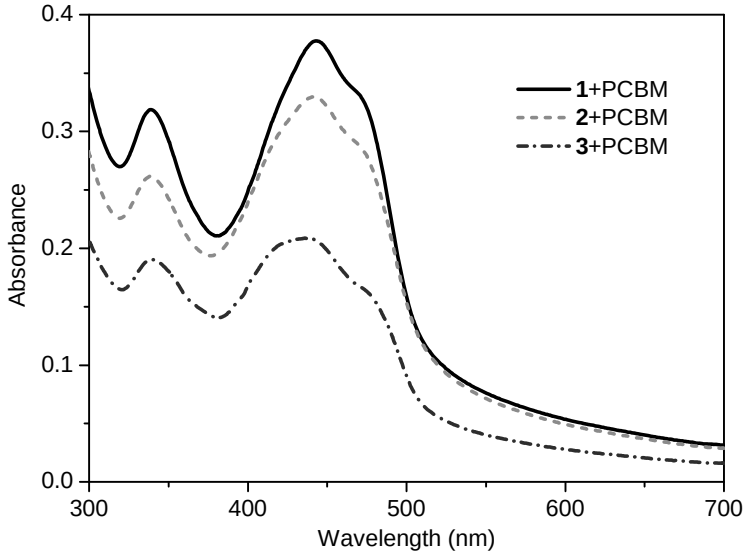

Figure 5.4. Absorption spectra of the BHJ devices of OPVs and PCBM.

excitons. These results above might suggest two things; OPV **1** formed the crystalline donor network in the film to achieve the efficient charge transport and thus a high FF. The crystalline network of OPV **1** prevented the PCBM aggregation to achieve the efficient PCBM exciton dissociation and thus the higher I_{SC}.

5.3.3. Surface morphology

To investigate the speculations above, the surface morphology of the bulk heterojunction films with OPVs and PCBM was investigated by AFM. Thin films were fabricated in the same manner as in the device except PDMS-b-PMMA buffer layer was not used. AFM height images (Figure 5.5) revealed that the films with OPV **2** and **3** showed the large sphere-like aggregated domains with the size of around 100 nm. These aggregated domains could be the aggregation of PCBM segregated from OPVs since similar shape of PCBM aggregation was observed in poly(p-phenylenevinylene):PCBM mixed films [33]. In sharp contrast, the film with OPV **1** did not show such large aggregation, indicating the prevention of PCBM aggregation in OPV **1** film. These differences in morphology could be explained by difference in crystallization manner of the molecules during the solvent evaporation in spin-coating process. The less soluble OPV **1** might crystallize first or at the same time with PCBM to form the OPV network and prevent the large aggregation of the PCBM. Oppositely, in the case of OPV **2** and **3** with better solubility, PCBM might crystallize first to form the aggregated domains in a large scale.

From all the results above, it was concluded that the large increase in FF in the OPV **1** device could be due to the formation of the better percolation of the carrier pathways, formed by the crystalline donor network, and the resulting prevention of the PCBM large aggregation could lead to efficient dissociation of PCBM excitons and thus the improved I_{SC} in the OPV **1** device.

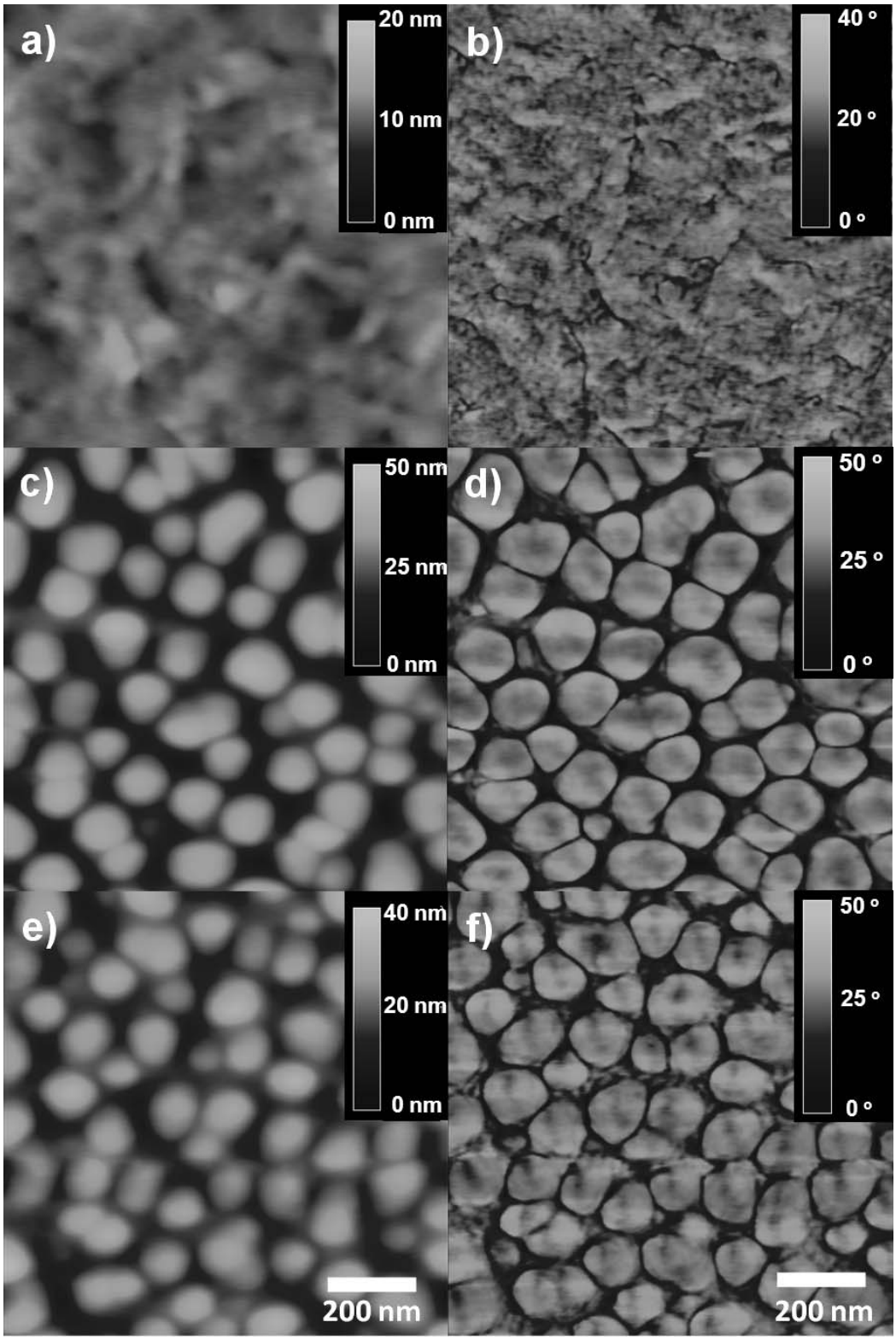

Figure 5.5. AFM height (a,c,e) and phase (b,d,f) images of the blend films of PCBM and OPV **1** (a,b), **2** (c,d), or **3** (e,f).

5.4. Conclusion

The effect of the crystallinity of the oligo(*p*-phenylenevinylene)s on the efficiency of the bulk heterojunction devices with PCBM were investigated to reveal that the crystalline OPV formed the network (percolated carrier pathways) and prevented the PCBM large aggregation, resulting in the efficient charge separation and transport. The results clearly demonstrated that the crystallinity of the donor materials is of high significance to form a proper nanostructure and thus to achieve a high efficiency in the oligomer:PCBM solar cells.

Appendix

Cyclic voltammetry

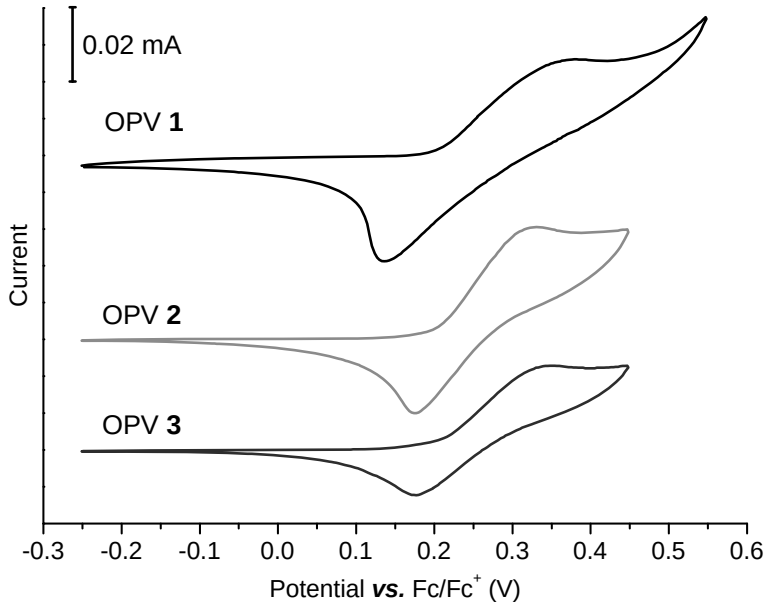

Figure S5.1. Molecular structures of oligo(*p*-phenylenevinylene)s, **1** (n = 1), **2** (n = 6), and **3** (n = 12).

References

1. S. Gunes, H. Neugebauer and N. S. Sariciftci, *Chem. Rev.*, 2007, **107**, 1324.
2. B. C. Thompson and J. M. J. Frechet, *Angew. Chem. Int. Ed.*, 2008, **47**, 58.
3. C. P. Chen, S. H. Chan, T. C. Chao, C. Ting and B. T. Ko, *J. Am. Chem. Soc.*, 2008, **130**, 12828.
4. A. Hayakawa, O. Yoshikawa, T. Fujieda, K. Uehara and S. Yoshikawaa, *Appl. Phys. Lett.*, 2007, **90**.
5. M. D. Irwin, B. Buchholz, A. W. Hains, R. P. H. Chang and T. J. Marks, *Proc. Natl. Acad. Sci. U.S.A.*, 2008, **105**, 2783.
6. J. Y. Kim, S. H. Kim, H. H. Lee, K. Lee, W. L. Ma, X. Gong and A. J. Heeger, *Adv. Mater.*, 2006, **18**, 572.
7. J. Y. Kim, K. Lee, N. E. Coates, D. Moses, T. Q. Nguyen, M. Dante and A. J. Heeger, *Science*, 2007, **317**, 222.
8. S. S. Kim, S. I. Na, J. Jo, G. Tae and D. Y. Kim, *Adv. Mater.*, 2007, **19**, 4410.
9. Y. Kim, S. Cook, S. M. Tuladhar, S. A. Choulis, J. Nelson, J. R. Durrant, D. D. C. Bradley, M. Giles, I. McCulloch, C. S. Ha and M. Ree, *Nat. Mater.*, 2006, **5**, 197.
10. J. K. Lee, W. L. Ma, C. J. Brabec, J. Yuen, J. S. Moon, J. Y. Kim, K. Lee, G. C. Bazan and A. J. Heeger, *J. Am. Chem. Soc.*, 2008, **130**, 3619.
11. G. Li, V. Shrotriya, J. S. Huang, Y. Yao, T. Moriarty, K. Emery and Y. Yang, *Nat. Mater.*, 2005, **4**, 864.
12. W. L. Ma, C. Y. Yang, X. Gong, K. Lee and A. J. Heeger, *Adv. Funct. Mater.*, 2005, **15**, 1617.
13. A. J. Moule and K. Meerholz, *Adv. Mater.*, 2008, **20**, 240.
14. J. Peet, J. Y. Kim, N. E. Coates, W. L. Ma, D. Moses, A. J. Heeger and G. C. Bazan, *Nat. Mater.*, 2007, **6**, 497.
15. M. Reyes-Reyes, K. Kim and D. L. Carroll, *Appl. Phys. Lett.*, 2005, **87**, 83506.
16. M. M. Wienk, M. Turbiez, J. Gilot and R. A. J. Janssen, *Adv. Mater.*, 2008, **20**, 2556.
17. H. Xin, F. S. Kim and S. A. Jenekhe, *J. Am. Chem. Soc.*, 2008, **130**, 5424.
18. H. L. Yip, S. K. Hau, N. S. Baek, H. Ma and A. K. Y. Jen, *Adv. Mater.*, 2008, **20**, 2376.
19. M. T. Lloyd, J. E. Anthony and G. G. Malliaras, *Mater. Today*, 2007, **10**, 34.
20. C. He, Q. G. He, Y. P. Yi, G. L. Wu, F. L. Bai, Z. G. Shuai and Y. F. Li, *J. Mater. Chem.*, 2008, **18**, 4085.
21. N. M. Kronenberg, M. Deppisch, F. Wurthner, H. W. A. Lademann, K. Deing and K. Meerholz, *Chem. Commun.*, 2008, 10.1039/b813341g.
22. F. Lincker, N. Delbosc, S. Bailly, R. De Bettignies, M. Billon, A. Pron and R.

Demadrille, *Adv. Funct. Mater.*, 2008, **18**, 3444.
23. M. T. Lloyd, A. C. Mayer, S. Subramanian, D. A. Mourey, D. J. Herman, A. V. Bapat, J. E. Anthony and G. G. Malliaras, *J. Am. Chem. Soc.*, 2007, **129**, 9144.
24. S. Roquet, A. Cravino, P. Leriche, O. Aleveque, P. Frere and J. Roncali, *J. Am. Chem. Soc.*, 2006, **128**, 3459.
25. F. Silvestri, M. D. Irwin, L. Beverina, A. Facchetti, G. A. Pagani and T. J. Marks, *J. Am. Chem. Soc.*, 2008, **130**, 17640.
26. A. B. Tamayo, B. Walker and T. Q. Nguyen, *J. Phys. Chem. C*, 2008, **112**, 11545.
27. L. Valentini, D. Bagnis, A. Marrocchi, M. Seri, A. Taticchi and J. M. Kenny, *Chem. Mater.*, 2008, **20**, 32.
28. A. M. Ballantyne, L. Chen, J. Dane, T. Hammant, F. M. Braun, M. Heeney, W. Duffy, I. McCulloch, D. D. C. Bradley and J. Nelson, *Adv. Funct. Mater.*, 2008, **18**, 2373.
29. R. C. Hiorns, R. de Bettignies, J. Leroy, S. Bailly, M. Firon, C. Sentein, A. Khoukh, H. Preud'homme and C. Dagron-Lartigau, *Adv. Funct. Mater.*, 2006, **16**, 2263.
30. W. Ma, J. Y. Kim, K. Lee and A. J. Heeger, *Macromol. Rapid Commun.*, 2007, **28**, 1776.
31. K. Tajima, Y. Suzuki and K. Hashimoto, *J. Phys. Chem. C*, 2008, **112**, 8507.
32. S. Yamakawa, K. Tajima and K. Hashimoto, *Org. Electron.*, doi:10.1016/j.orgel.2008.12.014.
33. H. Hoppe and N. S. Sariciftci, *J. Mater. Chem.*, 2006, **16**, 45.

Chapter 6.

Highly Uniaxial Orientation in Oligo(*p*-phenylenevinylene) Films Induced During Wet Coating Process

6.1. Introduction

The molecular orientation of π-conjugated polymers and oligomers in thin solid films is of great importance for achieving high performance in organic electronic devices such as field effect transistors [1, 2], light emitting diodes [3-5], and photovoltaic devices [6-8], given that the molecular shapes and the electronic properties of the organic materials are highly anisotropic. Various techniques have been used to align molecules in films including rubbing [9, 10], zone-casting [11], friction transfer [12], solution shearing [13, 14], and irradiation with polarized light [15, 16]. Among them, a rubbing method is one of the most widely used techniques for achieving uniaxial alignment of crystalline or liquid crystalline molecules. In this method, polymer thin films such as polyimides are mechanically rubbed and used as alignment layers. The molecules in contact with the alignment layers interact with the surface to orient their easy axes along the rubbing direction, and the alignment is transferred throughout the films. In conventional rubbing method, however, the driving force to transfer the alignment induced at the interface is self-organization of thermotropic liquid crystals [17] or the van der Waals interactions of the crystalline molecules during vacuum evaporations [18-20]. Thus, induction of the liquid crystal phase transition by thermal annealing or compatibility with a dry deposition technique is a prerequisite for this alignment method, which could limit molecular designs and device applications. If weak intermolecular interactions in solution such as π-π or polar/nonpolar interactions can be utilized in dynamic situations such as a spin-coating process to transfer the molecular orientation induced at the interface, it would be a useful approach for controlling the

alignment of molecules in thin solid films. Moreover, such spontaneous alignment of molecules without any special treatment such as induction of thermotropic liquid crystal phases would be easily applicable to the organic optoelectronic devices.

In this chapter, the highly uniaxial alignment of amphiphilic oligo(*p*-phenylenevinylene)s (OPVs) in the as-cast films spin-coated from solution onto rubbed polymer alignment layers such as poly(3,4-ethylenedioxythiophene):poly(styrene sulfonic acid) (PEDOT:PSS) film is described. The chemical structures of the OPVs are shown in Figure 6.1. By changing the alkyl side chain lengths, the π-π interactions between the oligo(*p*-phenylenevinylene) groups and the polar/nonpolar interaction of the molecules are tuned to realize the alignment of the molecules during the spin-coating process. The anisotropic structures of the OPVs in the thin films were investigated by measuring polarized absorption spectra and in-plane X-ray diffractions (XRD). Application to an electronic device was also demonstrated.

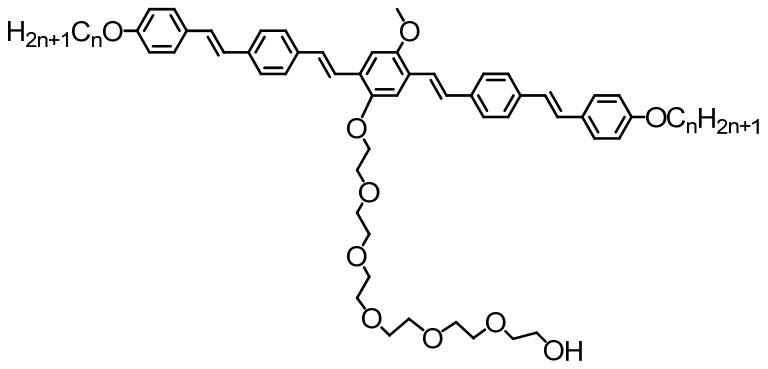

Figure 6.1. Molecular structures of oligo(*p*-phenylenevinylene)s, **1** (n = 6), **2** (n = 12), and **3** (n = 1).

6.2. Experimental

6.2.1. Synthesis and thin film preparation

OPV **1-3** were synthesized via a Horner-Emmons reaction and the detail of the syntheses was described in Chapter 4.

The thin films of OPVs were prepared as follows. Glass substrates were cleaned by an ultrasonic cleaner in detergent, distilled water, acetone and 2-propanol. The substrates were dried in a vacuum oven at 90 ºC for 30 min. PEDOT:PSS (Baytron P), filtered with 0.45 μm PVDF filters, was spin-coated onto the cleaned glass substrate at a spin rate of 3000 rpm for 30 s and the substrates were dried in an oven at 140 ºC in air for 20 min. After the film was cooled to room temperature, the PEDOT:PSS layer was manually rubbed 30 times in one direction with a micro fabric made from a polyester (TORAY TORAYSEE) for use as the alignment layer [21]. Finally, the oligo(*p*-phenylenevinylene) layer was spin-coated onto the rubbed PEDOT:PSS film from a chloroform solution of **1** (12 mg mL^{-1}), **2** (14 mg mL^{-1}) or **3** (4.25 mg mL^{-1}) at 2000 rpm for 5 s. Note that the films were completely dried after the spin-coating and no thermal treatment was conducted on the OPV films unless otherwise stated.

6.2.2. Measurement Instruments

The film thicknesses were measured by a profilometer (Dektak 6M, ULVAC). The polarized absorption spectra were measured on a JASCO V-650 spectrophotometer with a linear polarizer (Sigma Koki, USP-30C-38). The in-plane X-ray diffraction (XRD) patterns of the thin films were measured on a SmartLab 9kW (Rigaku) with an X-ray source of Cu-Kα at 45 kV-200 mA and an X-ray incident angle of 0.2º.

6.2.3. Photovoltaic device fabrication and evaluation

The photovoltaic devices were fabricated as follows. Indium tin oxide (ITO) coated glass substrates (sheet resistance: 10 Ω sq^{-1}, Kuramoto Japan) were cleaned by an ultrasonic cleaner

in detergent, distilled water, acetone and 2-propanol. The substrates were dried by air-blowing, and PEDOT:PSS was spin-coated (3000 rpm, 30 s) on the ITO substrates. The PEDOT:PSS layer was dried on a hotplate in air at 140 ºC for 20 min, and then rubbed in the same manner as the film preparation for absorption spectra. Note that the PEDOT:PSS layer is used as both alignment and hole-transporting layer in this case. The oligo(*p*-phenylenevinylene) layer was spin-coated onto the rubbed PEDOT:PSS film from a chloroform solution of **1** (1 mg mL^{-1}) at 2000 rpm for 5 s. The thin films were then transferred to the vacuum chamber to deposit the fullerene (1 nm) (nanom purple SUH, purity: > 99.9%, Frontier Carbon Corp., Japan) and bathocuproine (BCP) (10 nm) (sublimed, Dojindo Laboratories, Japan) layers under a high vacuum (5×10^{-5} Pa), which are used as electron-accepting and electron-blocking layers, respectively. Finally, the aluminum electrode was deposited to complete the devices.

Photosensitivity of the devices was measured on a Hypermonolight System SM-250F (Bunkoh-Keiki, Japan) using a linear polarizer (Sigma Koki, USP-30C-38). The light intensity was calibrated with a standard silicon solar cell (S1337-1010BQ, Bunkoh-Keiki, Japan). The active area of the devices was defined by the photo mask as 0.06 cm^2.

6.3. Results and Discussion

6.3.1. Polarized absorption spectra of thin film of OPV 1

The film thicknesses of the prepared samples as measured by a profilometer were approximately 96, 75, and 60 nm for **1**, **2**, and **3**, respectively. Figure 6.2 shows the absorption spectra of the as-cast film of **1** on a rubbed PEDOT:PSS film with the incident light linearly polarized parallel or perpendicular to the rubbing direction. Strong absorption was observed when the light was parallel while much weaker absorption was observed when it was perpendicular, resulting in a high dichroic ratio ($A_{//}$ / $A_{\perp}$) of 41.0 at the maximum absorption of 414 nm. The order parameter defined by $S = (A_{//} - A_{\perp}) / (A_{//} + 2A_{\perp})$ was calculated as 0.93, which is among the highest values reported for uniaxially aligned films with conventional conjugated liquid crystalline molecules [22-25]. It was confirmed that there was no anisotropic absorption without the rubbing procedure on the PEDOT:PSS films. These results indicate that **1** is highly uniaxially aligned with the long axis of the molecule parallel to the rubbing direction. Considering the fact that the sample is simply an as-cast film spin-coated from a dilute solution, this highly anisotropic absorption or alignment of the molecules throughout the film with the thickness of approximately 100 nm is quite surprising.

6.3.2. In-plane XRD measurement

To further investigate the uniaxial alignment of the molecules, in-plane XRD measurement of the film was conducted. Figure 6.3 shows the XRD patterns of the as-cast film of **1** with the incident X-ray beam parallel or perpendicular to the rubbing direction. When the incident X-ray beam was parallel, two peaks were observed at 2θ of 19.8° and 23.4° (*d*-spacings of 4.5 and 3.8 Å, respectively), which could be assigned to the π-π stacking of the oligo(phenylenevinylene) groups. The in-plane XRD pattern of the thermally annealed film at 150 °C showed only a single peak at 23.1° (Figure 6.4), suggesting that the peak at 19.8° is derived from the metastable packing of the molecules formed during spin-coating. In contrast, when the incident X-ray beam was perpendicular to the rubbing direction, no diffraction peak was observed in this

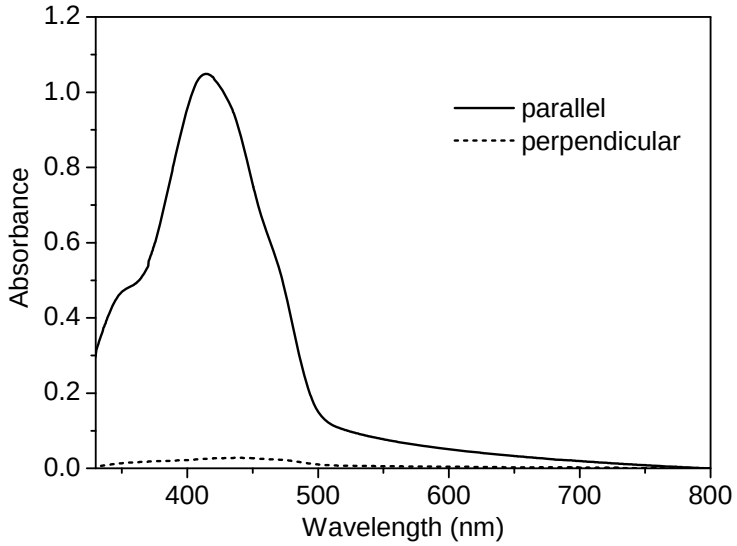

Figure 6.2. Absorption spectra of the as-cast film of **1** (n = 6) on a rubbed PEDOT:PSS layer with polarized incident light parallel (solid line) or perpendicular (dashed line) to the rubbing direction.

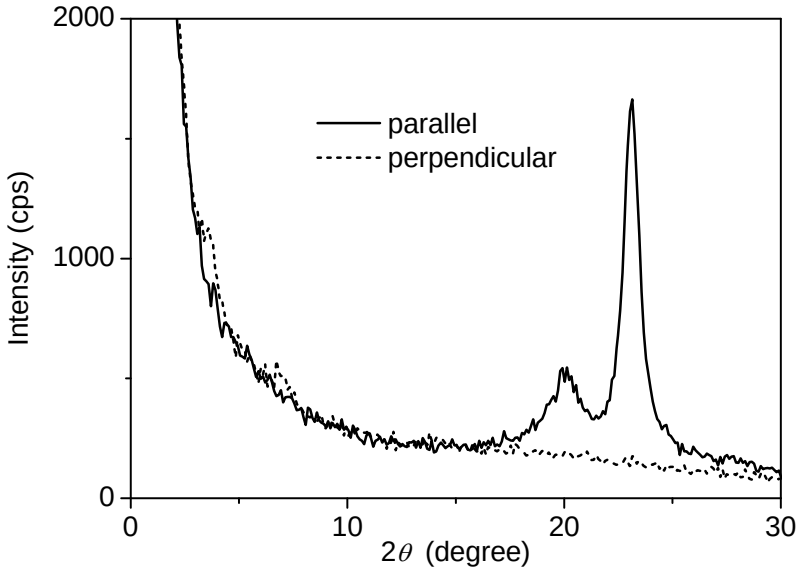

Figure 6.3. In-plane XRD patterns of the as-cast film of **1** (n = 6) on a rubbed PEDOT:PSS layer with incident X-ray beam parallel (solid line) or perpendicular (dashed line) to the rubbing direction.

region. These results indicate that the long axis of the molecules is uniaxially aligned parallel to the rubbing direction, which coincides with the results observed in the polarized absorption spectra. The presence of the diffraction peak from the π-π stacking distance in the in-plane measurement also indicates that the orientation of the conjugated plane of **1** is not parallel to the substrate (face-on) but is perpendicular to the substrate (edge-on) or tilted.

The dispersion of the alignment axes was also evaluated by rotating the substrate horizontally and monitoring the diffraction intensities at 23.4°. The rotation angle was set as 0° when the incident light was perpendicular to the rubbing direction. As shown in Figure 6.5, two diffraction peaks were observed at approximately 90° and 270°. The half-width-half-maximum value of the peak was estimated to be around 7°, which indicates a narrow distribution of the alignment axis in the film.

6.3.3. Other OPVs

The mechanism of the high molecular alignment during the spin-coating is not clear at this point. When the concentration of OPV increases in the solution during the solvent evaporation in the coating process, OPVs might start to crystallize from the surface and the orientation could be transferred to the whole organic film as the film is dried. It can be expected that the interfacial interactions between OPV in solution and the alignment layer first induce the orientation and that the intermolecular interactions between OPV molecules then induce the alignment throughout the film. Thus, these two interactions during the spin-coating process are of high importance for achieving such high alignment of the molecules in the films.

To investigate this notion, OPVs with different alkyl chain lengths (n = 12 for **2** and n = 1 for **3**) were compared. The thin films of the two also showed anisotropic absorptions with dichroic ratios of 18.8 (S = 0.86) at 415 nm for **2** and 3.76 (S = 0.48) at 442 nm for **3** (Figure 6.6 and 6.7). These values are lower than those of **1**, indicating that the molecular alignment is less ordered in the films of **2** and **3**. This might be attributed to differences in the crystallization behavior in solution during the spin-coating process. The longer alkyl chains of OPV **2** could provide better

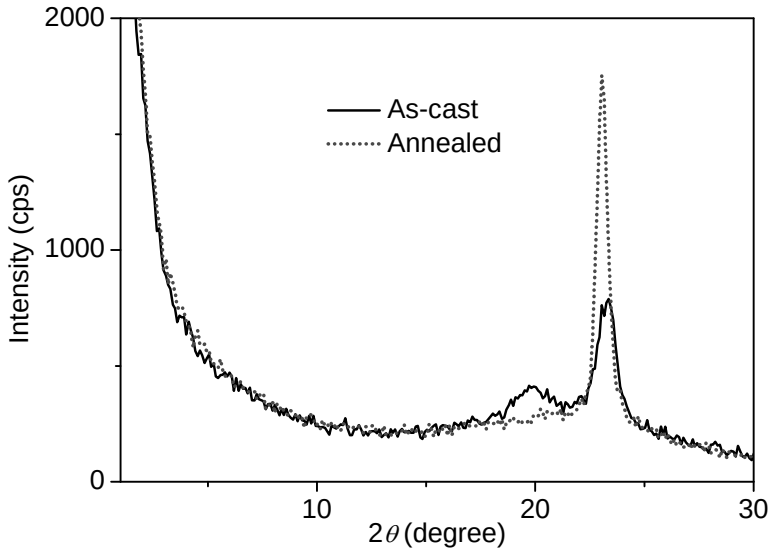

Figure 6.4. In-plane XRD patterns of the as-cast and annealed (150 ºC) films of **1** (n = 6) on a rubbed PEDOT:PSS layer with incident X-ray beam parallel to the rubbing direction.

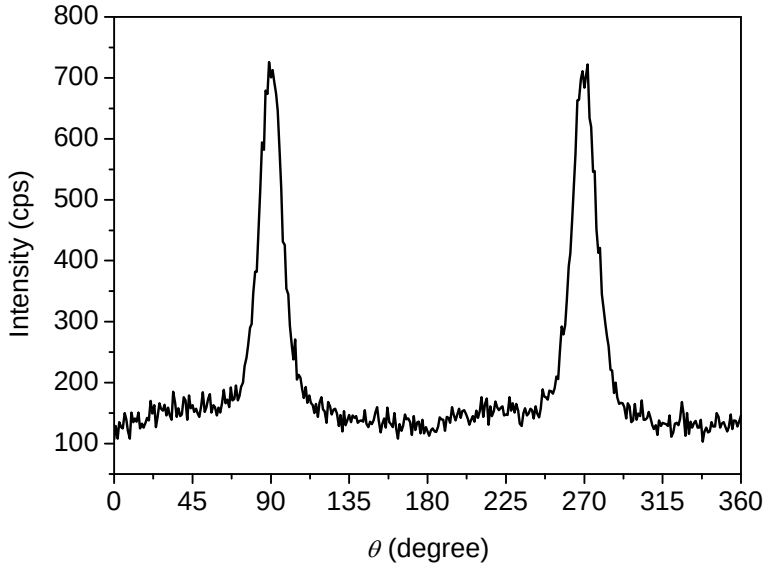

Figure 6.5. In-plane XRD intensity scan of the as-cast film of **1** (n = 6) on a rubbed PEDOT:PSS layer. The detector position is fixed at 2θ of 23.36º while the substrate is rotated horizontally.

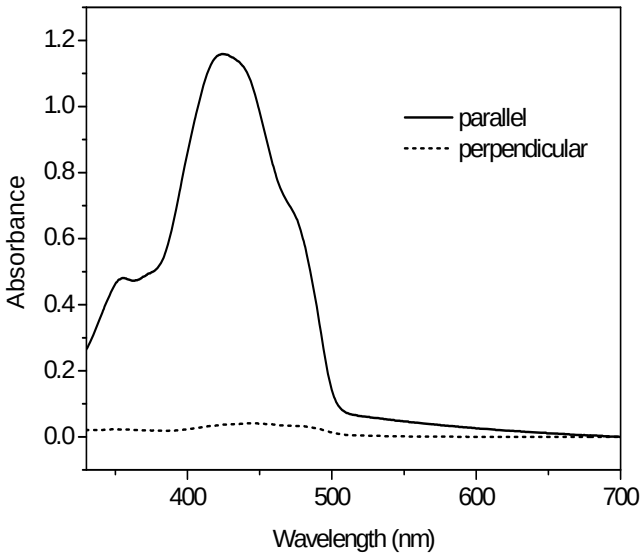

Figure 6.6. Absorption spectra of the as-cast film of **2** (n = 12) on rubbed PEDOT:PSS layer with polarized incident light parallel (solid line) or perpendicular (dashed line) to the rubbing direction.

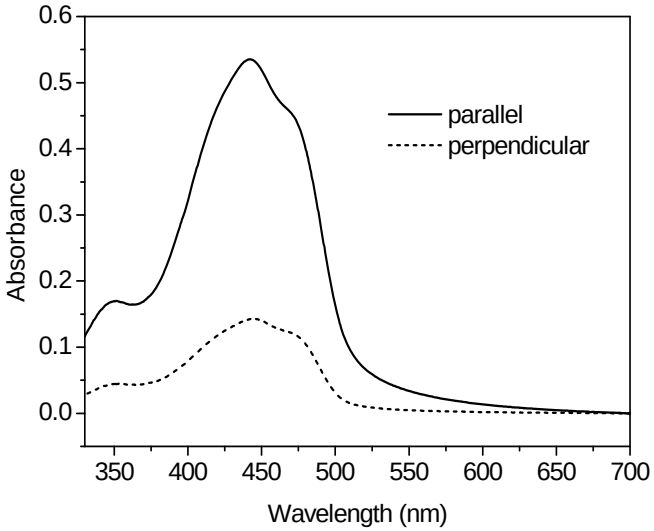

Figure 6.7. Absorption spectra of the as-cast film of **3** (n = 1) on rubbed PEDOT:PSS layer with polarized incident light parallel (solid line) or perpendicular (dashed line) to the rubbing direction.

solubility than **1** and therefore the crystallization of **2** could occur at a higher concentration in the liquid films. This might make the crystallization faster and thus lower the order of the packing of **2** in the films. In the case of OPV **3**, lower solubility and stronger intermolecular interactions could cause crystallization in solution with little influence from the interface at the alignment layer during the spin-coating, which hinders the transfer of the alignment from the substrate and thus lowers the order.

6.3.4. Other alignment layers

To investigate the effect of the alignment layer on the molecular orientation, OPV **1** film was also prepared on other alignment layers in the same manner. Interestingly, uniaxial alignment was also observed in the as-cast films of **1** on the rubbed surfaces of polyimide and poly(vinyl alcohol) with dichroic ratios of 21.7 (S = 0.87) and 40.5 (S = 0.93), respectively (Figure 6.8 and 6.9). The difference in the order parameters between the materials might suggest different interaction strengths between the surfaces and the OPVs, possibly due to polar interaction with the hexa(ethylene glycol) chains. Further investigation is necessary to elucidate the mechanism of the molecular alignment.

6.3.5. Photovoltaic devices

The molecular alignment is simply achieved by spin-coating without any further treatment, and thus can be easily applicable to thin film electronic devices. To demonstrate this, photovoltaic devices were fabricated with the configuration of ITO/PEDOT:PSS(rubbed)/OPV **1**/C_{60}/BCP/Al. Figure 6.10 shows the photosensitivity of the device under the irradiation of polarized monochromatic light. Photocurrent generation was observed when the incident light was parallel to the rubbing direction while it was almost silent when the polarization was perpendicular, resulting in a high anisotropic photosensitivity at 440 nm. Note that the small response around 350 nm in the spectrum under perpendicular light irradiation can be attributed to the contribution from the absorption of the fullerene layer. This result shows the compatibility of this molecular alignment method to the organic thin film electronic devices.

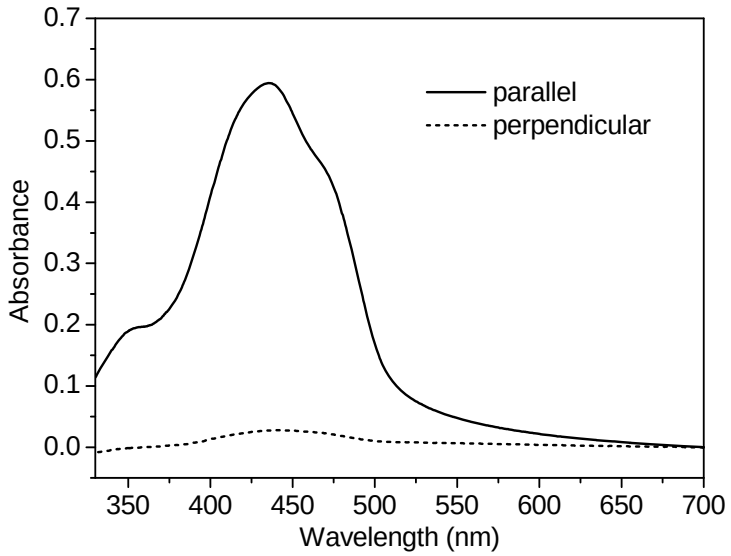

Figure 6.8. Absorption spectra of the as-cast film of **1** (n = 6) on rubbed polyimide layer with polarized incident light parallel (solid line) or perpendicular (dashed line) to the rubbing direction.

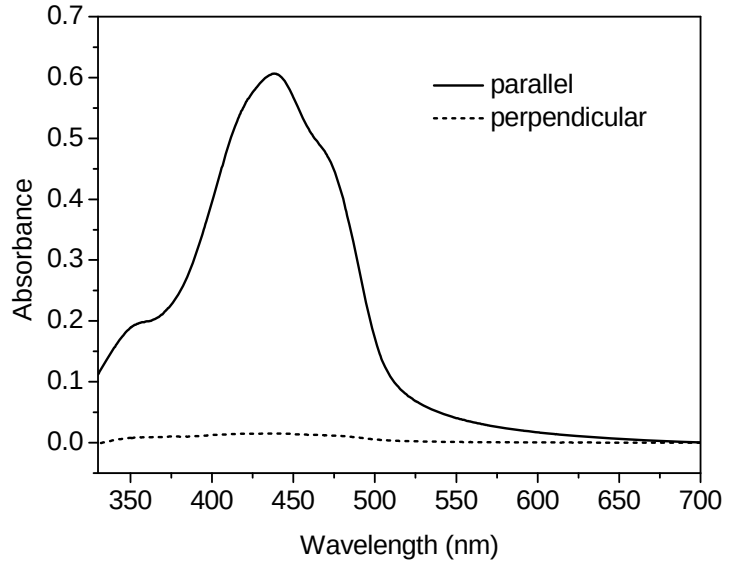

Figure 6.9. Absorption spectra of the as-cast film of **1** (n = 6) on rubbed poly(vinyl alcohol) layer with polarized incident light parallel (solid line) or perpendicular (dashed

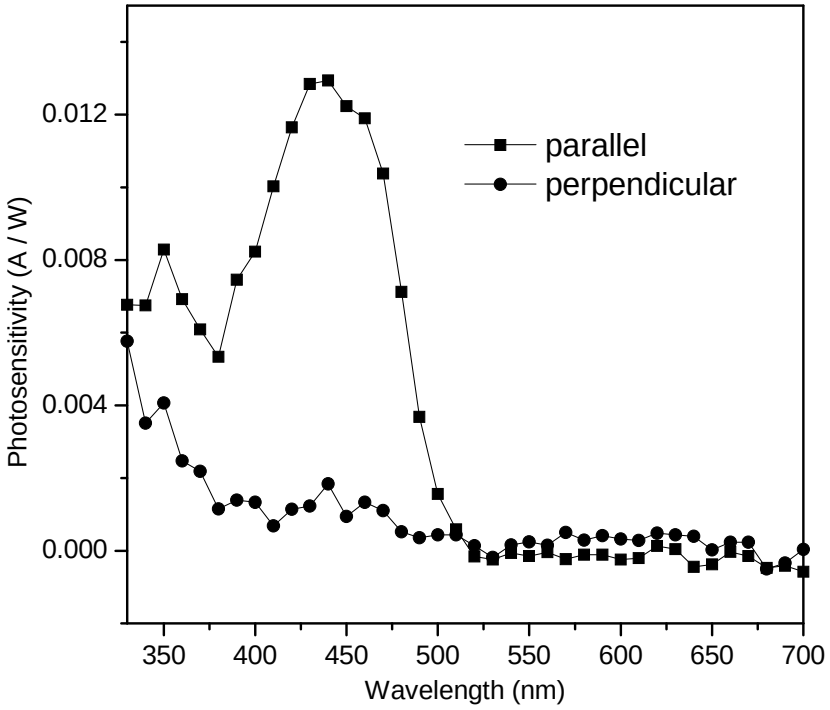

Figure 6.10. Photosensitivity of photovoltaic device with 1 (n = 6) under the irradiation of monochromatic polarized light parallel (squares) or perpendicular (circles) to the rubbing direction.

6.4. Conclusion

Highly uniaxial alignment of oligo(*p*-phenylenevinylene) derivatives was demonstrated in films during the spin-coating process by using polymer alignment layers. Application of this alignment to photovoltaic devices was also demonstrated to achieve a high anisotropic photosensitivity. This simple and easy approach provides highly aligned thin films of semiconducting OPVs both on the conductive (PEDOT:PSS) and the insulating (polyimide and poly(vinyl alcohol)) layers, which can be applied not only to photovoltaic devices but also to other organic electronic/optoelectronic devices (e.g. field effect transistors) to control the carrier flow thereby improving the efficiency of the devices.

References

1. S. Allard, M. Forster, B. Souharce, H. Thiem and U. Scherf, *Angew. Chem. Int. Ed.*, 2008, **47**, 4070.
2. Y. M. Sun, Y. Q. Liu and D. B. Zhu, *J. Mater. Chem.*, 2005, **15**, 53.
3. M. Grell and D. D. C. Bradley, *Adv. Mater.*, 1999, **11**, 895.
4. D. Neher, *Macromol. Rapid Commun.*, 2001, **22**, 1366.
5. M. Thelakkat, C. Schmitz, C. Neuber and H. W. Schmidt, *Macromol. Rapid Commun.*, 2004, **25**, 204.
6. P. Sullivan, T. S. Jones, A. J. Ferguson and S. Heutz, *Appl. Phys. Lett.*, 2007, **91**, 233114.
7. T. Nishizawa, K. Tajima and K. Hashimoto, *J. Mater. Chem.*, 2007, **17**, 2440.
8. S. Berson, R. De Bettignies, S. Bailly and S. Guillerez, *Adv. Funct. Mater.*, 2007, **17**, 1377.
9. J. Stohr and M. G. Samant, *J. Electron. Spectrosc. Relat. Phenom.*, 1999, **98-99**, 189.
10. J. Hoogboom, T. Rasing, A. E. Rowan and R. J. M. Nolte, *J. Mater. Chem.*, 2006, **16**, 1305.
11. A. Tracz, J. K. Jeszka, M. D. Watson, W. Pisula, K. Muellen and T. Pakula, *J. Am. Chem. Soc.*, 2003, **125**, 1682.
12. J. C. Wittmann and P. Smith, *Nature*, 1991, **352**, 414.
13. E. Di Cola, C. Fleury, P. Panine and M. Cloitre, *Macromolecules*, 2008, **41**, 3627.
14. H. A. Becerril, M. E. Roberts, Z. Liu, J. Locklin and Z. Bao, *Adv. Mater.*, 2008, **20**, 2588.
15. W. M. Gibbons, P. J. Shannon, S. T. Sun and B. J. Swetlin, *Nature*, 1991, **351**, 49.
16. K. Ichimura, *Chem. Rev.*, 2000, **100**, 1847.
17. M. Knaapila, R. Stepanyan, B. P. Lyons, M. Torkkeli and A. P. Monkman, *Adv. Funct. Mater.*, 2006, **16**, 599.
18. A. Gerlach, S. Sellner, S. Kowarik and F. Schreiber, *Phys. Status Solidi A*, 2008, **205**, 461.
19. R. Ruiz, D. Choudhary, B. Nickel, T. Toccoli, K. C. Chang, A. C. Mayer, P. Clancy, J. M. Blakely, R. L. Headrick, S. Iannotta and G. G. Malliaras, *Chem. Mater.*, 2004, **16**, 4497.
20. G. Witte and C. Woll, *J. Mater. Res.*, 2004, **19**, 1889.
21. S. W. Chang, A. K. Li, C. W. Liao and C. S. Hsu, *Jpn. J. Appl. Phys., Part 1*, 2002, **41**, 1374.

22. S. W. Culligan, Y. H. Geng, S. H. Chen, K. Klubek, K. M. Vaeth and C. W. Tang, *Adv. Mater.*, 2003, **15**, 1176.
23. C. Y. Chi, G. Lieser, V. Enkelmann and G. Wegner, *Macromol. Chem. Phys.*, 2005, **206**, 1597.
24. M. Knaapila, R. Stepanyan, B. P. Lyons, M. Torkkeli, T. P. A. Hase, R. Serimaa, R. Guntner, O. H. Seeck, U. Scherf and A. P. Monkman, *Macromolecules*, 2005, **38**, 2744.
25. M. Misaki, M. Chikamatsu, Y. Yoshida, R. Azumi, N. Tanigaki, K. Yase, S. Nagamatsu and Y. Ueda, *Appl. Phys. Lett.*, 2008, **93**, 023304.

Chapter 7.

Conclusion

π-Conjugated oligomer based molecules were designed and synthesized for forming proper nanostructures in organic thin film solar cells, that are proposed in this study; 10-20 nm scaled phase separated structure (formation of large interface) of the electron donor and acceptor for efficient charge separation, ordered and oriented structure of the molecules for efficient charge transport (Figure 1.1.4).

For controlling the phase separated structure of the donor and acceptor, covalently attached donor and acceptor molecule, oligothiophene-fullerene dyad was designed in Chapter 2. The dyad prevented the large phase separation which was observed in the physical mixture film of the corresponding donor and acceptor. The solar cells fabricated with the dyad achieved an improved photocurrent, compared to that in the mixture solar cells. Therefore this improvement in photocurrent generation in the dyad solar cell can be attributed to the large interface of the donor and acceptor. It is thus concluded that covalent attachment of donor and acceptor as in dyads is a promising strategy for forming a large donor/acceptor interface in the film.

Further studies of dyads were conducted in Chapter 3 and 4, aiming at formation of ordered nanostructure of the molecules to construct charge carrier pathways and thus to achieve efficient charge transport in the film. In Chapter 3, it was revealed that by mixing an oligothiophene donor into the corresponding oligothiophene-fullerene dyad, the π-π interaction of the donor groups was enhanced, leading to improvement in charge transport. Dyads with crystalline donor groups of oligo(*p*-phenylenevinylene)s (OPVs) were designed in Chapter 4. It was also revealed that introduction of crystalline OPV donors with the stronger π-π interaction achieved an improved charge transport. From these results, it is thus concluded that the strong π-π interaction of the donor groups in dyads is of importance for forming an ordered structure of the molecules and thus charge carrier pathways in the film, resulting in the efficient charge transport.

The crystalline OPV donors were also introduced to the blend film with PCBM (Chapter 5) to reveal that an OPV with the strong π-π interaction formed a crystalline network which prevented the formation of PCBM large aggregation and also formed percolated charge carrier pathways, resulting in efficient charge separation and transport in the film. It is thus concluded that the strong π-π interaction of donor materials is also of importance to form percolated charge carrier pathways as well as to prevent the large aggregation of PCBM in the mixture bulk heterojunction (BHJ) film.

Orientational control of the OPV donors in the film was conducted in Chapter 6. It was found that the designed amphiphilic OPV molecule achieves a highly uniaxially alignment on the rubbed polymer films, which was induced spontaneously during wet-coating process without any treatment such as induction of thermotropic liquid crystal phases by thermal treatment which has been applied in the conventional alignment methods. The preliminary application of this molecular alignment to solar cells was also demonstrated to achieve a high anisotropic photosensitivity. Although the mechanism of the alignment has not clarified in this study, it was suggested that amphiphilic property of the molecules can be an important factor to control the orientation of the molecules in the film.

From these achievements in this study, it is expected that introduction of orientational control into donor-acceptor dyad molecules can form highly ordered and oriented nanostructures of donor and acceptor. The schematic image of such the nanostructure is depicted in Figure 7.1. Recently, there have been computational studies on nanostructures of donor and acceptor and their efficiencies of charge separation and transport, which suggests that a chessboard-type nanostructure (Figure 7.2) is a promising structure for high efficiency [1, 2]. However, the result has not been clearly demonstrated in experiments since the formation of the chessboard-type nanostructure has been difficult. The nanostructure depicted in Figure 7.1 would thus be a model structure for experimentally proving such the computational results and also for further investigating correlation between a nanostructure of donor and acceptor and photo-induced charge transfer and subsequent charge transport in the film. Moreover, such highly ordered and oriented alignment is expected to dramatically improve the carrier transport in the film and achieve a high fill factor over 0.7 or even higher, comparable with that in inorganic

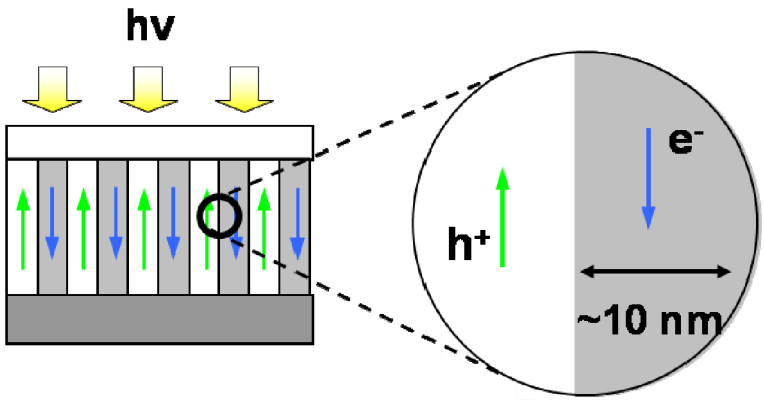

Figure 7.1. Schematic image of highly ordered and oriented nanostructure of donor and acceptor.

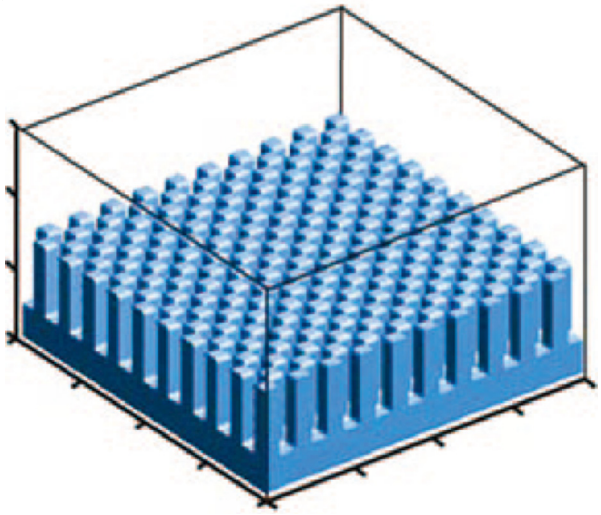

Figure 7.2. Chessboard-type heterojunction. (**ref**.2)

solar cells since the small molecules such as π-conjugated oligomers can achieve high carrier mobility over 1 cm^2 V^{-1} s^{-1} in the highly ordered and oriented thin films. It is also expected that such nanostructure can effectively absorb the incident light due to the strong coupling of the transition dipole of the molecules and the electromagnetic field of the light. This allows us to reduce the thickness of the active layer and thus distance of carrier transport, which can lead to the efficient charge transport.

The molecular orientation control in this study (Chapter 6) can also be easily applicable to other organic devices such as field effect transistors (FET) or light emitting diodes (LED). It is expected that the anisotropic orientation of the molecules can control carrier flow and opto-electronic properties of the devices including anisotropic carrier mobilities in FETs and polarized light emission in LEDs.

This study also demonstrated the high potential of donor-acceptor dyads as a photovoltaic material, and gave the insight that further molecular design such as introduction of low band gap donor can be promising strategy for achieving a high efficiency. Recently, Tamayo et al, reported that introduction of the low band gap oligomer including diketopyrrolopyrrole (α,α-DH6TDPP in Figure 1.2.37 (Chapter 1)) significantly improved the photocurrent in the BHJ device with PCBM, resulting in a high efficiency of 2.33% which is more than two-fold improvement compared to conventional oligomer-based BHJ devices [3]. Considering the efficient charge separation in dyads compared to that in mixture BHJ, demonstrated in this study, introduction of such low band gap oligomer as the donor group into dyads is expected to further improve the device efficiency. Furthermore, the orientation control of such low band gap dyads would overcome the highest efficiency reported with the state-of-the-art polymer:PCBM BHJ solar cells.

References

1. P. K. Watkins, A. B. Walker and G. L. B. Verschoor, *Nano Lett.*, 2005, **5**, 1814.
2. F. Yang and S. R. Forrest, *ACS Nano*, 2008, **2**, 1022.
3. A. B. Tamayo, B. Walker and T. Q. Nguyen, *J Phys Chem C*, 2008, **112**, 11545.

Acknowledgements

This study was conducted under the supervision of Professor Kazuhito Hashimoto from April 2006 to March 2009. In the first place, my deepest appreciation goes to Professor Kazuhito Hashimoto for his invaluable guidance on logical thinking and attractive presentation throughout the research. I would also like to appreciate his generosity to give me opportunities to attend international conferences.

I am deeply grateful to Dr. Keisuke Tajima for his direction on the research as well as organic synthesis, and fruitful discussion.

I am deeply indebted to Professor Hiroshi Irie, Professor Kayano Sunada, and Dr. Ryuhei Nakamura for their direction and stimulating suggestions during seminars.

I would like to express my profound gratitude towards the members in Dr. Tajima's group; Mr. Hady Kesuma Lim contributed greatly to the syntheses of oligo(*p*-phenylenevinylene)s; Mr. Qingshuo Wei for his help and discussion on whole research; Ms. Yue Zhang, Mr. Shoji Miyanishi, Mr. Motoshi Nakamura, Mr. Shigeyoshi Sato, Mr. Shimpei Yamakawa, Ms. Le Thu as well as ex-members in Dr. Tajima's group, Dr. Kouske Hirota, Mr. Yuya Suzuki, Ms. Kazuko Takanezawa, and Mr. Hideaki Fujimori for their kind help.

Special thanks also to Dr. Chunhe Yang and Dr. Erjun Zhou for fruitful discussion on organic photovoltaic cells as well as organic synthesis.

I am grateful to all the other members of Professor Hashimoto's Laboratory as well as ERATO and NEDO members for their help and discussion.

Finally, I would like to express my special thanks to my family and friends, who always supported and encouraged me to complete this work.

February 6, 2009

Takeshi NISHIZAWA

List of Publications

(1) “Supramolecular formation of fibrous nanostructure in donor-acceptor dyad film”

T. Nishizawa, K. Tajima, and K. Hashimoto

J. Mater. Chem., **17**, 2440-2445, 2007. *Selected as a Hot Paper*

(2)”The effect of crystallinity in donor groups on the performance of photovoltaic devices based on an oligothiophene-fullerene dyad”

T. Nishizawa, K. Tajima, and K. Hashimoto.

Nanotechnology, **19**, 424017, 2008.

(3)”Highly uniaxial orientation in oligo(p-phenylenevinylene) films induced during wet coating process”

T. Nishizawa, H. K. Lim, K. Tajima, and K. Hashimoto.

J. Am. Chem. Soc., in press.

(4)”Efficient dyad-based organic solar cells with highly crystalline donor group”

T. Nishizawa, H. K. Lim, K. Tajima, and K. Hashimoto.

manuscript is submitted.

(5)”Effect of the crystallinity on morphology and performance in oligomer-based solar cells”

T. Nishizawa, H. K. Lim, K. Tajima, and K. Hashimoto.

manuscript is submitted.